Analysis of drug polymorphism by diffuse reflectance visible spectroscopy- a novel approach

BY

TRACY OMOSOGHOGHO EHIWE

[BSc. (Hons.), AMRSC]

A thesis submitted in partial fulfilment of the requirements of the
University of Greenwich for the degree of Doctor of Philosophy

September 2011

School of Science,

University of Greenwich, Medway Campus,

Chatham Maritime, Kent ME4 4TB, UK.

DECLARATION

"I certify that this work has not been accepted in substance for any degree, and is not concurrently being submitted for any degree, other than that of the PhD, being studied at the University of Greenwich. I also declare that this work is the result of my own investigations except where otherwise identified by references and that I have not plagiarised another's work".

(Tracy O. Ehiwe)

…………………………………………………………………………………………..

PhD Supervisors

(Prof. J.C. Mitchell)

(Prof. M. J. Snowden)

09 -09-2011

ACKNOWLEDGEMENTS

I am grateful to God Almighty, through whom I exist. This thesis would have not been produced except for the input of people to whom I am ever grateful.

Foremost, I am deeply appreciative of and grateful to my main supervisor Professor John Mitchell. His positive attitude, patience, enthusiasm, and immense knowledge made research study an invaluable experience. The encouragement, sound advice and intellectual support he provided throughout the period of writing this thesis, ensured that I did an excellent work. My sincere thanks go to my co-supervisor Professor Martin Snowden. Thank you very much for all the words of encouragement, your faith in my abilities inspired me to work hard.

I wish to express my sincere gratitude to the Medway Science team, past and present for sharing their enthusiasm for science and for being such good friends. Their concern and support created a pleasant working environment.

I am indebted to my family for all the care and support they accorded to me. My parents, Godwin and Beauty never fail to motivate me. Their prayers, wise words and support both financially and emotionally have always been timely. I am grateful to my twin sister, Tammy, we literally started this journey together, you know firsthand what challenges I faced and with your support I triumphed. My younger siblings, Isabel and Peter, thank you very much for the many ways you supported me. Tolu and my other friends at church, whom I now call family, thank you for praying for creativity and inspiration to write this thesis. I'm truly blessed to have such wonderful people as family. Dr Stuart Jones, my boss at Laserchrom HPLC Laboratories Ltd, I am very grateful for the days and nights spent proof reading this work.

Franklin, thank you for always being there for me, and enriching my life in many ways.

ABSTRACT

Analysis of drug polymorphism by diffuse reflectance visible spectroscopy- a novel approach

The existence of polymorphic forms of drug substances has implications for therapeutic performance, handling and storage. This study investigates the development of a novel approach to surface analysis of drug polymorphs, with the aim of extending the capabilities of this approach to perform real time analysis of polymorphic transformation during pharmaceutical product development.

This was achieved here, using diffuse reflectance visible spectroscopy (DRVS) and the colour change which occurs when pH indicator dyes are deposited on the surface. The pH indicators used were phenol red (PR), thymol blue (TB) and methyl red (MR). Two polymorphs each of indomethacin (IMC), carbamazepine (CBZ), caffeine (CFN), sulfanilamide (SFN) and furosemide (FRS) were examined. The interaction of the adsorbed dye with each of the polymorphs showed different behaviour, manifested by different colours. An analysis of the crystal structures and the acid/base properties of the drug molecules provided a rationalisation for the different colours exhibited by the polymorphs' surfaces. The least stable form of each polymorphic pair studied showed more extensive interaction with the adsorbed dye molecules. Observed colour reveal underlying differences at a molecular level between the surfaces of pairs of polymorphs.

The different colours exhibited by the indomethacin polymorphs were further examined using hygroscopicity studies, contact angle measurements and computer simulation. The contact angles of several liquids with the polymorph surface were measured in order to characterise the nature of the functional groups exposed on the surface of the polymorphs. The surface structure and external morphologies of polymorphs were predicted by molecular modelling using the attachment energy model. The predicted morphology was confirmed by scanning electron micrographs (SEM) and the miller index of the dominant face was confirmed by X-ray powder diffraction (XRD). Results revealed that although the surfaces of both polymorphs are largely hydrophobic, the metastable form- IMC-α has a greater number of polar functional groups on the surface.

Further measurements were carried out using DRVS and adsorbed TB to study the kinetics of the solid-state transformation of SFN-β to SFN-γ . The rate of transformation was followed at 128ºC by monitoring the ratio of the two DRVS bands at 454 nm and 604 nm. The kinetic data was analysed using sixteen solid-state kinetic models to obtain the best fit. The thermally induced polymorphic transformation of the SFN-β (particle size of $\geq$ 450μm) can be best described by the first order kinetic model (R^2 = 0.992) with a rate constant, k of 2.43 x 10^2 s^{-1}. The DRVS instrument used herein is not adapted for *in situ* studies; however, because of its non-destructive interaction with the sample and rapid data collection time of 5s per spectrum, it does offer considerable potential as a tool for real time monitoring of polymorphic transformation.

Tracy Omosoghogho Ehiwe [BSc (Hons), AMRSC]

CONTENTS

LIST OF FIGURES

xiii

polymorphs.

LIST OF TABLES

ABBREVIATIONS

AA	*Adjacent Averaging algorithm*
API	*Active Pharmaceutical Ingredients*
BET	*Brunauer Emmett and Teller*
CBZ	*Carbamazepine*
CCSD	*Cambridge Crystal Strctural Database*
CFN	*Caffeine*
DRV	*Diffuse Reflectance Visible Spectroscopy*
DSC	*Differential Scanning Calorimetry*
EMEA	*European Medicines Agency*
E-T	*Energy- Temperature*
FRS	*Furosemide*
FDA	*Food and Drugs Agency*
FT	*Fourier Transform*
HOMO	*Highest Occupied Molecular Orbital*
HPLC	*High Performance Liquid Chromatography*
HSM	*Hot-Stage Microscopy*
ICH	*International Centre for Harmonisation*
IMC	*Indomethacin*
KM	*Kubelka-Munk*
LUMO	*Lowest Unoccupied Molecular Orbital*
MHRA	*Medicines and Health products Regulatory Agency*
MR	*Methyl red*
NIR	*Near infrared*
NMR	*Nuclear Magnetic Resonance*
PAT	*Process Analytical Technology*
PR	*Phenol red*
PXRD	*Powder X-ray Diffraction*
SEM	*Scanning Electron Microscopy*
SIMS	*Secondary ion mass spectrometry*
SFN	*Sulfanilamide*
SSA	*Specific Surface Area*

TB	*Thymol blue*
UV-Vis	*Ultraviolet –Visible Spectroscopy*
XPS	*X-ray photoelectron spectroscopy*

PUBLICATIONS AND PRESENTATIONS

PRESENTATIONS

Ehiwe, T. (Aug 2009). Molecular probes for the analysis of the surface chemistry of drug polymorphs. *Oral presentation at the International Union of Pure and Applied Chemistry (IUPAC) Congress, Glasgow, Scotland.*

Ehiwe, T. (Jul 2009). Molecular probes for the analysis of the surface chemistry of drug polymorphs. *Oral presentation at the National Analytical Research Forum (ARF), Kent, England.*

Ehiwe, T. (May 2009). Molecular probes for the analysis of the surface chemistry of drug polymorphs. *Oral presentation at the Emerging Analytical Professionals (EAP) Conference, Dunfermline, Scotland*

Ehiwe, T. (Jul 2008). Chromic probe for drug polymorphism. *Poster presentation at RSC Industry Tour of Pfizer, Kent, UK*

PUBLICATIONS

Ehiwe, T., Mitchell, J. and Snowden, M. (2011). Apparent discrimination of drug polymorphs by halochromic molecular probes. *Chem. Comm.* Manuscript in preparation.

Ehiwe, T., Mitchell, J, Alexander, B.. and Snowden, M. (2009) Molecular probes for the analysis of the surface chemistry of drug polymorphs. *Book of Abstracts IUPAC Congress*

DEDICATIONS

My Heavenly Father, Thank you

I never could have made it without You...

Chapter 1: Project Overview

1.1 Introduction

It is a very common occurrence for many small organic drug molecules (molecular weights less than 600) to exhibit polymorphism[1, 2]. Polymorphism is the ability of a particular solid substance to exist in multiple crystalline forms as a result of different arrangements and/or conformations of its molecules[3-5]. Non-covalent interactions (such as hydrogen bonding, van der Waals forces, π-π stacking and electrostatic interactions) between molecules of polymorphs results in differences in physical properties such as melting point, dissolution rate, hygroscopicity and stability. These in turn may affect pharmacological activity, handling and shelf-life[3]. Table 1.1 lists the physical properties that differ among polymorphs.

Table 1.1 List of physical properties that differ among various polymorphs[4]

Packing properties	Molar volume and density, refractive index, electrical and thermal conductivity and hygroscopicity
Thermodynamic properties	Melting and sublimation temperatures, internal energy, enthalpy, heat capacity, entropy, free energy and chemical potential
Spectroscopic properties	Electronic, vibrational and nuclear spin transitions.
Kinetic properties	Dissolution rate, rate of solid state reactions and stability
Surface properties	Surface free energy, surface chemistry, morphology
Mechanical properties	Hardness, tensile strength, compactability (tabletting) handling, flow and blending

1.2 Implication of drug polymorphism in the pharmaceutical industry

The implications of variation in the properties of polymorphs of a drug can be described under the following headings, which form the main concerns for the pharmaceutical industry.

1. <u>Pharmacological activity.</u> Polymorphism impacts a drug's pharmacological activity by affecting bioavailability. Bioavailability is the rate and extent to which a drug substance is absorbed and circulated *in vivo*[6]. Polymorphs have different dissolution rates, therefore different rates of *in vivo* absorption and thus differences in bioavailability. Differences in the rates of dissolution among polymorphs is typically less than tenfold[7]. Exceptional differences in dissolution rates have been observed, for example the drug ritonavir used for the treatment of (HIV) has two polymorphs (Form I and Form II) that differ substantially in dissolution rate. Form II has a dissolution rate that is fifty-fold slower than Form I [8, 9]. Hence Form I (with a faster dissolution rate) is the candidate polymorph used in formulations.

2. <u>Stability.</u> Variations in the chemical reactivity affect the stability (shelf-life) of polymorphs. Polymorphs possess differences in chemical reactivity, both intrinsically and under the influence of environmental factors such as light and moisture, formulation ingredients (excipients), manufacturing processes and packaging materials. Solid-state phase transformations, dehydration/desolvation, degradation and decompositions are many of the reactions that compromise the potency of the drug substance[10]. For example, the photostability of three polymorphs of carbamazepine namely Form I, Form II and Form III have been evaluated[11]. Form II showed the fastest discolouration rate under ultraviolet radiation.

3. <u>Ease of processing.</u> The differences in the mechanical properties such as tensile strength, flow, compactibility and crystal morphologies between various polymorphic forms have implications on the processing and compaction behaviour. For example paracetamol polymorphs show different mechanical properties, Form II can be directly compressed into tablets while Form I lacks such compactability[12].

4. <u>Regulatory Issues.</u> Regulatory agencies such as the UK Medicines and Health products Regulatory Agency (MHRA), US Food and Drug Agency (FDA) and European Medicines Agency (EMEA) function to ensure that manufactured drug products meet quality, safety and efficacy requirements.

Polymorphism can have an effect on drug product safety and efficacy, and hence drug quality. Therefore regulatory agencies set detailed controls in place to ensure compliance.

A comprehensive analysis of polymorphic behaviour in active pharmaceutical ingredients (APIs) is an essential and mandatory aspect of the drug development process. In order to gain approval for the marketing of a drug, a company must demonstrate that the proposed drug meets the adequate bioavailability, stability and processability requirements in regulatory document submissions [13-18].

5. <u>Patent establishment and protection.</u> Since the polymorphs of a substance represents different crystal structures with different properties the discovery or preparation of a new crystal modification are potentially patentable. This will bring economic benefit to innovative companies because the company will have exclusive rights not only for marketing, but also for further screening for potential new forms for a set time period.

1.3 Polymorphism analysis and process analytical technology (PAT)

Physical properties differ between polymorphs (Table 1.1) as a consequence of different crystal structures. The differences in properties allow the application of a broad spectrum of analytical techniques for polymorphism study and characterisation. Many solid-state analytical techniques such as spectroscopy, crystallography, microscopy and thermal methods, are used either alone or interfaced with another technique to characterise polymorphs[3-5, 19]. Many of the above mentioned techniques provide valuable information but they are not all capable of real time (*in situ*) analysis.

The Process Analytical Technology (PAT) framework, introduced by the United States Food and Drug Agency (FDA) in collaboration with industry experts encourages assimilation of technology capable of real time analysis to ensure quality control and assurance is built-in by design[13, 20-22]. PAT is a system of designing, analysing and controlling processes based on timely measurements of critical and quality attributes of raw and in process materials with the ultimate goal of ensuring quality.

In the context of polymorphism, PAT provides the continuous assurance that the desired form of a drug substance remains unchanged (critical sources of polymorphic variability can be easily identified and processes and conditions designed to control variability).

Better control means better understanding of the product and processes to reduce manufacturing time and lessen the chances of product failures and recalls. The pharmaceutical industry has, however, not fully incorporated real-time monitoring due to regulatory requirements, cost and technical training required to introduce new methods[23].

PAT tools are capable of rapid, reliable and reproducible data generation, resulting in increased throughput. Additionally, they also have a relatively easy mode of operation and sample preparation. Spectroscopic methods such as Near-infrared (NIR), mid-IR and Raman techniques, exhibit the aforementioned characteristics and so are the main PAT tools for *in situ* analysis of polymorphism. Examples of other current applications include the monitoring of pharmaceutical processes such as drying, blending, tabletting and monitoring of polymorphism[24-28].

1.4 Chromism and visible spectroscopy

Chromism describes the phenomenon of reversible change in the colour of a substance in response to a stimulus. Examples include thermochromism, photochromism, halochromism and solvatochromism; the respective stimuli being temperature, light, pH and solvent polarity. When a substance undergoes a colour change the electronic properties of the molecules also change. Hence visible spectroscopy (colourimetric analysis) offers an excellent way of characterising chromic substances.

The electronic structural change associated with a colour change could be at a molecular level or due to changes in crystal packing or a combination of both [19,20]. The polymorphs of certain solids have different colours; these solids are described as being crystallochromic in nature and their polymorphs have unique visible spectra. An example is 5-methyl-2-[(2-nitrophenyl) amino]-3-thiophenecarbonitrile, aka ROY. Figure 1.1 shows six of the polymorphs of ROY named OP, ON, R, Y, ORP and YN by their discoverers[29]. These polymorphs show colour and morphological variations that make them easily distinguishable, and hence readily analysed by visible spectroscopy.
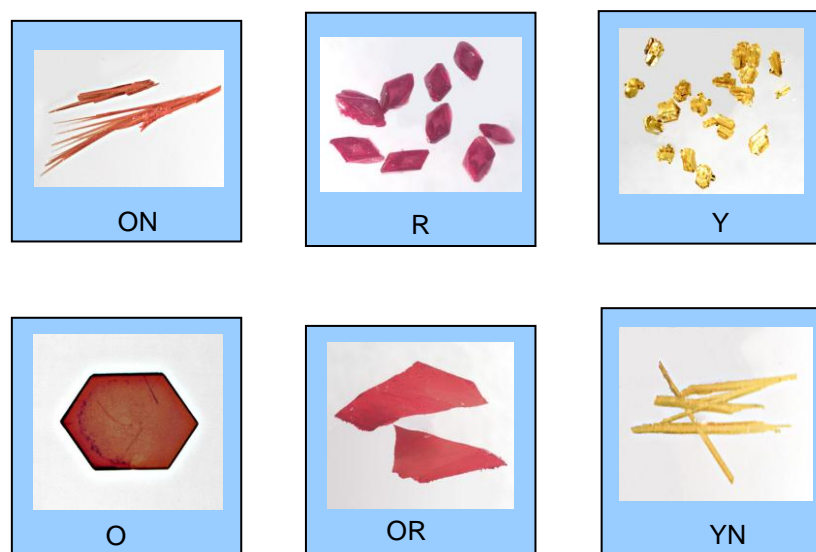
Figure 1.1 The polymorphs of crystallochromic 5-methyl-2-[(2-nitrophenyl) amino]-3-thiophenecarbonitrile aka ROY.

Drug polymorphs are inherently non-crystallochromic, so direct characterisation of polymorphs by visible spectroscopy is not common place. The indirect approach that this work explores is to characterise the interaction between polymorphs and a chromogenic substance. A chromogenic substance is one that is capable of exhibiting chromism, such as a pH indicator dye.

1.5 Surface acidity/basicity

The acidity or basicity of drug substances dissolved in an aqueous medium is expressed in term of the pH (=-log [H+]), however for solid surface acidity/basicity an adequate expression is lacking. A widely-employed means for the evaluation of the surface acidity of compounds of pharmaceutical interest is the indicator dye sorption method. This method is an empirical approach that observes the degree of ionisation of an adsorbed indicator dye[30-33].

Surface acidity/basicity of polymorphs could potentially provide a stimulus for colour changes. APIs are mainly weakly acidic or basic, and it is possible that the surface of their polymorphs will vary in acidity or basicity, it may therefore be possible to differentiate between polymorphs using a pH indicator dye.

1.6 Objectives of the project
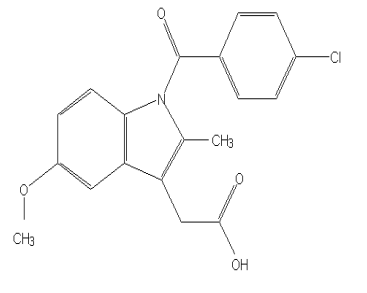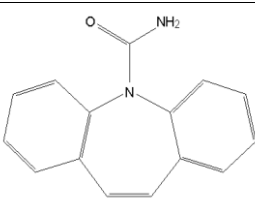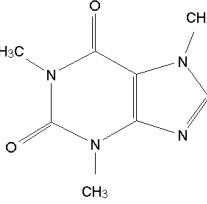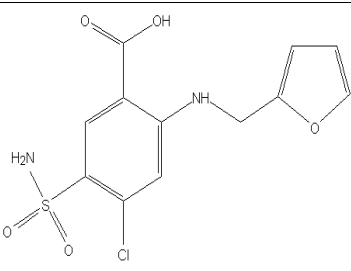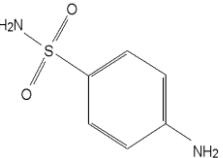
The aim of the work reported herein is to explore the possibility of characterisation of polymorphic forms of drug substances *in situ*, with the aid of a pH indicator dye and diffuse reflectance visible spectroscopy. This novel approach employs pH indicator dyes as "**colorimetric sensors**" for polymorphic form.

The surface acidity differences between polymorphs of a solid have not been previously characterised by pH indicator dyes. The work reported in this thesis also intends to substantiate the conjecture that the polymorphs of a drug substance can be characterised, because they expose different acidic or basic functional groups or different numbers of the same acidic or basic functional groups on their surfaces.

This approach potentially provides a relatively inexpensive method for the discrimination of polymorphism, and the monitoring of polymorphic transformation in real-time. It is comparatively quick and easy to use, and relatively cheap when compared to PAT tools such as Raman and infrared spectroscopy.
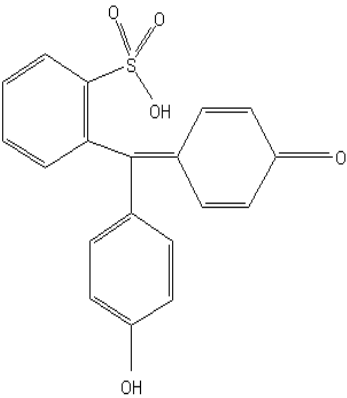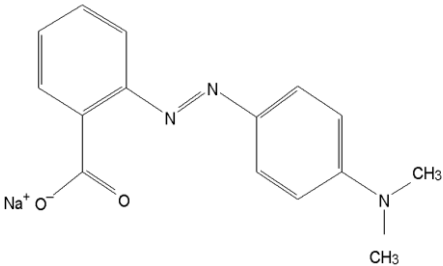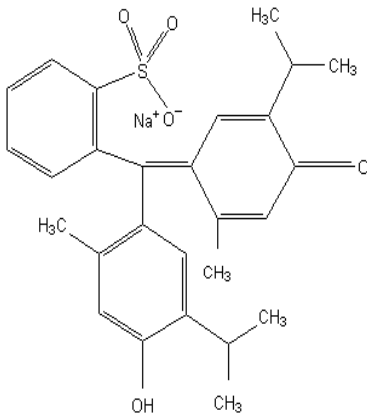
Five model drugs (indomethacin (IMC), carbamazepine (CBZ), caffeine (CFN), furosemide (FRS) and sulfanilamide (SFN) - Table 1.1) and three model pH indicator dyes (phenol red (PR), thymol blue (TB) and methyl red (MR) - Table 1.2) are used in the work reported in this thesis.

Table 1.2 The five model polymorphic drug systems used in this study and their physical properties

			Aqueous solubility[*] g/L:	Polymorphs studied:
Indomethacin (IMC)	**IUPAC Name:** [1-(4-chlorobenzoyl) - 5-methoxy-2-methyl-1H-indol-3-yl]acetic acid	**Molecular Weight:** 357.79 g/mol	0.02	α^{34}
	Therapeutic class: Analgesic, antipyretic	**Molecular Formula:** $C_{19}H_{16}ClNO_4$		γ^{35}
Carbamazepine (CBZ)	**IUPAC Name:** 5H-dibenzo [b,f]azepine-5-carboxamide	**Molecular Weight:** 236.27 g/mol	0.22	I^{36}
	Therapeutic Class: Anticonvulsant	**Molecular Formula:** $C_{15}H_{12}N_2O$		III^{37}
Caffeine (CFN)	**IUPAC Name:** 1,3,7-trimethyl-3,7-dihydro-1H-purine-2,6-dione	**Molecular Weight:** 194.19 g/mol	58.90	I^{38}
	Therapeutic Class: Stimulant	**Molecular Formula:** $C_8H_{10}N_4O_2$		II^{38}
Furosemide (FRS)	**IUPAC Name:** 5-(aminosulfonyl)-4-chloro-2-[(2-furyl methyl)amino] benzoic acid	**Molecular Weight:** 330.74 g/mol	0.12	I^{39}
	Therapeutic Class: Diuretic	**Molecular Formula:** $C_{12}H_{11}ClN_2O_5S$		II^{39}
Sulfanilamide (SFN)	**IUPAC Name:** 4-aminobenzene sulfonamide	**Molecular Weight:** 172.21 g/mol	11.10	β^{40}
	Therapeutic class: Antibacterial	**Molecular Formula:** $C_6H_8N_2O_2S$		γ^{41}

The aqueous solubilities of the drug compounds (at 25ºC) were obtained using the advanced chemistry development ACD/I-Lab Web service

Table 1.3 The model dye compounds used in this study and their physical properties

Molecular Formula	$C_{19}H_{14}O_5S$	$C_{15}H_{14}N_3O_2Na$	$C_{27}H_{29}O_5SNa$
IUPAC name	4-[3-(4-hydroxyphenyl)-1,1-dioxobenzo[c]oxathiol-3-yl] phenol	2-[4-(Dimethylamino)phenylazo]benzoic acid sodium salt	4-[3-(4-hydroxy-2-methyl-5-propan-2-ylphenyl)-1,1-dioxobenzo[c]oxathio l-3-yl]-5-methyl-2-propan-2-ylphenol sodium salt
Synonyms	Phenol red, Phenolsulfonphthalein	Methyl red sodium,	Thymolsulfonphthalein, Thymol blue sodium
M.Wt / gmol^{-1}	354	291	489
Solubility[42] /mgml^{-1}	3 (Water)	70 (Water)	60 (Water)
	4 (Ethanol)	40 (Ethanol)	40 (Ethanol)
Melting point/ °C	Decomposes at > 300	179-182	283-285
Dye class	Diprotic sulfonphthalein	Monoprotic azo dye	Diprotic sulfonphthalein

The following chapters in this work encompass the theoretical background and experimental studies crucial to the fundamental understanding of polymorphic drug systems and the novel application of diffuse reflectance visible spectroscopy (DRVS) to polymorphic form analysis.

A brief overview of the relevant background to drug polymorphism and surface acidity is presented in Chapter two in two parts. The first part deals with the theoretical tools of thermodynamics and structural aspects of polymorphism, generation and characterisation of polymorphic forms. The second part discusses the acid-base concepts both in solution and on the surface, and halochromic dye chemistry. The concept of perichromism was also introduced which examines the effect of the surrounding environment on the UV-Vis spectral properties of the pH indicator molecules.

In Chapter three, the main experimental techniques used in this work are described. These are, powder x-ray diffraction (PXRD), Raman spectroscopy, hot-stage microscopy (HSM), scanning electron microscopy (SEM), differential scanning calorimetry (DSC) and diffuse reflectance visible spectroscopy (DRVS). Instrument calibration, data interpretation, experimental factors that affect the quality of data are discussed.

The work reported in Chapter four covers the synthesis and characterisation of the five model polymorphic systems using the instrumental techniques described above.

Chapter five reports work undertaken on halochromic dyes which were attached to the model polymorphs and analysed by DRVS.

The mechanism of differential colouring of indomethacin (IMC) polymorphs has been further examined in Chapter Six. The study is performed using contact angle measurements, morphology prediction methods, scanning electron micrographs (SEM) and X-ray powder diffraction (PXRD).

The polymorphic transformation of form β to γ of sulfanilamide (SFN) monitored using the novel colourimetric approach is reported in Chapter Seven.

Although the DRVS system used for monitoring polymorphic transformation have not been adapted for *in situ* studies, the potential for in situ measurements is demonstrated.

1.7 References

1.   C. A. Lipinski, F. Lombardo, B. W. Dominy and P. J. Feeney, *Advanced Drug Delivery Reviews*, 2001, **46**, 3-26.

2.   U. Griesser and J. Stowell, in *Pharmaceutical Analysis*, eds. D. Lee and W. Micheal, Blackwell Publishing, Oxford, 2003.

3.   R. Hilfiker, *Polymorphism: In the Pharmaceutical Industry*, Wiley-VCH ; [Chichester : John Wiley [distributor]], Weinheim, 2006.

4.   H. G. Brittain, *Polymorphism in Pharmaceutical Solids*, Marcel Dekker, New York, 1999.

5.   J. Bernstein, *Polymorphism in Molecular Crystals*, Oxford University Press, New York ; Oxford, 2002.

6.   L. Illum, *International Journal of Pharmaceutics*, 2002, **241**, 391-393.

7.   L.-F. Huang and W.-Q. Tong, *Advanced Drug Delivery Reviews*, 2004, **56**, 321-334.

8.   S. R. Chemburkar, J. Bauer, K. Deming, H. Spiwek, K. Patel, J. Morris, R. Henry, S. Spanton, W. Dziki, W. Porter, J. Quick, P. Bauer, J. Donaubauer, B. A. Narayanan, M. Soldani, D. Riley and K. McFarland, *Organic Process Research & Development*, 2000, **4**, 413-417.

9.   J. Bauer, S. Spanton, R. Henry, J. Quick, W. Dziki, W. Porter and J. Morris, *Pharmaceutical Research*, 2001, **18**, 859-866.

10.   S. R. Byrn, W. Xu and A. W. Newman, *Advanced Drug Delivery Reviews*, 2001, **48**, 115-136.

11.   Y. Matsuda, R. Akazawa, R. Teraoka and M. Otsuka, *Journal of Pharmacy and Pharmacology*, 1994, **46**, 162-167.

12.   E. Joiris, P. D. Martino, C. Berneron, A.-M. Guyot-Hermann and J.-C. Guyot, *Pharmaceutical Research*, 1998, **15**, 1122-1130.

13.   Anon, ANDAs:Pharmaceutical solid polymorphism. Chemistry, Manufacturing and controls information, http://www.fda.gov/downloads/Drugs/GuidanceCompliance RegulatoryInformation/Guidances/ucm072866.pdf#7.

14.   A. S. Raw and L. X. Yu, *Advanced Drug Delivery Reviews*, 2004, **56**, 235-236.

15. A. S. Raw, M. S. Furness, D. S. Gill, R. C. Adams, F. O. Holcombe and L. X. Yu, *Advanced Drug Delivery Reviews*, 2004, **56**, 397-414.

16. L. X. Yu, M. S. Furness, A. Raw, K. P. W. Outlaw, N. E. Nashed, E. Ramos, S. P. F. Miller, R. C. Adams, F. Fang, R. M. Patel, F. O. Holcombe, Y. Y. Chiu and A. S. Hussain, *Pharmaceutical Research*, 2003, **20**, 531-536.

17. D. A. Snider, W. Addicks and W. Owens, *Advanced Drug Delivery Reviews*, 2004, **56**, 391-395.

18. D. J. W. Grant and S. R. Byrn, *Advanced Drug Delivery Reviews*, 2004, **56**, 237-239.

19. H. G. Brittain, *Spectroscopy of Pharmaceutical Solids*, Taylor & Francis, New York ; London, 2006.

20. D. Hinz, *Analytical and Bioanalytical Chemistry*, 2006, **384**, 1036-1042.

21. L. Bush, *Pharmaceutical Technology*, 2004, **28**, 34-44.

22. U. F. a. D. Administration, US Food and Drug Administration, 2004.

23. L. Abboud and S. Hensley, in *Wall Street Journal*, New York, 2003.

24. G. Févotte, J. Calas, F. Puel and C. Hoff, *International Journal of Pharmaceutics*, 2004, **273**, 159-169.

25. M. Blanco, M. Alcalá, J. M. González and E. Torras, *Analytica Chimica Acta*, 2006, **567**, 262-268.

26. J. Luypaert, D. L. Massart and Y. Vander Heyden, *Talanta*, 2007, **72**, 865-883.

27. J. J. Moes, M. M. Ruijken, E. Gout, H. W. Frijlink and M. I. Ugwoke, *International Journal of Pharmaceutics*, 2008, **357**, 108-118.

28. R. Kobayashi, Y. Fujimaki, T. Ukita and Y. Hiyama, *Organic Process Research & Development*, 2006, **10**, 1219-1226.

29. Reed S., Weakley Chen S., Guzei A. and Yu L. (2005). New polymorphs of ROY and new record for coexisting polymorphs of solved structures. *J. Ame. Chem. Soc.* **127**: 9881-9885.

30. B. W. Glombitza, D. Oelkrug and P. C. Schmidt, *European Journal of Pharmaceutics and Biopharmaceutics*, 1994, **40**, 289-293.

31. B. W. Glombitza and P. C. Schmidt, *European Journal of Pharmaceutics and Biopharmaceutics*, 1995, **41**, 114-119.

32. C. A. Scheef, D. Oelkrug and P. C. Schmidt, *European Journal of Pharmaceutics and Biopharmaceutics*, 1998, **46**, 209-213.

33. R. Govindarajan, A. Zinchuk, B. Hancock, E. Shalaev and R. Suryanarayanan, *Pharmaceutical Research*, 2006, **23**, 2454-2468.

34. X. Chen, K. R. Morris, U. J. Griesser, S. R. Byrn and J. G. Stowell, *Journal of the American Chemical Society*, 2002, **124**, 15012-15019.

35. T. J. Kistenmacher and R. E. Marsh, *Journal of the American Chemical Society*, 1972, **94**, 1340-1345.

36. A. L. Grzesiak, M. D. Lang, K. Kim and A. J. Matzger, *Journal of Pharmaceutical Sciences*, 2003, **92**, 2260-2271.

37. V. L. Himes, A. D. Mighell and W. H. De Camp, *Acta Crystallographica Section B*, 1981, **37**, 2242-2245.

38. G. D. Enright, V. V. Terskikh, D. H. Brouwer and J. A. Ripmeester, *Crystal Growth & Design*, 2007, **7**, 1406-1410.

39. Y. Matsuda and E. Tatsumi, *International Journal of Pharmaceutics*, 1990, **60**, 11-26.

40. A. M. O'Connell and E. N. Maslen, *Acta Crystallographica*, 1967, **22**, 134-145.

41. M. Alleaume and J. Decap, *Acta Crystallographica*, 1965, **19**, 934-938.

42. F. Green, *The Sigma-Aldrich Handbook of Stains, Dyes and Indicators*, Aldrich Chemical Company, Winsconsin, 1990.

Chapter Two: Drug polymorphism and Surface acidity/basicity

Part I: Polymorphism in drug substances

2.1 Definition of polymorphism

Polymorphism is the ability of a solid to exist IN different crystalline forms. These crystalline forms are chemically similar but structurally dissimilar. Chemical similarity refers to the fact that the same molecules (or conformers) make up the polymorphs and structural dissimilarity refers to differences in molecular packing motifs or difference in the crystal structure of the solid. An array of non-covalent intra- and intermolecular[1-3] interactions (such as van der Waals, hydrogen bonding and π-π stacking) between molecules in polymorphs allows for diversity in crystal structure. A consequence of the occurrence of polymorphism is variation in different physical properties, as listed in Table 1.1 (Chapter 1).

According to the pharmaceutical regulatory globalization project/International Conference of Harmonization (ICH) guidelines, the term polymorphism can be used to refer to the two solid state forms of a substance, where one is crystalline and the other amorphous (see Fig 2.1) [4-7]. The term can also be used to refer to two crystalline forms of a substance, where one contains a solvent of crystallisation and the other does not. The solvated form is referred to as a pseudopolymorph. However, true polymorphism refers to two or more forms of a substance which are chemically identical but exhibit different crystal structures.

 A crystalline solid is commonly defined as a solid with the dominant long-range molecular packing order while an amorphous solid is one where short-range molecular packing order or disordered packing is prevalent. The arrangement of molecules of an amorphous solid can be considered as random. Some degree of localized order is present in most amorphous solids but this localized order is not propagated as is the case for crystalline solids[8-10]. According to Cui[10], in the crystalline state molecules arrange highly regularly both in short-range (order amongst neighbouring molecules) and long-range while in the amorphous state neighbouring molecular order does not extend further than a couple of molecules.

Solvates are crystalline forms containing two different types of molecules with one of the molecules being an organic solvent or water (usually termed a hydrate).
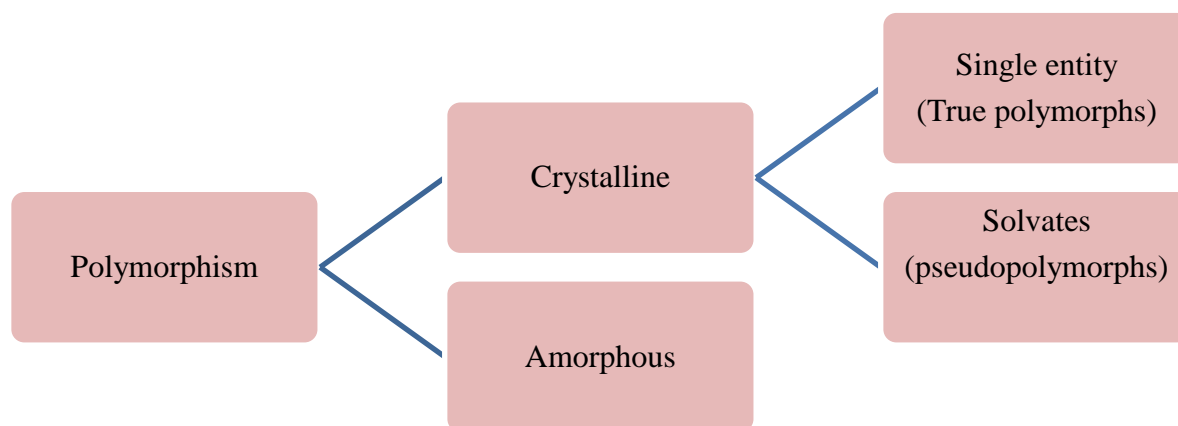
Figure 2. 1 The broad definition of polymorphism according to the ICH guidelines

The broad definition of polymorphism by the ICH is used in many regulatory documents. In general the different solid forms (especially crystalline forms) are discussed together but most authors draw a clear distinction between the true polymorphs and the other solid forms. True polymorphs are the main focus of this work and so, this is what is implied when the term polymorphism is used.

2.2 Structural and thermodynamic aspects of polymorphism

Non-covalent interactions between molecules of polymorphs result in differences in structure and thermodynamic stability. Thus an understanding of supramolecular or crystalline structure and thermodynamics of polymorphism are fundamental to effective analysis.

2.2.1 Structural aspects

Polymorphs are crystalline in nature and have a precise and ordered arrangement of the molecules in the crystal structure. An examination of the geometry of the internal structure, crystal packing and crystal morphology provides an appreciation of the differences that exists between polymorphs.

> ➤ Crystal Geometry

The crystal structure is a framework that contains a unique, regular and periodic arrangement of molecules in the solid, which are arranged in defined three dimensional planes. A crystal structure exhibits long-range order and symmetry; it can be described as a regular periodic three dimensional array of points that form a defined lattice, which can be defined mathematically. These lattice points have the same surroundings in the same orientation[11]. Crystal structures can be described by placing a structural motif on the lattice point. This structural motif can be an atom or a group of atoms. The fundamental unit that describes a crystal is the unit cell [12, 13]. Unit cells are the smallest repeating structural unit of a crystal, and form the basis of crystallographic classification [11]. Unit cells have classic geometric properties, and can be described by parameters of lengths of the crystal axes (*a*, *b* and *c*), the angles between these axes (α, β and γ) and hence definite volume *V*. By convention α is the angle between *b* and *c* axes, β is the angle between *a* and c axes, and γ is the angle between *a* and *b* axes. The unit cell can also be drawn with reference to three mutually perpendicular axes *x*, *y* and *z*, it follows that when $\alpha = \beta = \gamma = 90^{o}$, *a* = *x*, *b* = *y* and *c* = *z*. Figure 2.2 shows an example of a unit cell with references axes and corresponding cell lengths and angles.
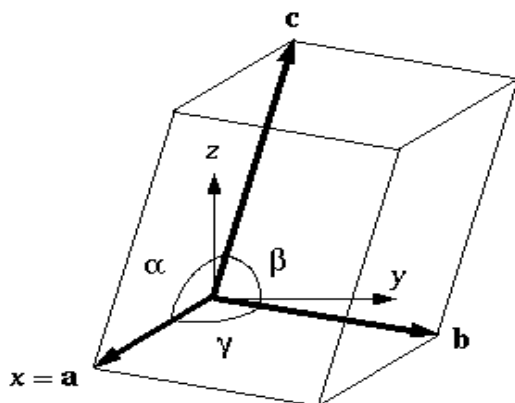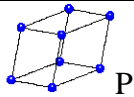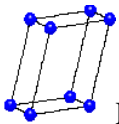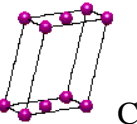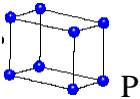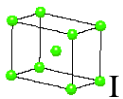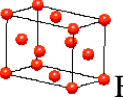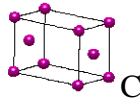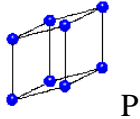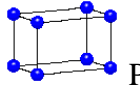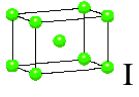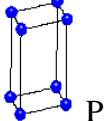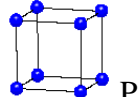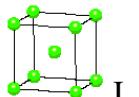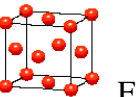
Figure 2.2 An example of a unit cell, showing the corresponding cell lengths and angles and references axes x, y and z (in this case *x* = *a*).

The polymorphs of a given substance have different unit cells, and hence different lattice parameters. Crystals may be classified by their inherent symmetry such that their structure can be assigned to a crystal system, Bravais lattice type, space group and number of molecules in the unit cell Z [14,15]. Table 2.1 shows this classification scheme based on the crystal system and the type of Bravais lattice.

Given the crystal system, the Bravais lattice and the space group, the periodic three dimensional arrays of crystalline solids can be defined down to the level of the spatial distribution of the atoms. The lattice parameters define the seven crystal systems and the fourteen distinct types of Bravais lattice shown below, while symmetry operations (for example plane of symmetry) define the 230 space groups. A compilation of Bravais lattices, space groups and symmetries can be found in the International tables for Crystallography[14]

Table 2.1 The crystallographic classification of unit cells according to the 7 crystal systems and 14 Bravais lattice structures[14, 15].

Crystal System	Unit cell shape	Bravais lattice structures
Triclinic	$a \neq b \neq c$ $\alpha \neq \beta \neq \gamma \neq 90º$	P
Monoclinic	$a \neq b \neq c;$ $\alpha = \gamma = 90º \; \beta \neq 90º$	P C
Orthorhombic	$a \neq b \neq c$ $\alpha = \beta = \gamma = 90º$	P I F C
Trigonal	$a = b = c$ $\alpha = \beta = 90º \; \gamma \neq 90º$	P
Tetragonal	$a = b \neq c$ $\alpha = \beta = \gamma = 90º$	P I
Hexagonal	$a = b \neq c$ $\alpha = \beta = 90º \; \gamma = 120º$	P
Cubic	$a = b = c$ $\alpha = \beta = \gamma = 90º$	P I F

For illustrative purposes the unit cells of the polymorphs of indomethacin (IMC) are shown in Figure 2.3. Table 2.2 shows the crystallographic data for all the polymorphic systems studied in this work except for furosemide form II, because of the difficulty in obtaining single crystals of a suitable size.
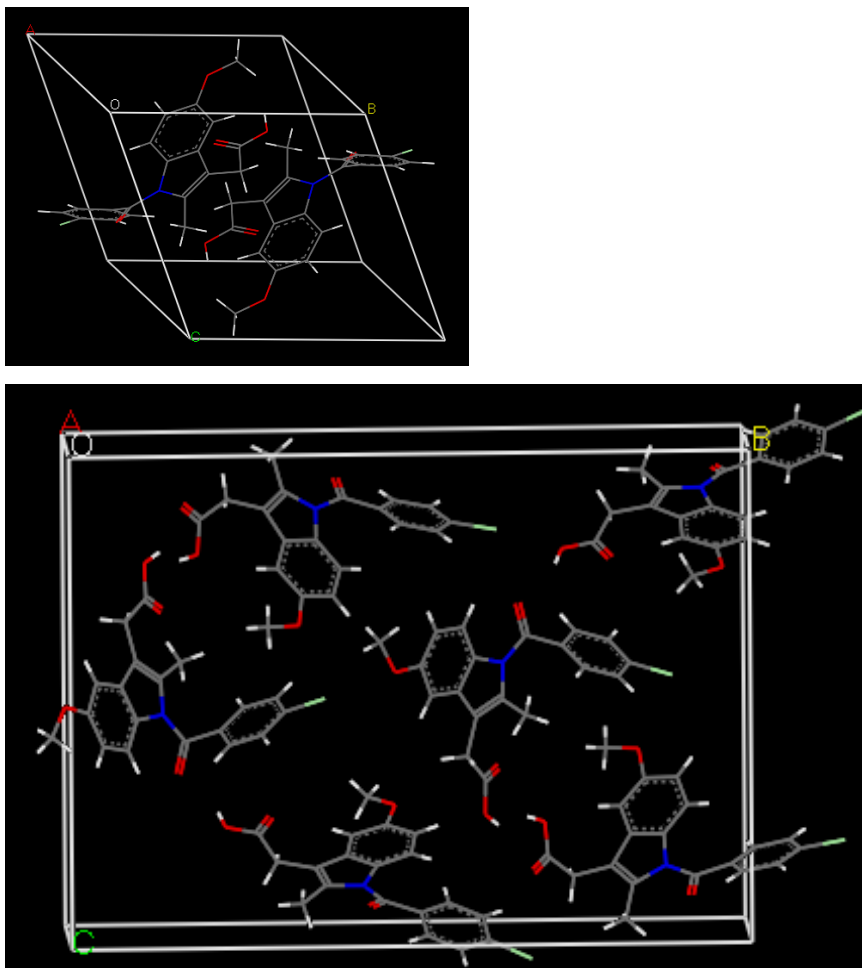
Figure 2.3 The unit cell structure for the polymorphs of indomethacin; IMC-γ (top) and IMC-α (bottom). The relative sizes of the unit cells are shown to scale.

Colour code- grey – carbon; red- oxygen; blue- nitrogen; white- hydrogen

Table 2.2 Crystallographic data for all the polymorphic systems examined in this work

		Crystal System	**Cell Parameters**	**Space group**	**Z**
IMC	α[16]	Monoclinic	a=5.46Å b=25.31Å c=18.15Å β= 94.38º α=γ=90º	P2$_1$	6
	γ[17]	Triclinic	a= 9.30Å b= 10.97Å c= 9.74Å α=69.38º β= 110.79º γ= 92.78º	P-1	2
CBZ	I[18]	Triclinic	a= 5.17Å b=20.57Å c=22.24Å α= 84.12º β= 88.00º γ= 85.19º	P-1	8
	III[19]	Monoclinic	a=7.54Å b= 11.06Å c= 13.91Å β= 92.86º α=γ=90.00º	P2$_1$/n	4
CFN	I[20]	Trigonal	a=14.83Å b=14.83Å c=6.76Å a=b=90.00º γ= 120.00º	R-3c	6
	II[20]	Monoclinic	a=42.52Å b=14.95Å c=6.79Å β= 97.82 α=γ=90.00º	C2/c	20
FUR	I[21]	Triclinic	a= 10.47Å b= 15.80Å c= 9.58Å α= 71.87º β= 115.04º γ= 108.48º	P-1	2
	*II				
SFN	β[22]	Monoclinic	a=7.95Å b=12.95Å c=7.79Å β=106.50º α=γ=90.00º	P2$_1$/c	4
	γ[23]	Monoclinic	a=8.98Å b=9.00Å c=10.04Å β=111.43º α=γ=90.00º	P2$_1$/c	4

*Crystallographic data have not been recorded because of the difficulty in obtaining large macroscopic crystals.

When comparing polymorphs, structural similarity or the lack of it cannot be assumed simply on the basis of the comparison of the geometric elements such as crystal system and space group as they do not provide any information on the supramolecular chemistry and molecular conformation.

➢ Crystal packing

In crystalline solids, molecules exist in an ordered arrangement as a result of intermolecular interactions and subsequent perturbations in molecular geometry [24]. Generally, there are three classes of intermolecular interactions that exist in crystalline molecular solids, namely: (a) non-bonded, non-electrostatic (b) electrostatic and (c) hydrogen bonding[3]. The non-bonded, non-electrostatic interactions are generally weak and occur between uncharged atoms or molecules. Examples of these interactions are steric repulsion. Electrostatic interactions include van der Waals forces and charge transfer interactions (i.e. π-π and σ-π). Hydrogen bonding is directional by nature; these are donor-acceptor interactions involving hydrogen atoms[25]. A schematic representation of a hydrogen bond interaction is D—H.....A[26]. In this interaction, hydrogen which is attached to an electronegative atom as the donor is attracted to an adjacent acceptor electronegative atom. D and A are electronegative atoms such as oxygen and nitrogen. Hydrogen bonding interactions can also involve hydrogen atoms attached to carbon. For example, C—H.....N and C—H.....N hydrogen bonds are intermolecular interactions present in the CFN-II polymorph[20].

Hydrogen bonding is the strongest and most prevalent intra/intermolecular interaction present in drug polymorphs because their molecules contains a number of hydrogen bond donors and acceptor[3]. Consequently, characterisation of hydrogen bond patterns among polymorphs serves as a means to examine the differences in internal structure. Hydrogen bonding motifs between polymorphs occur as intermolecular chains or rings or as intermolecular hydrogen bonding [3, 27] (See Fig 2.4).

Intermolecular interactions can potentially cause a distortion of the molecular geometry. The geometry or structure and characteristic three dimensional shape of a molecule is described by bond lengths, bond angles and torsion angles. In a non-linear chain of atoms A–B–C–D, the dihedral angle between the plane containing the atoms A, B, C and that containing B, C, D is the torsion angle [28]. Single crystal X-ray crystallography is the preferred analytical technique for determining bond lengths and angles[29]. Intermolecular interactions are generally not strong enough to distort bond angles and bond lengths. As a consequence, where a change in molecular conformation occurs, it is usually as a result of a change in torsion angles.

(a)   (b)

(c)
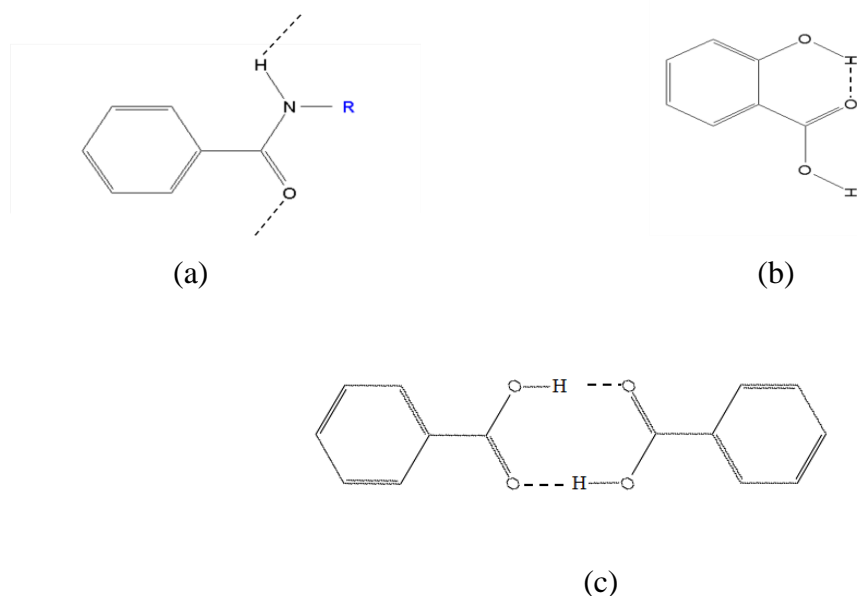
Figure 2.4 Common hydrogen bonding motifs in drug polymorphs (a) chain pattern (b) intramolecular pattern (c) ring pattern

Where the molecules in a pair of polymorphs are conformationally similar and the differences between the polymorphs arise from differences in the spatial arrangement of the molecules, this is known as packing polymorphism. Where the molecules in a pair of polymorphs are conformationally distinct (i.e. two or more conformers of the same molecule are present in the crystal structure) and the differences between the polymorphs arise from conformational differences in the molecules contained therein, this is known as conformational polymorphism. For example, indomethacin exhibits conformationally polymorphism. In IMC-α, the conformers exist in the unit cell while in IMC -γ there is only one conformer. Figure 2.5 shows the molecule of IMC and the set of torsion angles (τ_1 and τ_2) that describe the conformers in each polymorph.

	IMC-α	IMC-γ
τ_1/τ_2	159.7°/ 52.9°	26.2°/ 40.3°
τ_1/τ_2	23.3°/ 52.92°	-
τ_1/τ_2	21.4°/ 50.0°	-
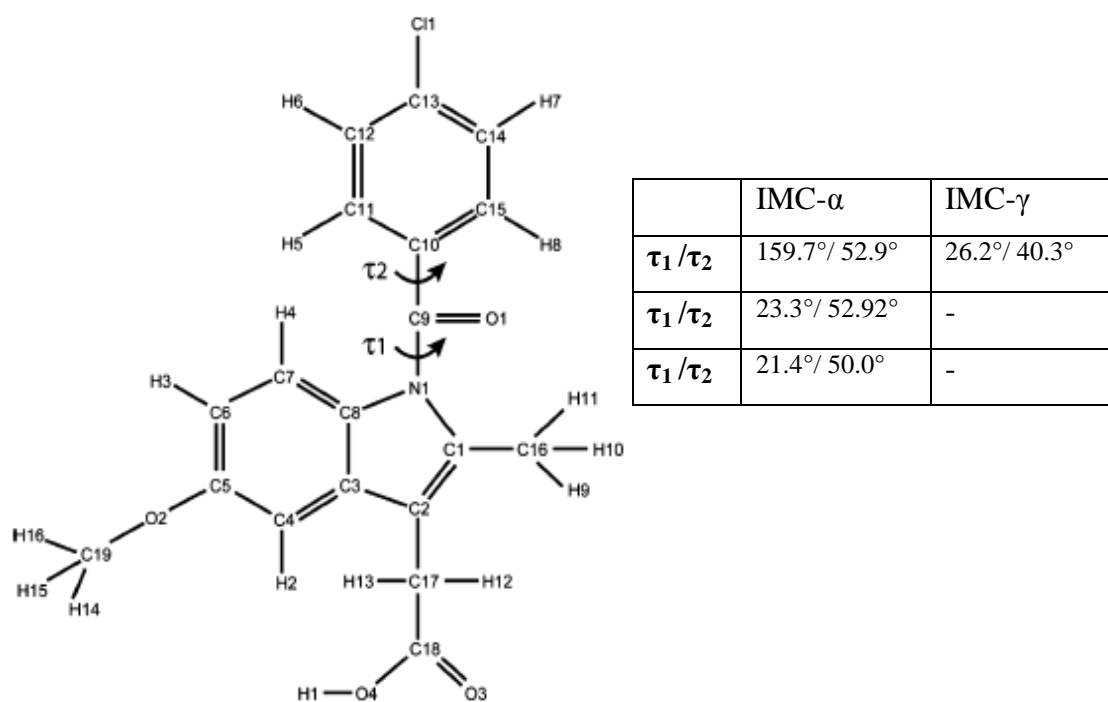
Figure 2.5 Indomethacin molecule with atoms indexed and two dihedral angles τ_1 (C1-N1-C9-O1) and τ_2 (O1-C9-C10-C15). *Table*: τ_1 and τ_2 values for the molecular conformers-three in α and one in γ polymorphic forms[30].

➢ Crystal morphology

The crystal morphology describes the shape and symmetry of a crystal. A crystal is defined as a solid with three-dimensional long range order of atoms and plane face boundaries. Figure 2.6 shows the six common crystal shapes (plate, flake, equant columnar, needle and lath) that are used to describe molecular crystals. The crystal morphology reflects the symmetry of the internal structure, except in certain circumstances, where the environment in which a crystal is formed influences the crystal shape. For example, different crystal shapes may result from crystallisation from different solvents. For many pharmaceutical compounds the morphology of the crystal can be different from that predicted by crystal symmetry, because of the uneven growth of certain faces.
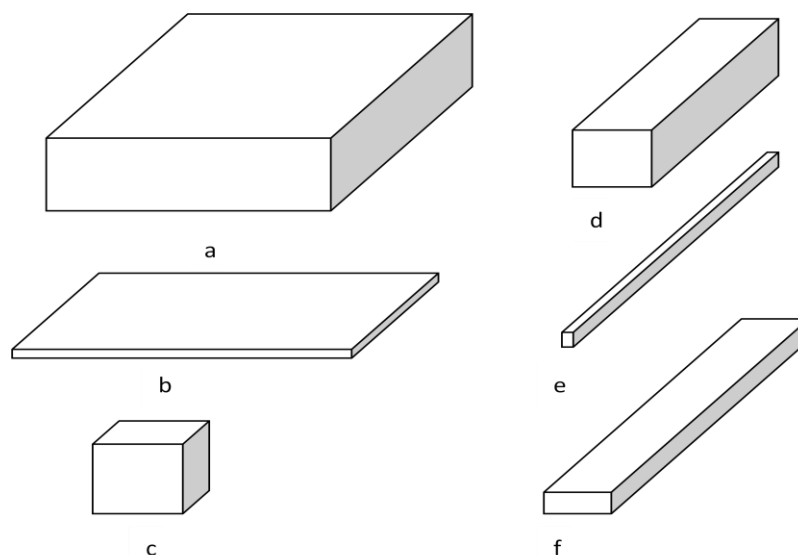
Figure 2. 6 The six basic crystal shapes for molecular crystals; (a) plate (b) flake (c) equant (d) columnar (e) needle and (f) lath[31].

The faces of a crystal are planes in three dimensional space, and can be labelled with respect to the unit cell axes by a notation called Miller indices. This is a set of three integers (*hkl*) that represent the orientation of a plane in a crystal lattice, and are defined as the reciprocals of the fractional intercepts which the plane makes with the crystallographic axes. A given crystal face intercepts the three reference crystallographic axes in ratios of *a/h*, *b/k* and *c/l*[11, 13]. Since the unit cell repeats in space, the notation actually represents a family of planes, all with the same orientation. Miller indices are not confined to the external faces of a crystal but can be used to label any plane of atoms. It is noteworthy, that a difference in the crystal morphology may not necessarily indicate different polymorphic forms as the growth conditions (environment) may change the crystal morphology but not the internal crystal structure.

2.2.2 Thermodynamic aspects

Thermodynamics is an important tool to understand the formation of polymorphs and the relationships between them. Assessing the relative thermodynamic stability relationship between solid state forms, especially polymorphs, is a requirement for drug development[32, 33]. An understanding of the macroscopic properties, (for example pressure and temperature) and the direction in which solid state transformations can occur, allows for better control of manufacturing and storage conditions. In thermodynamic terms, polymorphism results in the presence of closely spaced local energy minima on the Morse curves.

It is almost inevitable that the intermolecular distances will be different for each polymorph, given the different crystal structures, and there is no reason why their energies should be the same. A Morse curve represents the algebraic sum of curves of intermolecular (attractive and repulsive) interaction energies between a pair of molecules in a solid or liquid as a function of the mean intermolecular distance[34]. Figure 2.7 shows this curve for a hypothetical dimorphic system (i.e. consisting of two polymorphs) and it's corresponding liquid phase..
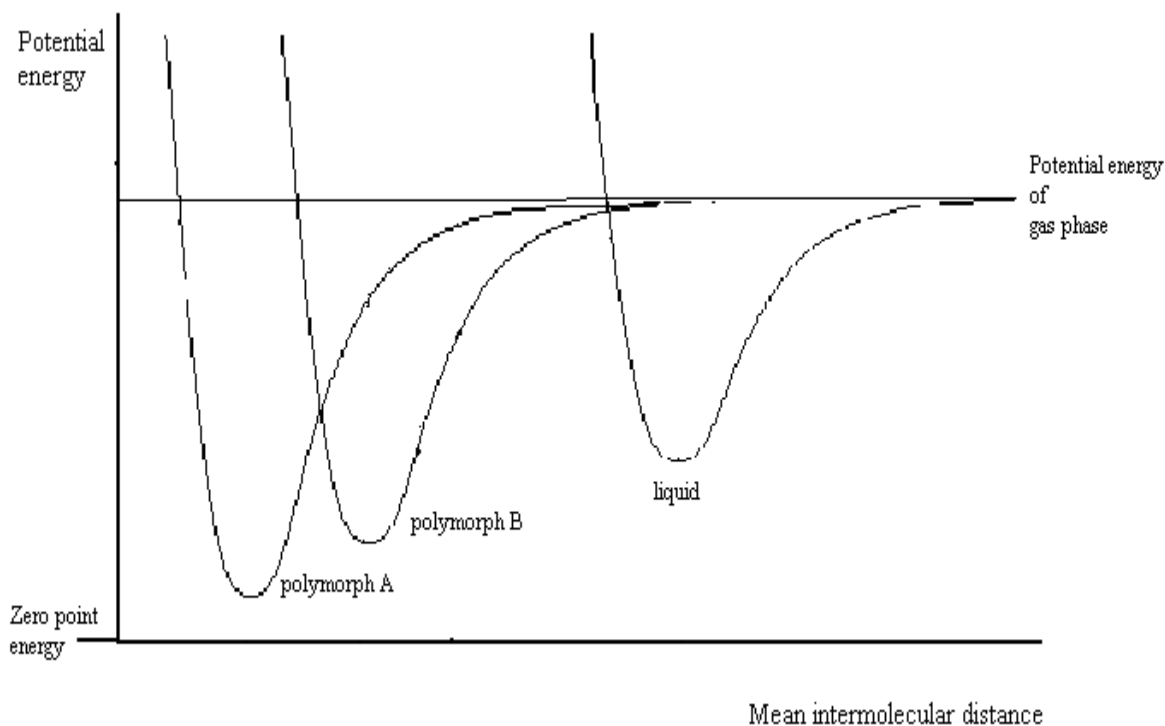
Figure 2.7 A series of Morse potential energy curves for a hypothetical dimorphic system consisting of polymorphs A and B and of the corresponding liquid phase.

At the local minima, attractive and repulsive forces are balanced to give the corresponding physical form of the material (solid or liquid). The local energy minima for the polymorphs can be described as a situation where the attractive and repulsive forces are balanced. The solid phases (polymorphs A and B) have lower potential energy levels than the liquid phase because the molecules are arranged in an orderly fashion, the molecules can sit together more tightly and pack more efficiently by directionally-specific intermolecular interactions such as hydrogen bonding.

The local minimum is analogous to the Gibbs free energy (G) of the phase. The free energy at constant temperature and pressure can be represented by;

$$G = H - TS$$

Equation 2.1

where G is the Gibbs free energy, H is the enthalpy, T is the temperature and S is the entropy.

The liquid phase has a higher G value than its corresponding polymorphic forms. Polymorph A (above) with the lowest energy minimum is the more stable polymorph. Polymorph B is generally metastable with respect to polymorph A. When comparing any pair of polymorphs, the one with the lower value of G is, by definition, the more stable.

For every pair of polymorphs a and b then, the following equation applies:

$$\Delta G = G_b - G_a = (H_b - H_a) - T(S_b - S_a)$$

Equation 2.2

If $\Delta G > 0$, then polymorph a is more stable; if $\Delta G < 0$, then polymorph b is more stable.

The stability of one polymorph with respect to another is dependent on temperature and pressure, and should be established within a range of pressures and temperatures. In pharmaceutical development, the optimum polymorph is typically the one that is most stable at ambient temperature and pressure conditions. This choice is made to avoid the risk of solid-state conversion.

Two different types of thermodynamic behaviour exhibited by polymorphic pairs are termed monotropy and enantiotropy (see next page). Energy-temperature (E-T) diagrams (constructed based on the Gibbs free energy equation) are commonly used to describe monotropic and enantiotropic relationships between polymorphs[8, 32, 35]. E-T diagrams contain two types of isobars: enthalpy versus temperature and Gibbs free energy versus temperature curves. These isobars are constructed for each polymorph and the corresponding liquid phase. The H versus T curves may be constructed experimentally by the determination of the heat capacity at constant pressure C_p by calorimetry. The relationship between H and C_p is shown in Equation 2.3

$$\left(\frac{\delta H}{\delta T}\right)_p = C_p$$

Equation 2.3

Also, the partial derivative of *G* with respect to temperature is:

$$\left(\frac{\delta G}{\delta T}\right)_p = -S$$

<div align="right">Equation 2.4</div>

The enthalpy increases with temperature so the slope of the *H* versus *T* isobar increases. The entropy of a system increases with increasing temperature so the *G* versus *T* isobar decreases with temperature because its slope is the negative value of the entropy. The relationship between the G, H and the entropic term (TS) of the Gibbs equation is graphically shown in Figure 2.8. At absolute zero temperature, *G* = *H* and *S* = 0.
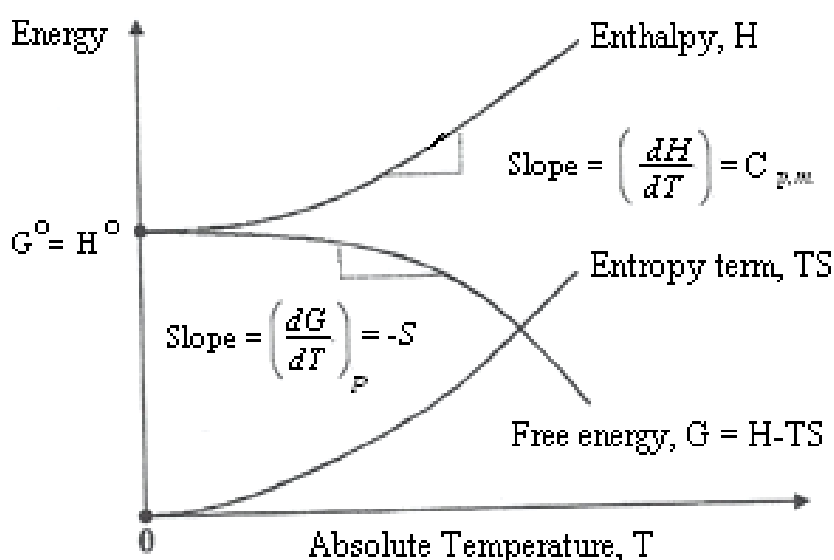
Figure 2. 8 Energy- temperature diagram of a crystalline solid under constant pressure

An enantiotropic pair of polymorphs is one where there is a transition temperature, below which one polymorph is the more stable, and above which the other is the more stable. Enantiotropic pairs can always be interconverted in the solid state by changing temperature, although the transition can be slow. The temperature at which interconversion occurs is called the transition temperature (T_t) and is, by default, below the melting points (T_m) of both polymorphs. **For monotropically related polymorphs**, the free energy relationship remains the same at all temperatures below the melting point. The higher melting polymorph will be the stable form at ambient conditions. Monotropic pairs cannot be interconverted in the solid state by merely changing the temperature – the liquid or solution state is needed.

The temperature at which the G-T isobar of the liquid (G_{liq}) intersects the G-T isobar of a polymorph is the melting point T_m of that polymorph. The T_t is the temperature of intersection of the G-T isobar of polymorph A and the G-T isobar of polymorph B. The transition temperature can be above or below ambient temperature. If it lies much below room temperature, enantiotropy will have little effect on drug development.

Figure 2.9 presents a schematic E-T diagram illustrating enantiotropy and monotropy.
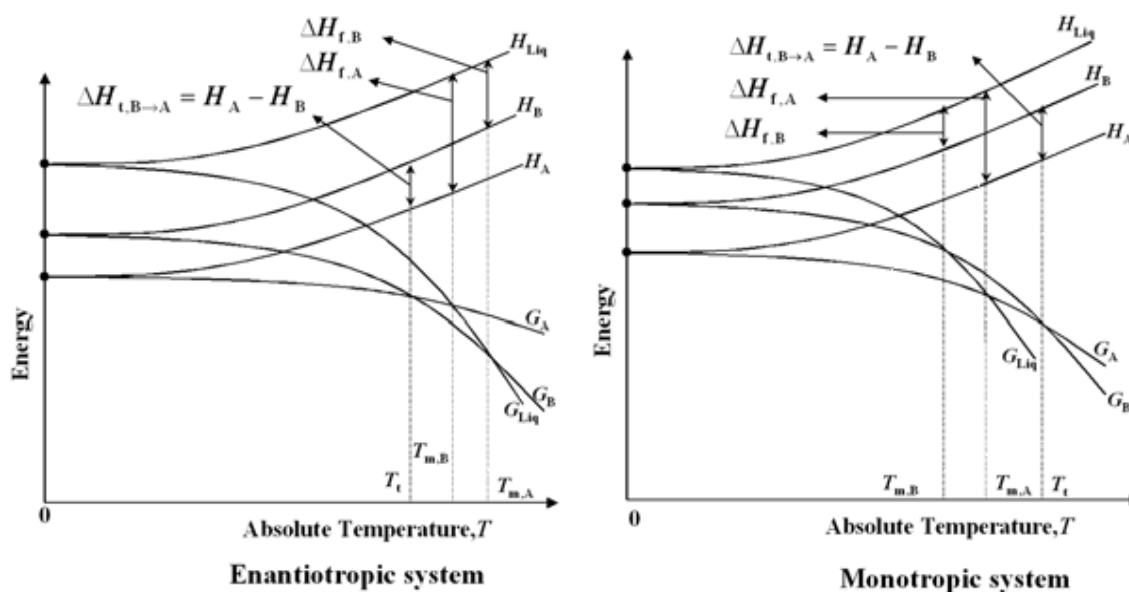
Figure 2. 9 Energy temperature diagram for an enantiotropic and a monotropic system[35]. *G* is the Gibbs free energy, *H* is the enthalpy, *T* is temperature. Polymorph A, polymorph B and liquid form are represented by subscripts A, B and liq respectively while subscripts m, f and t refer to melting, fusion and transition, respectively.

The following properties apply to the above enantiotropic pair of polymorphs A and B:

- Melting point of polymorph A < melting point of polymorph B
- Below T_t, $G_A < G_B$ therefore, $\Delta G > 0$; polymorph A is the more stable
- Above T_t, $\Delta G < 0$; polymorph B is the more stable.
- At T_t, $\Delta G = 0$; both polymorphs are stable.

The following properties apply to monotropic polymorphs:

- Melting point of polymorph A > melting point of polymorph B;
- $G_A < G_B$ at all temperatures below $T_{m, A}$ therefore, $\Delta G > 0$; polymorph A is more stable .

The thermodynamic stability relationships for the polymorphic systems used in this work are shown in Table 2.3. According to thermodynamic theory, the metastable form would tend to transform to the more stable form, which has the lower energy. However, the transformation is kinetically hindered because the activation energy barrier has to be overcome. The activation energy is defined as the minimum energy required for setting in motion such a transformation.

Table 2.3 Thermodynamic stability relationships between the model polymorphic systems employed in this work.

Polymorphic system	Thermodynamic stability relationship	Notes
IMC (α and γ)	Monotropy	IMC-γ is more stable at all T below T_m
CBZ (I and III)	Enantiotropy	CBZ-III is more stable at T below T_t; CBZ-I is more stable above T_t
CFN (I and II)	Enantiotropy	CFN-II is more stable at T below T_t; CFN-I is more stable above T_t
FRS (I and II)	-	-
SFN (β and γ)	Enantiotropy	SFN-β is more stable at T below T_t; SFN-γ is more stable above T_t

2.3 Methods for the preparation of polymorphs

The various methods for preparing different polymorphs of drugs include crystallisation from solution by cooling or precipitation, sublimation, crystallisation from a melt, heat induced transformation, and crystallisation from supercritical fluids. However, crystallisation from solution (employing various solvents and temperature regimes) is often preferred for ease and efficiency. Success in preparing various polymorphs frequently depends on appropriate control of the kinetics rather than the thermodynamics of crystallisation.

Changing the crystallisation conditions can lead to the formation of different polymorphs. It is therefore helpful to state, where possible, the crystallisation solvent, temperature range, rate of evaporation/cooling and any other conditions under which a polymorph is crystallised[3].

2.4 Analytical techniques for the characterisation of polymorphs

Physical properties differ between polymorphs as a consequence of different crystal structures. A comprehensive list of properties that differ between polymorphs is given by Brittain[2] and is shown in Table 1.1 (Chapter 1). Any technique which can be used to measure a property of the solid state can potentially be used for the study and characterisation of polymorphs. There are several distinct aspects in the analytical investigation of polymorphs. These can include identification, quantitation, and determination of structure-property relationships. Techniques such as spectroscopy, crystallography or thermal methods can be used alone or interfaced with another technique. Selection of the most appropriate techniques would be based on economics, compound sensitivity to the technique and the regulatory requirement for cross-validation. The different physical techniques used to characterise polymorphs and a summary of the information obtainable are contained in Table 2. 4.

Table 2.4 Common physical techniques for the characterisation of drug polymorphs.

Physical technique	Summary of information obtainable
Single crystal X-ray diffraction	Unique three dimensional data on unit cell parameters and molecular conformation and packing,
Powder X-ray diffraction	Unique two dimensional structural data of the diffraction pattern of X-rays by powder samples
Infrared/Raman spectroscopy	Characteristic molecular vibrational spectra, sensitive to intermolecular interactions like H bonding
Differential scanning calorimetry (DSC)	Information of phase changes. Unique melting points, enthalpy of fusion/ transition. Useful for determining relative thermodynamic stability.
Hot-stage microscopy (HSM)	Observational data on the nature of a thermal event; for example melting or solid-solid transition. Characteristic crystal habit
Scanning electron microscopy (SEM) / Optical microscopy	Characteristic crystal habit
Nuclear magnetic resonance (NMR) spectroscopy	Unique chemical shift because nuclei in the polymorphs exist in magnetically different environments

Chapter 3 provides information on several techniques such as PXRD, DSC, Raman spectroscopy, HSM and SEM used to characterise the model polymorphic systems.

Part II – Surface acidity and basicity

A standard method for the measurement of the acidity or basicity of a substance in aqueous solution can be expressed in terms of pH:

$$pH = -log_{10} \; [H_3O^+]$$

The surface acidity or basicity of a solid surface is not easily expressed. The surface is heterogeneous, with different functional groups each contributing to the acid-base properties and adsorbed species such as water may also contribute. An ideal representation of surface acidity can be the stoichiometry of the acidic or basic functional groups per unit area and their acid/base strength. The use of molecular probes to characterise the acid/base properties of a surface is common and characterisation is strongly dependent on the probe interacting with the surface. Sometimes the probe is unable to interact with the surface acid/base groups because of steric hindrance.

The surface area of a solid sample can be relatively easy to obtain if the surface is flat. For a powdered crystalline sample, the adsorption of a probe gas such as nitrogen will suffice, but again the measured surface area is dependent on the probe's ability to access the surface. Different molecular probes can also give a different acidity/basicity for a given sample because of their ability to access and interact with the acid base group. Hence, it is difficult to express surface acidity in terms of stoichiometry and strength per unit area.

Before considering this further it is instructive to examine some aspects of acid-base equilibria in solution.

2.5 Acid-base solution equilibria

There are several theories that express the characteristics of acids and bases. These include the Brønsted and Lewis theories.

The Brønsted theory describes acids as proton donors and bases as proton acceptors. Qualitatively, the strength of an acid may be defined as the tendency to give up a proton and base strength as the tendency to accept a proton.

Consider the hypothetical case of the dissociation of an acid HA shown in Equation 2.5

$$\underset{acid}{HA} + \underset{base}{H_2O} \rightleftharpoons \underset{conjugate\ base}{A^-} + \underset{conjugate\ acid}{H_3O^+} \qquad \text{Equation 2.5}$$
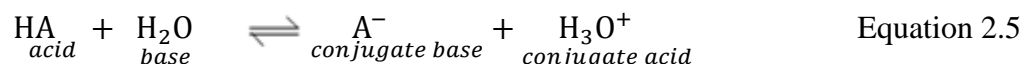
In the above equation, the conjugate base is related to the acid, and the conjugate acid is related to the base by the gain or loss of one proton. The acid donates a proton to water, to form the hydronium ion (H_3O^+); water acts as a base because it accepts the proton. The acid strength of HA is determined by the electron-withdrawing power of A, the stability of A^- (favoured by hydrogen bonding interactions with the solvent or with other acid molecules) and the ability of A^- to spread the negative charge over the whole moiety.

In a quantitative sense, by measuring the position of the equilibrium in dilute aqueous solution or in the gas phase, the relative strength of the acid and conjugate acid can be determined. The equilibrium constant K_a is expresses as follows:

$$K_a = \frac{[A][H_3O^+]}{[HA]} \qquad \text{Equation 2.6}$$

Although the strength of an acid can be expressed by the K_a value, a very common way of recording this number is as the pK_a value as expressed in equation 2.7.

$$pK_a = -\log_{10} K_a \qquad \text{Equation 2.7}$$

The pK_a of various acids is usually reported with respect to water. In the gas phase, where solvation effects are absent, the acidity order can be different.

pH is related to the pK_a according to the relationship:

$$pH = -log[\ H_3O^+] = pK_a + \log([A^-]/[HA]) \qquad \text{Equation 2.8}$$

The strength of a base can be expressed in terms of the pK_a of its conjugate acid. Therefore the ranking of acids and bases according to their strengths can be based solely on pK_a values (Table 2.5).

Table 2.5 Classification of acids and bases according to their strength[36]

Strength	Acid pK_a	Base pK_a
Very strong	<0	>14
Strong	0-4.5	9.5-14
Weak	4.5-9.5	4.5-9.5
Very Weak	9.5-14	0-4.5
Extremely Weak	>14	<0

All solvents are only capable of handling a maximum strength of acid or base and the threshold represents the strongest acid or base that can exist in a given solution. In a case where the acid is stronger than the conjugate acid of the solvent, a levelling effect is achieved by the complete transfer of the hydrogen ion to a proton-accepting solvent. For example, water has a levelling effect on the acidities of HCl and HI: dilute aqueous solutions of these acids at the same concentrations have the same acidities.

For instance, the strongest acid that can exist in water is the hydronium ion, H_3O^+. Hydrochloric acid, which is a stronger acid, becomes H_3O^+ by dissociating, as shown in equation 2.9:

$$HCl \ + \ H_2O \ \leftrightarrow \ H_3O^+ \ + \ Cl^- \qquad \qquad \text{Equation 2.9}$$
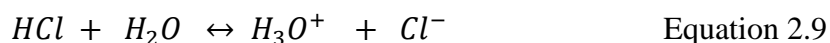
A corresponding levelling effect applies to strong bases in solvents capable of donating a proton.

The Lewis theory describes an acid as an electron pair acceptor and a base as an electron pair donor. Therefore a Lewis base B has an unshared pair of electrons that can react with a Lewis acid A which has a vacant orbital to form a co-ordinate covalent bond. The reaction of a Lewis acid and Lewis base are complexation or adduct formation reactions, where the highest occupied molecular orbital (HOMO) of the base with available lone electron pair(s) donates lone pairs of electrons to the electron-deficient acid's lowest unoccupied molecular orbital (LUMO) through a co-ordinate covalent bond.

Two schematic representations of Lewis adduct formation reactions[37] are as follows:

$A \ + \ B \ \leftrightarrow \ A - B$ e.g. $NH_3 \ + \ BF_3 \ \leftrightarrow \ H_3N - BF_3$

$A - B \ + \ A' - B' \ \leftrightarrow \ A - B' + \ A' - B$ e.g. $H - OCH_3 \ + \ CH_3 - Br \ \leftrightarrow \ CH_3 - O - CH_3 \ + \ H - Br$
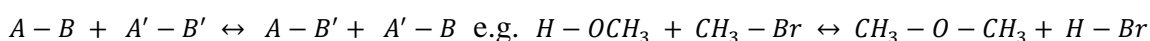
In the first case the Lewis adduct is formed because a co-ordinate covalent bond is formed by one species contributing a filled orbital and the other a vacant orbital. In the second case, two Lewis adducts with acidic and basic characteristics react by exchanging components.

The Lewis acid–base theory is more general than the Brønsted theory, because it can be applied to reactions that do not involve the donation or acceptance of a proton. The Brønsted definition is convenient for describing reactions in aqueous solutions, but it covers a narrower range, because the presence of proton is required. All Brønsted acids are Lewis acid–base adducts with the acid component being H^+, and all Brønsted bases are also Lewis bases. A generic representation of the strength of a Lewis acid by pK_a is not realistic because the strength of a Lewis acid depends on the nature of the base and vice versa for a Lewis base.

A quantitative measure of the strength of a Lewis acid or base is possible mainly by comparative measurement of the equilibrium constant K for adduct formation for a series of bases with a common reference Lewis acid and *vice versa*. Comparing the Lewis acid strength of molecules of the form MX_n, the acidity of MX_n decreases with increasing atomic radius of M, because the attraction between the positive nucleus M and the incoming electron pair is decreasing. The acidity increases with increasing electronegativity of X and the maximum acidity is found for the compounds where n is a minimum. Comparing the Lewis base strength of, for example, oxygen bases OM_2, the basicity of O increases with the increase in the electron donor properties of M. When M is a metallic element, the basicity at O increases with the increasing electropositivity of M and ionic radius[38].

In concentrated solutions, the activities rather than concentration are used to describe the equilibrium constant. The activity (a) of any interacting species i in solution is related to its molar concentration, $[m]$, by the expression:

$$a_i \ = \ [m]f_i$$
Equation 2.10

Where f_i is the activity coefficient of species i.

The Hammett acidity function H_o is therefore used in concentrated solutions to indicate the acid strength. In practice, the Hammett function is defined in terms of the ionisation of an acidic pH indicator dye.

For Brønsted acidity:

$$H_o = -\log a_{H+} \, f_B / f_{BH+} = pK_{BH+} + \log [B] / [BH^+]$$ Equation 2.11

where a_{H+} is the activity of the Brønsted acid, f_B and f_{BH+} are the activity coefficients for the neutral base and conjugate acid respectively, pK_{BH+} is analogous to pKa and [B] and [BH$^+$] are the concentrations of the base and conjugate acid.

For Lewis acidity:

$$H_o = -\log a_A \, f_A / f_{AB} = pK_a + \log [B] / [AB]$$ Equation 2.12

where a_A is the activity of the Lewis acid.

In both cases H_o is analogous to pH, such that in dilute solutions, the activity coefficients become 1 and consequently H_o=pH.

The degree of protonation, [BH$^+$]/[B] or Lewis adduct formation, [B]/[AB] is usually measured by means of UV–Vis spectroscopy. H_o is a solvent-independent quantitative measure of acidity, the implication of the levelling effect is reduced, and the acidities of different substances can be directly compared.

2 .6 Surface acidity of solids

A comprehensive study of the acid or base properties of a surface involves the determination of the following:

- stoichiometry of sites – the number of moles of acid or base sites per unit weight or surface area;
- nature of sites - Brønsted or Lewis type;
- strength of sites- ability to convert an adsorbed base into its conjugate acid[39]. The acid strength is expressed in terms of the Hammett acidity function, H_o.

A variety of techniques have been developed in order to obtain a description of surface acidity. These techniques are examined later. The heterogeneous nature of the surface of powdered crystalline solids means that surface acidity measurements are not straightforward.

2.6.1. Heterogeneous surface structure of crystalline powdered solids

A solid material is terminated by boundaries where the exposed moieties have a different coordination environment than those in the bulk[40]. At the microscopic level, these surfaces could be described as flat or stepped regions. For example, the heterogeneous nature of the surface of a paracetamol form I crystal is shown in Figure 2.10. The microscopic images show straight edged steps, small steps and flat regions. The local distributions of atoms around these surface sites are different; therefore their surface chemistries are different.
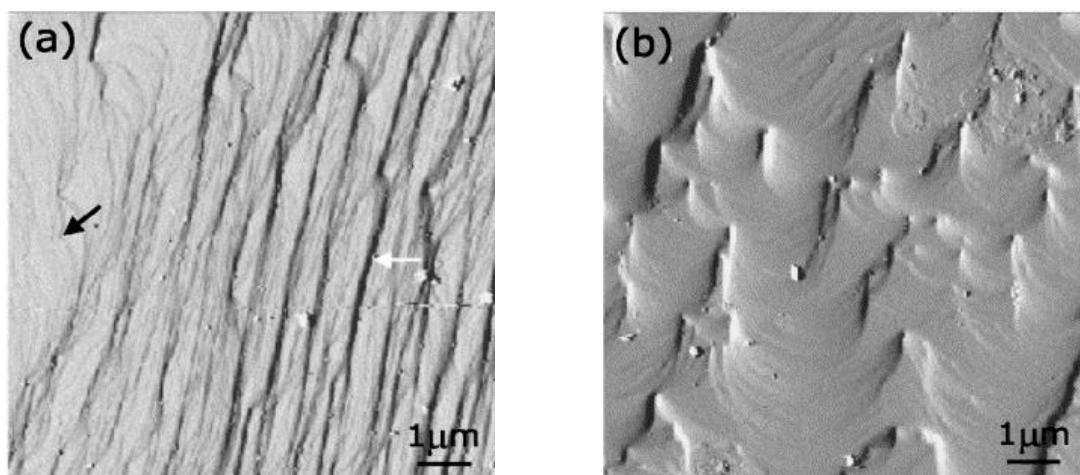
Figure 2.10 Atomic force microscopic images of surface of a paracetamol crystal[41], showing (a) straight-edged steps and (b) small steps and flat regions.

A powdered crystalline solid is a collection of small particles (crystallites), which present different possible lattice plane surfaces. Each crystallite may have many different surfaces, the faces, edges and corners all different in chemistry. These surfaces may expose polar and nonpolar groups, may be atomically smooth or rough, and may be high or low symmetry. The surfaces therefore offer a wide variety of possible sites for adsorption of gases and liquids. The differences in chemistry between the various facets exposed by a crystalline solid can be termed "anisotropic surface chemistry".

The anisotropic surface chemistry of a large single crystal of paracetamol form I was examined by Heng et al[42]. Two dominant faces of the crystal, Miller indexed (001) and (010), were analysed by X-ray photoelectron spectroscopy (Figure 2.11). In addition to CH functionalities, the hydrophilic 010 face exposes hydroxyl (OH) and carbonyl (C=O) groups while the hydrophobic 001 face exposes C=O without the OH groups.

The Face (010) (in comparison to face (001)) can form more hydrogen bonds with water by virtue of the OH surface characteristics.
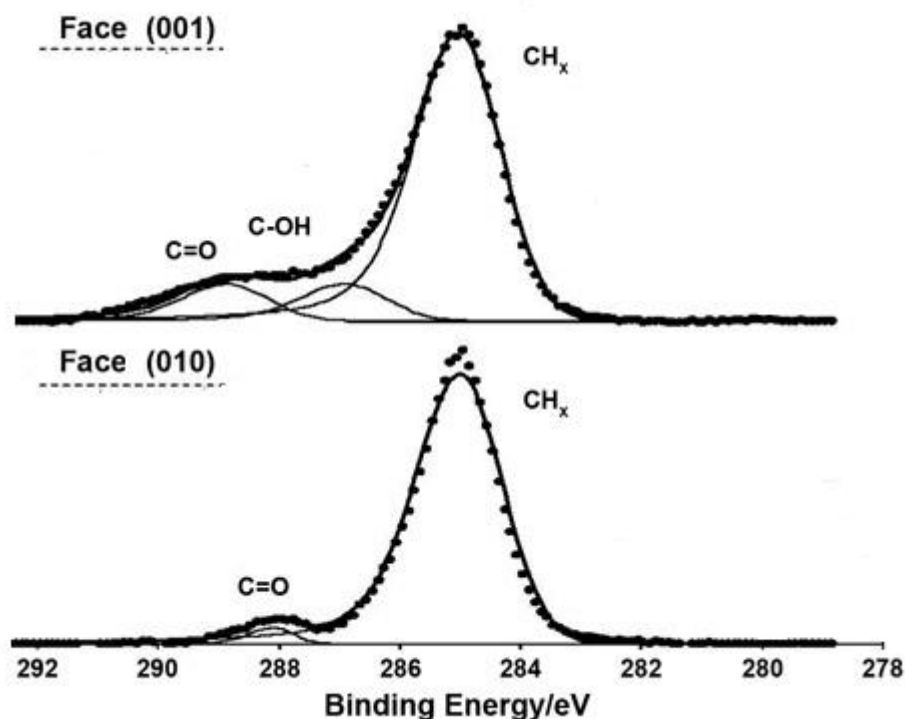
Figure 2.11 X-ray photoelectron spectra of face (001) *top* and face (010) *bottom* of a large single crystal of paracetamol form I. [42]

The surface structure of a crystal is a consequence of the internal structural order defined by the unit cell. The physical and chemical characteristics of the surface of a crystalline solid are governed by the structure of its exposed crystal faces. However, the chemistry of the dominant faces would greatly influence the chemical and physical properties of the solid.

2.6.2. Current methods for characterisation of surface acid/base chemistry

There are a number of methods used to characterise the acidity and basicity of solid surfaces. These techniques include titrimetry[37], spectroscopic methods such as infrared (IR)[43, 44], Raman [45-48], x-ray photoelectron spectroscopy, UV-Vis spectroscopy[37] (pH indicator dye sorption) , inverse gas chromatography[49], measurement of the pH of a slurry, liquid contact angles, temperature programmed desorption and isothermal calorimetry. Most of these surface acid/base characterisation methods require the use of molecular probes with acidic or basic character such as carbon monoxide (CO), carbon dioxide (CO_2), ammonia (NH_3), pyridine and pH indicator dyes.

The majority of the techniques mentioned have been used mainly for the analysis of inorganic solids used as industrial catalysts[38]. Table 2.6 shows a summary of the techniques used in the characterisation of surface acidity and basicity with the principles, probes used, and a note on the viability for the characterisation of the surface acidity or basicity of drug polymorphs.

Inherently, organic solids lack the highly reactive surface acid/base functionalities possessed by inorganic solid acids and bases[50]. As a result of their insensitivity, the aforementioned methods for surface acidity measurement are not usually employed for the analysis of organic solids. The slurry pH and UV-Vis spectroscopic methods are commonly used for the analysis of solids of pharmaceutical interest[51-53]. In the slurry pH method a concentrated suspension of the solid in water is prepared, and the pH is measured using a pH electrode. The pH of the concentrated slurry is considered to reflect the pH of the solid surface[54, 55]. There is however uncertainty as to whether the acidity measured by the direct potentiometry is a true reflection of the acidity of the surface[37]. For example, when in an aqueous slurry, water molecules can react with the solid surface, altering its acid/base properties, e.g. converting Lewis acid sites to Brønsted acid sites[37]. The UV-Vis method involves the spectral measurements following adsorption of pH indicators from aqueous or non-aqueous solutions. The degree of indicator protonation measured from UV–Vis spectral bands gives an indication of acid or base strength.

Table 2.6 Summary of the techniques used in the characterisation of surface acidity and basicity and comments on viability for the characterisation of the surface acidity of drug polymorphs.

Method	Principle	Factors affecting the viability for characterisation of the surface acidity of drug polymorph crystals.
Slurry pH determination	A suspension of the solid in water is prepared and the pH of slurry is measured using a pH electrode. The pH value reflects the acidity of the surface.	Suspension in a liquid can induce polymorphic transformation from metastable to stable form
Aqueous and non-aqueous titrimetry	The sample of interest is suspended in water or non-polar solvent and titrated with a standard acid or base. Measurements are recorded either by potentiometry or employing a pH indicator and the amount of acid/base sites are thus estimated from titration curves	Solvent-induced transformation from one polymorph to another is possible.
IR and Raman spectroscopy	Determination of the Lewis or Brønsted nature of the sites from characteristic IR absorption bands or Raman shifts of adsorbed probe molecules. Probes include carbon monoxide, carbon dioxide, ammonia and pyridine. pH indicator probes have been used in the special case of resonance Raman studies[47]	Harsh conditions of probe adsorption (high temperature and vacuum) can induce polymorphic transformation
UV-Vis spectroscopy	Spectra are collected following adsorption of pH indicators from aqueous or non-aqueous solutions. The degree of indicator protonation measured from UV–Vis spectral bands gives an indication of acid or base strength.	Solvent-induced transformation from one polymorph to another is possible.
X-ray photoelectron spectroscopy	Binding energy, E_B of surface exposed acid/base functionalities are obtained from the kinetic energy of ejected photoelectrons from X-ray irradiated surface. Low E_B corresponds to weak affinity to electron, hence more basic and high E_B corresponds to strong affinity to electron, hence more acidic.	Difficult to distinguish any surface enhancement because the X-rays penetrate 5 to 10 nm but we are interested in the first 0.3 nm.
Inverse gas chromatography	The solid of interest is immobilised in a column, and the surface energetic and acid–base properties are determined from the retention volume of acidic or basic molecular gas probes.	Insensitive to acid/base surfaces for organic molecular solids so relatively insensitive for discrimination of polymorphs
Liquid contact angles	The acid-base components of the surface energy are determined from the angle a liquid probe makes with the solid surface on contact. Better suited to large crystals.	Requires compaction of powdered samples and this can induce polymorphic transformation.
Calorimetry	Measures heat changes during the adsorption or desorption of a base. Calorimetric output can be used to determine acid strength and density of acid sites.	Samples are not recoverable after analysis.
Temperature programmed desorption (TDS)	Amounts of desorbed probe molecules on the solid of interest are measured as the temperature is linearly increased. The strength and density of the sites is determined from the temperature and amount of probe molecules desorbed.	Harsh conditions of probe adsorption (high temperature and vacuum) can induce polymorphic transformation.

2.6.3 Acid-base (pH) indicator chemistry

When the energy of the photons of UV-Vis light matches the energy difference (ΔE) between an occupied orbital (ground state) and an empty (excited state) orbital, the photon is absorbed, and an electron transits from its ground state to an excited state.

ΔE is associated with a wavelength, as shown in Eqn 2.13:

$$\Delta E = h \, \frac{c}{\lambda}$$ Equation 2.13

where h is Planck's constant (=6.6×10^{-34}Js), c is the speed of light and λ is the wavelength.

Electronic transitions (Fig 2.12) could occur from various occupied (bonding and nonbonding levels) to empty levels (antibonding), but in reality, excitation is between the frontier molecular levels, HOMO and LUMO. The $\pi - \pi^*$ and the $\eta - \pi^*$ are the allowed transitions in organic solids, so substances that can be analysed by UV-Vis must have chromophores which are sources of π- electrons. Examples of chromophores are carbonyl bonds or unsaturated aliphatic and aromatic carbon systems.
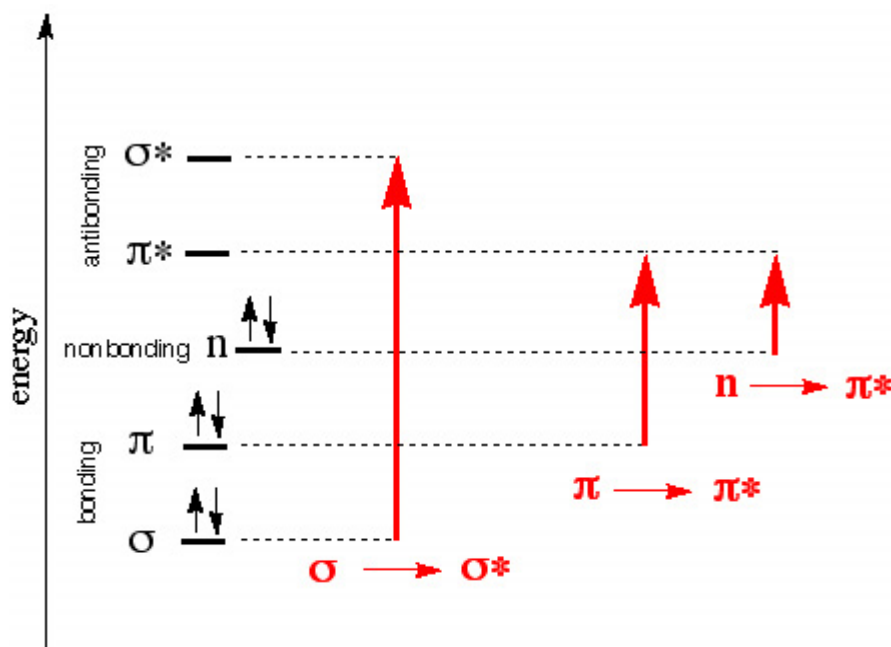
Figure 2.12 Electronic transition between molecular orbitals

The energy/wavelength associated with a given transition provides information on the structure of a molecule and determines properties such as colour. Coloured substances have a sufficient number of chromophores that allow absorption of photons not only in the UV but in the visible region. The visible spectrum is divided into colours, from violet to red (see Figure 2.13 below.) The apparent colour of a substance is the complementary colour from that which has been absorbed. Blue is the complementary colour to yellow, so a yellow coloured substance would absorb in the region around 420nm.
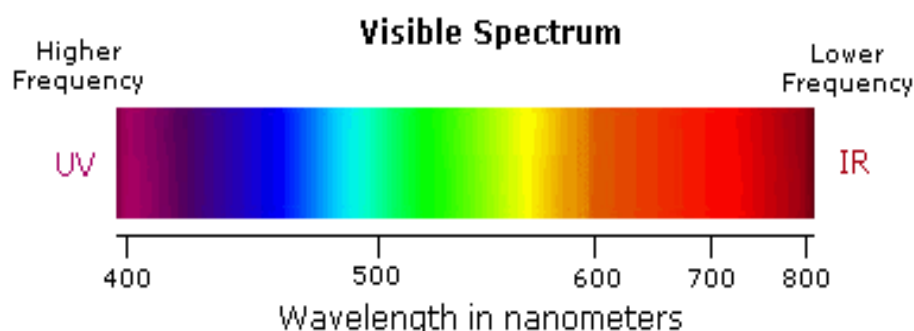
Figure 2. 13 Regions of the visible spectrum

pH indicator molecules exist as ionised, unionised or a mixture of both forms depending on the acidity of their environment. The ionised and unionised forms have different colours. The different species have different electronic structures because of the delocalisation of the π-electrons of their chromophores. Their chromophores represent an extensive system of conjugation of π-bonds in systems such as arenes, azo (N=N) groups and carbonyl (C=O) groups. Upon protonation, the extent of delocalisation of electrons, and consequently the planarity of the molecule, changes. The energy gap, ΔE, between the frontier orbitals decreases as the extent of delocalisation or planarity increases,.

A generic equilibrium of the two-stage ionisation of a diprotic indicator can be represented as:

$$InH_2 \underset{+H^+}{\overset{-H^+}{\rightleftharpoons}} InH^- \underset{+H^+}{\overset{-H^+}{\rightleftharpoons}} In^{2-} \qquad \text{Equation 2.14}$$

$$pKa_1 \qquad\qquad pKa_2$$
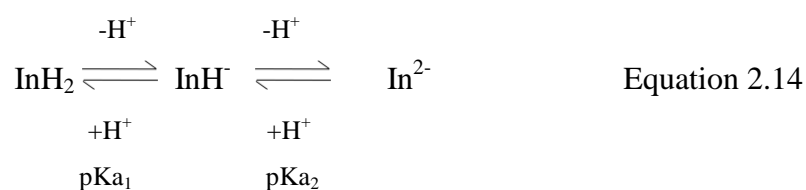
The unionised form (InH_2) is present mainly in very acidic solutions. With decreasing acidity it is ionised first to the mono-deprotonated species (InH^-), and then to the di-deprotonated (In^{2-}). The absorption peak of InH^- appears at a lower wavelength in comparison to the In^{2-} species; i.e. the wavelength is red shifted with increasing negative charge. Higher wavelength is related to greater degree of delocalisation, which in turn increases the planarity of the molecule and therefore lowers the energy gap ΔE between the frontier orbitals.

Fig 2.14 shows the visible absorption spectra of selected buffer solutions of thymol blue (TB), with the absorption bands assigned to the ionisation species. The colour of each overlaid visible spectrum represents the colour of the corresponding buffer solution.

At pH= 1.2 the InH_2 form predominates. It is red in colour, with an absorbance band at 547 nm. With an increase in pH to 1.8 the InH_2 and InH^- ions exists in approximately the same concentration. Hence 1.8 is the pK_{a1} for the first equilibrium (Eqn 2.14).

At pH= 8.6, the InH^- and In^{2-} species are at the same concentration and have absorbance at 434 nm and 598 nm respectively. Hence pH=8.6 represents the pK_{a2} The mono-deprotonated species is yellow in colour (pH 4.2) and the di-deprotonated species is blue (pH 8.92).

Depending on the pH of the solution the absorbance maxima decrease or increase as graphically represented in Fig 2.14 (*insert*). At low pH the absorbance maximum is at 547 nm for TB, and this band decreases and finally disappears at pH 4. At pH 4-6 only the absorption band at 434 nm is present, and from pH=7 upwards this peak decreases until it disappears at pH=9, when only the 598 nm band is present.
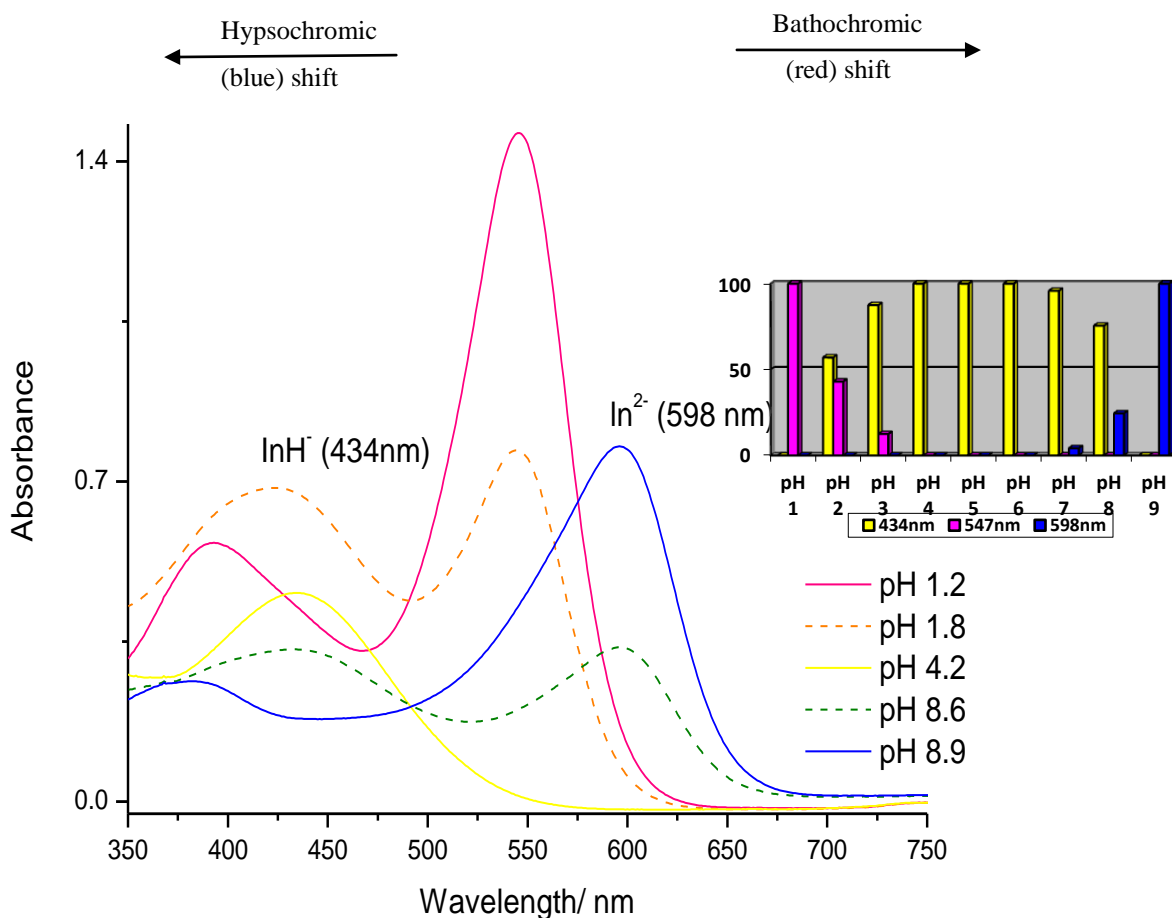
Figure 2. 14 Visible absorption spectra of TB in buffer solutions at varying pHs. The bar chart (*insert*) represents the absorbance, in percentage terms, of the indicator bands at different pH values.

So far the spectral data given for the model pH indicator was obtained in aqueous solution. The spectral properties are affected by the changes in its surrounding environment. The bands may shift towards higher or lower wavelength, known as bathochromic and hypsochromic shifts, respectively. These spectral shifts demonstrate changes in the intermolecular forces between the molecules of the indicator and its surroundings and hence provide information regarding the nature of the surroundings.

Perichromism is the term given to study of the effects of the surrounding medium on the spectral profile of a molecule containing a chromophore. UV-Vis band shifts of a molecule containing a chromophore are caused not just by changes to the surrounding solvent sphere, but by embedding in other surroundings such as solids, interfaces and surfaces[56-58].

The spectral changes depend on the intermolecular forces between indicator dye molecules, and between the dye molecules and their surroundings. These forces include electrostatic interactions and hydrogen bonding. Intermolecular interactions between a solute and surface moieties are complicated in nature and difficult to determine quantitatively.

2.6.4 The use of adsorbed pH indicators for the evaluation of surface acidity of solids of pharmaceutical interest

pH indicator molecules display strong bands in the UV-Vis region, attributed to $\pi-\pi^*$ and $n-\pi^*$ transitions. As their molecules change upon protonation or deprotonation, so does their electronic structure, which causes a shift in wavelength of absorption.

The use of adsorbed pH indicators to characterise surface acidity was first systematically studied by Walling[39]. The acid strength was defined as the ability of a surface to convert an adsorbed neutral base into its conjugate acid and it is expressed semi-quantitatively by the Hammett acidity function, H_o. The acidity of a surface to which a base (In$^-$) has been adsorbed is expressed as:

$$H_o = pK_{HIn} + \log [In^-] / [HIn] \qquad \text{Equation 2.15}$$

The acid strength of the surface is measurable by obtaining the degree of protonation, $[In^-]/[HIn]$, which is similar to the ratio of the intensity of their UV−Vis spectral bands. Similarly, the base strength of a surface is defined as the ability of the surface to convert an adsorbed acid into its conjugate base form. Decreasing values of H_o signify increasing acid strength, and estimates of the acidic strength of the surface can be obtained by visual observation of the colour change. If the colour of the adsorbed indicator is characteristic of the acid form (HIn), it would be interpreted that the H_o function of the surface is lower than the pKa of the indicator used. For example, a solid sample that is colourless with anthraquinone (pK$_a$ = -8.2) but is found to turn yellow with benzalacetophenone (pK$_a$ -5.6) has H_o that is between -5.6 and -8.2. A solid having H_o function >-5.6 will not change any of the indicators from the basic to the acidic colouration, whereas a solid with $H_o \leq$ -8.2 will change both of them[59].

Surface acidity or basicity of pharmaceutical solids is an empirical concept. Terms such as microenvironmental or solid surface pH[40, 52, 55, 60] and pH equivalent (pH$_{eq}$) [51, 52, 60, 61] are used to describe surface acidity. Serajuddin and Jarowski[55] defined the solid surface pH as the pH in the aqueous diffusion layer on the surface of a drug substance as the thickness of the layer, h, approaches zero (pH$_{h=0}$). In order to express the surface pH, the Hammett acidity function H_o (Equation 2.15) has also been applied to several crystalline and amorphous pharmaceutical solids[60, 62-66]. The logarithmic function of the H_o equation is obtained by means of a calibration plot (see below).

The calibration plot for a specific indicator is constructed as solution pH vs. log [peak ratio of acid:base form]. Fig 2.15 shows a typical calibration plot for the determination of the surface pH. For solid samples the log (peak ratio) of the dye in the adsorbed state is calculated from visible spectroscopic measurements, and the surface pH is obtained from the calibration curve.
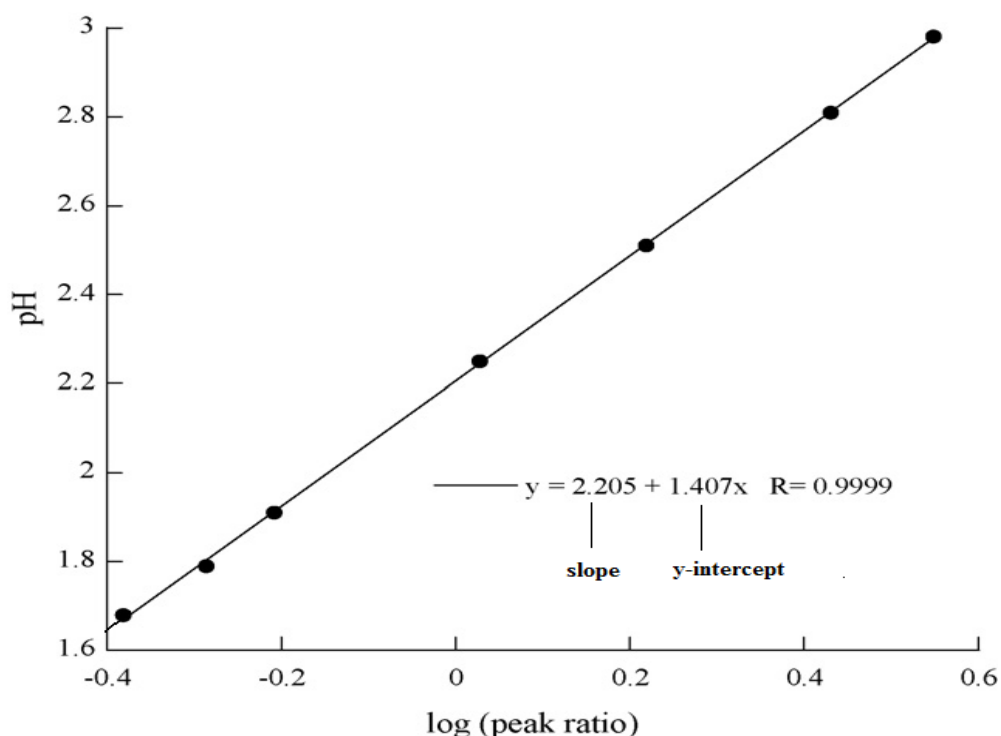
Figure 2.15 A calibration plot of log (peak ratio) of a pH indicator [(adapted from reference 64)].

Glombitza *et al[51]* determined surface acidity of pharmaceutical excipients but expressed it as pH equivalent (pH$_{eq}$) values. The colour changes due to the degree of indicator ionisation were again detected by visible spectroscopy. In this case the <u>absolute</u> absorbance peak ratios (rather than logarithm function) of ionized to unionized adsorbed indicator were correlated to the pH of buffered indicator solutions to predict the pH$_{eq}$ values. This method, developed by Glombitza and co-workers, was employed to evaluate the influence of surface acidity on the decomposition rate of acetylsalicylic acid [61]. Excipients with predicted pH$_{eq}$ values were coated with the drug, and surface acidity vs decomposition-rate profiles were drawn using calculated decomposition rate constants. Results indicated that the surface acidity-decomposition-rate profiles were similar to pH vs decomposition rate profiles of the drug in solution.

Scheef *et al[53]* studied the influence of particle size on the determination of pH$_{eq}$ for hydrophilic substances. Their results indicated that surface acidity was independent of particle size. The effect of formulation composition and processing variables such as wet and dry mixing on the solid state acidity in solid dosage forms, were also studied using the pH$_{eq}$ method [52]. Single excipients and excipient mixtures were ranked in order of acidity, and the effect of dry mixing and wet mixing of certain excipients were evaluated. Recently the surface pH of sixteen drug substances where determined by the pH$_{eq}$ method and by slurry pH measurement[40]. The surface acidity measured using the pH$_{eq}$ and slurry pH methods did not show good agreement for seven of the drug substances analysed.

The determination of solid state acidity by H_o is analogous to the pHeq method in that they both involve calculating absorbance peak ratios of ionised to unionised adsorbed dye indicators, and based on the assumption that the spectral characteristics of the ionised and unionised forms remain the same in solution and the adsorbed state. The values obtained using these two approaches can be shown to be equivalent, provided that the ratio of the extinction coefficients of indicator species in the solid state is similar to that in solution[62, 66].

Characterisation of acidity by H_o and pH$_{eq}$ functions presents a pragmatic approach based on the assumption that spectral properties of the ionisation form of the dye is unaltered in the adsorbed state. This assumption ignores the influence of the heterogeneous surface structure of solids. Adoption of this method also neglects the effect of several intermolecular interactions that affect the spectral behavior of pH indicators.

For the above mentioned reasons, neither H_0 nor pHeq measurements were used in this work to express the acidity of model polymorphic systems. Rather the spectral profiles of adsorbed pH indicators were examined based on possible dye-surface interactions, dye-dye interactions and the effect of adsorbed moisture.

Acid-base indicators and DRVS have also been employed to characterize the amorphous to crystalline solid state transformation in pharmaceutical excipients such as sucrose and trehalose [67]

2.7 References

1. M. Blanco, M. Alcalá, J. M. González and E. Torras, *Analytica Chimica Acta*, 2006, **567**, 262-268.

2. H. G. Brittain, *Polymorphism in Pharmaceutical Solids*, Marcel Dekker, New York, 1999.

3. J. Bernstein, *Polymorphism in Molecular Crystals*, Oxford University Press, New York ; Oxford, 2002.

4. A. S. Raw, M. S. Furness, D. S. Gill, R. C. Adams, F. O. Holcombe and L. X. Yu, *Advanced Drug Delivery Reviews*, 2004, **56**, 397-414.

5. A. S. Raw and L. X. Yu, *Advanced Drug Delivery Reviews*, 2004, **56**, 235-236.

6. Anon, ANDAs:Pharmaceutical solid polymorphism. Chemistry, Manufacturing and controls information, http://www.fda.gov/downloads/Drugs/GuidanceCompliance RegulatoryInformation/Guidances/ucm072866.pdf#7.

7. S. R. Chemburkar, J. Bauer, K. Deming, H. Spiwek, K. Patel, J. Morris, R. Henry, S. Spanton, W. Dziki, W. Porter, J. Quick, P. Bauer, J. Donaubauer, B. A. Narayanan, M. Soldani, D. Riley and K. McFarland, *Organic Process Research & Development*, 2000, **4**, 413-417.

8. G. G. Z. Zhang and D. Zhou, in *Developing Solid Oral Dosage Forms*, eds. Q. Yihong, C. Yisheng, G. Z. Z. Geoff, L. Lirong and R. P. William, Academic Press, San Diego, 2009, pp. 25-60.

9. H. K. Henisch, *Materials Research Bulletin*, 1983, **18**, 1584-1585.

10. Y. Cui, *International Journal of Pharmaceutics*, 2007, **339**, 3-18.

11. R. Tilley, *Crystals and crystal structure*, John Wiley & Sons, Chichester.

12. A. West, *Solid State Chemistry and its applications*, John Wiley and Sons, Chichester, 1984.

13. M. Ladd and R. Palmer, *Structure determination by X-ray Crystallography*, Kluwer Academic Publishers, New York, 2003.

14. T. Hahn and H. Klapper, *Space group symmetry, International Tables for Crystallography,* Kluwer Academic Publishers, Dordrecht, 1992.

15. S. Heyes, Structure of simple inorganic solids, http://www.chem.ox.ac.uk/icl/heyes/structure_of_solids/lecture1/lec1.html.

16. X. Chen, K. R. Morris, U. J. Griesser, S. R. Byrn and J. G. Stowell, *Journal of the American Chemical Society*, 2002, **124**, 15012-15019.

17. T. J. Kistenmacher and R. E. Marsh, *Journal of the American Chemical Society*, 1972, **94**, 1340-1345.

18. V. L. Himes, A. D. Mighell and W. H. De Camp, *Acta Crystallographica Section B*, 1981, **37**, 2242-2245.

19. A. L. Grzesiak, M. D. Lang, K. Kim and A. J. Matzger, *Journal of Pharmaceutical Sciences*, 2003, **92**, 2260-2271.

20. G. D. Enright, V. V. Terskikh, D. H. Brouwer and J. A. Ripmeester, *Crystal Growth & Design*, 2007, **7**, 1406-1410.

21. J. Lamotte, H. Campsteyn, L. Dupont and M. Vermeire, *Acta Crystallographica Section B*, 1978, **34**, 1657-1661.

22. A. M. O'Connell and E. N. Maslen, *Acta Crystallographica*, 1967, **22**, 134-145.

23. M. Alleaume and J. Decap, *Acta Crystallographica*, 1965, **19**, 934-938.

24. J. Wolff, *Angewandte Chemie (International Edition)*, 1996, **35**, 2195-2197.

25. Y. Erbil, *Surface Chemistry of Solid and Liquid Interfaces*, Blackwell Publishing, Oxford, 2006.

26. J. Steed and J. Atwood, *Supramolecular Chemistry*, John Wiley & Sons, Chichester, 2009.

27. J. Bernstein, R. Davis, L. Shimoni and N.-L. Chang, *Angewandte Chemie (International Edition)*, 1995, **34**, 1555-1573.

28. Anonymous, IUPAC Gold Book, 1997.

29. J. Glusker, M. Lewis and M. Rossi, *Crystal structure analysis for chemists and biologists*, VCH Publishers, New York, 1994.

30. C. Aubrey-Medendorp, M. Swadley and T. Li, *Pharmaceutical Research*, 2008, **25**, 953-959.

31. G. Nichols, in *Polymorphism in the Pharmaceutical industry*, ed. R. Hilfiker, Wiley-vch, Weinheim, 2006.

32. S. R. Vippagunta, H. G. Brittain and D. J. W. Grant, *Advanced Drug Delivery Reviews*, 2001, **48**, 3-26.

33. D. A. Snider, W. Addicks and W. Owens, *Advanced Drug Delivery Reviews*, 2004, **56**, 391-395.

34. P. W. Atkins and J. De Paula, *Physical Chemistry*, Oxford University Press, Oxford, 2006.

35. R. Hilfiker, *Polymorphism in the Pharmaceutical Industry*, Wiley-VCH ; [Chichester : John Wiley [distributor]], Weinheim, 2006.

36. P. Stahl and B. Sutter, in *Polymorphism in the Pharmaceutical Industry*, ed. R. Hilfiker, Wiley-VCH, Weinheim, 2006, pp. 309-365.

37. C. Sun and J. C. Berg, *Advances in Colloid and Interface Science*, 2003, **105**, 151-175.

38. A. Zecchina, C. Lamberti and S. Bordiga, *Catalysis Today*, 1998, **41**, 169-177.

39. C. Walling, *Journal of the American Chemical Society*, 1950, pp. 1164-1168.

40. M. Pudipeddi, E. A. Zannou, M. Vasanthavada, A. Dontabhaktuni, A. E. Royce, Y. M. Joshi and A. T. M. Serajuddin, *Journal of Pharmaceutical Sciences*, 2008, **97**, 1831-1842.

41. C. Thompson, M. C. Davies, C. J. Roberts, S. J. B. Tendler and M. J. Wilkinson, *International Journal of Pharmaceutics*, 2004, **280**, 137-150.

42. J. Heng, A. Bismarck and D. Williams, *AAPS PharmSciTech*, 2006, **7(4) 84**, E1-E9.

43. T. Dines, C. Rochester and A. Ward, *Journal of the Chemical Society, Faraday Transactions*, 1991, **87**, 1611-1616.

44. Z.-Y. Ma, C. Yang, W. Wei, W.-H. Li and Y.-H. Sun, *Journal of Molecular Catalysis A: Chemical*, 2005, **227**, 119-124.

45. P. J. Hendra, I. D. M. Turner, E. J. Loader and M. Stacey, *The Journal of Physical Chemistry*, 1974, **78**, 300-304.

46. R. Ferwerda, J. H. van der Maas and P. J. Hendra, *The Journal of Physical Chemistry*, 1993, **97**, 7331-7336.

47. T. J. Dines, L. D. MacGregor and C. H. Rochester, *Vibrational Spectroscopy*, 2003, **32**, 225-240.

48. T. J. Dines, L. D. MacGregor and C. H. Rochester, *Chemical Physics*, 2006, **322**, 445-458.

49. M. J. Telko and A. J. Hickey, *Journal of Pharmaceutical Sciences*, 2007, **96**, 2647-2654.

50. M. Puppedi, E. Zannou, M. Vasanthavada, A. Dontabhaktuni, A. Royce, Y. Joshi and A. Serajuddin, *Journal of Pharmaceutical Sciences*, 2008, **97**, 1831-1842.

51. B. W. Glombitza, D. Oelkrug and P. C. Schmidt, *European Journal of Pharmaceutics and Biopharmaceutics*, 1994, **40**, 289-293.

52. R. Govindarajan, A. Zinchuk, B. Hancock, E. Shalaev and R. Suryanarayanan, *Pharmaceutical Research*, 2006, **23**, 2454-2468.

53. C. A. Scheef, D. Oelkrug and P. C. Schmidt, *European Journal of Pharmaceutics and Biopharmaceutics*, 1998, **46**, 209-213.

54. A. Serajuddin and M. Rosoff, *Journal of Pharmaceutical Sciences*, 1984, **73**, 1203-1208.

55. A. Serajuddin and C. Jarowski, *Journal of Pharmaceutical Sciences*, 1985, **74**, 148-154.

56. C. Reichardt, *Chemical Reviews*, 1994, **94**, 2319-2358.

57. C. Reichardt, *Pure and Applied Chemistry*, 2004, **76**, 1903-1919.

58. C. Reichardt, *Pure and Applied Chemistry*, 2008, **80**, 1415-1432.

59. K. Tanabe, M. Misono, Y. Ono and H. Hattori, *New solid acids and bases: their catalytic properties.*, Kodansha, Tokyo, Japan, 1989.

60. R. Govindarajan, K. Chatterjee, L. Gatlin, R. Suryanarayanan and E. Y. Shalaev, *Journal of Pharmaceutical Sciences*, 2006, **95**, 1498-1510.

61. B. W. Glombitza and P. C. Schmidt, *European Journal of Pharmaceutics and Biopharmaceutics*, 1995, **41**, 114-119.

62. A. V. Zinchuk, B. C. Hancock, E. Y. Shalaev, R. D. Reddy, R. Govindarajan and E. Novak, *European Journal of Pharmaceutics and Biopharmaceutics*, 2005, **61**, 158-170.

63. K. Chatterjee, E. Y. Shalaev, R. Suryanarayanan and R. Govindarajan, *Journal of Pharmaceutical Sciences*, 2008, **97**, 274-286.

64. K. A. Alkhamis, *International Journal of Pharmaceutics*, 2008, **362**, 74-80.

65. K. A. Alkhamis, *Drug Development and Industrial Pharmacy*, 2009, **35**, 408-416.

66. G. R., C. K., G. L., S. E. and S. R., *European Journal of Pharmaceutics and Biopharmaceutics*, 2004, **61**, 158-170.

67. P. Major , *PhD thesi*s, *School of Science*, University of Greenwich, 2010.

Chapter 3: Principal experimental techniques and methods

Polymorphism results in changes in the physicochemical properties of the solid. Any technique which can be used to measure a property of the solid state can potentially be used for the study and characterisation of polymorphs. The most established and frequently used techniques are powder x-ray diffraction (PXRD), differential scanning calorimetry (DSC), hot-stage microscopy (HSM), scanning electron microscopy (SEM) and Raman spectroscopy. All of these are used in this work and are discussed here. The aforementioned techniques are referred to as bulk techniques because they measure properties of the whole solid and not just the surface. In order to obtain information specific to the surface of a polymorphic solid, an additional technique was required, and for this a novel application of diffuse reflectance visible spectroscopy was used with adsorbed pH indicator dyes.

The principles of each technique are discussed here, including sample preparation, factors influencing the quality of data, together with advantages and disadvantages of the techniques.

3.1 Powder X-ray Diffraction (PXRD)

X-ray diffraction (XRD) is the single most important method for identifying the structure of crystalline solids and can be regarded as definitive for the characterisation of polymorphs[1-3]. Analysis by X-ray diffraction can be classified into single crystal and powder methods. Single crystal XRD provides enough data for the complete structural characterisation of a single crystal, including bond lengths, bond angles, space group, unit cell dimensions etc. Powder XRD provides a structural fingerprint pattern of a crystal called a diffractogram. This is a plot of the intensity of x-rays diffracted at various angles by lattice planes against diffraction angle (normally expressed in $°2\theta$). $°2\theta$ is directly related to the interplanar spacing distance that exists in crystals.

Single crystal data can be used to computationally simulate the two dimensional PXRD data for a given sample. Both techniques are based on the diffraction of X-rays by ordered crystal lattices. As the main focus of this section is PXRD, it is described in some detail.

3.1.1 Diffraction of X-rays by powdered crystalline solids

XRD is based on the fact that each crystalline substance has a characteristic arrangement of atoms which diffracts X-rays in a unique pattern. Crystals have regular repeating structures, in a similar manner to optical diffraction gratings. Molecules show a unique capability for diffracting X-rays because the separation between their atoms are of the same order of magnitude as the wavelength of X-rays (~1Å) [4, 5].

Bragg's Law is the widely accepted approach to X–ray diffraction patterns from lattice planes in crystalline solids, and is expressed as:

$$n\lambda = 2d \; sin\theta \qquad\qquad \text{Equation 3.1}$$

where d is the distance between adjacent parallel planes (interplanar lattice spacing), λ is the wavelength of the X-rays, θ is the angle of reflection (or scattering angle) and n is the order of the reflection, which is a positive integer. Bragg's law is satisfied when there is constructive interference of X-ray beams diffracting from parallel planes in the lattice structure.

For reasons of simplicity Bragg's Law refers to the more complex process of diffraction as reflection, and regards crystals as lattice planes, defined by their unit cells. Bragg's law is only satisfied for the angles of incidence that produce beams in phase and that interfere constructively[4, 6]. Experimentally, λ is determined by the type of metal target used for X-ray generation. For a given pair of adjacent parallel lattice planes, n can be equal to 1, 2, 3, etc.

As polymorphs have different packing arrangement of their molecules, they diffract X-rays differently; hence their PXRD patterns are different. However, where the polymorphs are very similar in structure, they will produce very similar PXRD patterns [3, 7].

3.1.2 Powder X-ray Diffraction (PXRD) experiment

In a PXRD experiment, monochromatic radiation impinges on a powdered sample at different angles and the corresponding intensities of diffracted X-rays are measured.

The output of a PXRD experiment is a diffractogram. Figure 3.1 shows a diffractogram for the γ polymorph of indomethacin. It can be regarded as a structural fingerprint for a given solid material. Each crystalline material has a unique PXRD pattern.

The number of observed peak is related to the symmetry of the unit cell (low symmetry unit cells give more peaks compared to a higher symmetry unit cell). Each peak position (expressed as °2θ) is related to the interplanar spacing between parallel lattice planes. Each peak can be labelled with a corresponding Miller index, to indicate the set of planes responsible for the peak. The intensity of the peaks expressed as the % of the ratio of each peak relative to the most intense peak (I/I_{max} %), is related to the scattering power of the atoms in the lattice plane. Light atoms scatter X-rays weakly, while heavy atoms scatter X-rays more effectively.
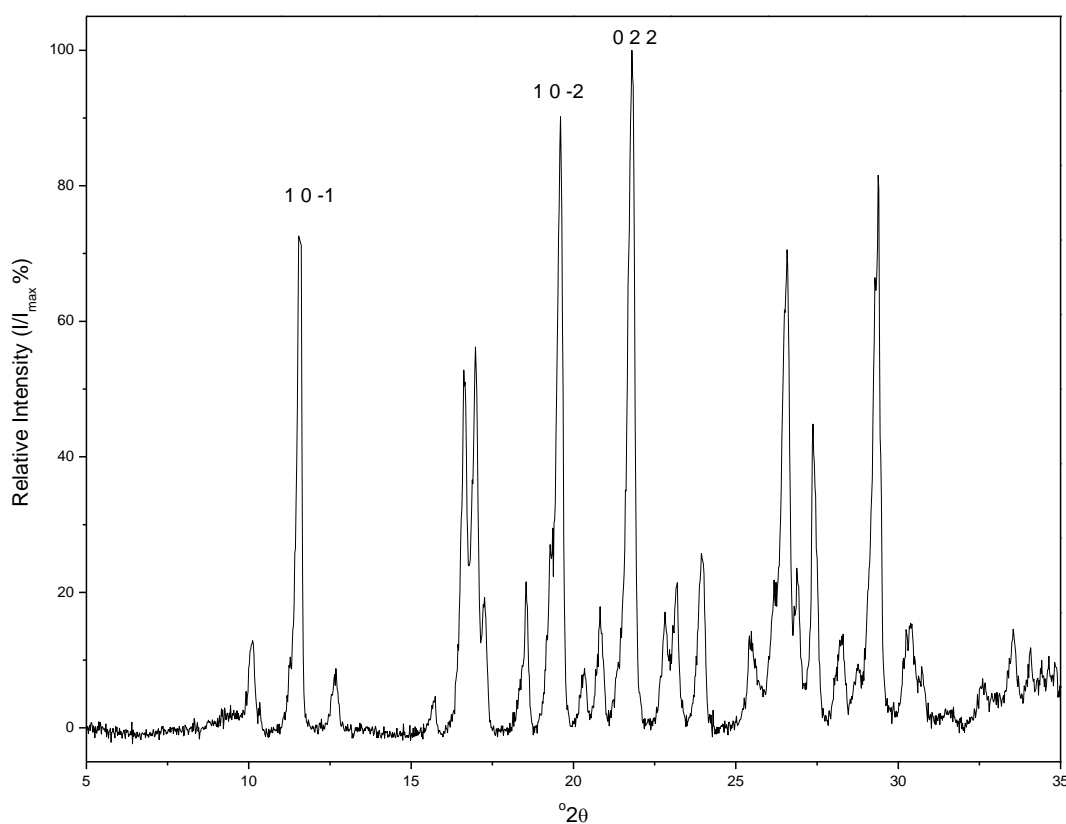
Figure 3.1 The PXRD pattern for the γ polymorph of indomethacin. Three peaks have been labelled with Miller indices, indicating the set of lattice planes responsible for that diffraction peak.

In this work, polymorphic identity/purity is established by matching experimental PXRD patterns with a pattern simulated from single crystal data. Experimental PXRD patterns were recorded on a Philips PW1729 powder x-ray diffractometer with a PW1050 goniometer (Lelyweg, Netherlands).

Fig 3.2 shows the schematic diagram and photograph of the PW1729 diffractometer. The basic parts of the PXRD instrumentation are an X-ray source, monochromator, sample mount and detector system.
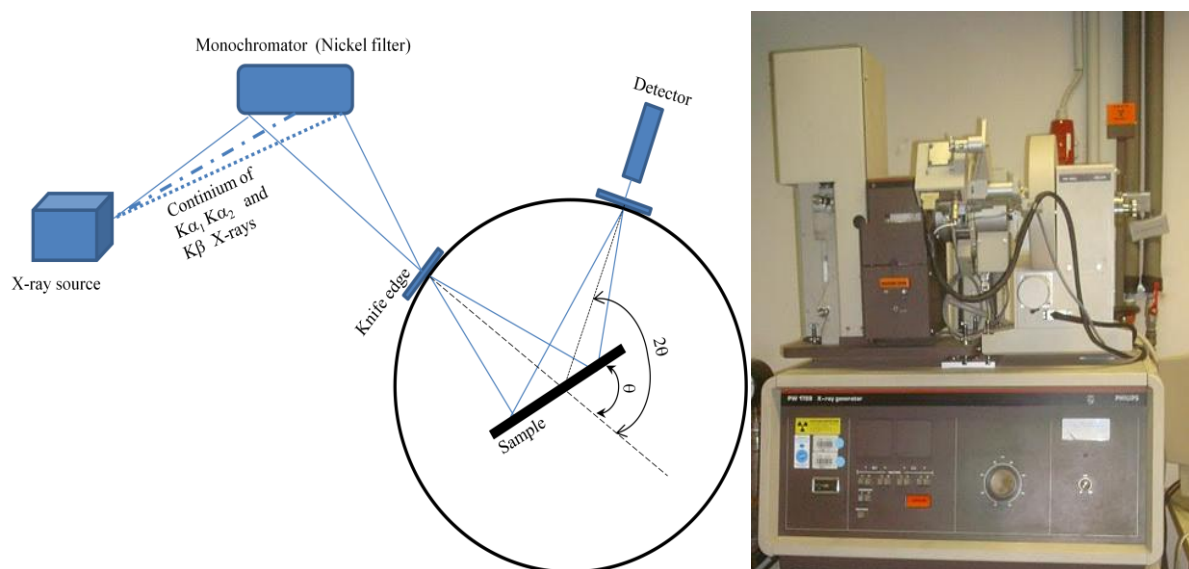
Figure 3. 2 Philips PW1729 powder x-ray diffractometer system.

The X-ray source is an evacuated tube with a copper anode and tungsten filament. It is energized by a generator at sufficient power to produce the continium of $K\alpha_1$, $K\alpha_2$ and $K\beta$ radiation. The sample mount moves relative to the X-ray source gradually increasing the angle of incidence. Because the angle of incidence must equal the angle of reflection, the detector arm moves in the same direction at twice the speed. Hence the sample rotates through angle θ while the detector rotates through angle 2θ (see diagram above).

This instrumental configuration is called Bragg-Braentano geometry and both circles are mounted on a goniometer which accurately measures angles.

PXRD relies on monochromatic radiation so the $K\beta$ X-rays are filtered out using a monochromator, in this case a Nickel filter. Some instruments employ single crystal monochromators such as graphite. After the monochromator, $K\alpha_1$ and $K\alpha_2$ radiation converge at the knife edge where the $K\alpha_2$ is removed. The monochromatic radiation impinges on the crystalline sample and diffraction occurs. The diffracted beam is detected by a moveable scintillation counter (the detector in the above diagram).

The detector is set to scan over a range of angles at a constant angular velocity or scanning speed. Routinely, a scan of 5 to 40 degrees (2θ) is sufficient to cover the most useful part of the powder pattern of drug polymorphs.

 A set of collimation systems or slits (horizontal apertures) in the path of the X-ray beam help to control the spread of the beam for enhanced resolution. The sizes of slits affect the resolution and intensity of peaks in the diffractogram. Small slit sizes give better resolution and lower intensity peaks. Larger slit sizes give higher intensity peaks but poorer resolution. The quality of data obtained is also affected by the particle morphology and particle size of the sample. For good quality PXRD patterns the sample particles (crystallites) should have a random orientation.

A random powdered sample is one that provides an equal probability for all crystallographic directions in the sample to be exposed to the impinging X-ray. Most synthetic and naturally occurring crystallites are inherently non-random in terms of size and morphology as a result of their growth conditions. The ideal particle size of the crystallites in a sample should be between 5-10 μm so that no specific crystallographic direction(s) are preferentially exposed to the X-ray. For drug polymorphs obtaining this particle size range would mean grinding or milling. Milling is known to alter polymorphic integrity by introduction of amorphous content, conversion to another polymorph, decomposition or solid-state reactions, and so is generally discouraged. Drug polymorphs have non-spherical morphology, so their crystallites prefer to orient themselves to occupy a minimum volume. For example platy crystals will lay flat, one on top of the other. The effect of this non-randomness, referred to as preferred orientation, leads to poor quality data. The intensities of peaks in a diffractogram are expressed as a percentage of the total. This assumes that all crystal planes are equally exposed to the X-ray beam.

Where a preferred crystal orientation exists, the planes exposed by the favoured orientation will give an enhanced signal, and those hidden by that crystal orientation will be significantly reduced or even absent. Hence the data obtained will be skewed.

The effects of preferred crystal orientation can be minimised by milling (providing that polymorphic integrity is not compromised), sieving the powdered sample to a small enough particle size range, and spinning the mounted sample during data collection.

The presentation of the sample is generally by gentle compaction into a holder such that the surface of the powder is levelled with the surface of the holder. The X-ray beam is focussed on the top of the sample holder and has a very shallow depth of field. Filling the holder too high or too low will cause the surface to be out of focus, which in turn gives rise to peaks being shifted in their positions in the diffractogram.

3.1.3 Advantages and disadvantages of powder x-ray diffraction

The main advantages of the PXRD method is that it is non-destructive (sample is recoverable after analysis). It also is a definitive method for characterising polymorphs because it provides a two dimensional structural fingerprint for a powdered sample.

The main disadvantage is that this method is plagued by the effects of preferred orientation.

3.2 Differential Scanning Calorimetry (DSC)

Differential scanning calorimetry (DSC) is one of the recognised methods employed for routine identification and characterisation of polymorphs. DSC is a technique used to study thermal events (i.e. those associated with the absorption or release of heat energy) such as melting, crystallisation or solid state transformation. Sample and reference materials are subjected to identical temperature regimes in an environment heated or cooled at a constant rate. Throughout the process the heat flow (power) required to maintain the two materials at identical temperature is measured.

The heat flow is related to the heat capacity, C_p of the sample material by the following expression:

$$\frac{dQ}{dt} = C_p \frac{dT}{dt} \qquad \qquad \text{Equation 3.2}$$

where, $\frac{dQ}{dt}$ is the heat flow and $\frac{dT}{dt}$ is the heating rate. Heat capacity, C_p is an intrinsic property of the sample material.

The DSC raw data is a plot of heat flow per gram of sample (measured in W/g) against temperature. This raw data can then be expressed as heat capacity versus temperature using equation 3.2. When a sample undergoes a thermal event such as melting or recrystallisation, the heat capacity changes. This change in heat capacity is shown in a DSC output (thermogram) as an endothermic or exothermic peak. The onset of the peak gives the temperature of the event and the integral of the peaks of a thermogram gives the enthalpy associated with that particular event. Figure 3.3 shows the DSC thermogram for caffeine polymorph, Form II.
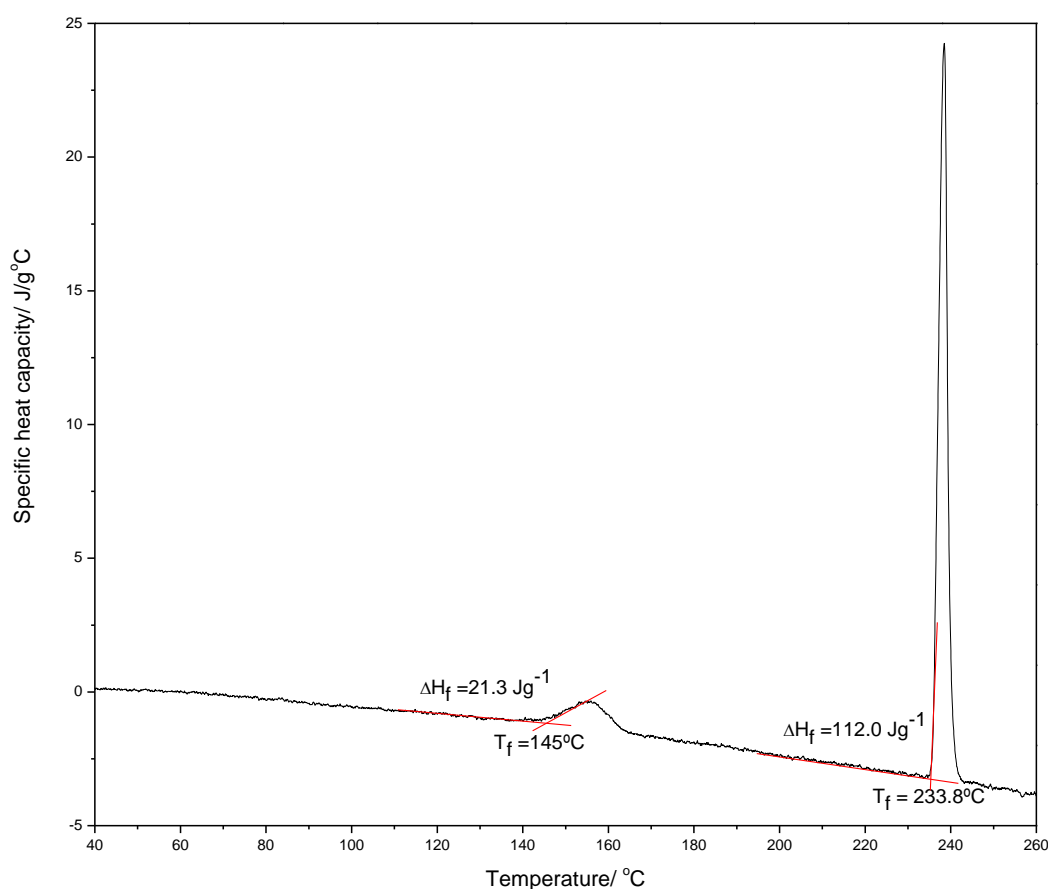
Figure 3.3 DSC thermogram for caffeine polymorph, Form II. Two endothermic events are observed. The temperature onsets of these events are determined from the intersection point of two tangents. The enthalpies of these events are calculated from the area under the peak.

3.2.1 Differential scanning calorimetry (DSC) experiment

Polymorph characterisation by DSC is performed on the basis of melting point differences, the study of transformation behaviour of metastable systems, and the thermodynamic stability relationship between polymorphic forms[8-10].

In this work, DSC thermograms were recorded using a Mettler Toledo FP85 DSC system (Greifense, Sweden). Figure 3.4 shows the schematic diagram of the FP85 DSC instrument. The construction of the FP85 measuring cell consists of a cylindrical aluminium furnace designed to heat a sample crucible and a fixed, factory installed, reference material at a controlled rate from room temperature to a maximum of 400ºC. An inert purge gas (nitrogen) is passed through the cell at a constant flow rate. The sample and reference are enclosed in the furnace, and the heat energy required to maintain the sample and reference materials at nearly identical temperature during heating, is recorded.
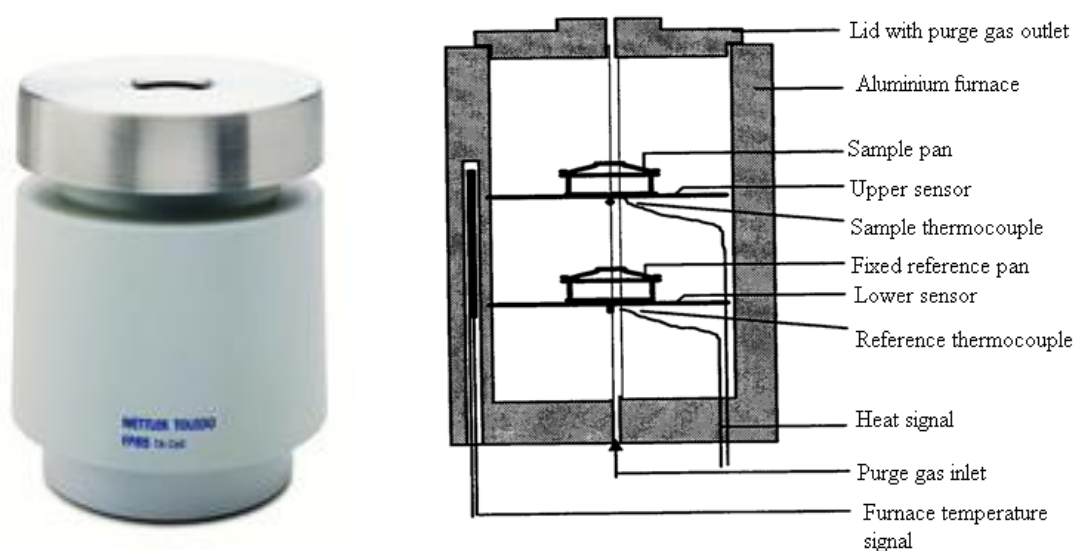
Figure 3.4 The Mettler Toledo FP85 differential scanning calorimeter heat flux system.

The aluminium furnace dissipates heat to the specimens via a disc which is attached to the furnace. The disc has two raised platforms on which the sample and reference pans are placed. Thermocouples are attached to the underside of each platform. A separate thermocouple is embedded in the furnace. The heat signals from these thermocouples are processed into a DSC thermogram.

 The heating rate affects the resolution of the peaks. The higher the heating rate, the poorer the resolution but faster data acquisition times and *vice versa* for lower heating rates. A suitable heating rate is established by carrying out measurements at a number of heating rates, examining the effect on the thermograms, and selecting the rate that gives the best compromise of good resolution and reasonable data acquisition time.

The DSC instrument is calibrated using pure reference materials such as indium and zinc. The melting point and enthalpy of fusion of these reference materials are obtained to calibrate calorimeter response. Experimental factors that can influence the quality of DSC data are mass of sample, particle size and morphology, thermal lag between the sample and the crucible and crystal imperfection or impurities. Increasing the mass of sample increases the sensitivity of the calorimeter to detect low energy thermal events. The particle size and morphology affect the heat transfer resistance. Larger particles have large heat transfer resistance when compared to small particles so keeping the particle size as small as practically possible gives quality data.

Additionally, chemical or polymorphic impurities decrease the onset of melting and broaden the melting point range.

3.2.2 Advantages and disadvantages of DSC

DSC provides very precise measurement of melting points and enthalpies, which makes it ideal for detecting the existence of very similar species such as polymorphs.

A fundamental disadvantage of DSC is that it is an invasive technique, where sample is usually non-recoverable for further analysis.

3.3 Hot stage microscopy (HSM)

In hot-stage microscopy, the sample of interest is observed using an optical microscope, as the temperature of a sample is changed. In terms of polymorphism, the size and shape of particles, habit transformation, sublimation, melting and degradation may be readily observed. The information obtained from HSM can be used to assist in the interpretation of thermal events shown in DSC thermograms.

3.3.1 Hot-stage microscopy experiment

In order to obtain further information regarding the thermal events observed from DSC data hot stage microscopy (HSM) videos are recorded. The thermal events observed in this work, were examined using a Leica optical microscope (Wetzlar, Germany) fitted with a Mettler FP52 hot stage apparatus (Greifense, Switzerland). Figure 3.5 shows the FP90 hot stage microscope used in this work.
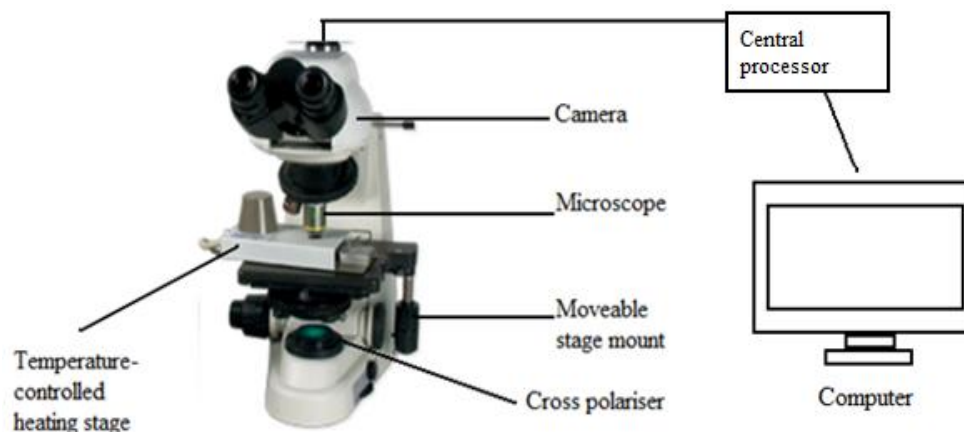
Figure 3.5 Experimental set-up for the FP90 Mettler Toledo hot-stage microscopy system.

The three main parts of a HSM instrument are the polarising microscope, a temperature controlled heating stage and a camera. The sample of interest is placed on a microscope slide and inserted into the chamber of the temperature controlled heating stage. Figure 3.6 shows the HSM pictures for the heating of CBZ-III at a constant heating rate. The thermal events that occurred during the heating regime are recrystallisation of the plate-like CBZ-III to needle CBZ-I crystal, and melting of CBZ-I.
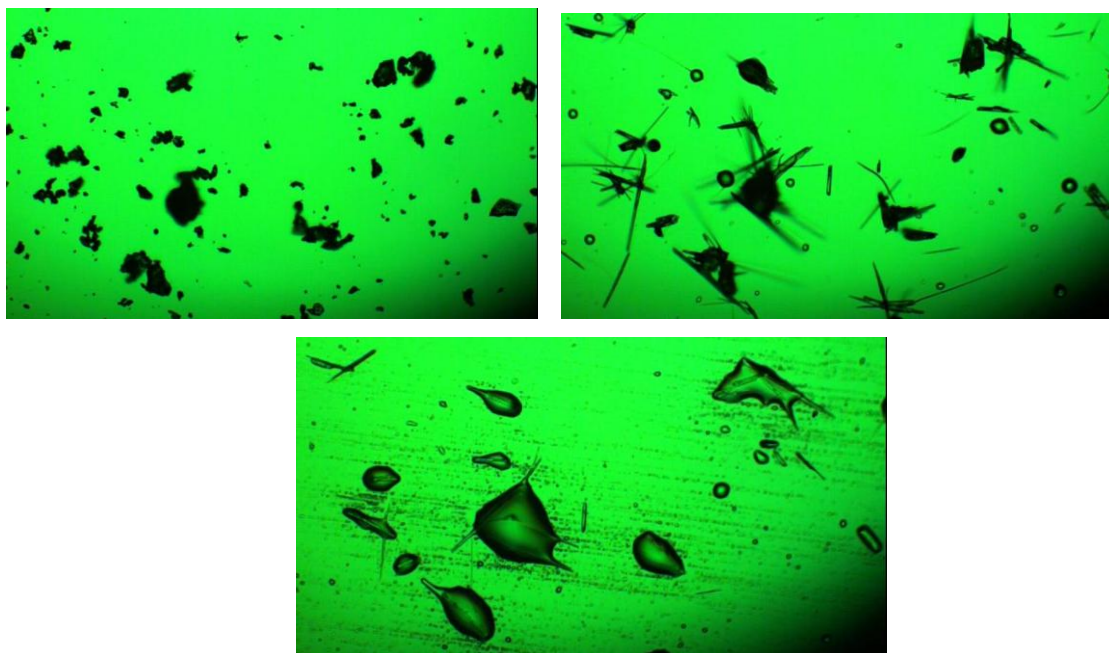
Figure 3.6 HSM pictures for the heating of CBZ-III at a constant heating rate. The thermal events that occurred during the heating regime are recrystallisation of the plate-like CBZ-III (top right) to needle CBZ-I crystal (top left), and melting of CBZ-I (bottom).

3.4 Scanning electron microscopy (SEM)

In comparison to optical microscopes, SEM uses electrons instead of light to form an image. In the study of polymorphs it can be used to characterise the crystal morphology.

3.4.1 SEM experiment

A beam of electrons is produced at the top of the microscope by an electron gun. The electron beam follows a vertical path through the microscope, which is held within a vacuum. The beam travels through electromagnetic fields and lenses, which focus the beam down toward the sample. Once the beam hits the sample, electrons and X-rays are ejected from the sample. Detectors collect the backscattered electrons and secondary electrons and convert them into a signal that is sent to a screen to produce the final image. The final image is displayed as a micrograph. Figure 3.7 shows the SEM micrographs for two polymorphs of carbamazepine. Form I has a needle-like morphology, while Form III has a plate-like morphology.

Figure 3.7 SEM micrographs for two polymorphs of carbamazepine: crystals of Form I are needles (left), while crystals of Form III are plates.

In this work a Cambridge Stereoscan S-360 scanning electron microscope (Cambridge, UK) equipped with a stereoscan electronic control and imaging system was used. Fig 3.8 shows the schematic diagram of the SEM setup. Because the SEM operates under vacuum conditions and uses electrons, the sample has to be specially prepared.

Non-metallic samples need to be made conductive by covering the sample with a thin layer of conductive material such as gold.
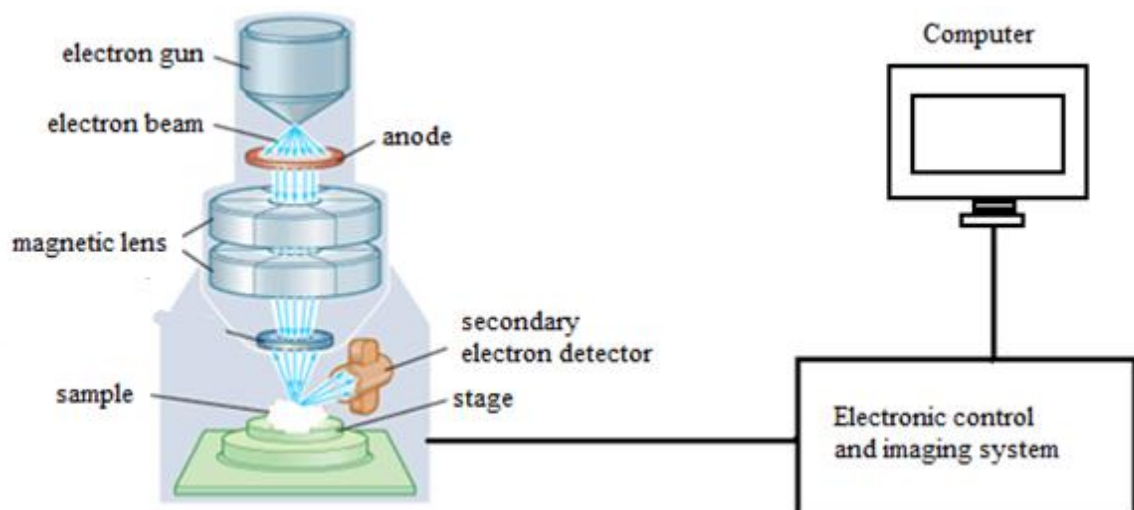
Figure 3.8 Schematic diagram of the Stereoscan 360 scanning electron microscope equipped with an electronic control and imaging system.

3.4.2 Advantages and disadvantages of SEM

SEM has a large depth of field (it allows much more of a specimen to be in focus at one time). The images produced by SEM have better image resolution that those obtained by optical microscopy. Very little sample is needed for SEM analysis. Disadvantages of SEM are that the sample must be stable under vacuum, and that it must be electrically conductive. Non-conducting samples must be coated with a layer of gold.

3.5 Raman Spectroscopy

3.5.1 Fundamentals of Raman spectroscopy

Laser light can be scattered by a sample elastically or inelastically. In elastic scattering, the energy (or frequency) of the light scattered by a sample is the same as the energy of incident light. In the case of inelastic scattering, the energy of scattered radiation is enhanced or diminished relative to the incident radiation. The frequency difference between incident and scattered radiation corresponds to the frequency of the molecular vibration induced within the sample. In the Raman effect, when a laser beam strikes a sample, approximately one in a million of all scattered radiation is inelastically scattered. Inelastically scattered radiation can occur at lower (Stokes) or higher (anti-Stokes) frequencies with respect to the elastically scattered (Rayleigh) frequency. Conventional Raman analysis is based on the Stokes line because it is relatively more intense than the anti-Stokes line.

Raman spectroscopic technique provides information on molecular functional groups to aid identification of materials, by probing the vibrational modes of bonds in a compound [11, 12]. Incident laser light excites a molecule to a higher energy vibrational state. When the molecule relaxes it emits a photon and it returns to a different rotational or vibrational state. The difference in energy between the ground state and this new state leads to a shift in the emitted photon's frequency away from the excitation wavelength. Raman bands are expressed as wavenumber shifts is expressed in units of cm^{-1}.

Not all molecular vibrations are Raman active. A vibration will be Raman active if there is a change in amount of deformation of the electron cloud (or a change in molecular polarisability) during such a vibration.

For polymorphic materials where the same molecule is packed differently, small differences in spectra are expected. These differences involve small variation in peak positions, shape and/or intensity and appearance of new peaks[13, 14]. In most cases the differences between spectra is sufficient enough for distinguishing polymorphic forms and providing insights into the arrangement of molecules.

3.5.2 Raman experiment

Raman spectrometers measure the light emitted by a sample under laser illumination. The intensity and Raman shift of emitted light is shown in a spectrum. The units are emittance units and wavenumber (cm^{-1}) respectively. Raman shift spanning the range 4000-10 cm^{-1} is a measure of the difference between the observed spectral bands and wavelength used by the excitation laser beam. Figure 3.9 shows the Raman spectrum of the β polymorph of sulfanilamide.
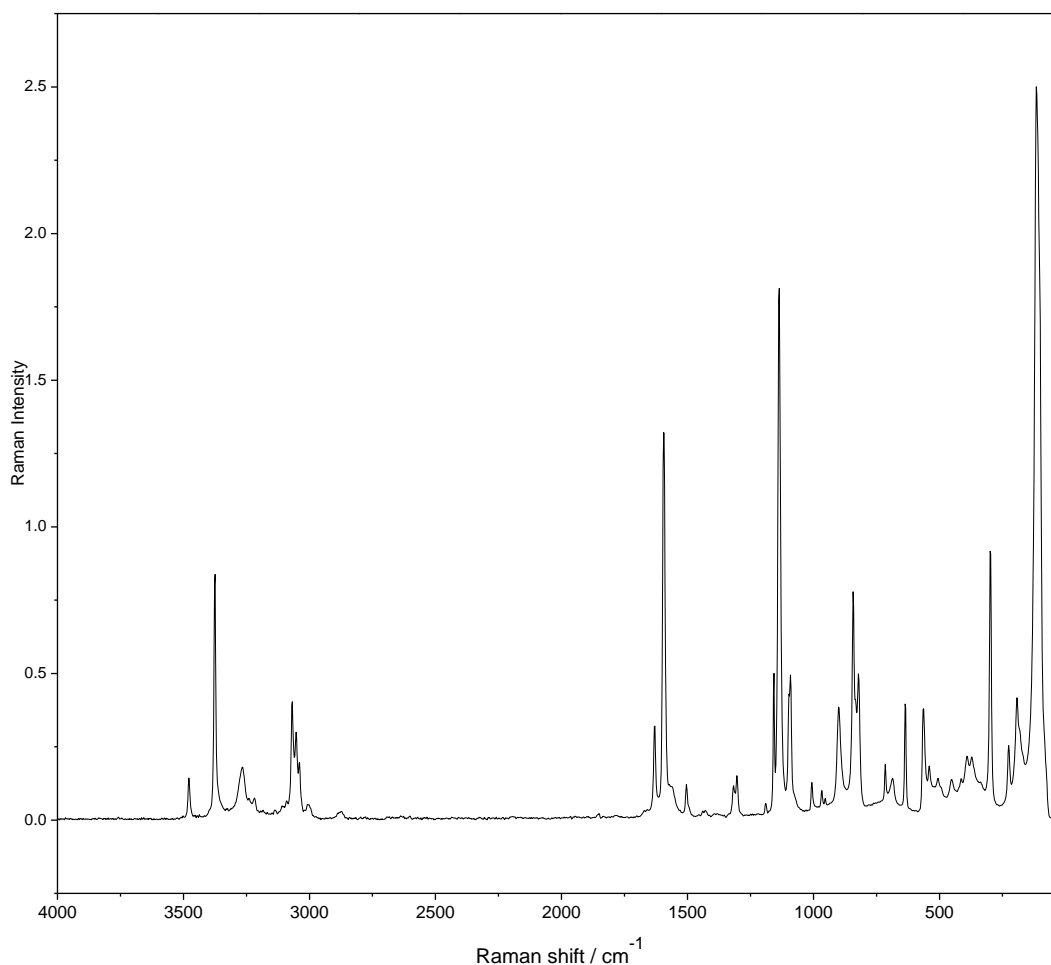
Figure 3.9 Raman spectrum of the β polymorph of sulfanilamide.

Figure 3.10 shows the schematic diagram of the Thermo-Nicolet NXR FT-Raman 9610 spectrometer (Wisconsin, USA) used in this work. The sample placed in a glass tube, is presented to the Nd:YAG (neodymium-doped yttrium aluminium garnet; $Nd:Y_3Al_5O_{12}$) excitation laser. Emitted radiation is directed to the Michelson interferometer which measures all frequencies simultaneously and modulates the intensity of individual Raman shifts emitted by the sample. The radiation from the interferometer travels to the detector which converts it to an electrical signal to produce an interferogram. An interferogram, which is a plot of intensity versus position of corresponding moving mirror, is first produced. Using a Fourier-transformation (FT), the computer converts the interferogram into a spectrum.
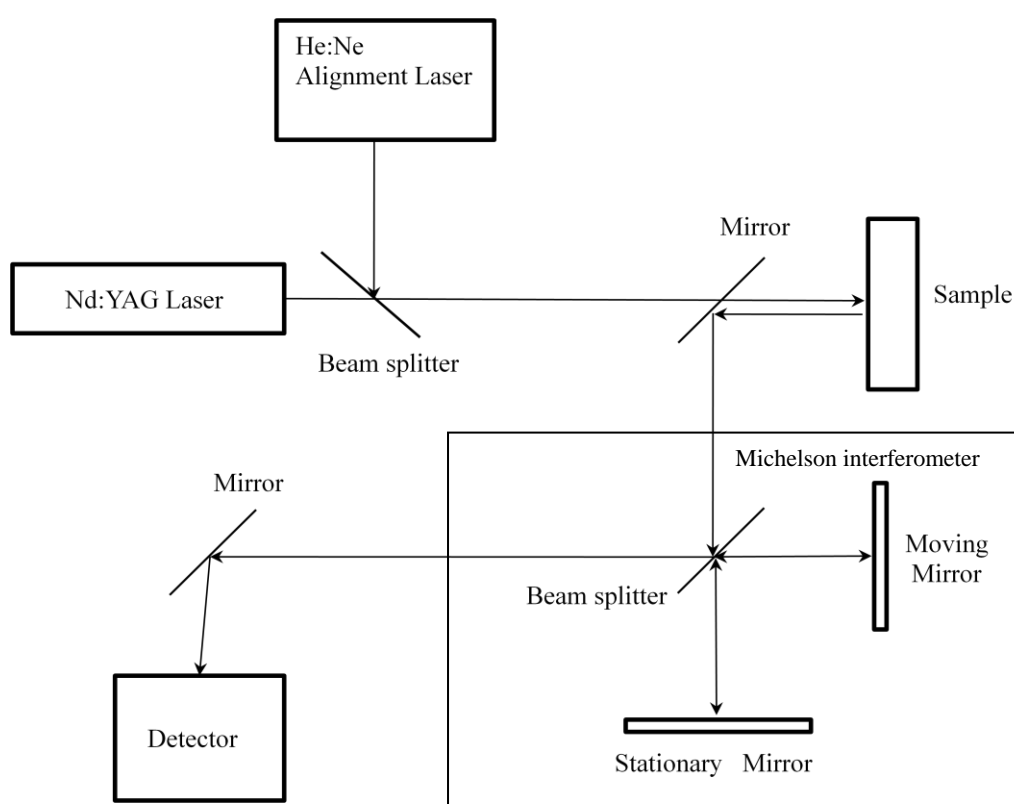
Figure 3.10 Schematic diagram of a Thermo-Nicolet FT-Raman 9610 spectrometer system.

In this work Raman analysis is carried out for the comparison of polymorphs. The Raman spectra for different polymorphs exhibit similar features in many respects but differences showing up in particular (distinguishing) bands. Spectral similarities and differences are examined with assignment (tentative or definite) of bands to functional groups.

3.5.3 Advantages and disadvantages of Raman spectroscopy

One main advantage of Raman is its non-invasive and non-destructive nature. No sample preparation is required and it is suited to analysis in situ.

Raman spectroscopy suffers from interference from fluorescence. The mechanisms controlling fluorescence and Raman scattering are similar, so there is always a likelihood of both phenomena occurring together. A Raman laser at wavelength of 1064 nm gives low excitation energy, such that fluorescence is rarely generated. Another disadvantage is that the Raman effect is very weak, so suffers in analytical sensitivity.

3.6 Diffuse Reflectance Visible Spectroscopy (DRVS)

When light interacts with matter, it can be absorbed, transmitted, scattered or reflected. Visible spectroscopy in the transmission mode can be used to study the absorption of visible light by molecules in solution. But for opaque solids and surface analysis, reflectance spectroscopy is required. Reflectance spectroscopy measures the amount of light reflected by the surface of the solid. There are two main categories of light reflectance, namely specular reflectance and diffuse reflectance. Specular reflectance, also known as mirror type reflectance, is characterised by the reflection of incident light by a surface, with no transmission into the bulk of the sample. Conversely, diffuse reflectance is associated with reflected radiation that penetrates the solid, and then emerges. This type of reflected radiation contains spectral information.
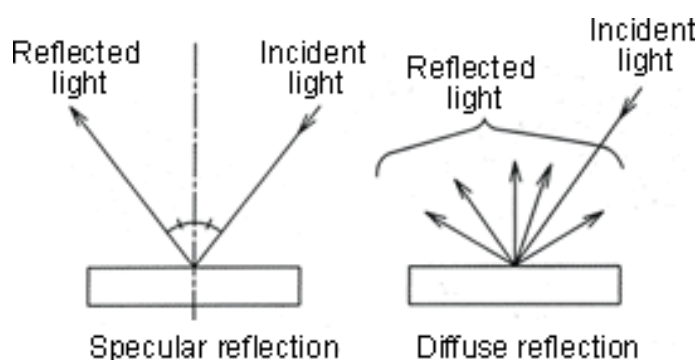
Figure 3.11 The two forms of reflection; specular *(left)* and diffuse *(right)* reflection.

Fig 3.11 shows the two forms of reflection, for specular reflection the incident light reflected symmetrically with respect to the normal line, for diffuse reflection incident light is scattered in different directions. Smooth surfaces generally show mainly specular reflectance.

3.6.1 Kubelka-Munk (KM) theory

Spectral data for DRVS analysis is commonly expressed as a plot of diffracted light intensity, *F(r)* versus wavelength in nanometres. KM accounts for the influence of scattered light from the powdered samples. KM theory[12] states that the diffusely reflected light intensity from a sample at a given wavelength can be expressed as:

$$F(r) = \frac{(R-1)^2}{2R} = \frac{k}{s}$$

Equation 3.1

where R is the reflectance light intensity of the sample (R ranges from 0-1), *k* and *s* represent absorption and scattering coefficients of the sample, respectively.

3.6.2 DRVS experiment

Polymorphs examined in this study do not have sufficient chromophores to allow analysis by visible spectroscopy. Therefore samples were chromogenically treated by the adsorption of dye on their surfaces. Conventional methods of adsorption involve mixing the solid in the solution of the dye and **slowly** evaporating the solvent, and centrifuging a dye-containing sample suspension and filtering off the solid. These methods are unsuitable for drug polymorphs because they can cause polymorphic transformation. A suitable method will be one that minimises solvent-mediated polymorphic transformation, solvate formation and perturbation of the surface of the crystals. For many pharmaceutical solids, deposition of dye solutions on the solid sample and the subsequent drying in air or in an oven, is a common adsorption method[15-17].

3.6.2.1 Chromogenic treatment of drug polymorphs by dye adsorption

The chromogenic treatment employed for most systems in this work is mainly by drop-wise addition of dye solution to the powdered sample, gently mixing to form a homogeneous paste and evaporation of the solvent by drying in an oven (Fig 3.12). Dye solution for most systems was made from 90%:10% water/methanol or 99.7% methanol (see section 5.2.4, Chapter 5).
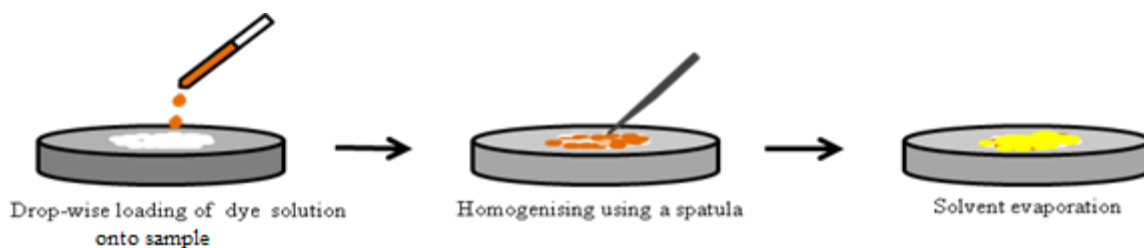
Figure 3.12 Experimental procedure for the chromogenic treatment of most drug polymorphs used in this study.

The typical amount of dye adsorbed per gram of solid was 0.1mg. This was achieved by depositing 1ml of a 200mg/L dye solution on 2g of sample. This value represents the optimum loading to minimise dye-dye interactions so that visible spectral data represents optimum surface-dye interaction, albeit at the limit of detection of the instrument. The limit of detection of an instrument is defined as the concentration of the analyte at which the signal to noise ratio (S/N) is 3:1. Figure 3.13 shows DRVS raw data for TB, with loading amounts of 0.1, 0.05 and 0.02 mg/g on CFN-II polymorph. The S/Ns and the noise levels are also shown.
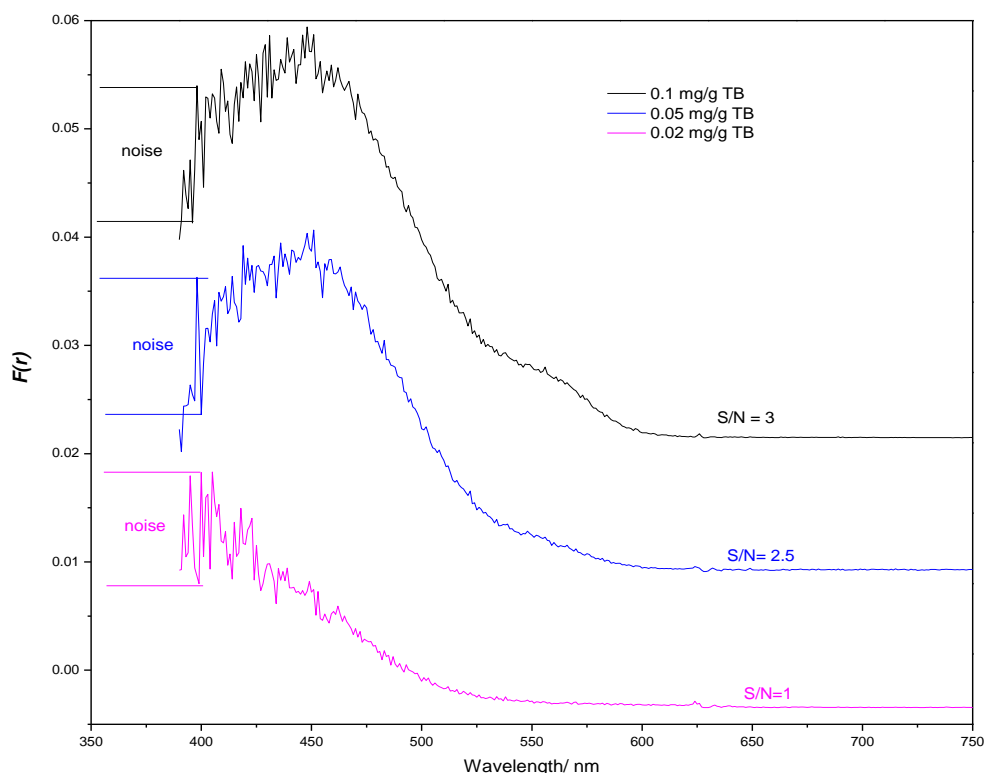
Figure 3. 13 Typical DRVS spectra of polymorph treated with indicator dye and the noise levels obtained at these low concentrations.

The S/N ratio for all dye treated polymorphic systems at 1.0 mg/g was $\geq$ 3: 1.

Dye sorption for SFN-γ and CBZ-I was achieved by heating their corresponding dye sorbed enaiotropes, SFN-β and CBZ-III, respectively above their transition temperatures until complete transformation. It was important to chromogenically treat SFN-γ and CBZ-I pre-transformation to minimise solvent induced polymorphic transformation and solvate formation. A sample blank for DRVS measurements was the untreated polymorph.

3.6.2.2 Instrumentation

All DRVS spectral data was obtained using a Hewlett-Packard 8453 photodiode Array UV-Vis Spectrophotometer (California, USA) equipped with a Labsphere RSA-HP-8453 diffuse reflectance accessory (Illinois, USA). The diffuse reflectance accessory is a 95 mm diameter integrating sphere with an inner surface coating of polytetrafluoroethylene (Spectralon®)**.** The schematic diagram for the DRVS instrumentation used in the experimental sections of this work is shown in Fig 3.14. Visible light from the tungsten-halogen lamp of the Labsphere RSA-HP-8453 module impinges on the sample which is mounted on the integrating sphere. The light diffusely reflected from the sample is concentrated on the photodiode array detector system by the integrating sphere. The reflected light is dispersed by a grating such that specific wavelengths fall on individual diodes for simultaneous measurement of the complete visible spectrum. The data acquisition time is 5 seconds per spectrum, each spectrum had a wavelength range of 400-800 nm.

Raw data is collected as percentage reflectance, which represents the relative reflectance with respect to the reflectance of the reference standard Spectralon. These values are converted to KM data using Equation 3.1. Spectralon is a diffuse white plastic that provides a highly Lambertian surface. This is a surface that evenly scatters light in all directions, and the scattered light intensity is proportional to the cosine of the angle of observation. This material reflects more than 98% of light in the range 400 – 1500 nm, has good long-term stability, is hydrophobic and chemically inert. The integrating sphere is an essential part of DRVS measurements because it spatially integrates the diffusely reflected light from the sample and concentrates it on the detector.
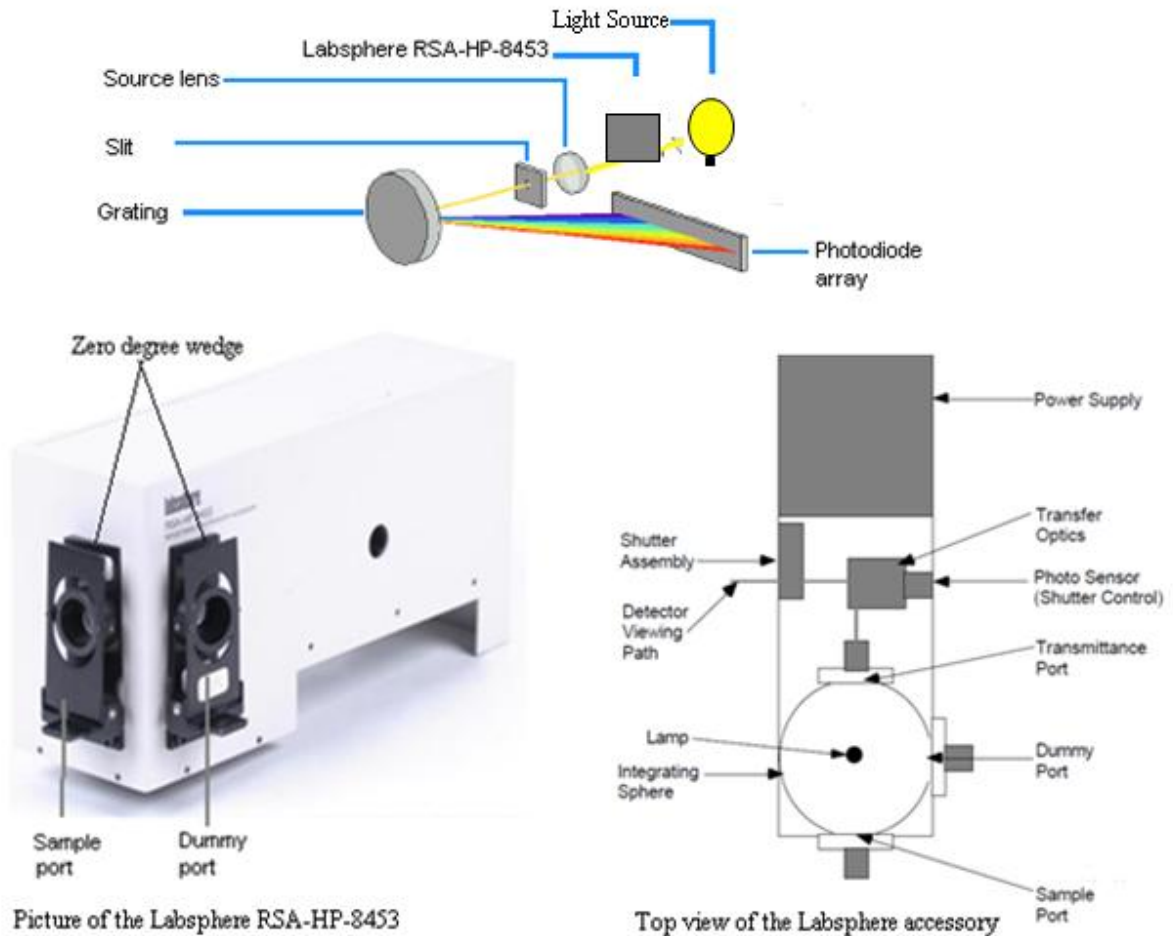
Figure 3.14 Schematic representation of a Hewlett-Packard 8453 photodiode Array UV-Vis Spectrophotometer equipped with a Labsphere RSA-HP-8453 reflectance spectroscopy accessory. A picture of the diffuse reflectance accessory and a schematic of top view of the diffuse reflectance accessory are also shown.

As already alluded to, the sphere is coated with highly reflective Spectralon plastic. The sample is mounted in such a way that the reflected light enters the sphere, is collimated by the Spectralon surface and reflected towards the detector. Fig 3.14 shows a picture of the Labsphere RSA HP 8453 accessory used in DRVS measurements. It has a sample slide assembly with a zero-degree wedge which ensures that the sample surface is perpendicular the incident beam. When light is directed at the sample at an angle of 90°, specular reflected light exits the integrating sphere and is not detected. As a result, only diffuse reflected light is measured.

Before using DRVS for sample measurements, a blank scan must be run to establish a baseline for the instrument. The blank DRVS spectrum is then subtracted from every subsequent sample spectrum. Given that this is a diode array instrument, the blank scan records an intensity level for each diode, which is then treated as zero. The DRVS instrument comes with sample of Spectralon for use as a blank. In this work, the blank used was a sample of the polymorph without the dye added. For comparison, the blank polymorph was run using Spectralon as a blank (Fig 3.15), but all coloured polymorph samples were run using the untreated polymorph as blank.
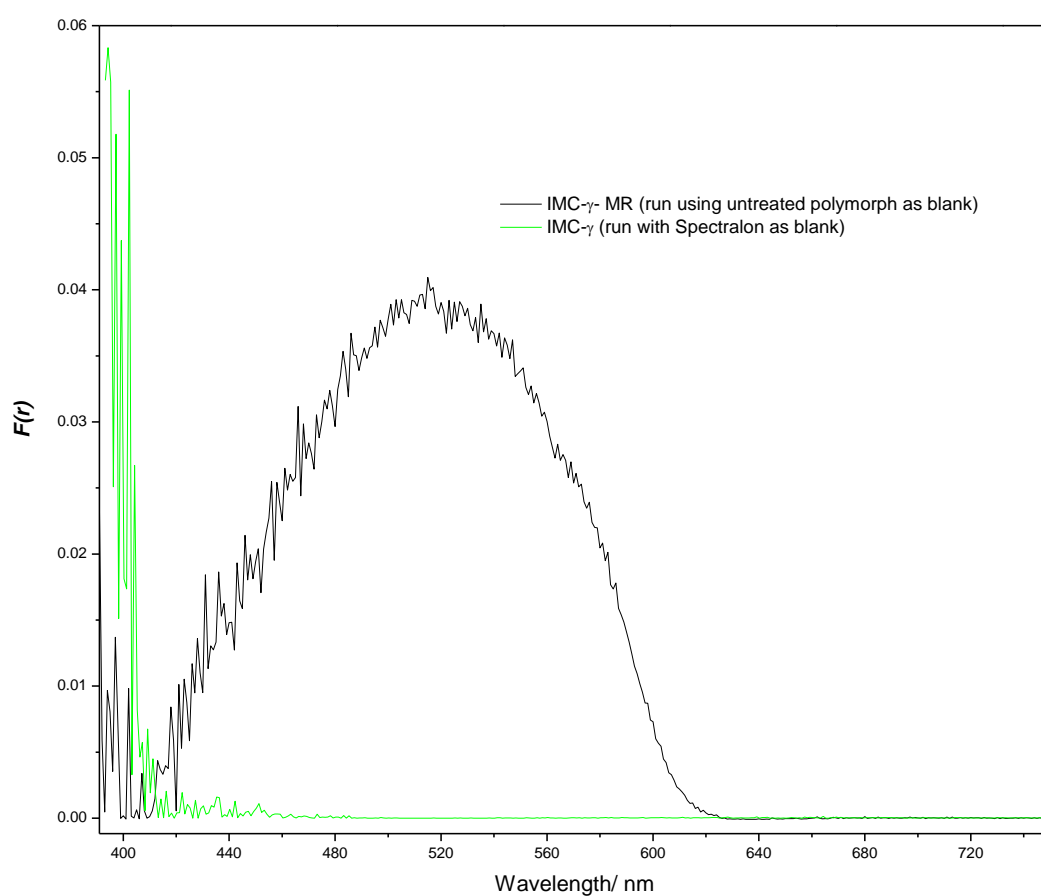
Figure 3. 15 DRVS of dyed and untreated polymorph

Several factors affect the quality of the data obtained from DRVS:

Particle size – the scattering co-efficient is inversely proportional to the root mean square of the particle diameter. Therefore reducing the particle size reduces the contribution of specular reflectance and *vice versa*. The recommended particle size to satisfy KM requirement is within the range 0.1-1μm[12].

But for particle sizes less than less than 0.1μm the scattering coefficient exhibits an unacceptably strong dependence on wavelength of incident radiation. When a dye is adsorbed on a non-reflective material, *k* is essentially determined by the light absorption of the dye, while *s* is governed by the properties of a material itself. At low concentrations of adsorbed dye, the effect of sample particle size on the absorption coefficient is negligible. Even though s is inversely proportional to the root mean square of the particle diameter, particle size effects may be ignored when the data is measured against a standard that is treated in a similar way to the sample, but without the presence of dye.

Sample packing– The thickness of the sample layer should be between 1 and 5 mm and the sample should be loosely but evenly packed in the sample holder to maximize beam penetration and minimize specular reflectance

Sample positioning- The inherent geometry of the DRVS instrument is designed such that that the sample is properly irradiated and the specular reflectance component is minimised. For accuracy the sample holder should be precisely located.

Single integrating spheres have an inherent error called **substitution error**. This error is a systematic error caused by the difference between the sphere throughput when the reference makes up a portion of the wall, and when the sample is substituted for the reference. The throughput is usually lower when the sample is present, since a reference material of high reflectance (nearly 100%) is usually used. For samples with very low reflectance the substitution error will be very small. For low reflectance and transmittance samples, the substitution error is so small that it probably falls within the random noise of the instrument. For qualitative analysis, where the locations of reflectance peaks rather than their exact value are important, this error could also be ignored.

3.6.2.3 Data treatment

The three main data treatments were applied to DRVS are outlined as follows.

Adjacent averaging (AA) smoothing algorithm: This algorithm, performed by Origin software (OriginPro 7.0), takes the average of a specified number of data points around each point and replaces that point with the new average value hence smoothing a noisy spectrum. The spectra obtained for the treated polymorphs were noisy as a result of the insensitivity of the detector. All data was smoothed based on a 20 point average. Fig 3.16 shows the raw and smoothed data for PR-treated CBZ-polymorphs. Note the difference in DRVS spectrum for the two polymorphs.
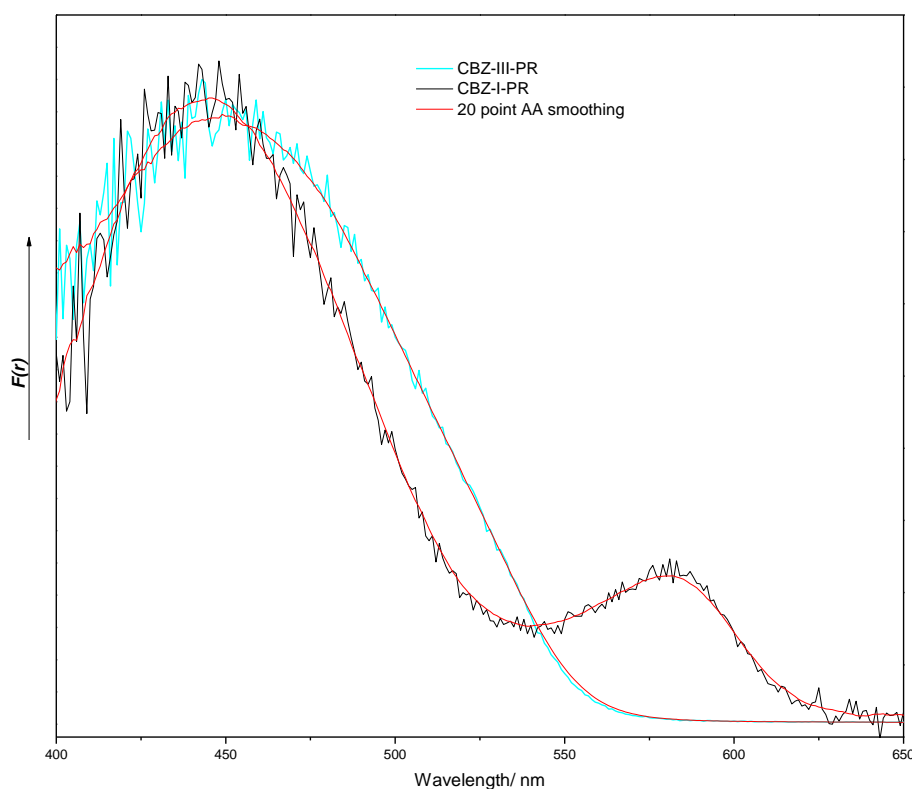
Figure 3.16 Raw data and 20 point AA smoothed DRVS spectra of PR treated polymorphs.

Normalisation: To aid comparison between the polymorphs, the maximum absorption band from the DRVS spectra were normalised.

<u>Derivative spectral analysis</u>: Derivative spectra were computed where necessary to ascertain accurately the wavelength of spectral bands. The absorption band λ_{max} was obtained from the zero intercept d F(r) /dx =0 of the 1st derivative spectrum. Figure 3.17 shows the effects of derivative spectral analysis on raw data.

Raw spectrum   First derivative   Second derivative
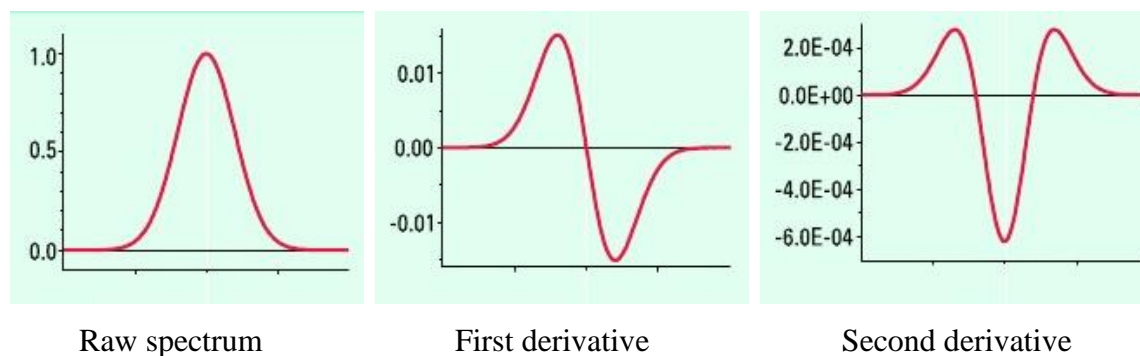
Figure 3.17 Derivative spectral analysis raw UV-Vis spectrum

Fig 3.18 shows the 1st derivative spectra of CBZ-I-PR and the accurately determined wavelengths of peak maxima at 446 nm and 580 nm.
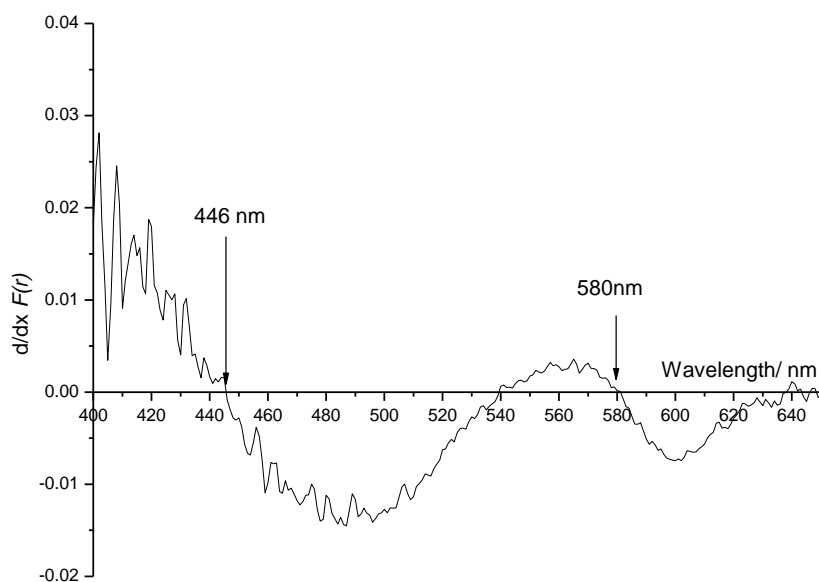
Figure 3.18 First derivative spectrum of CBZ-I-PR showing determination of wavelength of peak maxima at 446 and 580 nm (zero intercept).

3.6.3 Assessment of reproducibility

By careful and constant sample preparation and positioning, operational variability was minimised. The standard deviation for wavelength of maximum absorption after three consecutive measurements on a sample was found to be ± 2 nm (using 1st derivative spectra).

3.6.4 Advantages and disadvantages of DRVS

The main advantages of DRVS are fast analysis times, especially when a photodiode array detector is used, and the ease of operation, sample preparation and analysis of data. It is also capable of surface analysis. The main drawbacks are that light reflection by solid samples is governed by the particle size and analysis is prone to interference from specular reflectance.

3.7 References

1. H. G. Brittain, *Polymorphism in Pharmaceutical Solids*, Marcel Dekker, New York, 1999.

2. S. R. Vippagunta, H. G. Brittain and D. J. W. Grant, *Advanced Drug Delivery Reviews*, 2001, **48**, 3-26.

3. J. Bernstein, *Polymorphism in Molecular Crystals*, Oxford University Press, New York ; Oxford, 2002.

4. M. Ladd and R. Palmer, *Structure Determination by X-ray Crystallography*, Kluwer AcademiC Publishers, New York, 2003.

5. A. West, *Solid State Chemistry and its Applications*, John Wiley and Sons, Chichester, 1984.

6. R. Tilley, *Crystals and Crystal Structure*, John Wiley & Sons, Chichester.

7. R. Hilfiker, *Polymorphism in thePharmaceutical Industry*, Wiley-VCH ; [Chichester : John Wiley [distributor]], Weinheim, 2006.

8. D. Giron, *Thermochimica Acta*, 1995, **248**, 1-59.

9. D. Q. M. Craig and M. Reading, *Thermal Analysis of Pharmaceuticals*, CRC ; London : Taylor & Francis [distributor], New York, 2007.

10. D. Craig, in *Polymorphism in the Pharmaceutical Industry*, ed. R. Hilfiker, Wiley-VCH, Weinheim, 2006.

11. D. E. Bugay, *Advanced Drug Delivery Reviews*, 2001, **48**, 43-65.

12. H. G. Brittain, *Spectroscopy of Pharmaceutical Solids*, Taylor & Francis, New York ; London, 2006.

13. T. Threlfall, *Analyst*, 1995, **120**, 2435-2460.

14. T. Threlfall, in *Handbook of Vibrational Spectroscopy*, eds. P. Chalmers and P. Griffiths, John Wiley & Sons Ltd, Chichester, 2002, pp. 3557-3573.

15. B. W. Glombitza, D. Oelkrug and P. C. Schmidt, *European Journal of Pharmaceutics and Biopharmaceutics*, 1994, **40**, 289-293.

16.   M. Puppedi, E. Zannou, M. Vasanthavada, A. Dontabhaktuni, A. Royce, Y. Joshi and A. Serajuddin, *Journal of Pharmaceutical Sciences*, 2008, **97**, 1831-1842.

17.   R. Govindarajan, A. Zinchuk, B. Hancock, E. Shalaev and R. Suryanarayanan, *Pharmaceutical Research*, 2006, **23**, 2454-2468.

Chapter Four: Synthesis and characterisation of drug polymorphs

4.1 Introduction

The preparation and physical characterisation of all the polymorphic materials used throughout this study are presented in this chapter. Two polymorphs each of indomethacin (IMC) (α and γ), carbamazepine (CBZ) (I and III), caffeine (CFN) (I and II), furosemide (FRS) (I and II) and sulfanilamide (SFN) (β and γ) have been prepared and analysed using x-ray diffraction, calorimetry, microscopy and Raman spectroscopy.

Although more than two polymorphs exist for each polymorphic system, the choice of which polymorph to study was influenced by the accessibility i.e. the ease of preparing them, and stability at ambient conditions. Three additional polymorphs of IMC have been recorded but they reconvert to either IMC-α or IMC-γ on standing or heating[1]. IMC-γ is the most thermodynamically form under ambient conditions, but IMC-α, although metastable, has been shown to persist at room temperatures for longer than eighteen months without transformation[1]. There are four recorded polymorphs of CBZ, labelled I-IV [2]. The order of stability from experimental and theoretical data at ambient conditions is CBZ-III > CBZ-I > CBZ-IV> CBZ-II[2, 3]. Only two polymorphs exist for CFN. CFN-II is more stable at room temperature, CFN-I supercools readily and can persist at room temperature for 12 hours[4, 5]. Three polymorphs of FRS have been recorded and stability at ambient conditions is of the order FRS-I > FRS-II > FRS-III. Increasing temperature and moisture accelerates conversion of FRS-II or FRS-III to FRS-I[6, 7]. Four polymorphs of SFN, namely α, β, γ and δ have been recorded, but β and γ are more stable. Of these, the β form is the most stable form under ambient conditions.

4.2 Materials

4.2.1 Reagents

The purity, grade and manufacturer details of all materials are listed in Table 4.1.

Table 4.1 List of materials used containing details of manufacturer, percentage purity and reagent grade.

Material	% Purity and Grade	Manufacturer
Indomethacin	>99.2. Biochemical	Fluka, Sigma Aldrich
Carbamazepine	>99.2	Sigma Aldrich
Caffeine	>99.0	Fluka, Sigma Aldrich
Furosemide	>99.0	Sigma Aldrich
Sulfanilamide	>99.0 Ultra	Sigma Aldrich
Ethanol Absolute	>99.8 HPLC	VWR, BDH
n-Butanol	>99.8 AnalR	Sigma Aldrich
Water	Ultra pure	prepared in-house using Elga purification system

4.2.2 Preparation of polymorphs

4.2.2.1 Indomethacin

IMC-α was recrystallised from commercial IMC by precipitation from a saturated ethanol-IMC solution at 80°C with water, using the method of Chen *et al* [8, 9]. Crystals were filtered and dried under vacuum. Commercial IMC was found to contain only IMC-γ, and was used with no further treatment.

4.2.2.2 Carbamazepine

CBZ-I was prepared according to Grzesiak *et al* [2] by heating commercial CBZ at 170ºC for 2 hours. Commercial CBZ (CBZ-III) was used with no further treatment.

4.2.2.3 Caffeine

It is difficult to be certain that CFN-II is pure, because for all the analytical methods used here, traces of form I are almost impossible to detect. The commercial sample was clearly CFN-II. Below 140°C form II is the most stable, and at 100°C the rate of conversion is rapid. So to eliminate any traces of CFN-I it was annealed at 100°C for 12 hours[4]. CFN-I was prepared by heating a sample of CFN-II at 180°C (above the sublimation temperature) for 15 hours in a closed vessel[10]. As suggested by Manduva *et al*[4] samples were analysed within 12 hours of preparation to minimize interconversion.

4.2.2.4 Furosemide

FRS-I was prepared by the rapid cooling of a hot saturated solution of commercial furosemide in ethanol. The FRS-I crystals were then harvested by suction filtration. FRS-II was prepared by recrystallisation of commercial furosemide from a saturated n-butanol solution by allowing to cool at room temperature.[6]

4.2.2.5 Sulfanilamide

SFN-β was prepared by recrystallisation in water[11]. Commercial sulfanilamide was dissolved in hot water (at 100°C) and left to cool at room temperature (23.5 °C). SFN-β crystals were filtered and dried over calcium chloride in a vacuum desiccator. SFN-γ was obtained by recrystallising the commercial sample from ethanol[12].

All polymorphs were stored in a vacuum desiccator over calcium chloride (0% RH) prior to analysis to eliminate moisture-induced transformations.

4.3 Methods

4.3.1 Powder x-ray diffraction (PXRD)

4.3.1.1 Experimental PXRD patterns

Unless otherwise stated, powder x-ray diffraction patterns were obtained at room temperature on a Philips PW 1729 diffractometer fitted with a PW1050 goniometer with a θ-2θ geometry, divergence slits, receiving slits and a nickel filter. The copper Kα radiation (λ=1.54056Å) used was generated at a power of 40 kW and 20 mA. The data were collected over an angular range of 5° to 35° 2θ and a scan rate of 0.05° per second. Samples were sieved to ≤ 125 µm and packed into 20 mm x 15 mm x 1 mm (length x width x depth) glass wells cut into an aluminum sample holder.

4.3.1.2 Generation of simulated PXRD patterns

Single crystal data for all polymorphs (Table 4.2) obtained from the Cambridge Crystal Structural Database (CCSD) were imported into the Reflex Module of Materials Studio 5.0 software program (Accelrys, San Diego) to obtain simulated powder x-ray data and miller indices for all reflections.

Table 4.2 Single crystal data for all polymorphs studied.

Material		Crystal System	CCSD code
IMC	α^8	Monoclinic	INDMET01
	γ^{13}	Triclinic	INDMET
CBZ	I^2	Triclinic	CBMZPN10
	III^{14}	Monoclinic	CBMZPN11
CFN	I^{15}	Trigonal	NIWFEE04
	II^{10}	Monoclinic	NIWFEE05
FRs	I^{16}	Triclinic	FURSEM01
	*II		
SFN	β^{17}	Monoclinic	SULAMD03
	γ^{18}	Monoclinic	SULAMD02

*Single crystal data is unavailable on the CCSD

4.3.2 Raman Spectroscopy

FT-Raman spectra were recorded on a Thermo-Nicolet NXR FT-Raman module system equipped with an indium gallium arsenide (InGaAs) detector and Nd: YAG laser operating at 1064nm. The powdered samples were placed in thin walled glass sample tubes and spectra collected at 200 scans and a resolution of 4 cm^{-1} over the wavenumber range of 4000-10 cm^{-1}. Band wavenumbers were calibrated against internal laser frequencies with an accuracy of ±1cm^{-1}. The Raman shift of a diagnostic band was observed for three consecutive measurements on a single sample. Raman shifts had a deviation of ±1 cm^{-1}.

4.3.3 Differential Scanning Calorimeter (DSC)

Unless otherwise stated, thermograms of all samples were recorded on a Mettler Toledo FP90 DSC system equipped with a FP85 DSC cell. Samples (3.0 -3.4 mg) were placed in crimped aluminum pans. The thermal events were studied at a heating rate of 5˚C/min over a temperature range of 30˚C-190˚C for IMC, SFN and FRS. For CFN and CBZ polymorphs the temperature ranges studied were 30˚C-260˚C and 30˚C-220˚C, respectively. Measurements were carried out in triplicate. The instrument was calibrated with an indium standard; onset of melting (T_f) at 156.6 °C and enthalpy of fusion (ΔH_f) of 28.4 J g^{-1} values obtained complied with standard values.

4.3.4 Hot stage microscopy (HSM)

The thermal events observed in this work, were examined using a Leica optical microscope (Wetzlar, Germany) fitted with a Mettler FP52 hot stage apparatus (Greifense, Switzerland).

4.4 Results and Discussions

4.4.1 Indomethacin polymorphs

The experimental and simulated PXRD patterns for α and γ polymorphs are shown in Figure 4.1 and 4.2. The PXRD patterns of IMC-α and IMC-γ are different and can be easily distinguished. Experimental data shows defined and sharp peaks which are indicative of their crystalline nature. Diagnostic peaks for IMC-α are at 8.44, 11.86, 13.90, 14.18, 14.50, 17.56, 18.06, 18.46 and 22.04 °2θ and for IMC-γ at 11.63, 16.71, 18.55, 19.62, 20.87, 21.81, 22.86 and 26.61 °2θ.

Figure 4.1 PXRD patterns for IMC-α; the top pattern is the experimental data and the bottom one simulated from single crystal structures.

Figure 4.2 PXRD patterns for IMC-γ; the top pattern is the experimental data and bottom one simulated from single crystal structures

Diffraction angles (º2θ), relative intensities for simulated and experimental data, and the corresponding miller indices data for both polymorphs are listed in Tables 4.3 and 4.4. Angles agree within ±0.20° of simulated data indicating polymorphic purity. Peak intensities varied more significantly as a result of preferred orientation of samples. The identities of both polymorphs are established by the good agreement between experimental and simulated diffraction patterns.

Table 4. 3 Diffraction angles and relative intensities for PXRD peaks for IMC-γ

Miller plane			Simulated		Experimental	
h	k	l	º2theta	I/I_{max} (%)	º2theta	I/I_{max}(%)
1	0	0	10.21	29.81	10.17	12.45
0	0	1	10.40	1.01	10.37	5.30
1	0	-1	11.65	87.18	11.63	43.99
1	1	0	12.80	14.9	12.75	6.74
0	1	-1	15.75	2.01	15.74	3.65
0	2	1	16.71	67.46	16.71	23.32
1	0	1	17.04	31.26	17.02	66.66
0	2	0	17.33	37.1	17.27	14.88
1	-1	-2	18.61	14.12	18.55	12.40
1	0	-2	19.64	49.77	19.62	100.00
2	-1	-1	20.40	13.98	20.35	5.50
1	-2	0	20.92	1.35	20.87	22.26
0	2	2	21.86	100	21.81	61.64
2	-1	-2	22.90	19.38	22.86	8.59
1	2	-1	23.20	19.24	23.14	11.14
1	1	-2	24.05	20.1	24.01	35.64
2	-2	-2	25.58	14.44	25.51	7.79
2	0	1	26.24	12.6	26.19	22.31
1	2	2	26.66	79.4	26.61	71.87
2	1	-2	26.96	12.12	26.87	13.93
1	-1	-3	27.50	10.49	27.45	19.18
1	-2	-3	28.35	12.35	28.30	10.39
3	0	-1	28.83	12.34	28.78	8.48
1	0	-3	29.38	29.23	29.35	86.53
3	-1	-2	30.35	6.31	30.32	10.01
2	0	-3	30.82	6.92	30.76	8.89
0	3	-1	31.56	1.94	31.56	2.76
2	2	-2	32.60	2.26	32.61	3.18
3	-1	0	32.95	1.33	32.98	4.16
1	1	-3	33.59	9.25	33.58	25.81
2	2	2	34.16	10.93	34.12	7.83
2	0	2	34.48	4.67	34.45	11.70

Table 4.4 Diffraction angles and relative intensities for PXRD peaks for IMC-α

Miller plane			Simulated		Experimental	
h	**k**	**l**	**º2theta**	**I/I$_{max}$ (%)**	**º2theta**	**I/I$_{max}$(%)**
0	2	0	6.98	31.41	6.96	19.92
0	2	1	8.52	72.55	8.44	60.18
0	0	2	9.77	1.95	9.64	8.71
0	1	2	10.37	14.95	10.28	13.42
0	3	1	11.56	22.66	11.48	25.90
0	2	2	12.01	69.30	11.86	60.66
0	4	0	13.98	33.01	13.90	55.95
0	3	2	14.34	40.69	14.18	58.46
0	0	3	14.67	65.17	14.50	78.15
0	4	1	14.82	15.45	14.72	30.61
0	1	3	15.08	27.61	14.92	20.68
0	2	3	16.26	21.31	16.08	23.70
1	1	-1	16.99	3.56	16.94	22.66
1	1	1	17.70	28.17	17.56	33.15
1	2	-1	18.05	18.98	18.06	61.27
1	0	-2	18.35	32.18	18.46	52.84
1	3	0	19.38	19.52	19.42	52.63
1	3	-1	19.69	19.33	19.72	63.73
0	5	2	20.08	11.66	20.06	39.67
0	2	4	20.83	41.60	20.66	51.35
1	2	-3	22.24	99.90	22.04	100.00
1	0	3	22.80	100.00	22.66	81.69
0	6	2	23.25	4.11	23.30	63.86
1	5	0	23.98	19.32	23.98	44.77
0	0	5	24.57	7.86	24.50	71.63
1	4	-3	25.41	11.34	25.24	54.88
0	5	4	26.40	8.83	26.38	46.76
1	5	2	26.43	7.66	26.48	48.61
1	6	0	26.71	14.62	26.74	28.14
1	6	1	27.40	4.67	27.24	21.40
1	6	-2	28.06	6.47	28.14	59.28
0	4	5	28.38	8.98	28.38	59.76
0	8	1	28.62	7.09	28.58	35.14
0	0	6	29.59	3.84	29.62	26.77
1	6	-3	29.98	9.39	30.00	23.04
1	1	5	30.87	2.55	31.00	41.75
0	3	6	31.47	17.83	31.34	40.41
1	6	-4	32.57	1.17	32.58	21.06
1	2	-6	33.57	1.74	33.52	30.91
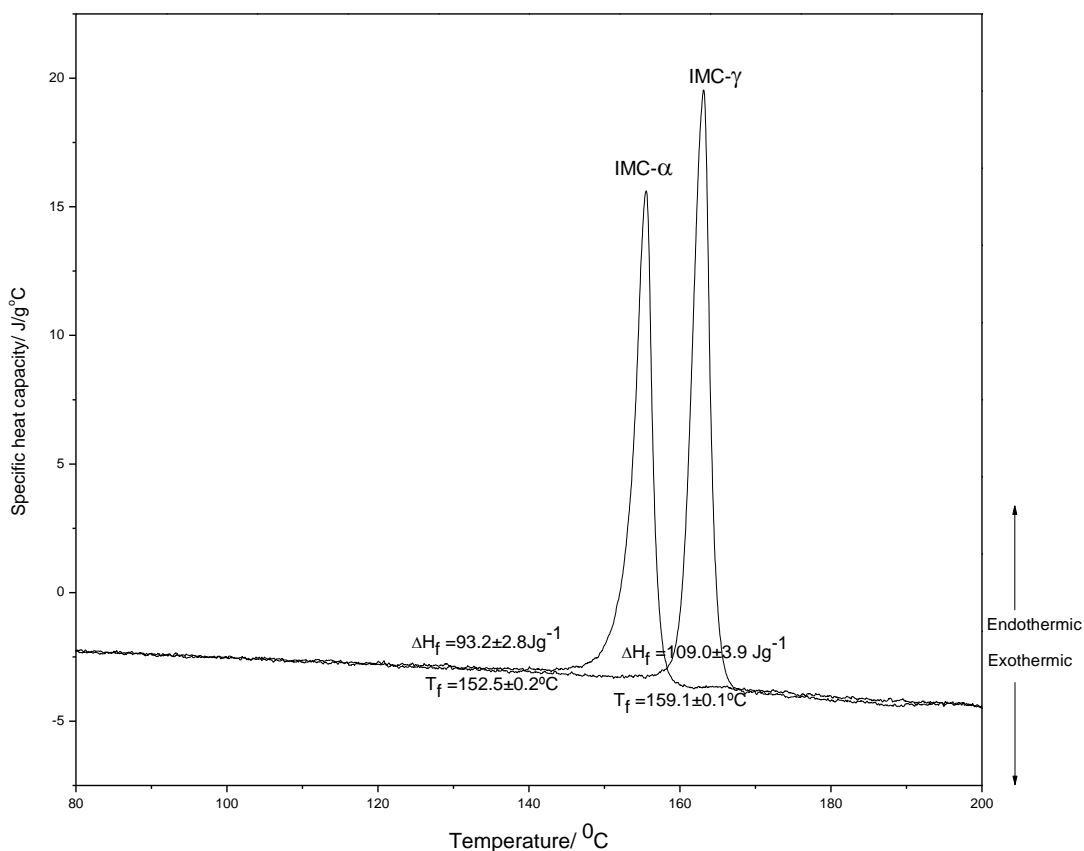
Figure 4.3 DSC thermograms of IMC polymorphs α and γ. Each thermogram is labelled with the corresponding polymorph.

DSC thermograms for IMC polymorphs are shown in Fig 4.3. In each case a single endothermic peak is observed attributed to melting. The onset temperature (T_f) and enthalpy of fusion ΔH_f values averaged over three determinations are:

$T_f = 159.1 \pm 0.1$°C and $\Delta H_f = 109 \pm 3.9$ J g^{-1} for IMC-γ, and

$T_f = 152.5 \pm 0.2$°C and $\Delta H_f = 93.2 \pm 2.8$ J g^{-1} for IMC-α.

These values agree with those reported by other authors [19, 20]. Fusion temperature and enthalpy of fusion values for IMC-γ are higher than for IMC-α, showing that IMC-γ is the more stable form, while IMC-α is metastable.

The Raman spectra for IMC polymorphs are presented in Figure 4.4. Table 4.5 shows the tentative Raman assignment[21, 22] for each polymorph.
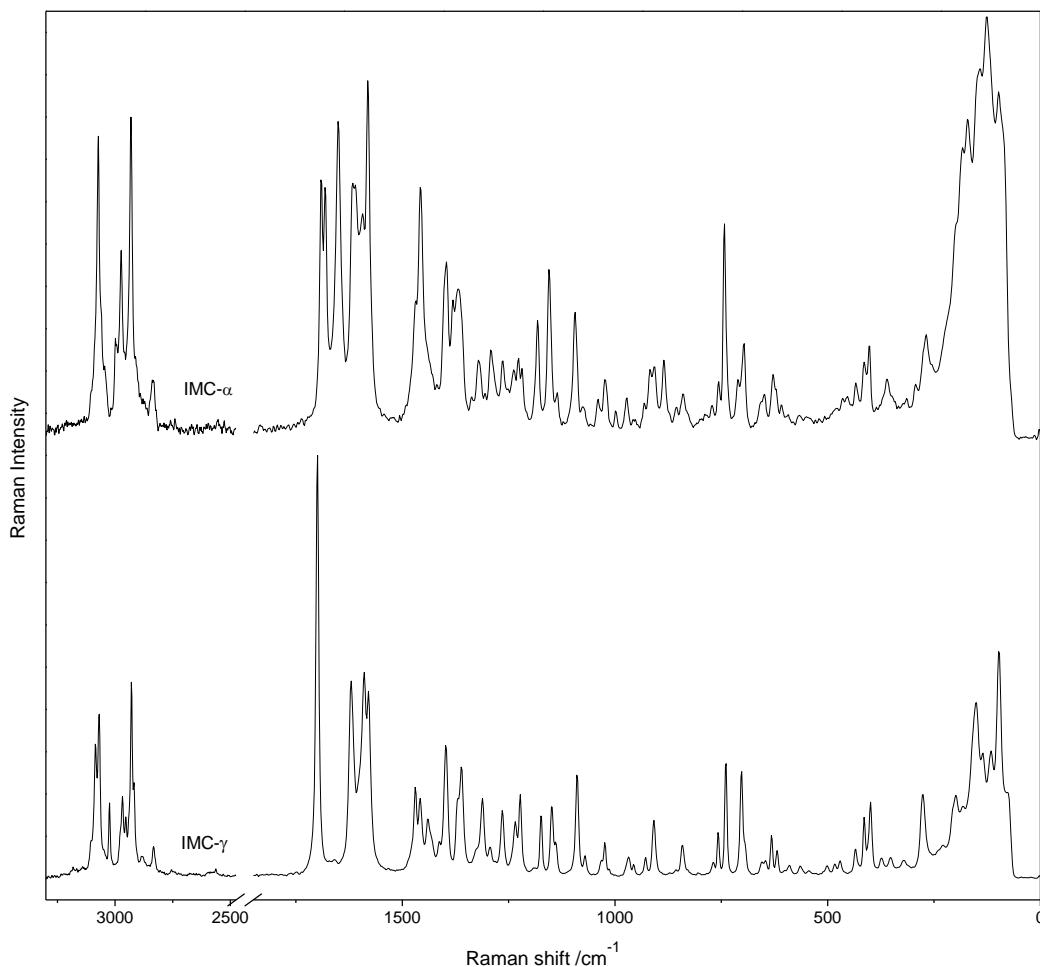
Figure 4. 4 Raman spectra of IMC polymorphs; IMC-α (top) and IMC-γ (bottom)**.**

Table 4.5 Tentative Raman assignments and frequencies for the two polymorphs of IMC.

Assignment	I MC-α /cm^{-1}	IMC-γ/cm^{-1}
s(C-H)$_{ar, al}$	3073, 3043, 2998, 2974, 2931, 2838.5	3085, 3069, 3024, 2968, 2954, 2929, 2918, 2833
s(C=O)	1690, 1681, 1650	1700
s(C=C), s(Ph)	1616, 1593, 1581, 1457	1620, 1589, 1580, 1469, 1458, 1440
s(C-N)	1396, 1381	1397
b(C-H), s(C-O-C)	1369, 1320, 1291, 1264, 1238, 1227	1361, 1312, 1294, 1265, 1234, 1223
Lattice vibrations	402, 361, 293, 269, 183, 171, 142, 126, 98	399, 373, 277, 199, 151, 135, 116, 97

s= stretch, b= bend, ar= aryl, al= alkyl

The polymorphs show distinct differences in the C-H stretching (3100-2800 cm^{-1}), C=O stretching (1800-1500 cm^{-1}) and lattice vibration regions. There are more C-H stretching bands for γ compared to α.

For CH stretching of aryl and olefinic groups, two peaks at 3073 and 3043 cm^{-1} are observed for α and three bands at 3084.9, 3069.0 and 3024.0 cm^{-1} appear for γ. For alkyl C-H stretching four bands are observed for α and five observed for γ; these bands are at 2998.2, 2973.6, 2931.0, 2838.5 cm^{-1} and 2968.0, 2953.5, 2928.9, 2918.2, 2833.1cm^{-1}, respectively.. A recent study by Cox *et al*[23] on the crystal structure of γ revealed C-H...π interactions between methyl hydrogen and indole ring and π-π interactions between chlorophenyl rings. The presence of these interactions involving alkyl and phenyl groups in the γ form explains the differences in the Raman spectra between the two polymorphs in C-H stretching region.

Bands seen at 1690.4, 1681.0, 1650.2 cm^{-1} for IMC-α and 1699.5 cm^{-1} for IMC-γ are assigned to C=O stretching. Single crystal structural analysis of IMC polymorphs show that α crystals are made up of three conformationally different molecules in comparison to γ which has only one.

Fig 4.5 shows the hydrogen bonding pattern between the molecules in the single crystal of IMC polymorphs. For IMC-α, two of the three conformationally different molecules form a carboxylic acid dimer and the carboxylic acid group of the third molecule forms an O–H…..O hydrogen bond with the amide carbonyl group of one of these two molecules. In IMC-γ two conformationally similar molecules form an acid dimer. The differences in conformational flexibility of the molecules and the hydrogen bonding among the polymorphs are therefore reflected in the Raman spectra.
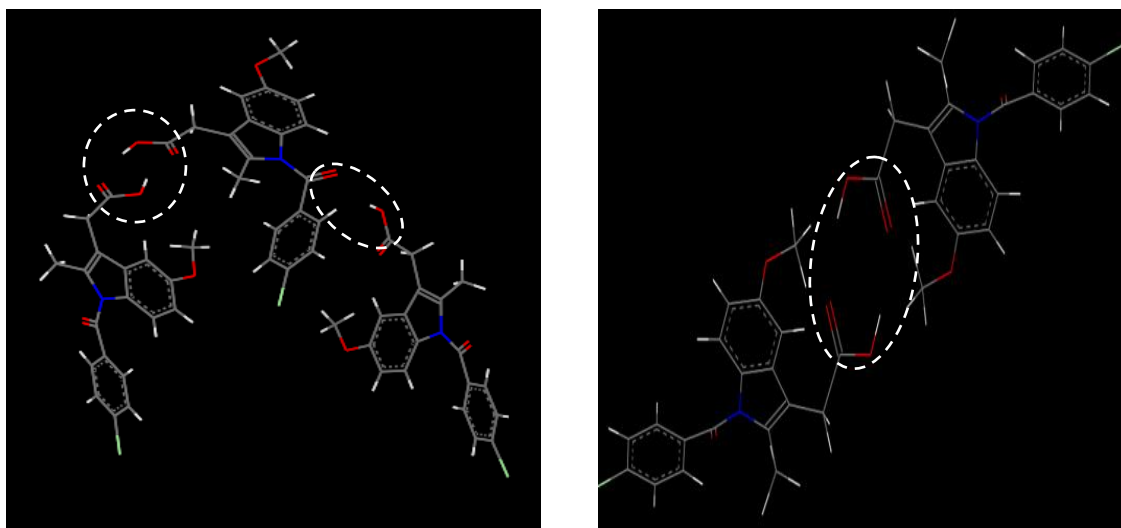
Figure 4. 5 Hydrogen bonding patterns in IMC polymorphs; IMC-α (left) and (right). Dashed circled regions show hydrogen bonding two between carboxylic acid groups in IMC-γ and between two carboxylic acid groups and between a carboxylic acid group and amide group in IMC-α. *Colour code : grey-carbon, white-hydrogen, blue-nitrogen and red-oxygen.*

4.4.2 Carbamazepine polymorphs

Figures 4.6 and 4.7 show the experimental and simulated PXRD patterns acquired for CBZ-I and CBZ-III, respectively. Diffraction angles (2θ), relative intensities, Miller indices and corresponding simulated data, for both polymorphs are listed in Table 4.6 and 4.7. As a consequence of different crystal structures, the forms are easily distinguishable from each other by their PXRD patterns. Diagnostic peaks for CBZ-I and CBZ-III are at $^{\circ}2\theta$ = 5.55, 6.11, 7.92, 8.61, 9.36, 12.25 and 19.99 and $^{\circ}2\theta$= 13.03, 15.00, 15.28, 15.81, 19.46, 24.95 and 27.30, respectively. Experimental and simulated values compare well, especially in terms of the 2θ positions. However the intensities vary because of the preferred orientation effects. PXRD data for both polymorphs is also in good agreement with the previously published experimental data[2].
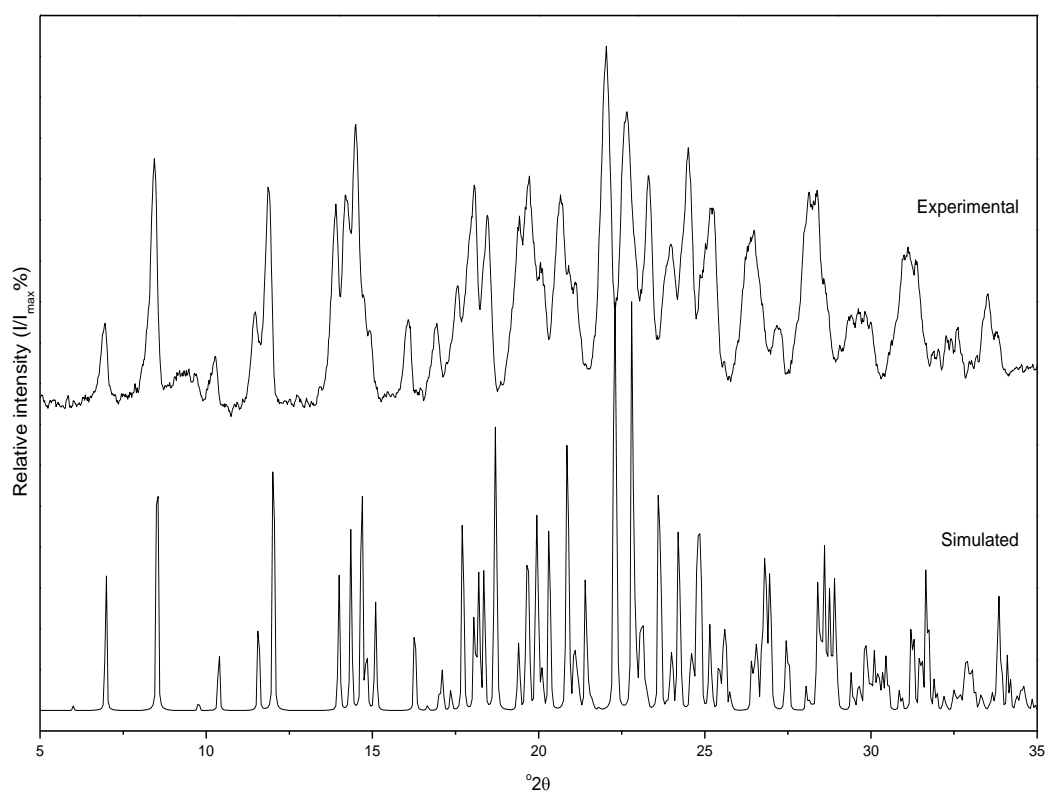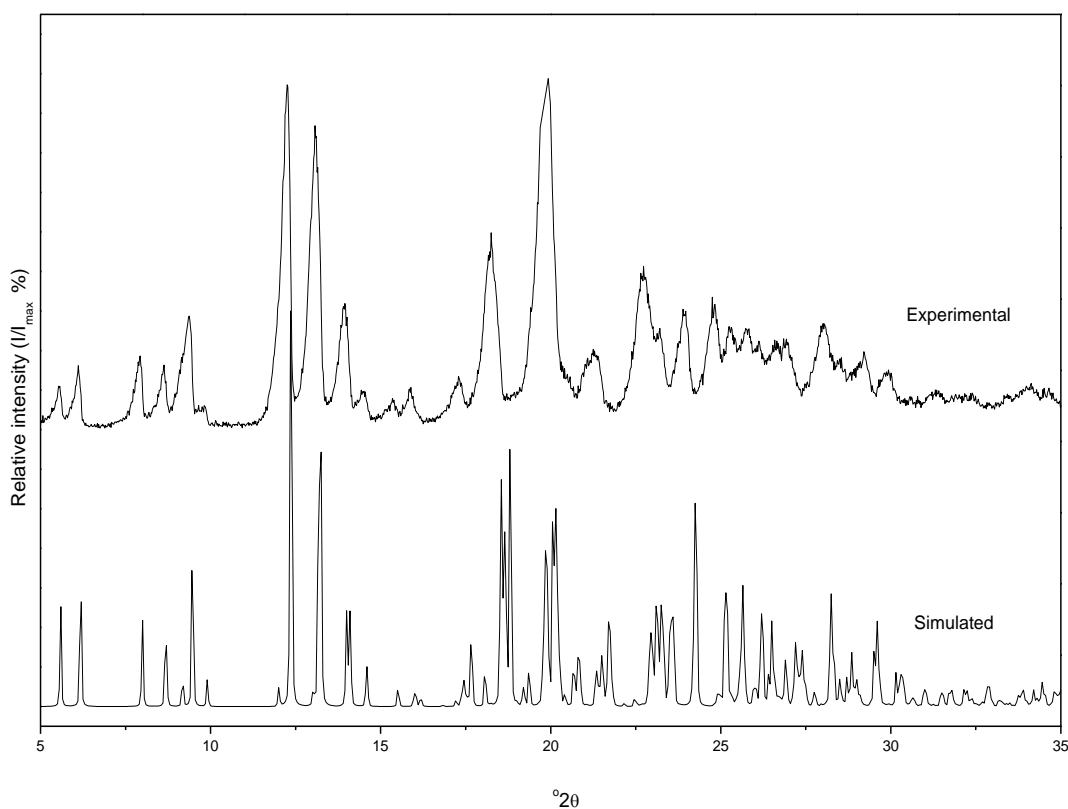

Figure 4.6 PXRD patterns for CBZ-I; the top pattern is the experimental data and bottom one simulated from single crystal structures.

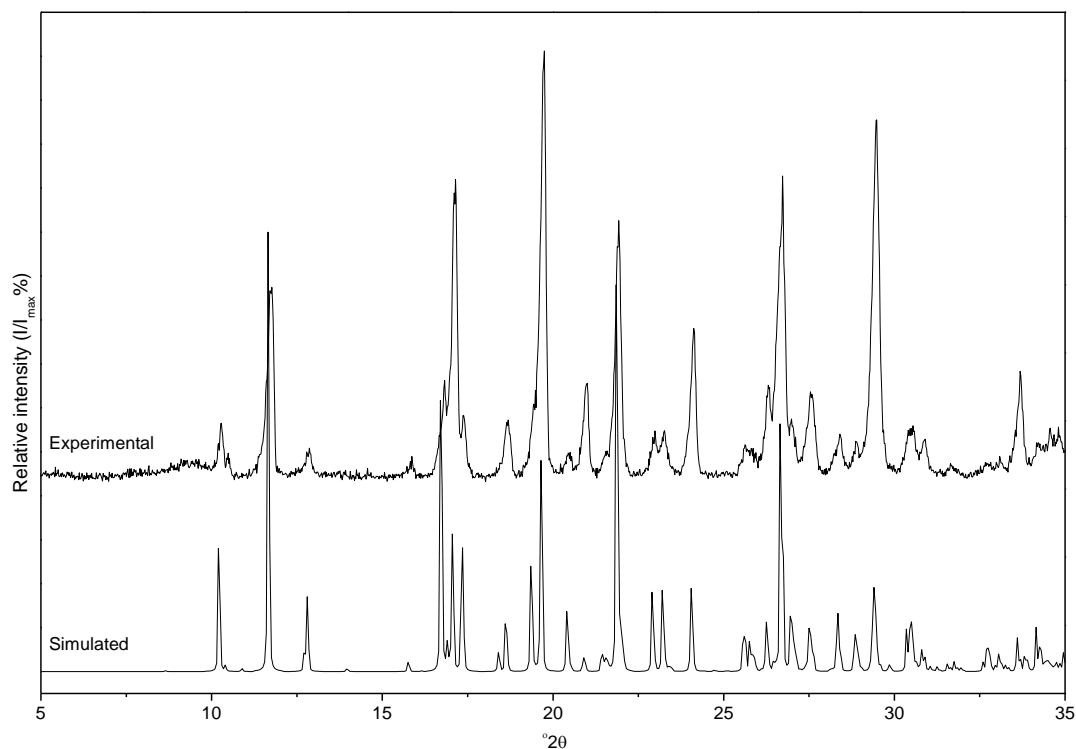**Figure 4.7** PXRD patterns for CBZ-III; the top pattern is the experimental data and bottom one simulated from single crystal structures.

Table 4.6 Diffraction angles and relative intensities for PXRD peaks for CBZ-I.

Miller plane			Simulated		Experimental	
h	**k**	**l**	**º2theta**	**I/I_{max} (%)**	**º2theta**	**I/I_{max}(%)**
0	1	1	5.60	25.23	5.55	11.06
0	1	-1	6.20	26.29	6.11	17.47
0	0	2	8.00	21.81	7.92	19.58
0	2	0	8.70	15.38	8.61	15.93
0	1	-2	9.45	34.36	9.36	31.99
0	2	-1	9.90	6.76	9.84	5.42
0	1	3	12.35	100.00	12.25	100.00
0	1	-3	13.20	55.53	13.08	87.90
0	3	1	13.25	64.32	13.20	59.10
0	3	-1	14.00	24.22	13.93	34.04
0	2	3	14.10	24.15	14.02	27.21
0	3	2	14.60	10.06	14.55	9.79
0	2	-3	15.50	4.12	15.36	6.95
0	3	-2	16.00	3.27	15.87	9.65
0	4	0	17.45	6.67	17.29	14.48
1	-1	0	18.05	7.53	18.12	44.55
0	4	-1	18.10	5.55	18.25	56.54
1	-1	-1	18.55	57.37	18.47	27.66
0	4	-2	19.85	39.37	19.72	99.76
0	0	5	20.15	50.07	19.99	94.38
1	2	-2	20.80	20.40	20.99	16.20
1	-2	-2	21.50	12.85	21.25	22.08
0	3	5	22.95	18.62	22.73	44.11
1	0	4	23.25	25.67	23.21	28.21
0	5	-2	23.97	0.14	23.93	32.39
0	1	6	24.25	51.42	24.03	28.27
0	2	6	24.90	13.16	24.83	35.52
0	4	5	25.15	28.76	25.27	27.55
1	-4	-1	25.65	30.64	25.78	27.84
1	0	5	26.20	23.41	26.11	23.89
0	6	2	26.50	21.64	26.63	23.15
0	6	-1	26.90	11.71	26.91	23.73
1	-2	-5	27.95	0.65	28.04	28.36
1	5	3	28.25	28.50	28.48	19.01
1	1	6	29.00	6.81	29.22	21.37
0	3	7	29.60	21.56	29.88	14.97
1	6	3	31.50	3.41	31.36	9.50
0	0	8	32.15	4.27	32.32	8.32
1	-4	5	33.20	1.50	33.43	8.53
1	7	0	34.20	4.20	34.07	11.02

Table 4.7 Diffraction angles and relative intensities for PXRD peaks for CBZ-III.

Miller plane			Simulated		Experimental	
h	k	l	º2theta	I/I_{max} (%)	º2theta	I/I_{max}(%)
0	1	1	10.16	5.20	10.11	4.83
0	0	2	12.73	7.55	12.58	1.27
1	0	-1	13.08	89.56	13.03	79.10
1	0	1	13.64	12.73	13.61	18.73
1	1	0	14.18	26.48	14.14	29.05
0	1	2	15.01	34.44	15.00	61.91
1	1	-1	15.31	100.00	15.28	91.40
0	2	0	15.88	51.55	15.81	63.75
0	2	1	17.12	20.14	17.09	22.02
1	1	-2	18.70	43.08	18.67	41.25
1	1	2	19.49	43.62	19.46	51.32
1	2	0	19.79	9.70	19.80	16.92
0	2	2	20.40	30.94	20.34	44.75
1	2	-1	20.63	17.93	20.40	43.62
0	1	3	20.75	5.43	20.64	22.90
1	0	-3	22.01	7.82	22.00	7.08
1	2	-2	23.28	9.07	23.30	32.88
1	1	-3	23.42	27.87	23.38	33.07
1	2	2	23.93	45.61	23.86	51.59
0	3	1	24.76	29.07	24.75	73.65
2	1	0	24.95	15.01	24.95	57.07
1	3	0	26.72	44.44	26.69	66.97
0	3	2	27.18	44.57	27.11	96.56
1	3	-1	27.35	43.29	27.30	100.00
1	3	1	27.63	50.65	27.60	66.80
2	2	-1	29.05	7.01	29.02	12.21
1	3	-2	29.43	9.23	29.38	12.87
1	1	4	29.93	5.10	29.86	7.40
0	3	3	30.81	2.37	30.74	7.74
0	4	0	32.07	13.14	32.05	21.02
1	3	-3	32.72	3.29	32.67	5.16
2	2	-3	33.95	4.29	33.85	7.17

DSC thermograms of CBZ polymorphs are shown in Fig 4.8; a single endothermic peak (T_f =187.8 ±0.1°C and ΔH_f =97.3 ±2.6 J g^{-1}) is observed for CBZ-I, attributed to its fusion, while two events were observed for CBZ-III. For CBZ-III, the first event (T_f = 165.0 ±0.9°C; ΔH_f =13.1 ±0.2J g^{-1}) is the transformation of III→I and the second event is the subsequent melting of CBZ-I (T_f =188.4±0.2°C; ΔH_f =110±3.6J g^{-1}), observable using hot stage microscopy. During the heating process the plate-like crystals of CBZ-III melt and immediately recrystallise to the needle-like crystals of CBZ-I, which subsequently melt. The values and observations recorded for both polymorphs agree with those reported by other authors [19, 20, 24]. CBZ-I and CBZ-III are enantiotropically related. CBZ-III is the thermodynamically stable form at lower temperatures while CBZ-I is the more stable form at higher temperatures.
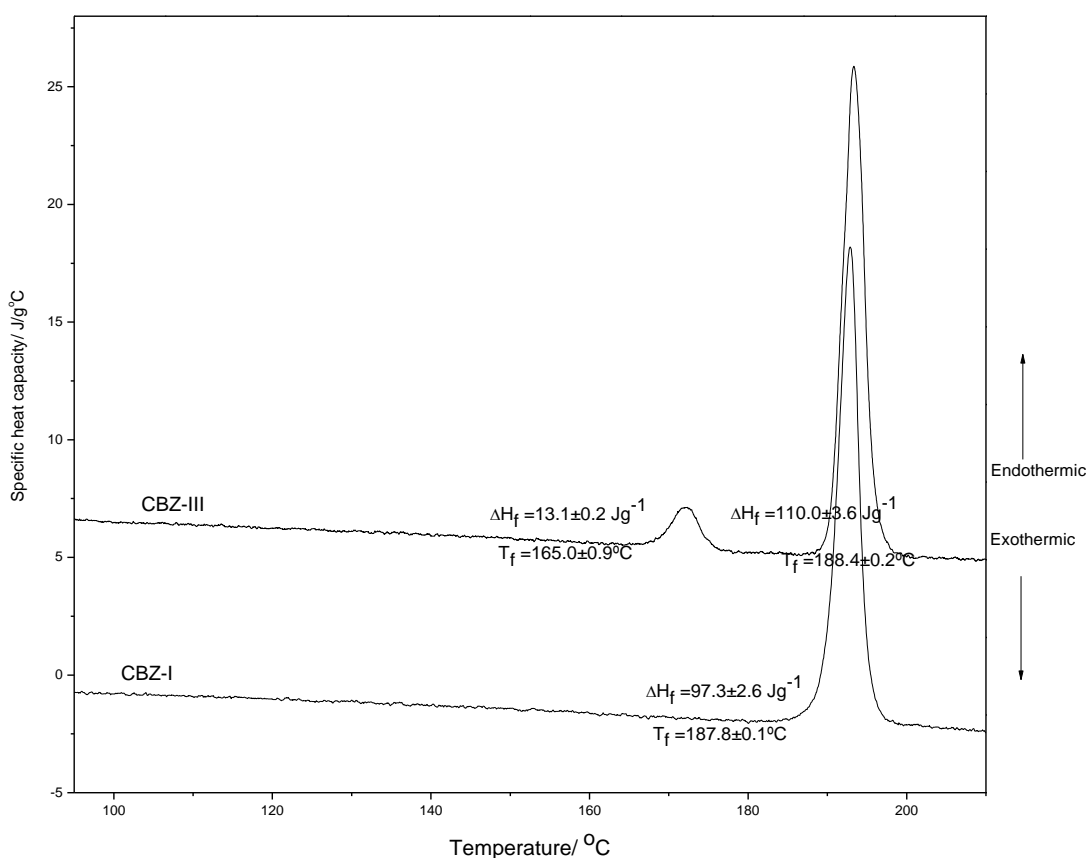
Figure 4.8 DSC thermograms of CBZ polymorphs CBZ-I and CBZ-III. Each thermogram is labelled with the corresponding polymorph.

Raman spectra for the polymorphs of CBZ are presented in Figure 4.9. To facilitate the evaluation of the differences and similarities in spectra, distinguishing peaks are tabulated (Table 4.8). Band assignments to specific molecular vibrations were performed with reference to published data[25]. CH stretching appears at 3071, 3043 and 3020cm^{-1} for Form III and 3061 and 3024 cm^{-1} for Form I . In the 1700-1500cm^{-1} region which contains the C=O stretch, a set of 3 peaks is observed for each form. 1622, 1599 and 1562 cm^{-1} corresponding to Form I and 1624, 1600 and 1565 cm^{-1} corresponding to Form III. Unlike the conformationally different polymorphs of IMC, the spectra of both polymorphs are similar in the 1700-1500cm^{-1} region. The single crystal study of CBZ polymorphs by Grzesiak *et al*[2] reveals that molecular conformations and hydrogen bonding schemes are very similar in both forms.
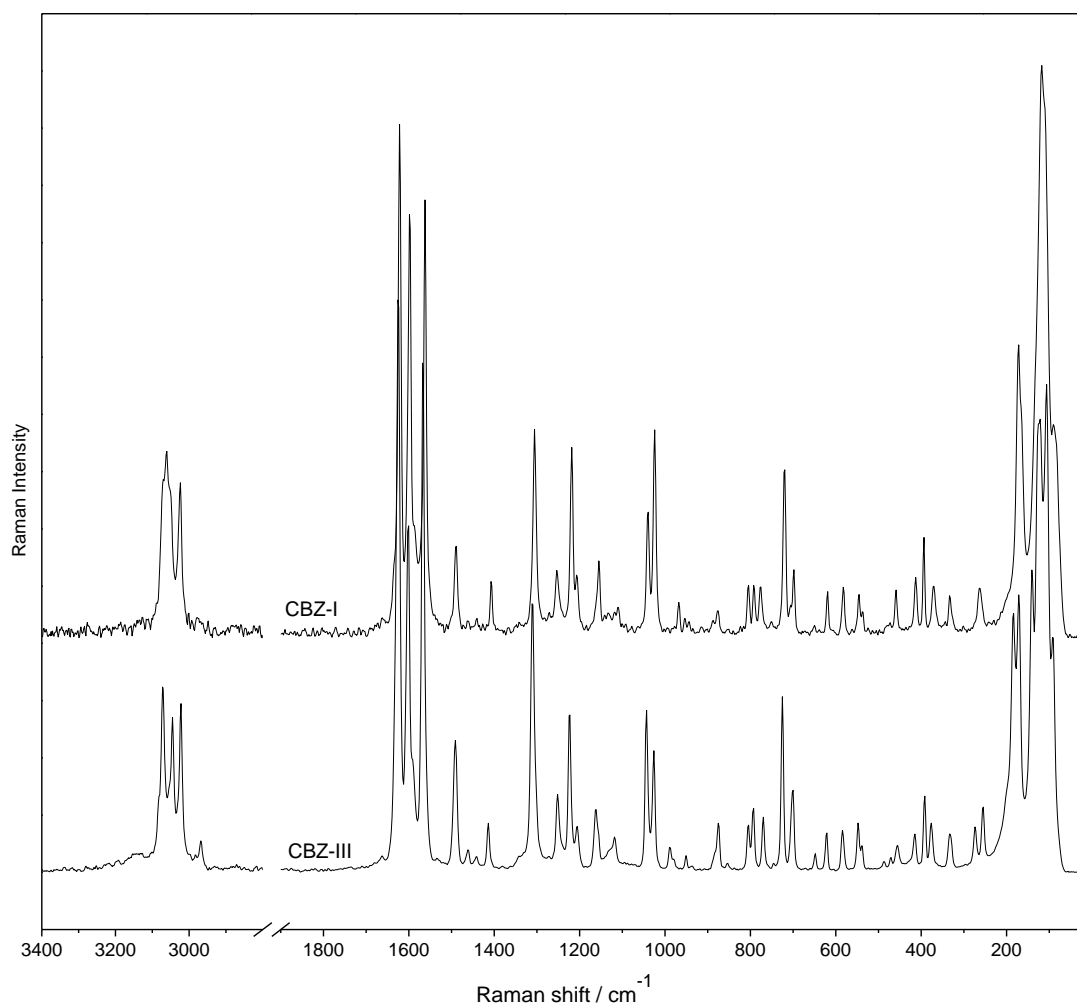
Figure 4. 9 Raman spectra of CBZ polymorphs; CBZ-I (top) and CBZ-III (bottom**).**

Table 4.8 Raman assignment and frequency of the two polymorphs of CBZ

Assignment[26]	CBZ-I/cm^{-1}	CBZ-III/cm^{-1}
s(CH)	3062, 3025	3469, 3045, 3022
s(C=O), s(C=C), s(C-C)	1622, 1563, 1490, 1408, 1208	1625, 1567, 1491, 1414, 1206
b(NH$_2$)	1599	1602
b(CH)	1306, 1041, 1025	1311, 1044, 1026
s(C-N)	1254, 1219, 969	1252, 1224, 989
s(C-N-C)	890, 878, 721	885, 875, 725
Lattice vibrations	414, 395, 372, 334, 264, 173, 119	414.9, 392.0, 376.5, 332.8, 274, 255, 171, 184, 140, 122, 106

s= stretch, b= bend

Unit cells for CBZ- I and CBZ-III both contain four molecular conformers that form dimers via intermolecular hydrogen bonding (O....H-N) between the carboxamide (-CONH$_2$) groups.

Figure 4.10 shows the packing pattern in CBZ polymorphs. The differences in the **packing** of these carboxamide dimer units (via weak C-H....O interactions) distinguishes both forms[2]. The lattice vibrational region of their Raman spectra show subtle differences.
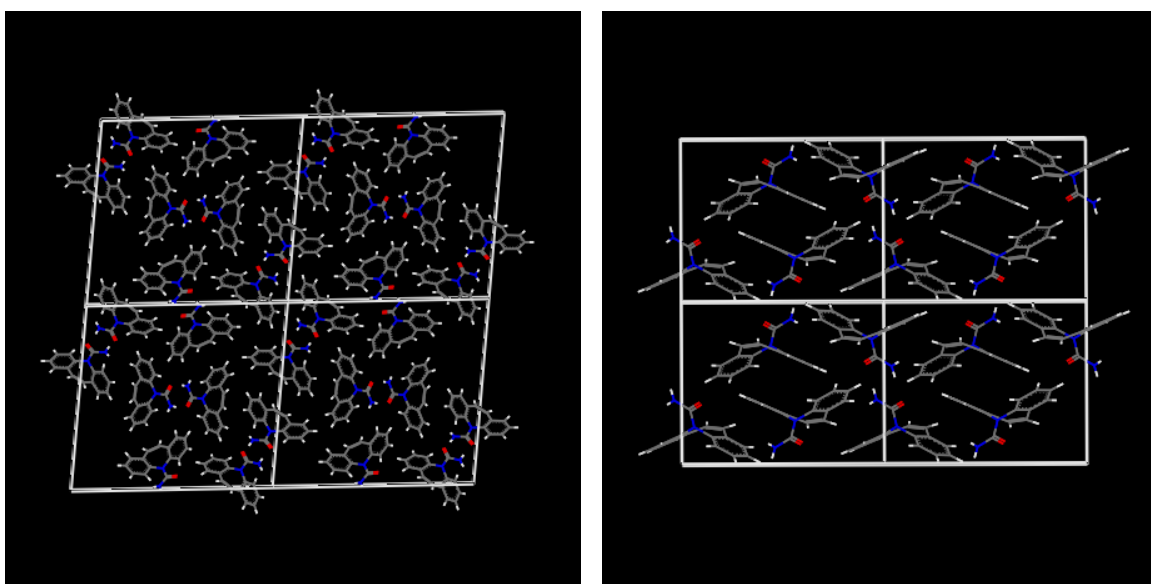
Figure 4. 10 Molecular packing patterns of CBZ polymorphs (a) CBZ-I and (b) CBZ-III

Colour code: grey-carbon, white-hydrogen, blue-nitrogen and red-oxygen.

4.4.3 Caffeine polymorphs

The PXRD and simulated patterns for both polymorphs are shown in Figure 4. 11 and 4.12, with 2θ angles, intensity and Miller indices listed in Table 4.9 and 4.10. The polymorphs of CFN have the most symmetrical unit cells of all the polymorphs examined in this study. This is supported by the PXRD patterns, which contain relatively few peaks. There is good agreement between experimental and simulated patterns.
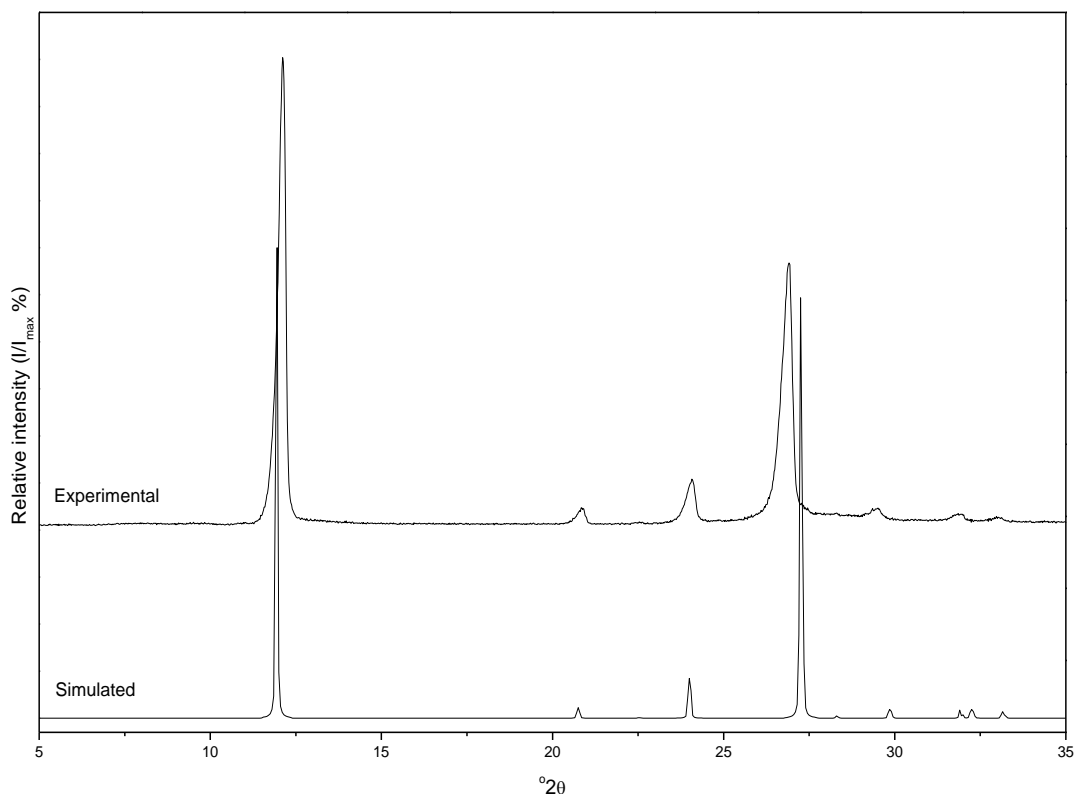
Figure 4.11 PXRD patterns for CFN-I; the top pattern is the experimental data and bottom one simulated from single crystal structures.

Table 4.9 Diffraction angles and relative intensities for PXRD peaks for CFN-I.

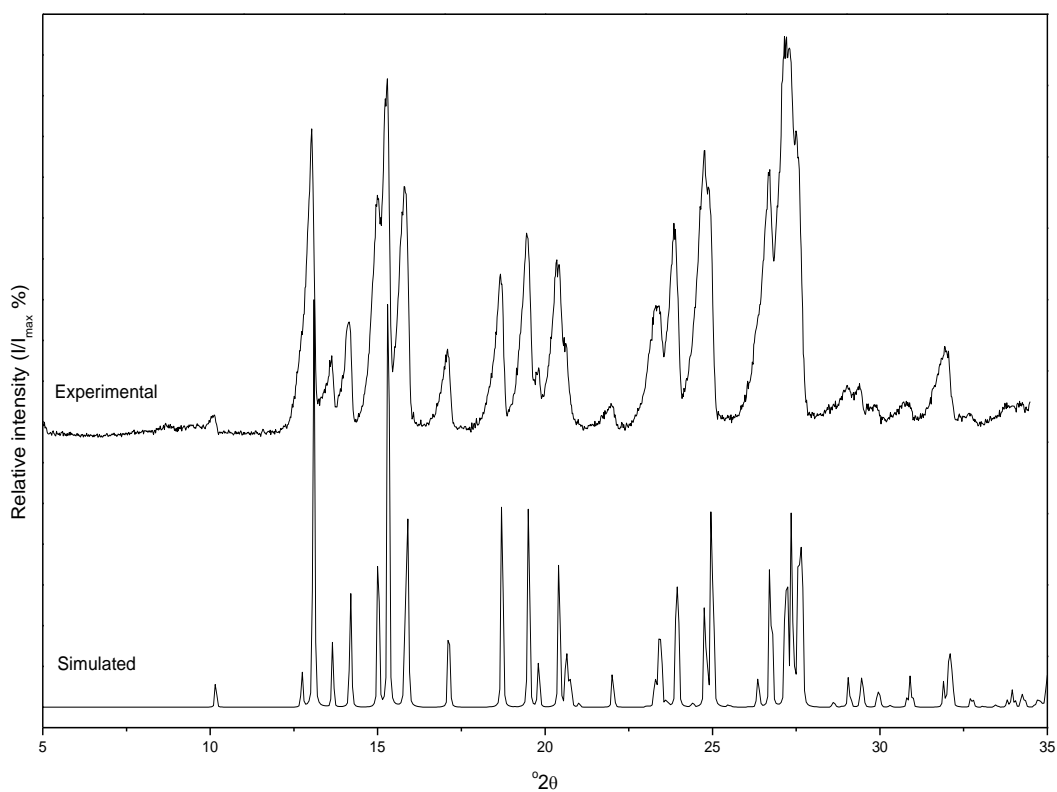| Miller plane			Simulated		Experimental	
h	k	l	º2theta	I/I_{max} (%)	º2theta	I/I_{max}(%)
1	1	0	11.92	100.00	11.74	100.00
3	0	0	20.73	2.89	20.49	3.13
2	1	1	22.52	0.19	22.13	0.24
2	2	0	23.98	11.43	23.70	9.42
1	0	2	27.24	92.84	26.52	55.67
2	0	2	29.83	2.77	29.13	3.12
4	1	0	31.90	1.77	31.60	1.52
2	1	2	32.23	2.94	32.64	0.98
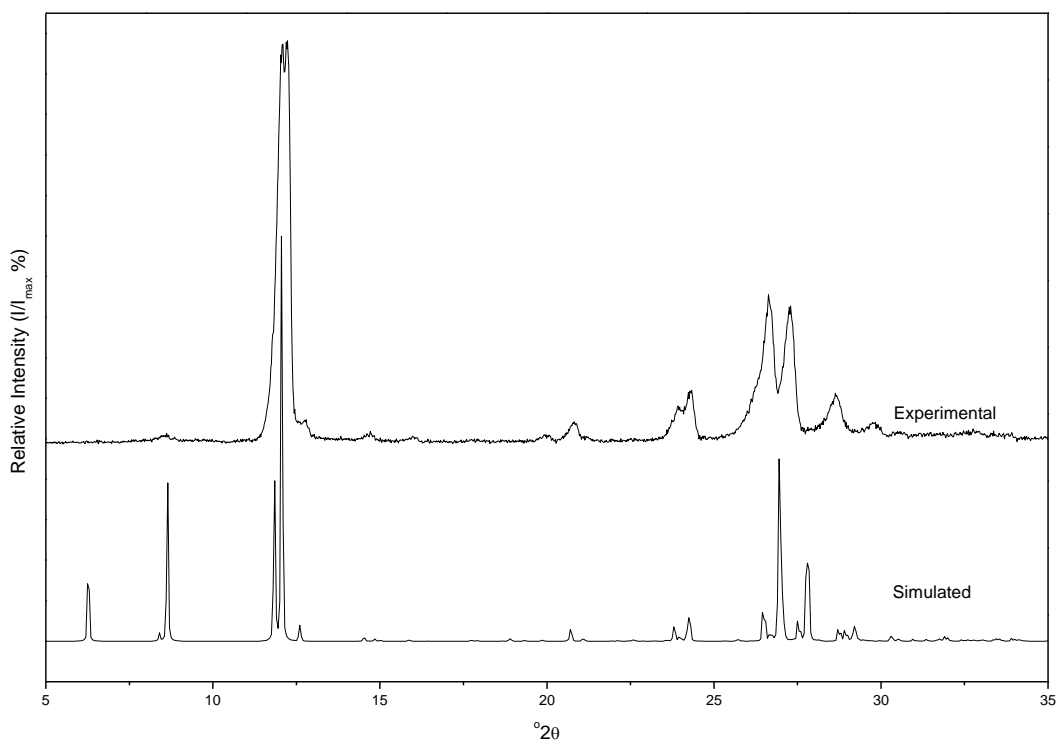
Figure 4. 12 PXRD patterns for CFN-II; the top pattern is the experimental data and bottom one simulated from single crystal structures.

Table 4.10 Diffraction angles and relative intensities for PXRD peaks for CFN-II.

Miller plane			Simulated		Experimental	
h	k	l	º2theta	I/I_{max} (%)	º2theta	I/I_{max}(%)
4	0	0	8.39	1.80	8.22	1.54
0	2	0	11.83	44.91	11.70	98.77
5	1	0	12.05	100.00	11.85	100.00
2	2	0	12.56	0.74	12.38	5.33
4	2	0	14.52	1.22	14.33	1.91
7	1	0	15.86	0.33	15.66	0.93
0	2	1	17.72	0.33	17.48	0.29
9	1	0	19.86	0.32	19.61	1.24
8	2	0	20.62	0.23	20.44	4.54
0	4	0	23.79	4.63	23.56	8.36
10	2	0	24.23	9.00	23.94	11.72
0	0	2	26.47	14.09	26.28	34.94
4	0	-2	26.67	2.80	26.35	32.27
1	1	-2	26.94	60.62	26.90	31.31
13	1	0	28.15	0.23	28.29	11.08
7	1	-2	29.18	5.88	29.39	4.01
6	2	-2	30.28	2.04	30.16	1.63
1	3	2	32.39	0.11	32.45	1.76
10	4	-1	33.56	0.52	33.48	0.65

Figure 4.13 shows DSC data for the two polymorphs of caffeine. A single endothermic event (T_f =234.1 ±0.1°C and ΔH_f =110.3 ±4.5 Jg^{-1}) attributed to melting was observed for CFN-I. However two endothermic transitions (T_f =148.4 ±0.3°C; ΔH_f =21.3 ±0.4 Jg^{-1} and 233.8 ±0.1°C; ΔH_f =112.0 ±2.0 Jg^{-1}) were observed for CFN-II attributable to II→I transformation and melting of CFN-I respectively. As observed by hot stage microscopy, the II→I is via a solid-gas-solid i.e. CFN-II sublimes and then recrystallises as CFN-I.
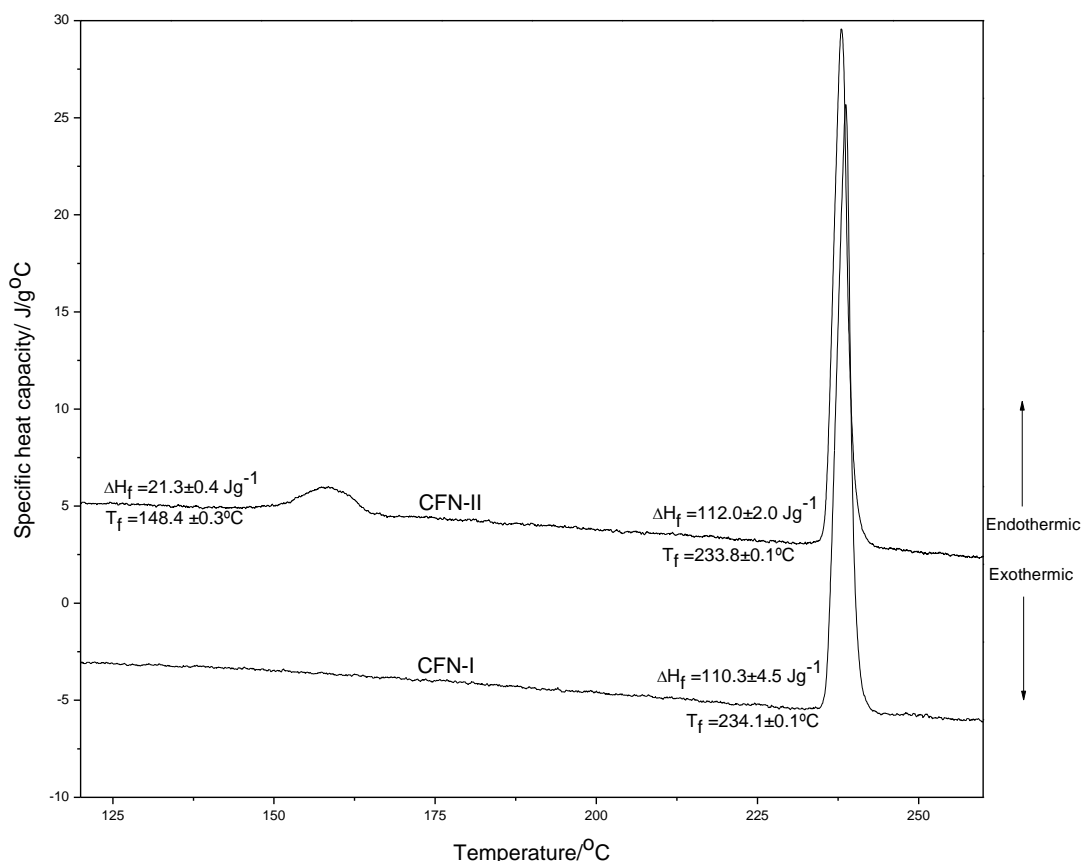
Figure 4. 13 DSC thermograms of CFN polymorphs CFN-I and CFN-II.

The Raman spectral data of the two polymorphs of caffeine (Fig 4.14, Table 4.11) exhibit very similar features throughout most of the spectral range. Spectra differed only subtly in background level and in the lattice vibration region suggesting similarity in molecular conformation and intermolecular interactions . The background of CFN- I spectra is higher than CFN-II and there are more bands in the lattice vibration region. CFN-II shows two bands (104.0 and 82.9 cm^{-1}) more than CFN-I, The effect of packing on the vibrational characteristics of bonds is not sufficiently large to be evident in their Raman spectra.
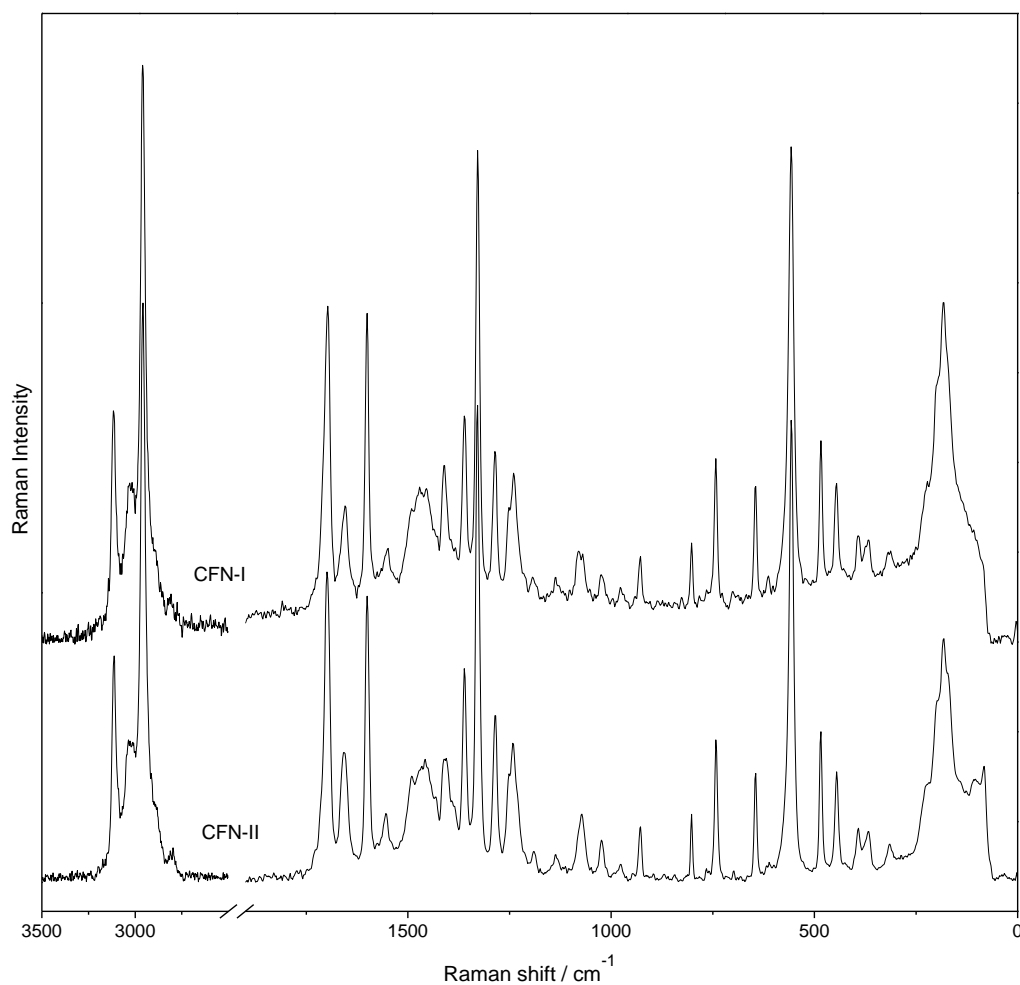
Figure 4. 14 Raman spectra of CFN polymorphs; CFN-I (top) and CFN-II(bottom)

Table 4.11 Raman assignment and frequency of the two polymorphs of CFN

Assignment	CFN-I/cm^{-1}	CFN-II/cm^{-1}
s(C-H)$_{ol, al}$	3116, 3034, 3017, 2959	3113, 3036, 3013, 2959
s(C=O)	1697, 1656,	1699, 1657
s(C=C)	1601, 1554	1601, 1554
b(CH), s(C=N) s(C=N)	1469, 1411, 1361, 1328, 1286	1468, 1406, 1361,1329, 1285
Lattice vibrations	484, 446, 392, 369, 313, 183	485, 445, 392, 367, 315, 182, 104, 83

s= stretch, b= bend

A single crystal study by Enright *et al*[15] revealed that the differences in molecular packing in both polymorphs are affected mainly by 'molecular positional disorder'. The unit cell of CFN-I (Fig 4.15) contain only entirely disordered caffeine molecules. Hence although the molecules lie in the same positions within the unit cell, they have no definite orientation, and hence are represented in Fig 4.15 not by a molecular drawing but regions of uncertainty. In Form II only part of the molecule is disordered and some molecules are completely ordered (see Fig 4.16, where the fully ordered molecules are clearly recognizable, but the partially ordered molecules are represented by crosses to indicate the regions of uncertainty).

Their study also revealed that both polymorphs contain similar molecular packing motifs of π-stacked molecular columns and hexagonal arrays. A comprehensive analysis of intermolecular interactions in CFN- I is hampered by entire-molecule disorder.
However analyses of intermolecular interactions for CFN-II show an array of CH…O and CH…N hydrogen bonds.
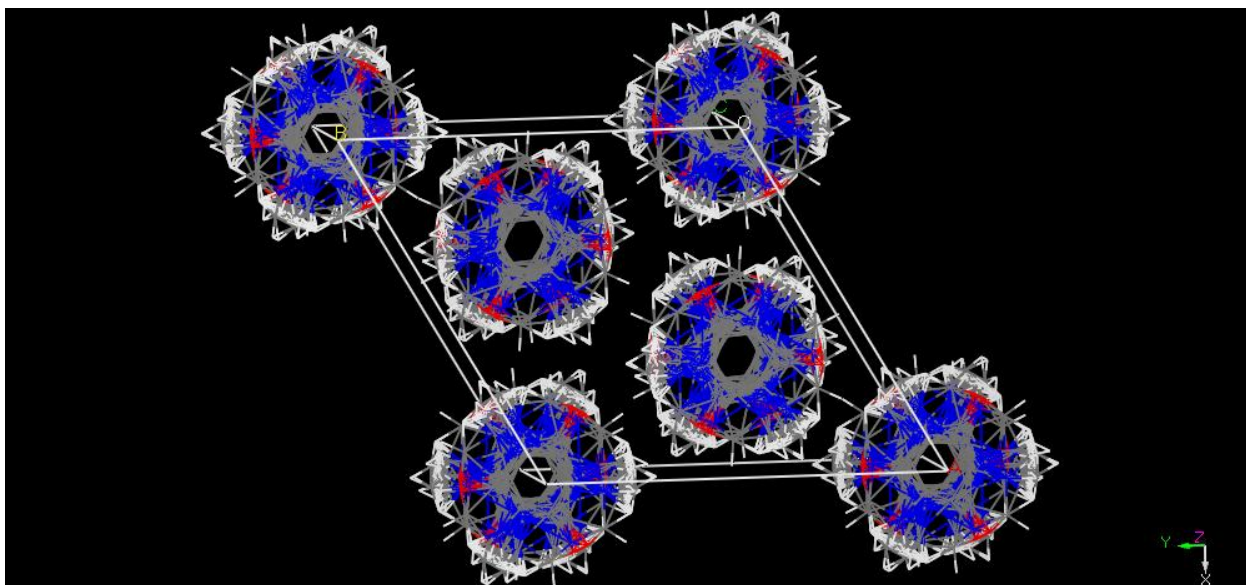
Figure 4. 15 Unit cell of CFN-I showing six molecules; showing extensive whole molecule disorder. *Colour code : grey-carbon, white-hydrogen, blue-nitrogen and red-oxygen.*
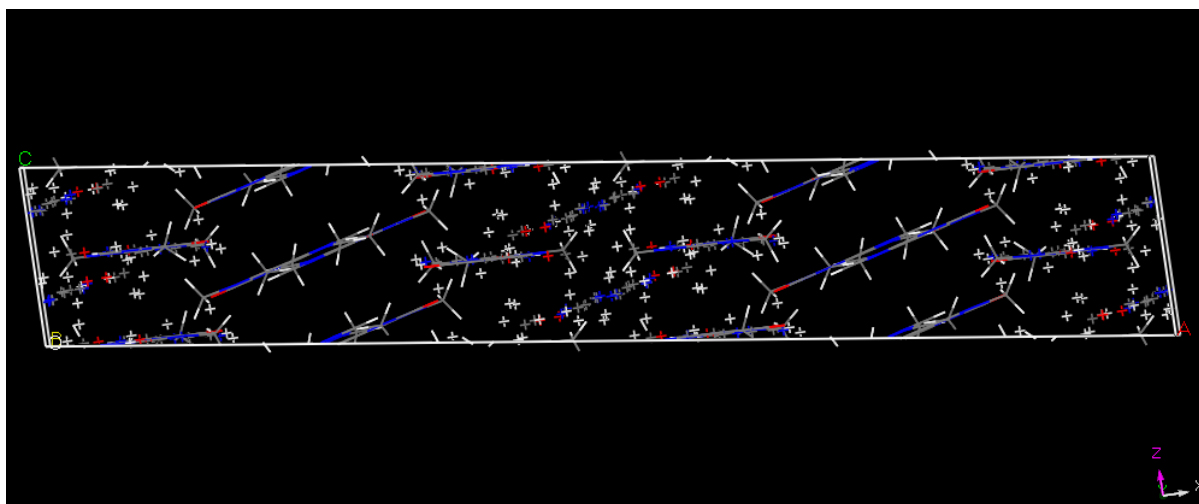
Figure 4. 16 Unit cell of CFN-II showing twenty molecules; some molecules show partial disorder. *Colour code : grey-carbon, white-hydrogen, blue-nitrogen and red-oxygen.*

4.4.4 Furosemide polymorphs

The experimental PXRD patterns for both FRS polymorphs and the simulated pattern of FRS-I are shown in Fig 4.17. Single crystal data for FRS-II was not available and hence no simulated PXRD data was generated. The patterns for both forms are different. Peaks at °2θ values of 6.44, 11.88, 17.09, 19.60, 19.81 and 29.28 are present for FRS-II but absent for FRS-I. Conversely, peaks at °2θ values of 18.87, 19.12, 20.63, 21.16 and 21.47 are present for FRS-I but absent for FRS-II. Table 4.12 shows experimental 2θ angles and relative intensities for both polymorphs and the simulated data and corresponding Miller indices for FRS-I only. 2θ angles agree within ± 0.15° of simulated data indicating the polymorphic purity of FRS-I. The simulated patterns show a higher peak resolution than experimental pattern, as expected. Peak intensities varied more significantly due to preferred orientation of sample. As the simulated pattern for FRS-II was not obtainable, polymorphic purity could not be ascertained.
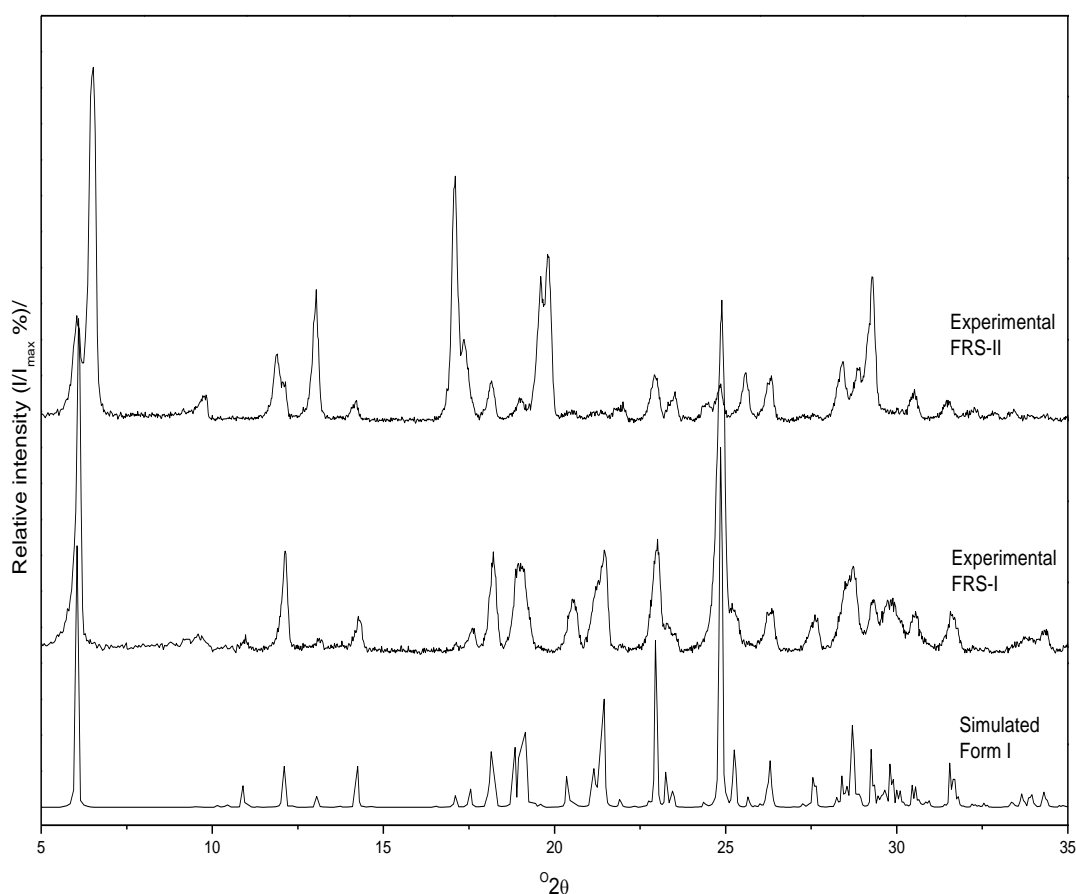
Figure 4. 17 PXRD patterns for FRS polymorphs; the top pattern is the experimental data for FRS-II, middle pattern is experimental data for FRS-I and bottom pattern is the simulated data for FRS-I from single crystal structures.

Table 4.12 Diffraction angles and relative intensities for PXRD peaks for FRS polymorphs.

Miller planes FRS-I			Simulated FRS-I		Experimental FRS-I		Experimental FRS- II	
h	k	l	º2theta	I/I_{max} (%)	º2theta	I/I_{max} (%)	º2theta	I/I_{max} (%)
0	1	0	6.02	72.97	6.10	94.98	5.97	24.55
-	-	-	-	-	8.21	0.85	6.08	28.22
1	0	0	9.54	0.65	9.57	3.65	6.44	100.00
0	1	1	10.90	3.64	10.95	2.58	6.56	95.16
0	2	0	12.06	14.07	12.13	28.07	9.81	6.42
0	1	-1	13.06	2.69	13.14	2.71	11.88	19.76
0	2	1	14.22	9.90	14.28	8.68	12.14	11.56
2	1	-1	17.08	2.65	17.12	2.26	13.03	36.85
1	1	1	17.60	0.01	17.65	6.55	14.19	5.75
2	0	-1	18.21	8.38	18.21	28.40	17.09	72.99
2	1	0	18.80	21.64	18.87	23.49	17.35	25.14
2	0	0	19.15	14.84	19.12	23.40	18.16	12.20
0	1	2	20.51	18.84	20.63	12.65	19.01	6.30
2	1	-1	21.10	13.48	21.16	15.52	19.60	44.43
2	2	-2	21.41	39.79	21.47	28.45	19.81	51.47
0	2	2	21.89	1.68	21.97	1.50	20.53	2.81
0	1	-2	22.94	36.52	23.01	31.92	21.27	1.92
2	3	0	23.43	5.14	23.55	4.29	21.76	3.43
2	2	0	24.83	100.00	24.88	100.00	21.98	4.04
2	1	1	25.23	14.94	25.32	10.19	22.92	14.14
2	1	1	26.18	4.33	26.21	10.97	23.00	12.90
0	2	-2	26.30	8.79	26.36	11.16	23.52	8.87
2	4	0	27.57	10.18	27.69	9.45	24.44	4.99
0	4	-1	28.41	7.17	28.46	17.71	24.84	10.15
2	2	1	28.69	13.37	28.73	24.05	25.58	14.62
2	3	0	29.26	13.67	29.33	14.69	26.33	13.64
1	2	2	29.72	0.10	29.77	13.59	27.28	1.48
0	5	0	30.45	4.68	30.58	9.68	28.42	18.10
0	0	3	31.56	11.85	31.59	10.20	28.89	15.72
3	2	0	33.81	0.01	33.82	3.73	29.28	44.43
2	4	0	34.28	3.23	34.33	5.33	30.50	8.49
							31.49	5.14
							32.29	3.35
							32.87	2.06
							33.43	2.99
							34.34	1.00

The DSC thermograms for FRS polymorphs are shown in Fig 4.18. FRS-I and FRS-II show very similar thermal events. This is indicative of similar crystal structure for both polymorphs. Three main events occur (as evidenced by hot stage microscopy). Firstly a polymorphic transformation, melting followed immediately by decomposition. The weak endotherm attributable to recrystallisation to new polymorph occurs at T_f =128.4 ±0.8°C (ΔH_f =3.7 ±1.0 Jg^{-1}) and T_f =126.8 ±0.7°C (ΔH_f = 4.9±1.0 Jg^{-1}) for FRS-I and FRS-II respectively. Themelting endotherm at 207.3±0.7 $^\circ$C and 210.9±0.7 $^\circ$C for FRS-I and FRS-II respectively is followed immediately by a sharp and intense exothermic peak attributable to decomposition.
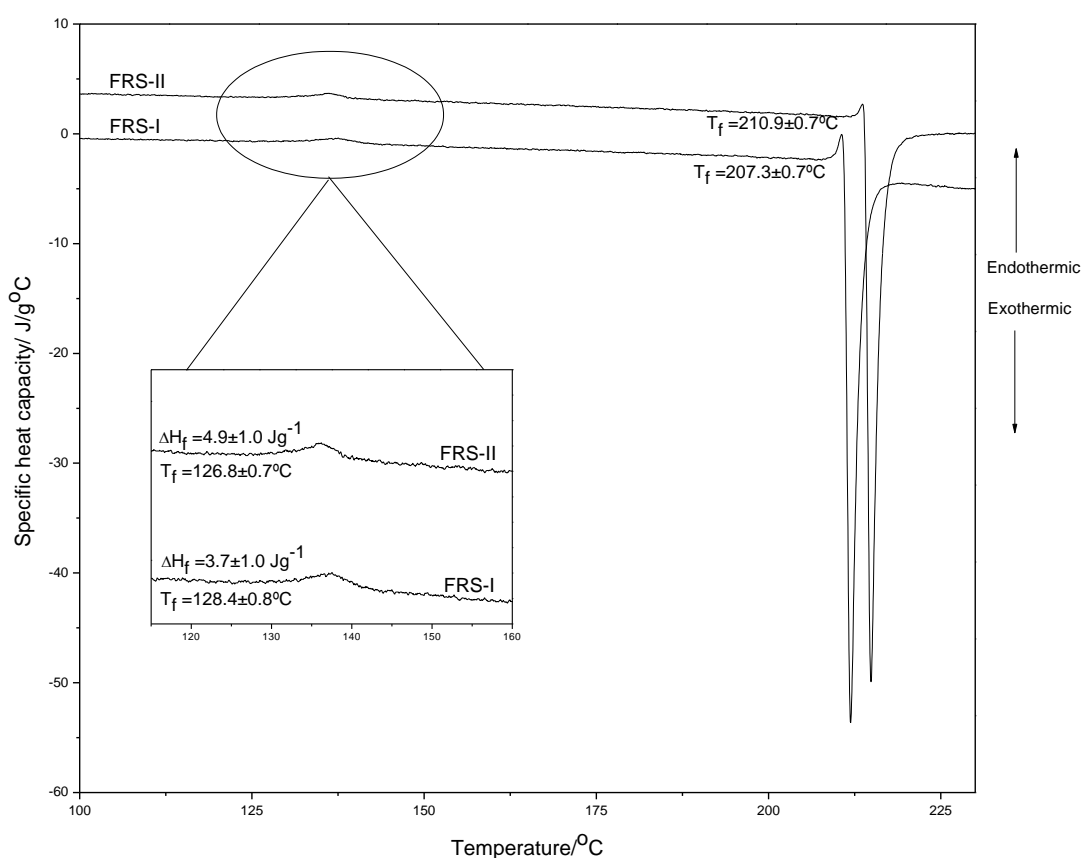
Figure 4. 18 DSC thermograms of FRS polymorphs. Each thermogram is labelled with the corresponding polymorph.

The Raman spectra for FRS polymorphs are presented in Figure 4.19. Table 4.13 shows tentative Raman assignment for each polymorph. For the N-H and C-H stretching region, band positions are very similar for both polymorphs with small variation in peak positions and intensity. Spectral differences between both polymorphs are evident as noticeable Raman shifts (1597.7, 1570.0 cm^{-1} for FRS-I and 1628.9, 1592.3 cm^{-1} for FRS-II in the N---H and C=O stretching vibrations suggesting difference in hydrogen bonding sequence.

As expected from the crystallographic study FRS-I contain inter- and intra-molecular hydrogen bonds[16, 27].
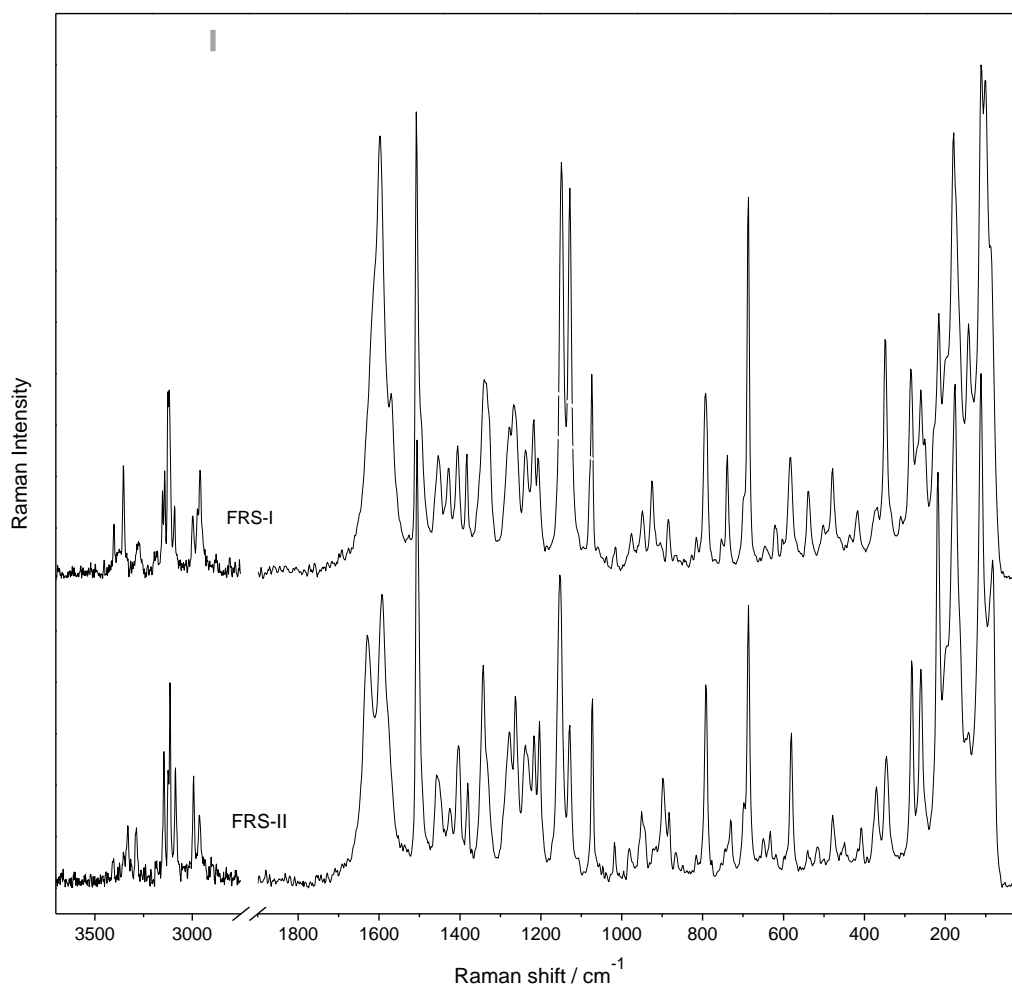
Figure 4. 19 Raman spectra of FRS polymorphs; FRS-I (top) and FRS-II(bottom**).**

Table 4. 13 Tentative Raman assignments and frequencies for the two polymorphs of FRS.

Assignment	FRS-I/cm^{-1}	FRS-II/cm^{-1}
s(N-H)	3402, 3353, 3277	3404, 3330, 3286
s(C-H)$_{ar,ol,al}$	3153, 3141, 3124, 3118, 3091, 2998, 2980, 2960	3145, 3124, 3114, 3086, 2993, 2963
s(C=O), b(N-H)	1598, 1570	1629, 1592
s(C=C), s(Ph)	1508, 1454, 1428, 1406	1506, 1457, 1425, 1404
Lattice vibrations	417, 369, 348, 310, 285, 260, 216, 180, 143, 111, 101	408, 370, 346, 283, 260, 218, 176, 143, 112, 83

s= stretch, b= bend, ar=aryl, al=alkyl, ol=olefin

4.4.5 Sulfanilamide polymorphs

The experimental and simulated PXRD patterns for SFN-β and SFN-γ polymorphs are shown in Figs 4.20 and 4.21. The PXRD patterns are different and can be easily distinguished. Experimental data shows defined and sharp peaks which are indicative of their crystalline nature. The identity of both polymorphs is established by the good agreement between experimental and simulated diffraction patterns. The simulated patterns show higher peak resolution than the experimental pattern, as expected. 2θ angles, relative intensities and Miller indices and corresponding simulated data for both polymorphs are listed in Table 4.14 and 4.15. Experimental 2θ angles agree within ± 0.20º of simulated data confirming polymorphic purity. However peak intensities vary significantly as a result of preferred orientation of several atomic planes to the incident X-ray beam.
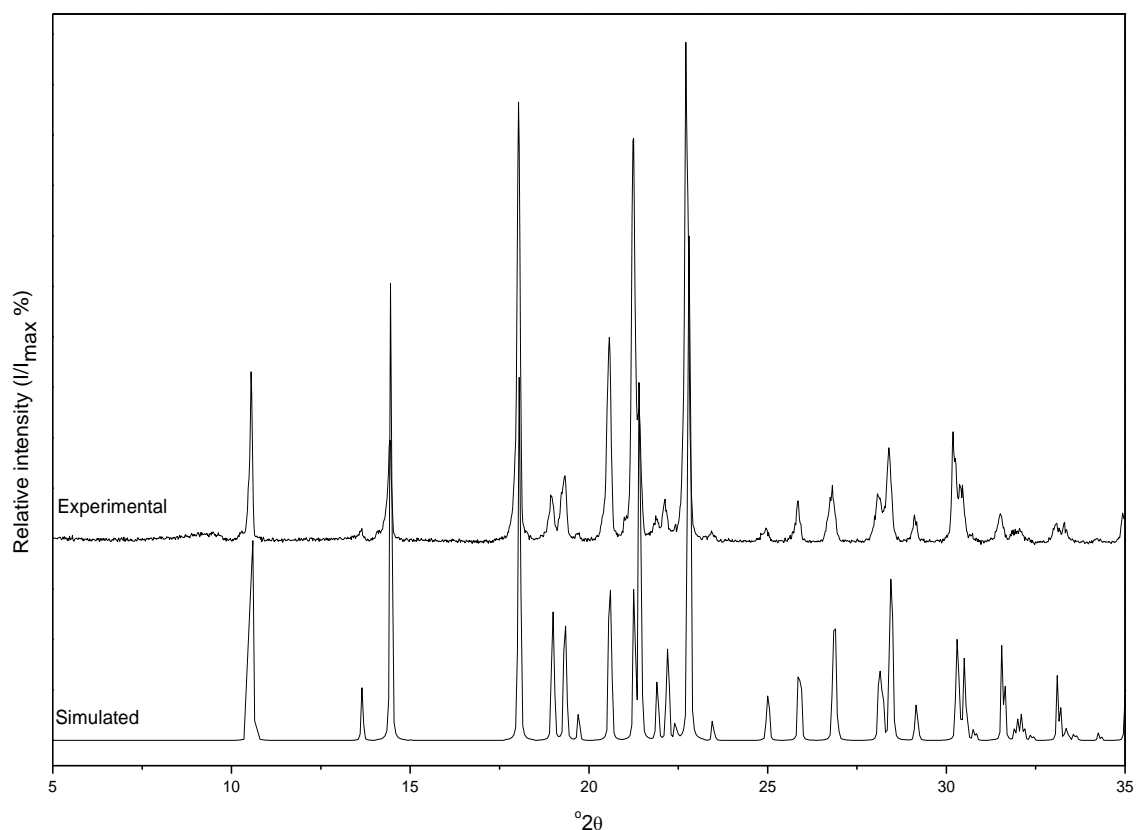
Figure 4. 20 PXRD patterns for SFN-β; the top pattern is the experimental data and bottom one simulated from single crystal structures.

Table 4. 14 Diffraction angles and relative intensities for PXRD peaks for SFN-β.

Miller plane			Simulated		Experimental	
h	k	l	º2theta	I/I_{max} (%)	º2theta	I/I_{max}(%)
-	-	-	-	-	9.48	1.30
1	0	0	10.58	29.09	10.55	37.70
0	1	1	13.64	7.12	13.63	2.18
1	1	0	14.45	63.30	14.43	22.46
1	0	-2	18.04	61.10	18.03	98.06
0	0	2	18.98	27.08	18.96	10.00
1	1	1	19.32	26.56	19.32	14.58
0	2	0	19.70	3.84	19.70	1.64
1	1	-2	20.57	37.09	20.57	45.64
-	-	-	-	-	21.02	4.78
2	0	0	21.25	22.51	21.24	92.09
0	1	2	21.41	58.37	21.42	27.13
0	2	1	21.89	9.15	21.90	5.13
2	1	-1	22.18	18.84	22.12	9.64
1	2	-1	22.78	100.00	22.72	100.00
2	1	0	23.46	3.18	23.43	2.41
1	0	2	24.98	9.44	24.95	3.09
1	2	1	25.87	18.64	25.85	9.21
1	2	-2	26.83	22.92	26.80	12.30
2	1	1	28.17	12.42	28.10	10.21
1	1	-3	28.43	38.01	28.39	21.07
2	2	0	29.14	7.03	29.12	5.30
2	2	-2	30.28	21.45	30.20	23.76
2	1	-3	30.49	14.48	30.40	12.17
3	1	-1	31.56	18.37	31.52	6.26
1	3	-1	31.92	2.55	31.87	2.11
3	0	0	32.11	3.61	32.02	2.42
2	2	1	33.11	11.59	33.07	3.97
1	2	-3	33.33	2.61	33.29	4.15
1	3	1	34.25	1.33	34.22	0.62
0	2	3	35.00	0.09	34.94	6.52
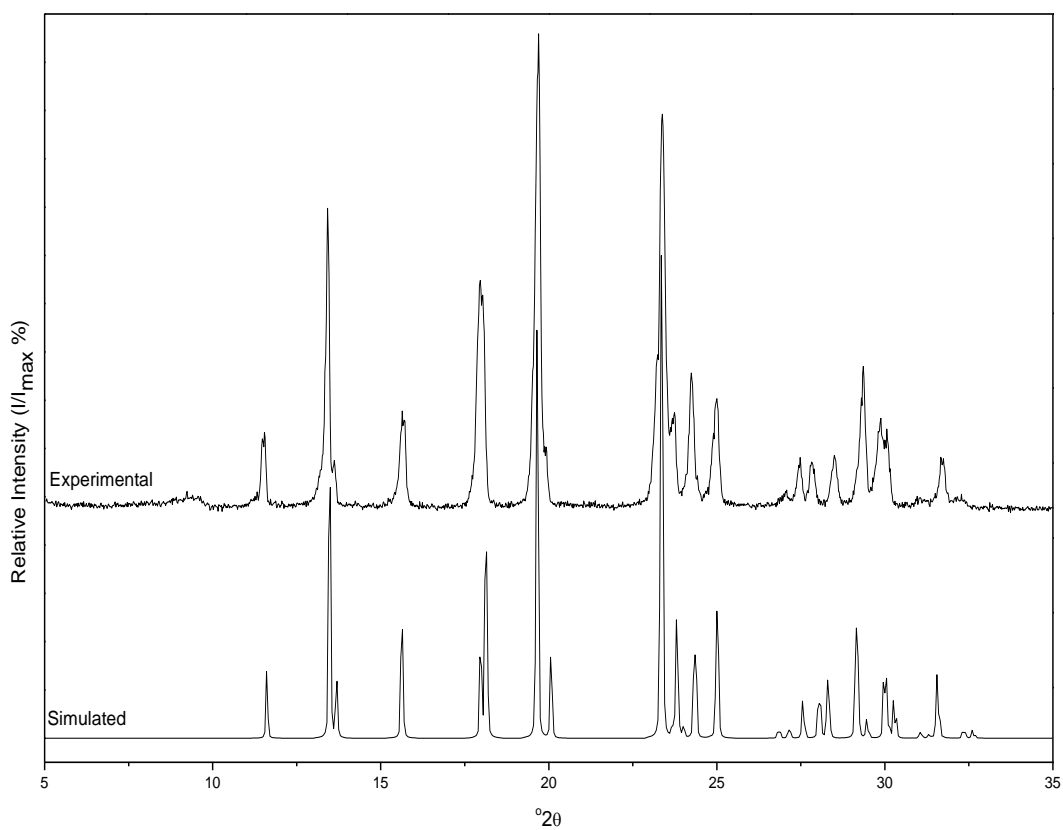
Figure 4. 21 PXRD patterns for SFN-γ; the top pattern is the experimental data and bottom one simulated from single crystal structures.

Table 4. 15 Diffraction angles and relative intensities for PXRD peaks for SFN-γ.

Miller plane			Simulated		Experimental	
h	k	l	º2theta	I/I_{max} (%)	º2theta	I/I_{max}(%)
-	-	-	-	-	9.32	1.81
-	-	-	-	-	11.47	14.22
1	0	0	11.60	12.53	11.55	16.37
1	1	0	13.47	69.80	13.43	66.75
0	1	1	13.68	13.40	13.61	10.13
1	1	-1	15.62	31.39	15.61	16.78
			-	-	15.72	19.62
1	2	0	17.96	22.61	17.96	50.45
0	2	1	18.12	60.55	18.07	40.43
1	2	-1	19.64	96.19	19.69	100.00
1	1	1	20.05	17.55	19.93	13.19
2	0	0	23.32	13.02	23.19	30.01
1	0	-2	23.34	100.00	23.38	87.80
0	3	1	23.79	21.85	23.73	20.98
2	1	0	24.32	27.42	24.25	29.83
1	3	-1	24.99	36.41	24.99	24.20
2	2	0	27.13	2.18	27.05	3.48
0	4	0	27.54	2.07	27.47	9.36
1	3	1	28.03	14.33	27.83	10.16
2	0	-2	28.29	16.44	28.49	11.53
2	1	-2	29.13	37.39	29.36	31.65
1	4	0	29.97	15.57	29.86	18.78
0	4	1	30.07	3.73	30.07	15.83
1	4	-1	31.04	1.74	31.07	1.83
2	2	-2	31.54	16.61	31.70	9.88
0	3	2	31.66	0.29	31.76	9.45
2	2	1	32.32	2.68	32.34	1.75

The thermal behaviour of SFN polymorphs are shown in Fig 4.22. DSC thermograms show a single endothermic event for SFN-γ T_f =162.3 ±0.3°C and ΔH_f =146.0 ±1.0 Jg^{-1} attributed to melting. However, three endothermic transitions (T_f =128.3 ±1.3°C; ΔH_f =6.9±3.0 Jg^{-1}, T_f =156.0±1.3°C; ΔH_f =1.33±0.5 Jg^{-1} and T_f =162.3±0.3°C; ΔH_f =121.0±3.5 Jg^{-1}) were observed for SFN-β attributable to incomplete β → γ transformation, melting of residual SFN-β and melting of SFN-γ respectively. These observations agree with results previously recorded[11]. Inherently, factors such as solvent used, particle size and crystal defects affect the extent to which the β → γ transformation goes to completion. With larger particle sizes (>450 μm) the β → γ transformation goes to completion, (See the DSC thermogram Fig 7.7, Chapter 7).
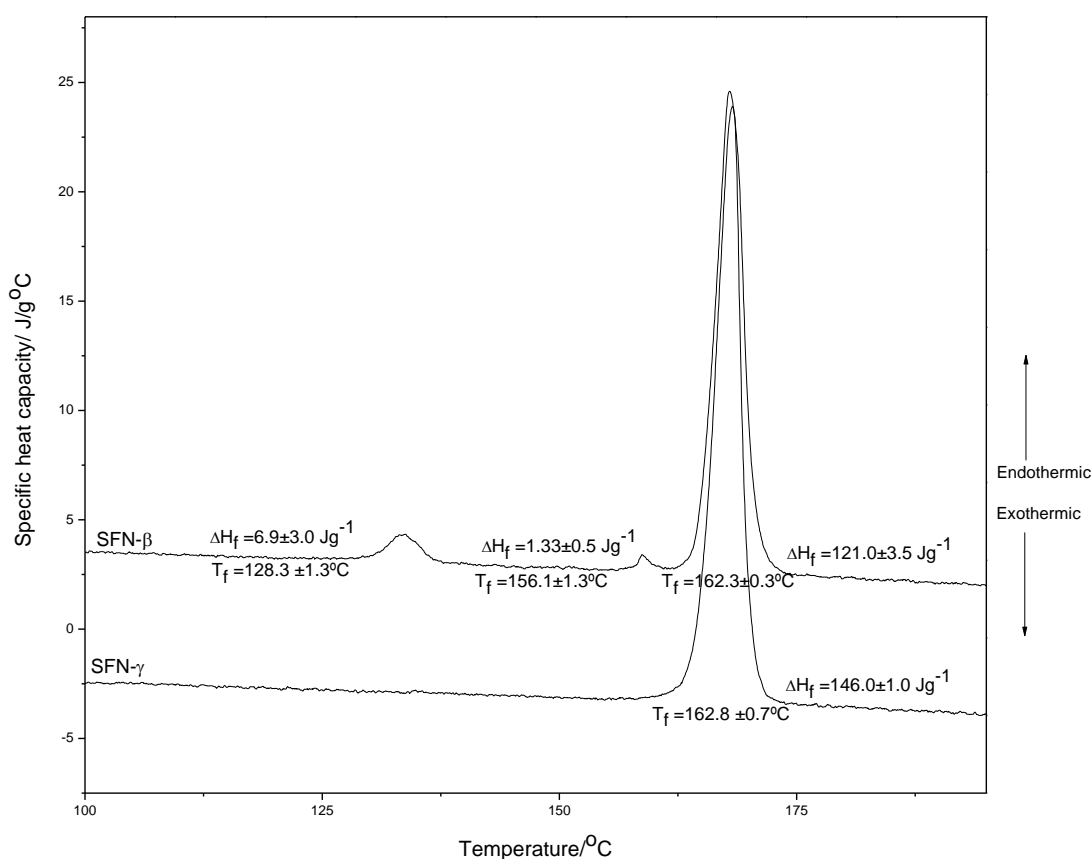
Figure 4. 22 DSC thermograms of SFN polymorphs- SFN-β and SFN-γ, each thermogram is individually labelled.

The Raman spectra for SFN polymorphs are presented in Fig 4.23. Table 4.16 shows Raman assignments[21] for each polymorph. The polymorphs are very similar but show subtle differences as a result of aromatic C-H vibrations. For aryl stretching four bands are observed at 3069, 3053, 3040, 3008 cm^{-1} for SFN-β and three are observed at 3077.7, 3044.6, 3006.2 cm^{-1} for SFN-γ. Similarly for aryl C-H bending, SFN-β shows five bands (1304, 1157, 1092, 1007 and 842 cm^{-1}) whereas SFN-γ shows three (1090, 1007 and 841 cm^{-1}). Hydrogen bonding in the crystal structure of the polymorphs of SFN is similar, involving the phenyl - NH_2 and the sulfonamide group[18, 28, 29]. Additionally π-π interactions involving the phenyl rings stabilise the crystal structure of packing SFN-β.
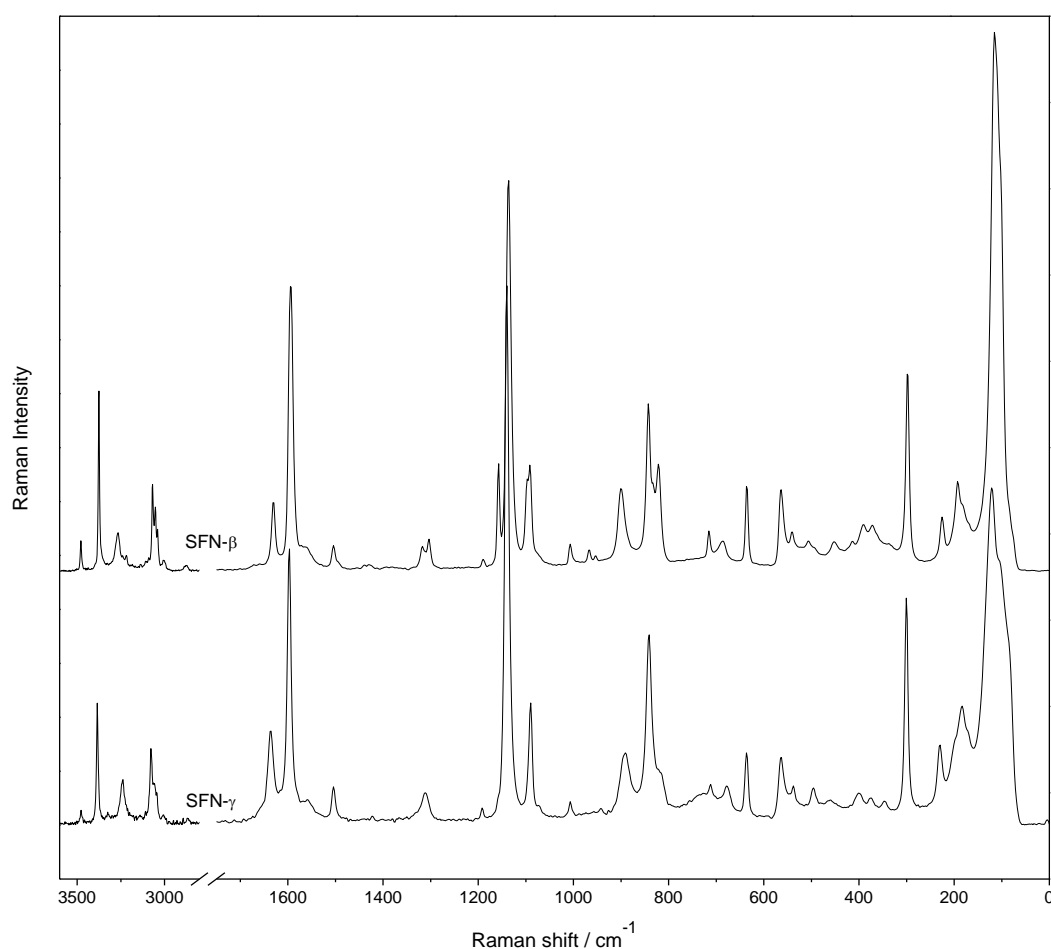
Figure 4. 23 Raman spectra of SFN polymorphs; SFN-β (top) and SFN-γ (bottom)**.**

Table 4.16 Raman assignments and frequencies for the two polymorphs of sulfanilamide.

Assignment[30]	SFN-β/cm^{-1}	SFN-γ/cm^{-1}
s(NH$_2$)	3478, 3376, 3266	3478, 3385, 3239
s(CH)$_{ar}$	3069, 3053, 3040, 3008	3078, 3045, 3006
b(NH$_2$)	1631	1636
s(Ph)	1594, 1559,1504, 1190	1597, 1559, 1504, 1192
s(SO$_2$)	1317, 1137	1311, 1140
b(CH)$_{ar}$	1304, 1157, 1092, 1007, 842	1090, 1007, 841,
s(SN)	900	891
Lattice vibrations	452, 414, 391, 372, 298, 225, 192, 115	460, 400, 375, 347, 301, 230, 183, 121

s= stretch, b= bend, ar= aryl, Ph= phenyl

4.5 Conclusions

The multi-analytical approach involving the use of X-ray diffraction, calorimetry, hot-stage microscopy and Raman spectroscopy to study the polymorphs of five model compounds demonstrates a unique capability to extract a wealth of information that would not be obtainable using only one technique. PXRD analysis involved experimental and simulated data-matching to confirm polymorphic purity. However the phenomenon of preferred orientation affected the quality of data matching. The polymorphic purity for FRS-II was not determined because single crystal data for the generation of a simulated pattern has not been recorded for this polymorph. DSC, in conjunction with HSM, allowed the thermal profiles of polymorphs to be generated. Events such as polymorphic transition, melting and decomposition were observed. Raman spectroscopy allowed for the discrimination of polymorphs based on perturbation of bond vibrations as a consequence of distinct molecular packing. Molecular packing from single crystal studies substantiates spectral data interpretation. CFN polymorphs were the least distinguishable by Raman because the polymorphs are structurally similar.

4.6 References

1. P. A. Slavin, D. B. Sheen, E. E. A. Shepherd, J. N. Sherwood, N. Feeder, R. Docherty and S. Milojevic, *Journal of Crystal Growth*, 2002, **237-239**, 300-305.

2. A. L. Grzesiak, M. D. Lang, K. Kim and A. J. Matzger, *Journal of Pharmaceutical Sciences*, 2003, **92**, 2260-2271.

3. A. J. Florence, A. Johnston, S. L. Price, H. Nowell, A. R. Kennedy and N. Shankland, *Journal of Pharmaceutical Sciences*, 2006, **95**, 1918-1930.

4. R. Manduva, V. L. Kett, S. R. Banks, J. Wood, M. Reading and D. Q. M. Craig, *Journal of Pharmaceutical Sciences*, 2008, **97**, 1285-1300.

5. G. D. Enright, V. V. Terskikh, D. H. Brouwer and J. A. Ripmeester, *Crystal Growth & Design*, 2007, **7**, 1406-1410.

6. Y. Matsuda and E. Tatsumi, *International Journal of Pharmaceutics*, 1990, **60**, 11-26.

7. Y. Matsuda and E. Tatsumi, *Journal of Pharmacobio-Dynamics*, 1989, **12**, 38.

8. X. Chen, K. R. Morris, U. J. Griesser, S. R. Byrn and J. G. Stowell, *Journal of the American Chemical Society*, 2002, **124**, 15012-15019.

9. P. A. Slavin, D. B. Sheen, E. E. A. Shepherd, J. N. Sherwood, N. Feeder, R. Docherty and S. Milojevic, in *13th International Conference on Crystal Growth held in conjunction with the 11th International Conference on Vapor Growth and Epitaxy*, Elsevier Science Bv, Kyoto, Japan, 2001, pp. 300-305.

10. A. Cesaro and G. Starec, *Journal of Physical Chemistry*, 1980, **84**, 1345-1346.

11. S. Toscani, S. Thorén, V. Agafonov, R. Céolin and J. Dugué, *Pharmaceutical Research*, 1995, **12**, 1453-1456.

12. A. Porteri, R. Harris, R. Fletton, R. Lancaster and T. Threlfall, *Magnetic Resonance in Chemistry*, 2004, **42**, 313-320.

13. T. J. Kistenmacher and R. E. Marsh, *Journal of the American Chemical Society*, 1972, **94**, 1340-1345.

14. V. L. Himes, A. D. Mighell and W. H. De Camp, *Acta Crystallographica Section B*, 1981, **37**, 2242-2245.

15. G. D. Enright, V. V. Terskikh, D. H. Brouwer and J. A. Ripmeester, *Crystal Growth & Design*, 2007, **7**, 1406-1410.

16. J. Lamotte, H. Campsteyn, L. Dupont and M. Vermeire, *Acta Crystallographica Section B*, 1978, **34**, 1657-1661.

17. A. M. O'Connell and E. N. Maslen, *Acta Crystallographica*, 1967, **22**, 134-145.

18. M. Alleaume and J. Decap, *Acta Crystallographica*, 1965, **19**, 934-938.

19. B. Legendre and Y. Feutelais, *Journal of Thermal Analysis and Calorimetry*, 2004, **76**, 255-264.

20. K. Masuda, S. Tabata, H. Kono, Y. Sakata, T. Hayase, E. Yonemochi and K. Terada, *International Journal of Pharmaceutics*, 2006, **318**, 146-153.

21. L. S. Taylor and G. Zografi, *Pharmaceutical Research*, 1997, **14**, 1691-1698.

22. D. Lin-Vien, N. Colthup, W. Fateley and G. Jeanette, *The Handbook of Infrared and Raman Characteristic frequencies of organic molecules*, Academic press, San Diego, 1991.

23. P. J. Cox and P. L. Manson, *Acta Crystallographica Section E-Structure Reports Online*, 2003, **59**, O986-O988.

24. G. Defossemont, S. Randzio and B. Legendre, *Journal of Thermal Analysis and Calorimetry*, 2007, **89**, 751-755.

25. C. J. Strachan, S. L. Howell, T. Rades and K. C. Gordon, *Journal of Raman Spectroscopy*, 2004, **35**, 401-408.

26. L. E. O'Brien, P. Timmins, A. C. Williams and P. York, *Journal of Pharmaceutical and Biomedical Analysis*, 2004, **36**, 335-340.

27. J. N. Latosinska, M. Latosinska, W. Medycki and J. Osuchowicz, *Chemical Physics Letters*, 2006, **430**, 127-132.

28. A. Portieri, R. K. Harris, R. A. Fletton, R. W. Lancaster and T. L. Threlfall, *Magnetic Resonance in Chemistry*, 2004, **42**, 313-320.

29. R. J. Roberts and R. C. Rowe, *International Journal of Pharmaceutics*, 1996, **129**, 79-94.

30. H. T. Varghese, C. Y. Panicker and D. Philip, *Spectrochimica Acta Part A: Molecular and Biomolecular Spectroscopy*, 2006, **65**, 155-158.

Chapter Five: Diffuse reflectance visible spectroscopic analysis of the surface chemistry of drug polymorphs using pH indicator dyes

5.1 Introduction

The intrinsic differences in the surface chemistry of crystalline drug polymorphs may be observed macroscopically as variation in properties such as chemical reactivity and stability. A novel approach to surface analysis of drug polymorphs based on the visible spectroscopic analysis of adsorbed pH indicators is presented herein.

UV-Vis analysis of adsorbed pH indicators dyes have been employed extensively to characterise the surface acidity of many solids especially inorganic compounds. For pharmaceutical solid surfaces, strong acidity or basicity is uncommon[1]. These solid surfaces lack the highly reactive groups present in many inorganic systems such as the oxides of silicon, aluminium, magnesium and zinc, capable of proton or electron donating or sharing[1]. Nevertheless the surface acidity of solids of pharmaceutical interest has been characterised in the past using adsorbed pH indicators to explain drug-excipient interactions, and other formulation issues[1-6]. Most drug substances are weak acids or bases, so their molecules contain at least one site that can reversibly dissociate to lose a proton or associate with a proton depending on the acidity/basicity of their environment.

Acid/base solution equilibria of pH indicators have been used successfully to interpret behaviour in the adsorbed state. Phenol red (PR), thymol blue (TB) and methyl red (MR), whose solution acid/base properties have been extensively studied, show intense electronic absorption bands in the visible region attributed to π-π* and n-π* transitions. The solution equilibria of diprotic sulfonphthalein dyes PR and TB show three species as shown in Fig 5.1. Upon protonation their absorption maxima shift to longer wavelengths, with an increase in their molar absorption coefficients. The pKa_1 and pKa_2 of the sulfonphthalein dye correspond to the acid/base dissociation constant of the sulphonic acid group (SO_3H) and phenolic group, respectively.
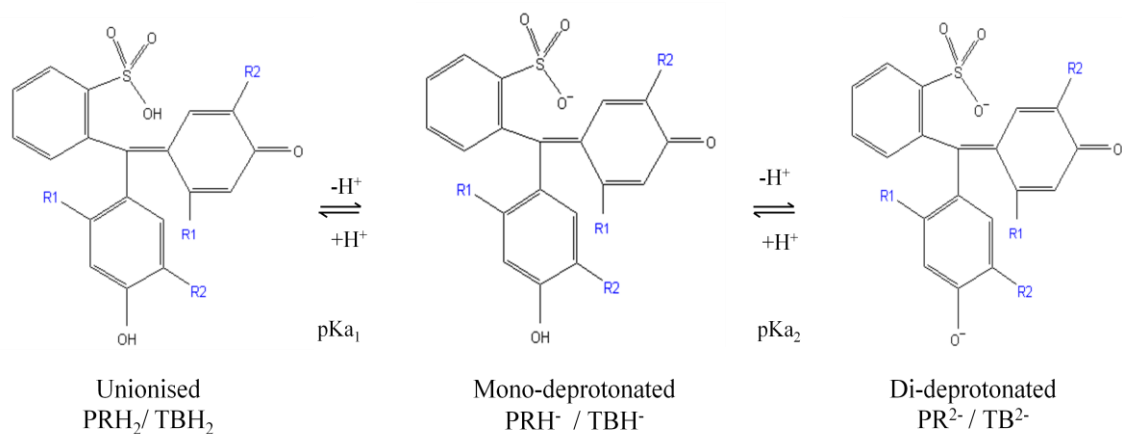
Figure 5. 1 The acid/base solution equilibria for diprotic sulfonphthalein dyes, phenol red (PR) and thymol blue (TB) showing the dye ionisation states. R1 and R2 are ring substituents. In PR, R1=R2=H; In TB, R1= CH_3 R2= $CH(CH_3)_2$

Azo monoprotic dye MR has complex solution equilibria; four species are observed (Fig 5.2) namely: neutral/unionised, deprotonated, protonated, and zwitterionic forms[7, 8].
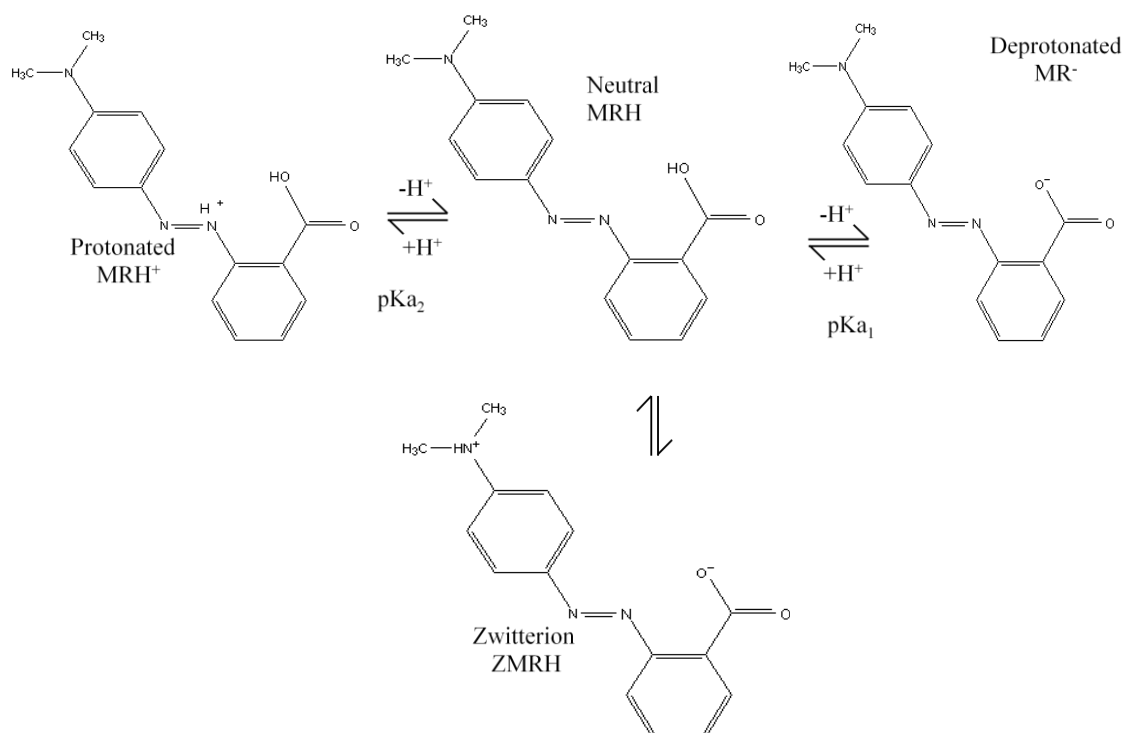
Figure 5. 2 The acid/base solution equilibria for monoprotic azo dye methyl red (MR) showing the ionisation states.

MR spectra are generally characterised by broad absorption bands, sometimes with pronounced shoulders. The intensities and positions of the spectral bands are variable and solvent-dependent[9]. These bands are very sensitive to the polarity of their environment. The pKa_1 and pKa_2 of MR correspond to the acid dissociation constant of the carboxylic acid group and the conjugate acid of the azo (azonium) group, respectively.

In principle, the UV-Vis spectra of a chromophore contain information about its interaction with its environment, be it in a solution or in the adsorbed state. In this study, the DRVS spectra of adsorbed dye species will represents the sum of all dye-surface and dye-dye interactions. However the acid-base interactions will dominate, so long as the pH dye molecules can access the surface acid/base functionalities. This effect is called perichromism, as described by Reichardt[10-12]. He states that the spectral properties of a dye are governed by interactions (such as electrostatic, non-electrostatic and hydrogen bonding) between the dye and its surrounding solid surface[10, 13]. When monitoring the chromophore of an adsorbed pH indicator (one that is responsive to Brønsted acidity and to hydrogen bonding), the observed spectrum is still not an absolute measure of the acidity of the environment, because it is influenced by factors such as adsorbed water and surface polarity.

In work reported in this chapter, the ionisation state of PR, TB and MR was studied by diffuse reflectance visible spectroscopy (DRVS) whilst adsorbed on the polymorphs of IMC, CBZ, CFN, FRS and SFN. Drug polymorphs each expose different acid/base functional groups (or a different number of the same functional group) and hence could ionise adsorbed pH indicator dyes to different extents. The mechanisms for differential coloration of adsorbed indicator dyes can be explained based on acid/base properties in solution, and a closer examination of the intermolecular interactions in the crystal structure of the polymorphs. This study provides a new insight at the molecular level for the difference in surface chemistry between drug polymorphs.

5.2 Materials and methods

5.2.1 Materials

Analytical grade acid- base indicators phenol red (PR), thymol blue sodium salt (TB) and methyl red sodium salt (MR) and methanol (99.7%) were purchased from Sigma Aldrich (Gillingham, Dorset). Table 5.1 and Table 5.2 show details of the acid/base character of drug substances and pH indicators used in this study. Details of the high purity (>99%) samples of the model drug compounds indomethacin (IMC), carbamazepine (CBZ), caffeine (CFN), furosemide (FRS) and sulfanilamide (SFN) and solvents used are listed in Table 4.1 (Chapter 4).

Table 5. 1 Details of the pH indicators used in this study.

Indicator	pK_a	Colour, form and λ_{max}[b] of ionisation species
Phenol red (PR)	-0.90 ± 0.30 (Sulphonic acid)	Red PRH_2 506 nm
	7.89 ± 0.10 (Phenolic group)	Yellow PRH^- 434 nm
		Red PR^{2-} 558 nm
Thymol blue (TB)	1.65^a (Sulphonic acid)	Red TBH_2 547 nm
	8.80 ± 0.10 (Phenolic group)	Yellow TBH^- 434 nm
		Blue TB^{2-} 598 nm
Methyl red (MR)	3.66 ± 0.36 (Carboxylic acid)	Red MRH_2^+ 525 nm
	3.28 ± 0.36 (Azonium group)	Red ZMR 550 nm
		Red MRH 490 nm
		Yellow MR^- 429 nm

[a] pKa values were obtained using the ACD/I-Lab Web service (ACD/pKa 12.0). ACD/pK_a 12.0 calculates pKa values in aqueous solutions a t zero ionic strength and 25°C except for pKa_1 of TB which was experimentally determined.

[b] Colour and λ_{max} of the corresponding ionisation species was experimentally determined by preparing buffered indicator solutions at 23°C prepared covering a range from 1-10 pH units using KCl/HCl, $KHC_8H_8O_4$/HCl, KH_2PO_4/NaOH and Na_2HPO_4/NaOH buffers. Vis- absorption spectra of buffered indicator solutions were recorded on a Varian-Cary 100 Bio UV-Vis spectrophotometer (Melbourne, Australia).

Table 5. 2 Acid/base properties of model drug compounds used in this study.

Drug	Aqueous solubilities (g/l, Mol/litre)	pH of sat. aqueous solution	pKa(s) of ionisable group	Strength of ionisable group
Indomethacin (IMC)	0.02 6.1×10^{-5}	4.37	R-COOH (carboxylic acid) 3.96 ± 0.30	Moderate acid
Carbamazepine (CBZ)	0.22 9.4×10^{-4}	7.00	$R\text{-}CONH_2$(amide) 13.94 ± 0.20	Very weak acid
			$\text{-}RCONH_2$ (amide) -0.49 ± 0.20	Extremely weak base
Caffeine (CFN)	58.9 0.3	7.15	R-N=C (imine) 0.52 ± 0.70	Very weak base
			NR_3 (tertiary amine) -3.83 ± 0.20	Extremely weak base
Furosemide (FRS)	0.12 3.9×10^{-4}	3.53	$R\text{-}SONH_2$ (sulfonamide) 9.79 ± 0.60	Very weak acid
			R-COOH (carboxylic acid) 3.04 ± 0.36	Moderate acid
			R_2NH (secondary amine) -2.49 ± 0.36	Extremely weak base
			$R\text{-}SONH_2$ (sulfonamide) -7.72 ± 0.70	Extremely weak base
Sulfanilamide (SFN)	11.1 0.064	6.27	$R\text{-}SONH_2$ (sulfonamide) 10.10 ± 0.10	Very weak acid
			$R\text{-} NH_2$ (primary amine) 1.85 ± 0.10	Very weak base
			$R\text{-}SONH_2$ -7.73 ± 0.70	Extremely weak base

Aqueous solubilities, pH of saturated aqueous solutions and pKa values at 25^oC were obtained using the ACD/I-Lab Web service.

5.2.2 Preparation and characterisation of the polymorphs

The polymorphs of the IMC, CBZ, CFN, SFN and FRS were prepared and characterised by PXRD, DSC and Raman spectroscopy according to procedures detailed in the experimental section of Chapter 4.

5.2.3 Surface area measurement by BET method

The BET (Brunauer, Emmett and Teller) method[14] is based on adsorption of gas on the clean surface of dry solid powders, The amount of gas adsorbed at a given pressure is proportional to the surface area. In a gas sorption experiment, the material is heated and degassed under vacuum or by inert gas purging to remove adsorbed foreign molecules. Controlled doses of an inert gas such as nitrogen are introduced and the gas is adsorbed. The sample material is placed in a vacuum chamber at a constant and very low temperature, usually that of liquid nitrogen (-195.6°C), and subjected to a wide range of pressures, to generate a series of adsorption and desorption isotherms. The amounts of gas molecules adsorbed or desorbed are determined by the pressure variations due to the adsorption or desorption of the gas molecules by the material. Various amounts of gas molecules will be adsorbed or desorbed at different doses of the gas. Knowing the area occupied by one nitrogen molecule, σ (σ= 16.2 $\mathring{A}^2$), and using an adsorption model, the total surface area of the material can be determined.

The most well known and widely used is the BET equation for multilayer adsorption:

$$\frac{P}{n(P_0 - P)} = \frac{1}{cn_m} + \frac{c-1}{cn_m}\frac{P}{P_0} \qquad \text{Eqn 5.1}$$

P is the adsorption pressure, P_O is the saturation vapour pressure, c is the BET constant, representing the amount adsorbed (moles per gram of adsorbent) at the relative pressure P/P_O, n is the quantity of adsorbed gas, and n_m is the monolayer adsorbed gas quantity. Through the slope and intercept of a plot of $P/[n(P_O-P)]$ against (P/P_O), n_m can be determined.

The specific surface area, S, can then be derived:

$$S = N_A \, n_m \, \sigma \qquad\qquad \text{Eqn 5.2}$$

N_A is Avogadro's number and σ is the area occupied by one nitrogen molecule. The specific surface area that can be determined by gas sorption ranges from 0.01 to over 2000 m^2/g. The specific surface area per gram (SSA) of each polymorph was determined by the BET method on a Gemini 2365 from Micromeritics Instrument Corp using nitrogen as the adsorbate. Prior to measurement the samples were evacuated using dry N_2 purging for at least 30 minutes.

5.2.4 Chromogenic treatment and diffuse reflectance visible spectroscopy (DRVS)

Chromogenic treatment by dye deposition was achieved using a 200 mg/L solution. Solutions of the pH dyes were prepared by dissolving in either methanol or a mixture of methanol-water (10%/90% v/v). These were selected so as to minimise dissolution of the drug polymorph during deposition of the dye, and to minimise perturbation of the surface structure. So for solids that are very slightly soluble or practically insoluble[15] in water eg. IMC, FRS and CBZ (aqueous solubility values are 0.02, 0.12 and 0.22 g/L, respectively at 25ºC) the methanol-water mixture was employed. The methanol solution was used for SFN and CFN polymorphs which are sparingly/slightly soluble[15] in water (aqueous solubility values are 11.1 and 58.9 g/L respectively at 25 ºC).

The typical amount of dye adsorbed per gram of solid polymorph was 0.1mg. This amount of dye was selected as it corresponded to the limit of detection of adsorbed dye by the DRVS instrument for most of the investigated polymorphic systems (see Chapter 3 section 3.6.2.1). The surfaces of the polymorphs were loaded with the same weight of dye, hence different molar loadings for PR, TB and MR of 0.28µmol/g, 0.20µmol/g and 0.34µmol/g respectively. Dye loading was achieved for most polymorphs by drop-wise addition of 1ml of dye solution directly unto 2 g of solid, carefully mixing using a spatula and drying the solid.

The method of drying varied from polymorph to polymorph. FRS and IMC samples were air-dried or oven dried as they do not form hydrates. CBZ polymorphs were always oven dried as air-dried samples sometimes contained hydrated forms. SFN-β was always air-dried as oven-drying sometimes introduced SFN-γ impurities. CFN-I and CFN-II were dried at 170ºC and 100ºC, respectively to minimise polymorphic impurities.

For SFN-γ, dye deposition was achieved by heating dye treated SFN-β at the temperature of 125ºC for 30 minutes. This heat-induced transformation method is suitable for SFN-γ because it is prone to solvent-induced polymorphic transformation to SFN-β. Heating at this temperature should have no effect on dye because of their high thermal stability (decomposition temperature for PR and TB is >270ºC). Dye treated CBZ-I was also prepared by heat-induced transformation from dye treated CBZ-III at 170ºC for 60 minutes. Direct solvent-deposition untreated CBZ-I and heat-induced transformation gave similar results.

DRVS spectra of samples were collected using an Agilent UV/Vis spectrophotometer. The spectrometer was coupled to a diffuse reflectance accessory Labsphere RSA-HP-8453 having an integrating sphere. The data acquisition time was 5 seconds per spectrum. Each spectrum was analysed as a plot of Kubelka-Munk (KM) units versus wavelength (nm). KM transformation accounts for the influence of scattered light from the powdered samples, as discussed in Chapter 3. Spectra were smoothed using a 20-point adjacent averaging algorithm and first derivative spectra were calculated to facilitate assignment of peak maxima. Polymorphs with no adsorbed dye served as blank for DRVS measurement.

The effects of relative humidity on the DRV spectra were evaluated using IMC, CBZ and SFN polymorphs. Dye-treated samples were placed in desiccators for 7 days under controlled RH conditions of 11% and 43% at room temperature (23.5ºC) using LiCl and K_2CO_3 saturated solutions, respectively. Storage at the different RHs showed minimal effect on DRVS measurement. Polymorphic samples are non-hygroscopic, adsorbing less that 0.2% water even at 77% RH.

5.2.5 Characterisation of dye-treated polymorphs

The pure and dye-treated polymorphs were analysed to ensure that polymorphic integrity or crystalline structure remained intact after chromogenic treatment. The analytical techniques of PXRD and DSC were employed. The instrumental conditions for analysis are given in the Chapter 3 sections 3.1.2 and 3.2.1, respectively.

5.3 Results and discussion

5.3.1 Characterisation of polymorphic samples

PXRD patterns for IMC-α chromogenically treated with PR, TB and MR have been compared to the untreated polymorph (Fig 5.3) The diagnostic peaks for IMC-α; 8.44, 11.86, 13.90, 14.18, 14.50, 17.56, 18.06, 18.46 and 22.04 $^{O}2\theta$ were examined after dye treatment. Variation of no more than ±0.2˚ was observed after chromogenic treatment, thus proving that polymorphic integrity had been maintained. Peak intensities varied as expected because of the preferred orientation of the samples, but by no more than ±14% relative intensity.
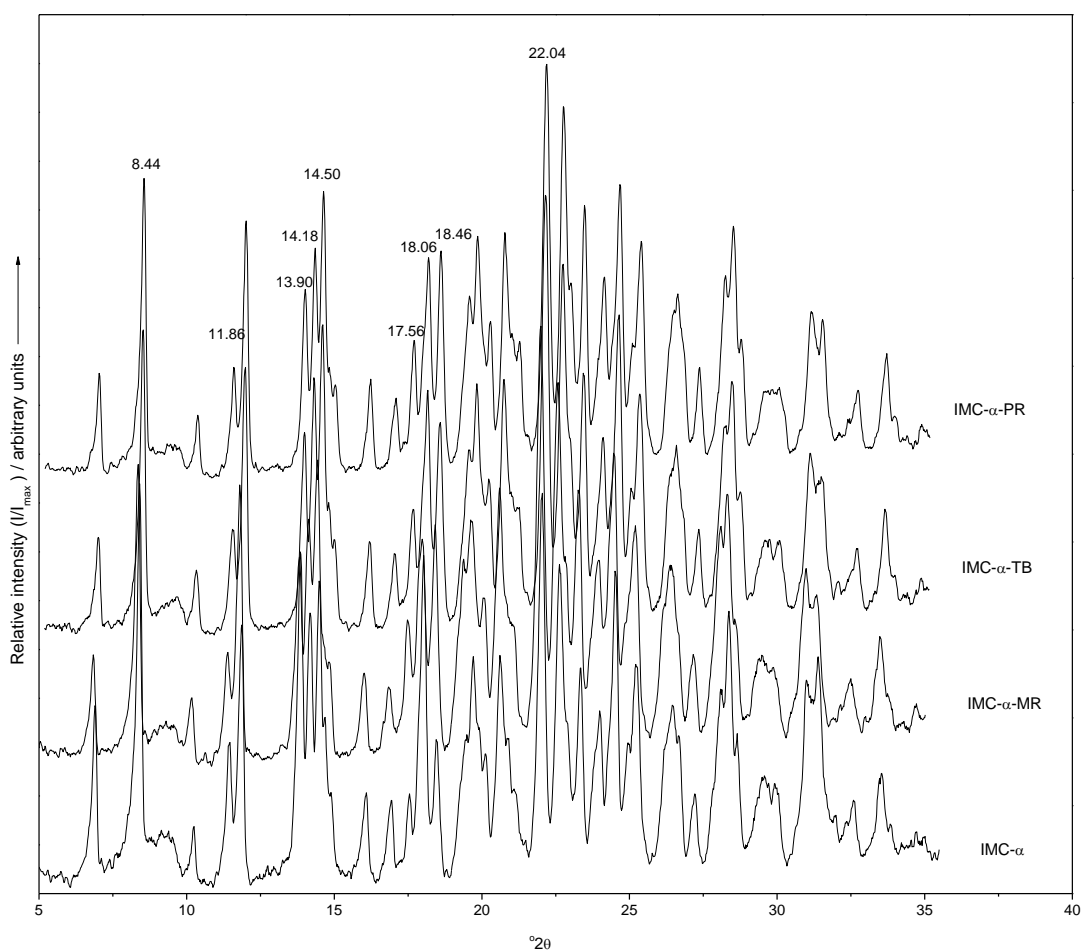
Figure 5.3 PXRD patterns for IMC-α chromogenically treated with PR, TB and MR.

DSC thermograms of IMC-α chromogenically treated with PR, TB and MR have been compared to the untreated polymorph (Fig 5.4). For all thermograms, a single endothermic peak is observed attributed to melting. The onset temperature (T_f) and enthalpy of fusion ΔH_f values are:

$T_f = 152.5 \pm 0.2$ºC and $\Delta H_f = 93.2 \pm 2.8$ Jg^{-1};

$T_f = 151.8 \pm 0.5$ºC and $\Delta H_f = 105.0 \pm 1.0$ Jg^{-1};

$T_f = 151.6 \pm 0.2$ºC and $\Delta H_f = 106.0 \pm 1.0$ Jg^{-1} and

$T_f = 151.9 \pm 0.5$ºC and $\Delta H_f = 105.0 \pm 1.0$ Jg^{-1},

for IMC-α, IMC-α-MR, IMC-α-TB and IMC-α-PR respectively.
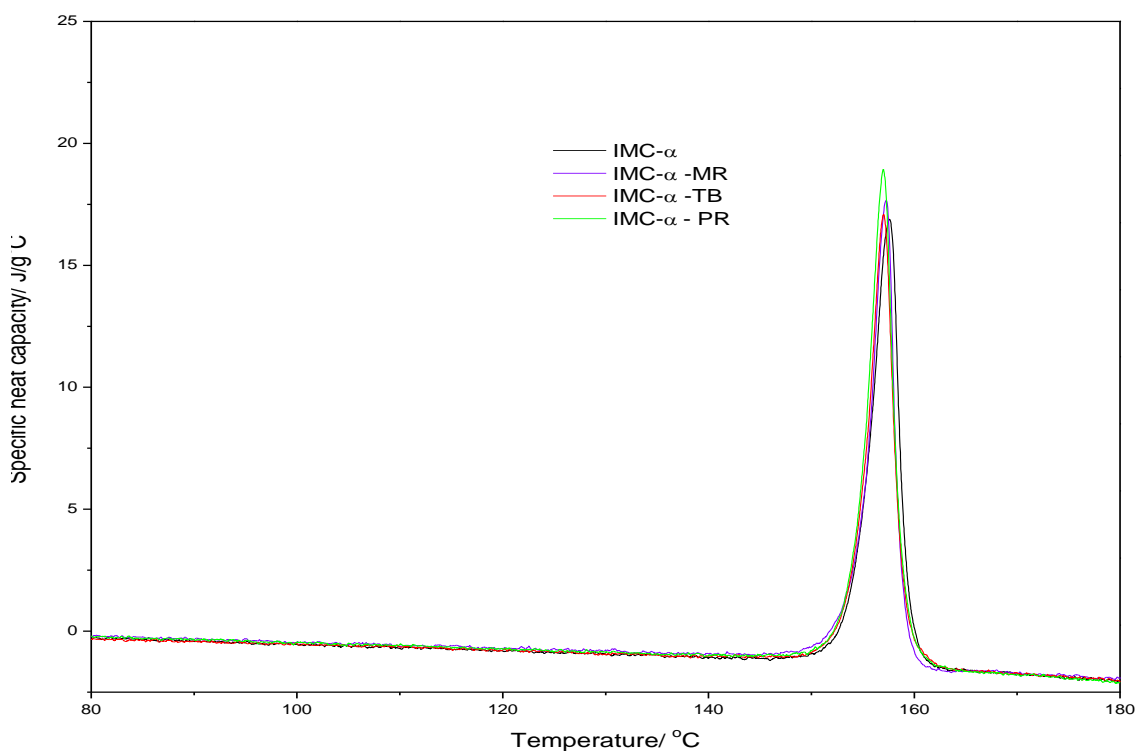
Figure 5.4 DSC thermograms of IMC-α chromogenically treated with PR, TB and MR

PXRD patterns for the IMC-γ chromogenically treated with PR, TB and MR have been compared to the untreated polymorph (Fig 5.5). The diagnostic peaks for IMC-γ; 11.63, 16.71, 17.02, 18.55, 19.62, 20.87, 21.81 and 26.61 $^O2\theta$ were examined after treatment, and variation of no more than ±0.1° was observed after chromogenic treatment. Peak intensities varied more significantly, as expected because of the preferred orientation of the samples.

Figure 5.5 PXRD patterns of IMC-γ samples; untreated and dye-treated polymorphs.

DSC thermograms of IMC-γ chromogenically treated with PR, TB and MR have been compared to the untreated polymorph (Fig 5.6). Untreated and dye-treated polymorphs show similar thermal behaviour. For all thermograms, a single endothermic peak is observed and is attributed to melting. The onset temperature (T_f) and enthalpy of fusion ΔH_f values are:

$T_f = 159.1 \pm 0.5 \text{°C}$ and $\Delta H_f = 109.0 \pm 3.9 \text{ Jg}^{-1}$;

$T_f = 158.2 \pm 0.5 \text{°C}$ and $\Delta H_f = 110.0 \pm 1.0 \text{ Jg}^{-1}$;

$T_f = 158.9 \pm 0.2 \text{°C}$ and $\Delta H_f = 106.0 \pm 1.0 \text{ Jg}^{-1}$; and

$T_f = 158.5 \pm 0.5 \text{°C}$ and $\Delta H_f = 117.0 \pm 0.5 \text{ Jg}^{-1}$

for IMC-γ, IMC-γ-MR, IMC-γ-TB and IMC-γ-PR, respectively.

Figure 5.6 DSC thermograms of IMC-γ samples; untreated and dye-treated polymorphs.

PXRD patterns for the CBZ-I chromogenically treated with PR, TB and MR has been compared to the untreated polymorph (Fig 5.7). The diagnostic peaks for CBZ-I; 5.55, 6.11, 7.92, 8.61, 9.36, 12.25 and 19.99 $^{O}2\theta$ were examined after treatment, and as seen for IMC-α, variation of no more than ±0.2° was observed after chromogenic treatment. Peak intensities varied as expected because of the preferred orientation of the samples.

Figure 5. 7 PXRD patterns of CBZ-I samples; untreated and dye-treated polymorphs.

DSC thermograms of CBZ-I chromogenically treated with PR, TB and MR have been compared to the untreated polymorph (Fig 5.8). Untreated and dye-treated polymorphs show similar thermal behaviour. For all thermograms, a single endothermic peak is observed attributed to melting. The onset temperature (T_f) and enthalpy of fusion ΔH_f values are:

$T_f = 187.8 \pm 0.1$°C and $\Delta H_f = 97.3 \pm 2.6$ Jg^{-1};

$T_f = 187.7 \pm 0.1$°C and $\Delta H_f = 102.0 \pm 1.0$ Jg^{-1};

$T_f = 188.6 \pm 0.1$°C and $\Delta H_f = 90.4 \pm 1.0$ Jg^{-1},

$T_f = 188.0 \pm 0.2$°C and $\Delta H_f = 114.0 \pm 1.0$Jg^{-1}

for CBZ-I, CBZ-I-MR, CBZ-I-TB and CBZ-I-PR respectively.
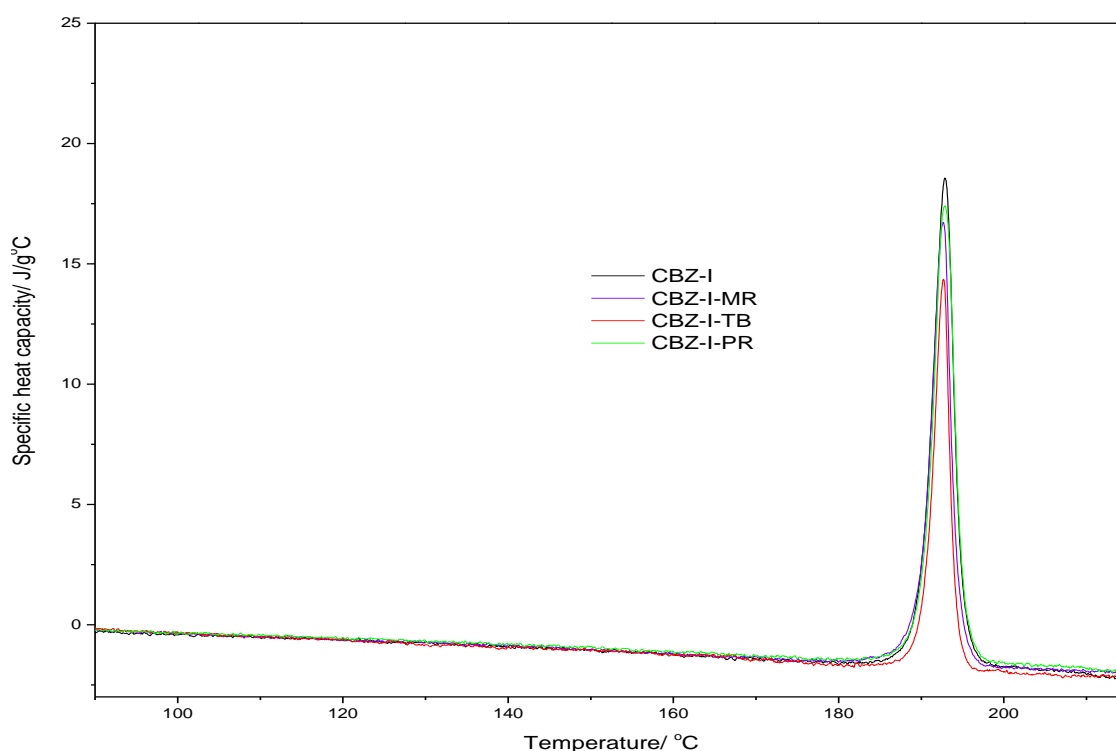
Figure 5.8 DSC thermograms of CBZ-I samples; untreated and dye-treated polymorphs.

PXRD patterns for the CBZ-III chromogenically treated with PR, TB and MR have been compared to the untreated polymorph (Fig 5.9). The diagnostic peaks for CBZ-III; 13.03, 15.00, 15.28, 15.81, 19.46, 24.95 and 27.30 $^{O}2\theta$ were examined after chromogenic treatment, and variation of no more than $\pm0.2°$ was observed. Peak intensities varied by more than $\pm15\%$ intensity because of the preferred orientation of the samples.
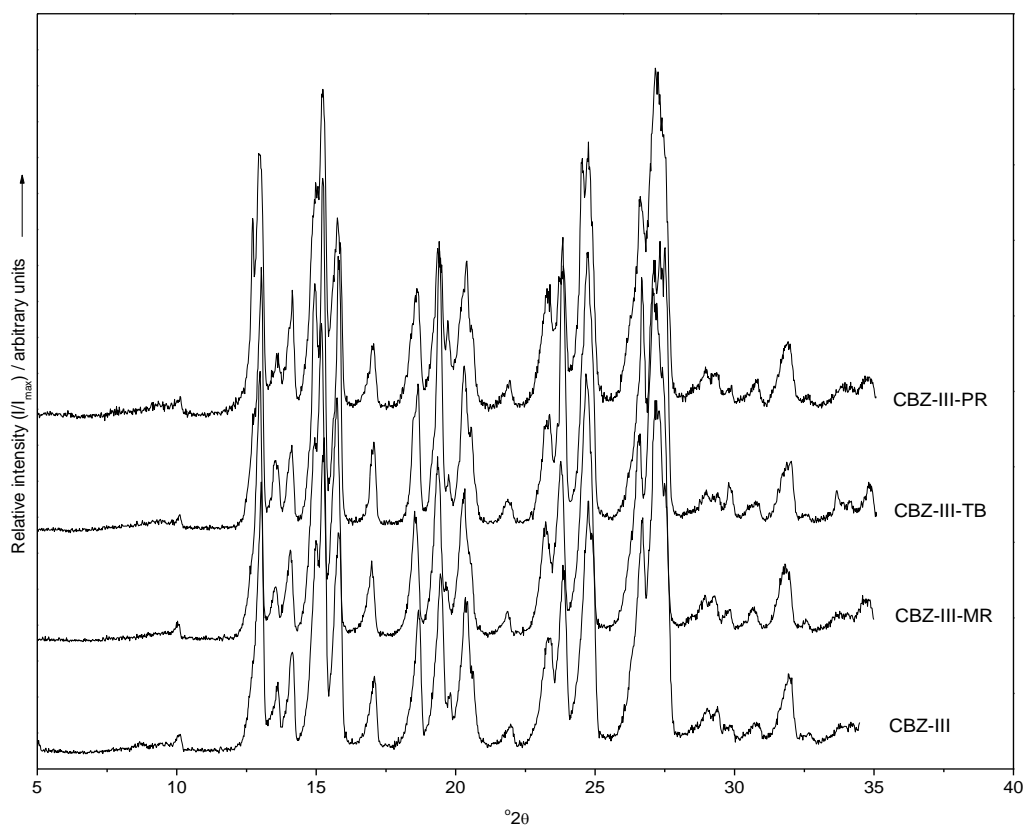
Figure 5. 9 PXRD patterns of CBZ-III samples; untreated and dye-treated polymorphs.

DSC thermograms of CBZ-III chromogenically treated with PR, TB and MR have been compared to the untreated polymorph (Fig 5.10). For all thermograms, two thermal events are evident. The first event is the transformation of III→I and the second event is the subsequent melting of CBZ-I. The onset temperature of the III→I transformation decreased in all dye-treated samples.

Sample	First thermal event	Second thermal event
CBZ-III	$T_f = 165.0 \pm 0.9°C$ $\Delta H_f = 13.1 \pm 0.2$ Jg^{-1}	$T_f = 188.4 \pm 0.2°C$ $\Delta H_f = 110.0 \pm 3.6$ Jg^{-1}
CBZ-III-MR	$T_f = 160.4 \pm 0.5°C$ $\Delta H_f = 12.1 \pm 1.0$ Jg^{-1}	$T_f = 188.7 \pm 0.5°C$ $\Delta H_f = 120.0 \pm 2.0$ Jg^{-1}
CBZ-III-TB	$T_f = 158.6 \pm 0.5°C$ $\Delta H_f = 9.5 \pm 1.0$ Jg^{-1}	$T_f = 188.5 \pm 0.3°C$ $\Delta H_f = 83.2 \pm 1.5$ Jg^{-1}
CBZ-III-PR	$T_f = 162.7 \pm 0.5°C$ $\Delta H_f = 11.9 \pm 0.5$ Jg^{-1}	$T_f = 187.9 \pm 0.5°C$ $\Delta H_f = 116 \pm 1.0$ Jg^{-1}

Figure 5. 10 DSC thermograms of CBZ-III samples; untreated and dye-treated polymorphs.

PXRD patterns for the CFN-I chromogenically treated with PR, TB and MR have been compared to the untreated polymorph (Fig 5.11). The diagnostic peaks for CFN-I; 11.74, 23.70 and 26.52 $^O2\theta$ were examined after treatment. A variation of no more than ±0.05˚ was observed after chromogenic treatment. Peak intensities varied as expected because of the preferred orientation of the samples. PXRD patterns for the
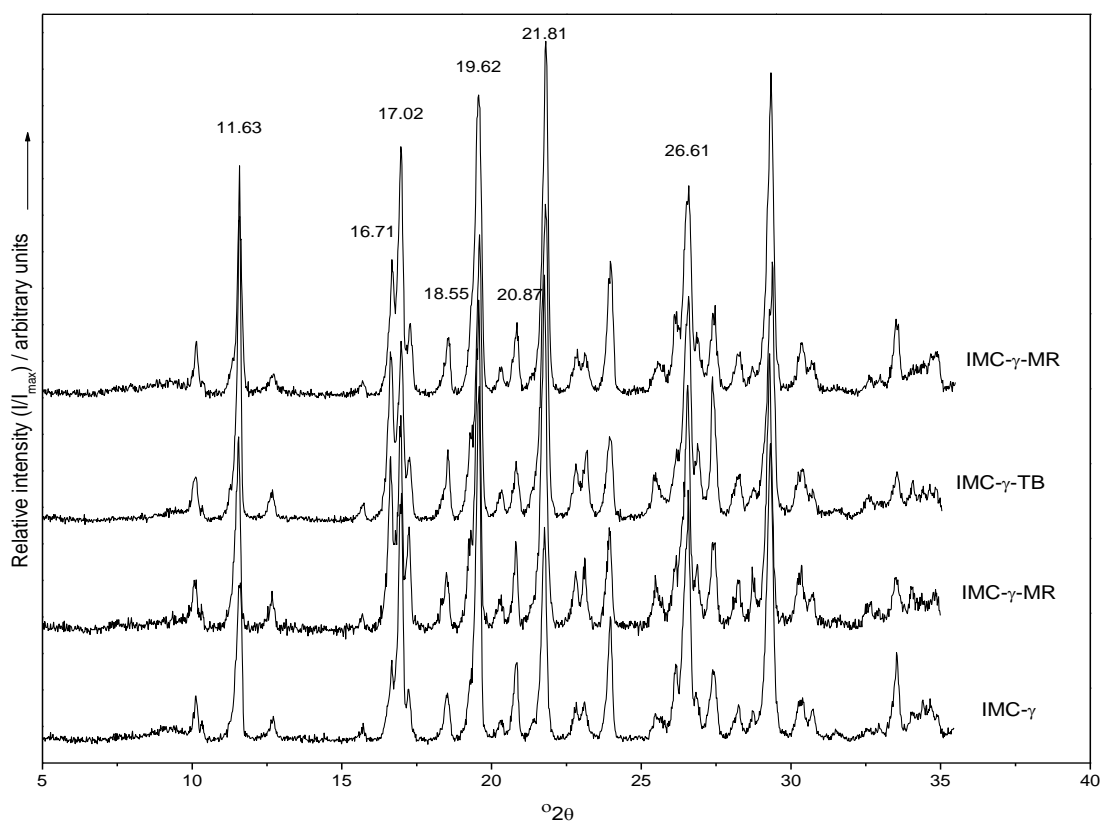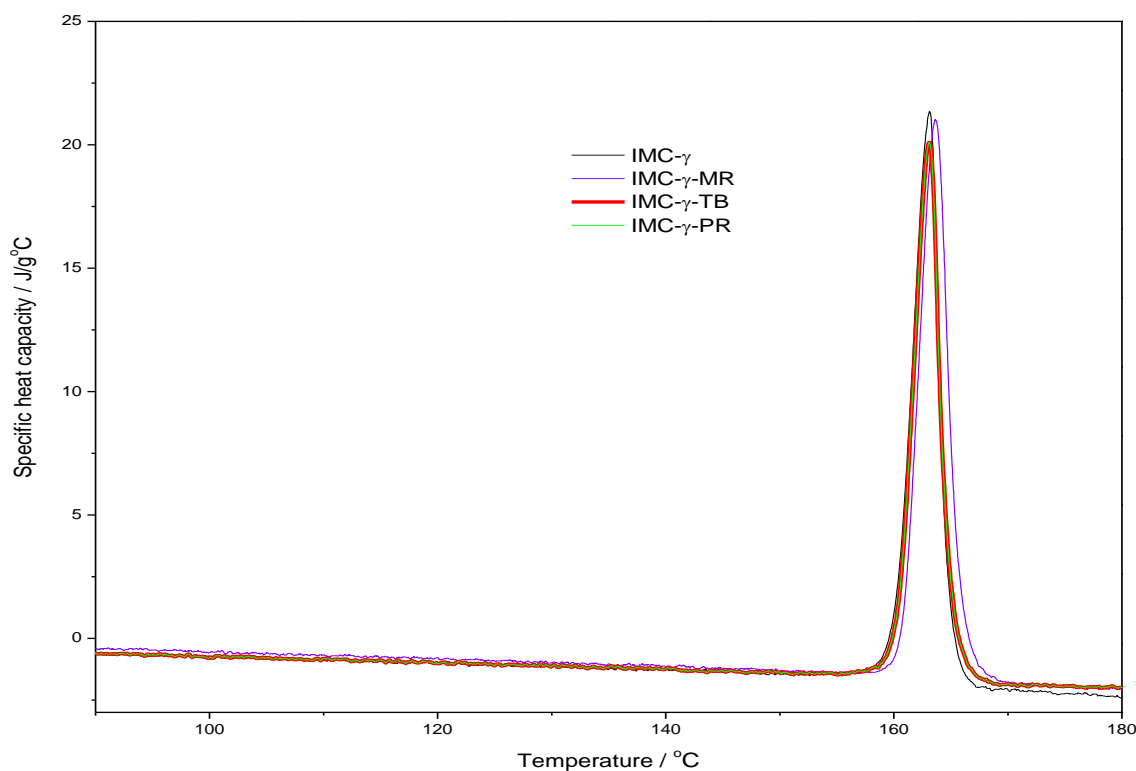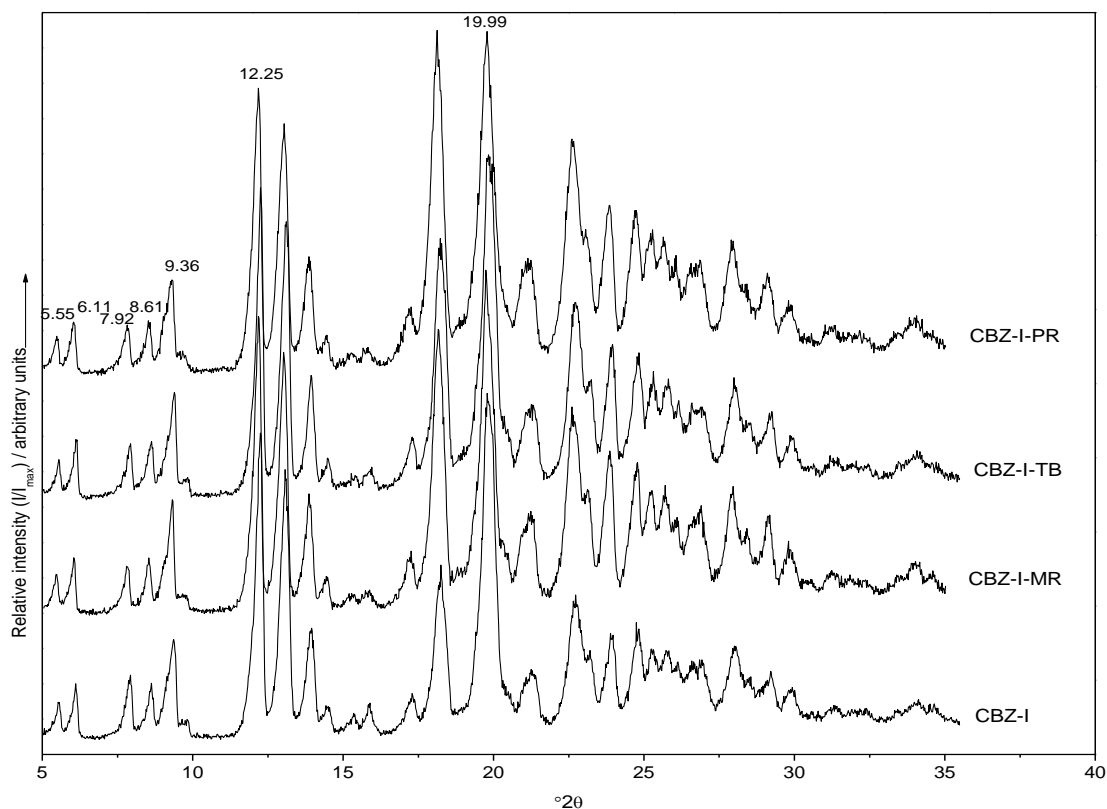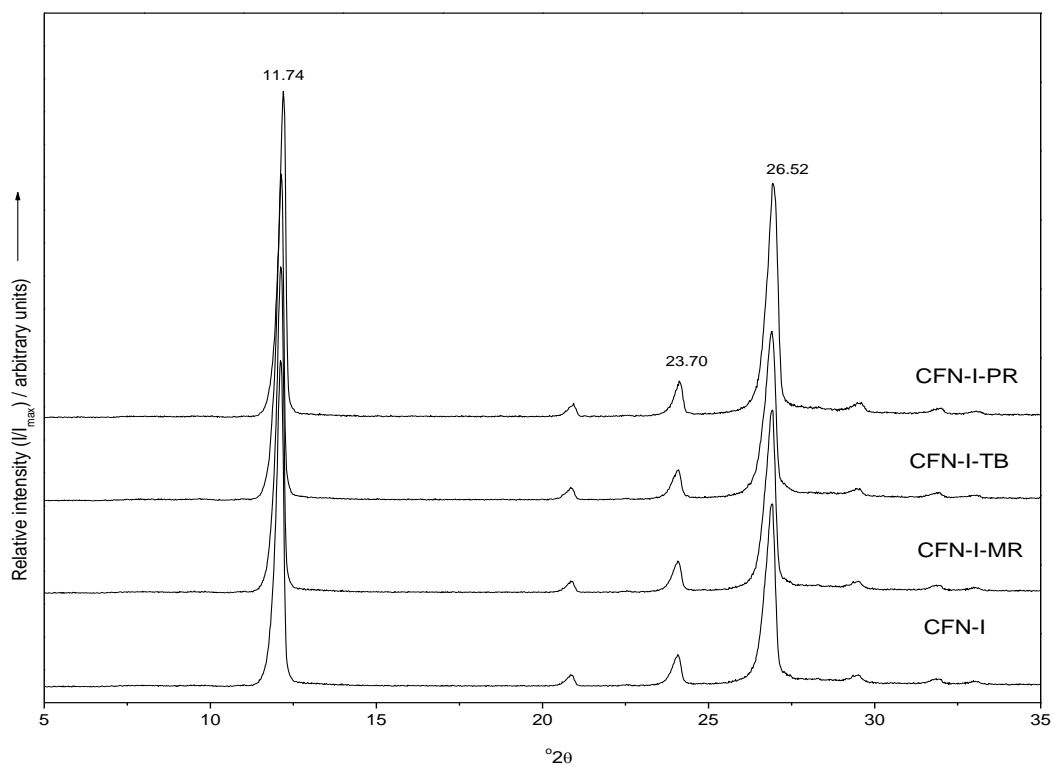

Figure 5. 1 PXRD patterns of CFN-I samples; untreated and dye-treated polymorphs.

For all thermograms for CFN-I samples (Fig 5.12), a single endothermic peak is observed attributed to melting (fusion). The onset temperature (T_f) and enthalpy of fusion ΔH_f values are:

T_f =234.1±0.1ºC and ΔH_f =110.3±4.5 Jg^{-1};

T_f =233.9±0.5ºC and ΔH_f =115.0±1.0 Jg^{-1};

T_f =232.7±0.5ºC and ΔH_f =114.0±1.0 Jg^{-1},

T_f =233.6±0.5ºC and ΔH_f =116.0±1.0 Jg^{-1}

for CFN-I, CFN-I-MR, CFN-I-TB and CFN-I-PR, respectively.
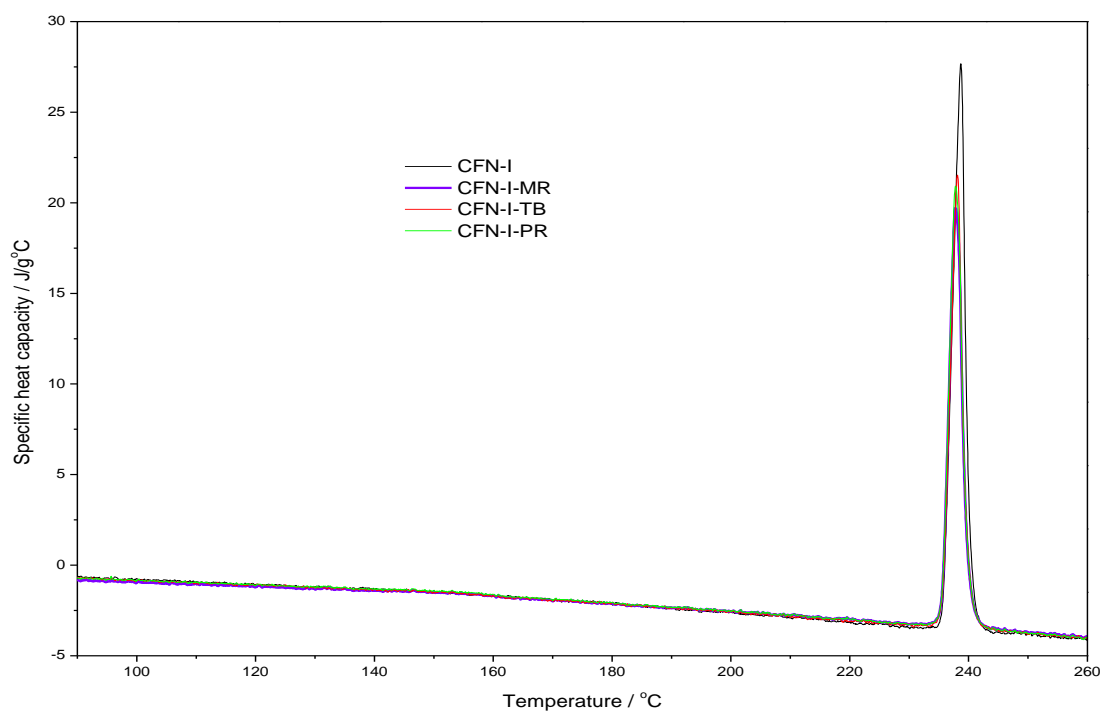
Figure 5. 12 DSC thermograms of CFN-I samples; untreated and dye-treated polymorphs.

CFN-II chromogenically treated with PR, TB and MR have been compared to the untreated polymorph (Fig 5.13).

A variation of $\pm 0.6°$ was observed for CFN-II diagnostic peaks (11.85, 26.90 and 28.29 $°2\theta$) after treatment. Peak intensities varied because of the preferred orientation of the samples.
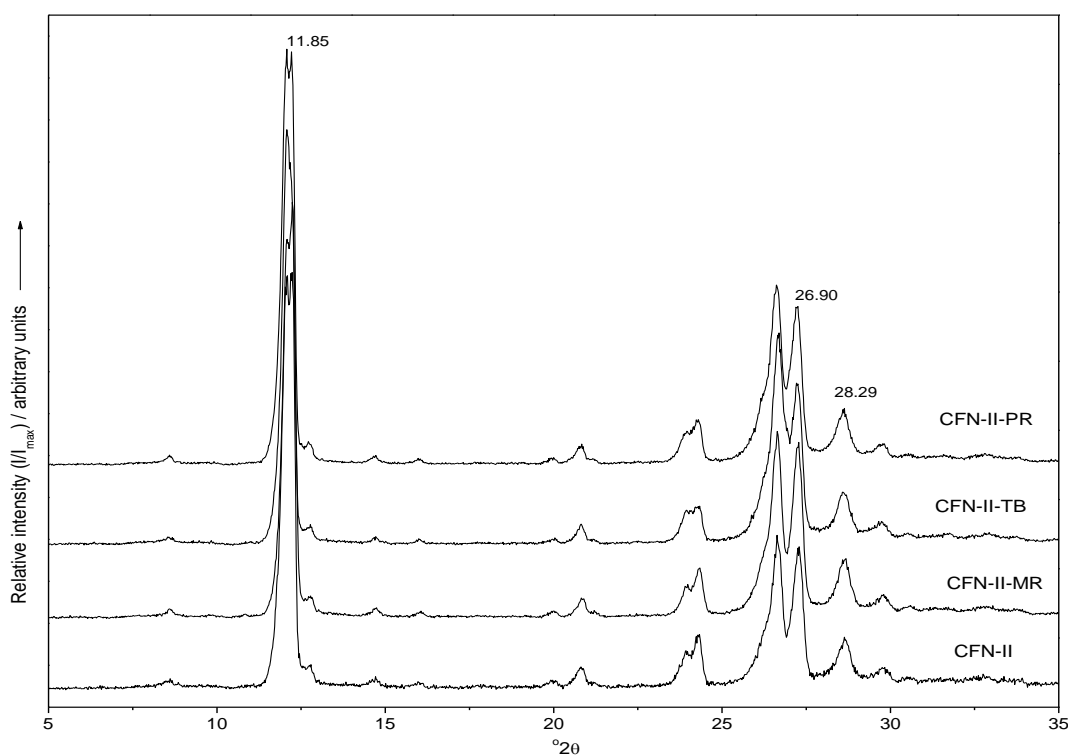
Figure 5. 13 PXRD patterns of CFN-II samples; untreated and dye-treated polymorphs.

DSC thermograms of CFN-II chromogenically treated with PR, TB and MR have been compared to the untreated polymorph (Fig 5.14). For all thermograms, two endothermic thermal events are evident. The first event is the II→I transformation via sublimation and the second event is the subsequent melting of CFN-I. In contrast to the thermal behaviour of CBZ-III, the shape and onset of the 1st endotherm is not significantly affected by the dyes.

| Sample	First thermal event	Second thermal event
CFN-II	$T_f = 148.4 \pm 0.3$ºC $\Delta H_f = 21.3 \pm 0.4$ Jg^{-1}	$T_f = 233.8 \pm 0.1$ºC $\Delta H_f = 112.0 \pm 2.0$ Jg^{-1}
CFN-II-MR	$T_f = 145.1 \pm 0.5$ºC $\Delta H_f = 18.1 \pm 1.0$ Jg^{-1}	$T_f = 233.6 \pm 0.5$ºC $\Delta H_f = 117.0 \pm 1.0$ Jg^{-1}
CFN-II-TB	$T_f = 147.7 \pm 0.5$ºC $\Delta H_f = 19.9 \pm 1$ Jg^{-1}	$T_f = 232.9 \pm 0.5$ºC $\Delta H_f = 112.0 \pm 1.2$ Jg^{-1}
CFN-II-PR	$T_f = 145.0 \pm 0.5$ºC $\Delta H_f = 19.9 \pm 1$ Jg^{-1}	$T_f = 233.3 \pm 0.4$ºC $\Delta H_f = 127 \pm 1.0$ Jg^{-1}
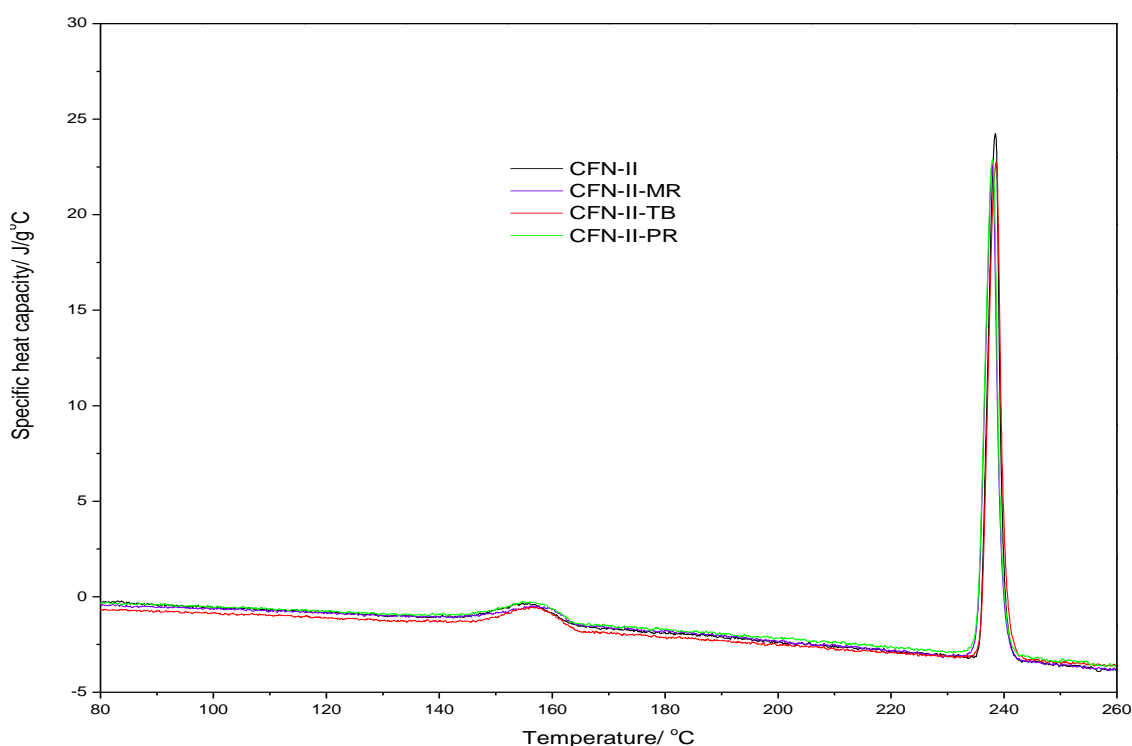
Figure 5. 14 DSC thermograms of CFN-II samples; untreated and dye-treated polymorphs.

PXRD patterns for FRS-I chromogenically treated with PR, TB and MR has been compared to the untreated polymorph (Fig 5.15). Peaks at $^{\circ}2\theta$ values of; 6.10, 18.87, 20.63, 21.47 and 24.88 agreed within $\pm 0.15^{\circ}$ of untreated data. Peak intensities varied more significantly due to preferred orientation of samples.

Figure 5. 15 PXRD patterns of FRS-I samples; untreated and dye-treated polymorphs.

DSC thermograms of FRS-I chromogenically treated with PR, TB and MR have been compared to the untreated polymorph (Fig 5.16).

Three main events occur, polymorphic transformation, melting followed immediately by an intense exothermic peak attributable to decomposition. The polymorphic transformation is a weak endotherm

$T_f = 128.4 \pm 0.8^{\circ}$C, and $\Delta H_f = 3.7 \pm 1.0$ Jg^{-1},

$T_f = 131.4 \pm 0.8^{\circ}$C, and $\Delta H_f = 2.9 \pm 1.0$ Jg^{-1}

$T_f = 130.1 \pm 0.7^{\circ}$C and $\Delta H_f = 3.6 \pm 1.0$ Jg^{-1};

$T_f = 126.8 \pm 0.8^{\circ}$C, and $\Delta H_f = 3.8 \pm 1.0$ Jg^{-1}

or FRS-I, FRS-I-MR, FRS-I-TB and FRS-I-PR, respectively.

The weak melting endotherm is discernable for FRS-I (207.3±0.7 $^{\circ}$C) and FRS-I-MR (208.0±0.5 $^{\circ}$C) and not for FRS-I-TB and FRS-I-PR FRS-I-TB and FRS-I-PR. However the onset of decomposition is more accurately determined as 205.9±0.5 $^{\circ}$C and 204.9±0.5 $^{\circ}$C for FRS-I-TB and FRS-I-PR, respectively.
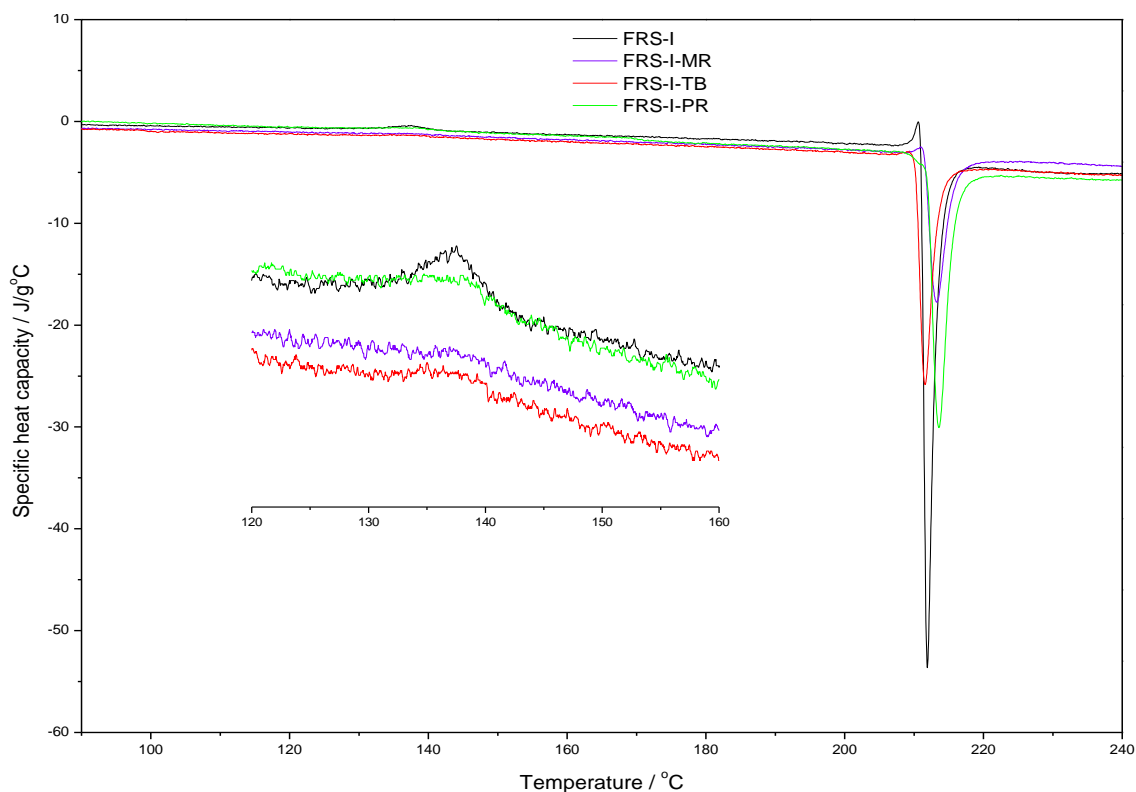
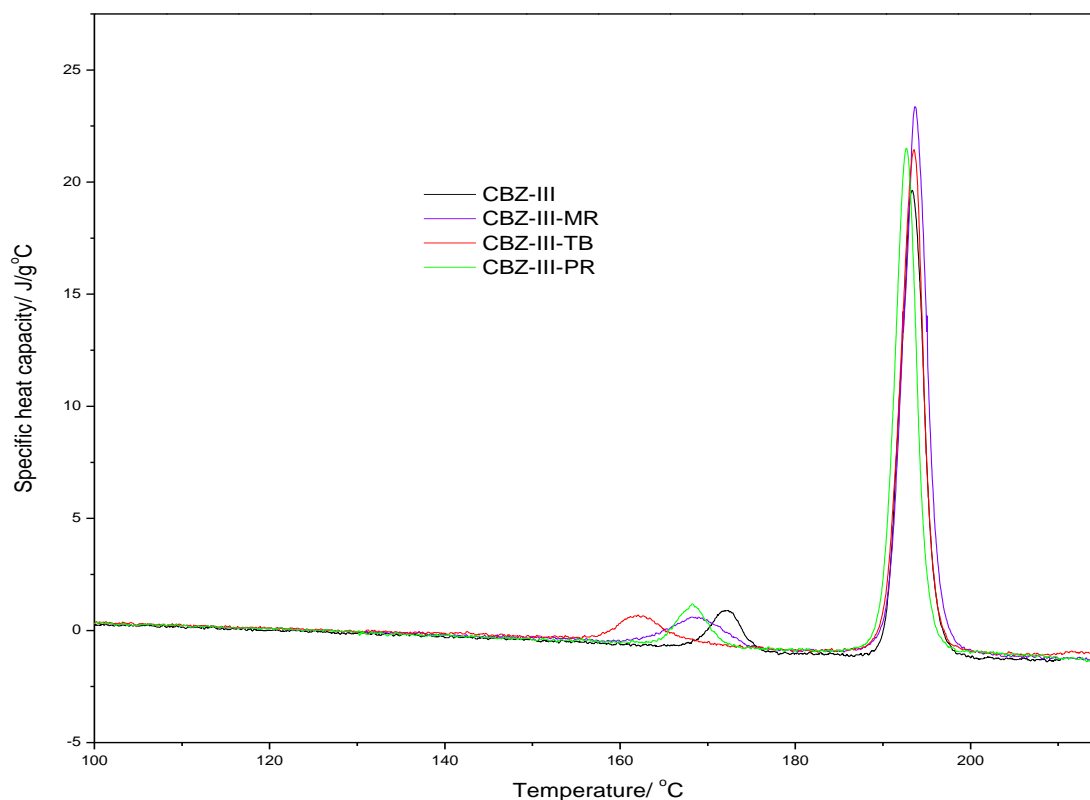**Figure 5. 16** DSC thermograms of FRS-I samples; untreated and dye-treated polymorphs.

PXRD patterns for FRS-II chromogenically treated with PR, TB and MR have been compared to the untreated polymorph (Fig 5.17). Peaks at °2θ values of; 6.44, 11.88, 17.09, 19.60, 19.81 and 29.28 agreed within ± 0.15° of untreated data. Peak intensities varied more significantly due to preferred orientation of samples.
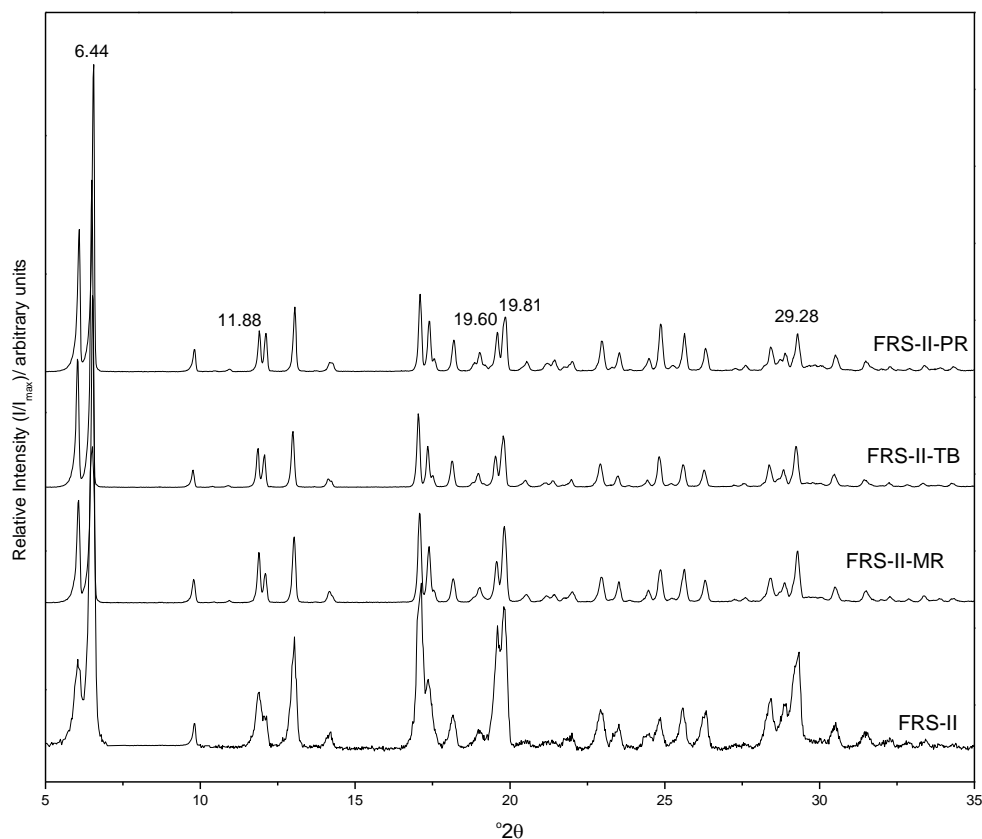
Figure 5. 17 PXRD patterns of FRS-II samples; untreated and dye-treated polymorphs.

DSC thermograms of FRS-II samples are shown in Fig 5.18. Similarly to FRS-I, the FRS-II samples show three thermal events. The polymorphic transformation is a weak endotherm

T_f =126.8 ±0.7°C, and ΔH_f =4.9±1.0 Jg^{-1},

T_f =127.2±0.5°C, and ΔH_f =3.9±1.0 Jg^{-1}

T_f =125.8±0.5°C and ΔH_f = 3.9±1.0 Jg^{-1};

T_f =128.9 ±0.5°C, and ΔH_f =3.8±1.0 Jg^{-1}

for FRS-II, FRS-II-MR, FRS-II-TB and FRS-II-PR, respectively.

The weak melting endotherm is discernable for FRS-I (210.9±0.7 $^\circ$C) and FRS-II-MR (206.2±0.5 $^\circ$C) and not for FRS-I-TB and FRS-I-PR FRS-I-TB and FRS-I-PR. However the onset of decomposition is more accurately determined as 205.1±0.5 $^\circ$C and 205.4±0.5 $^\circ$C for FRS-II-TB and FRS-II-PR respectively.
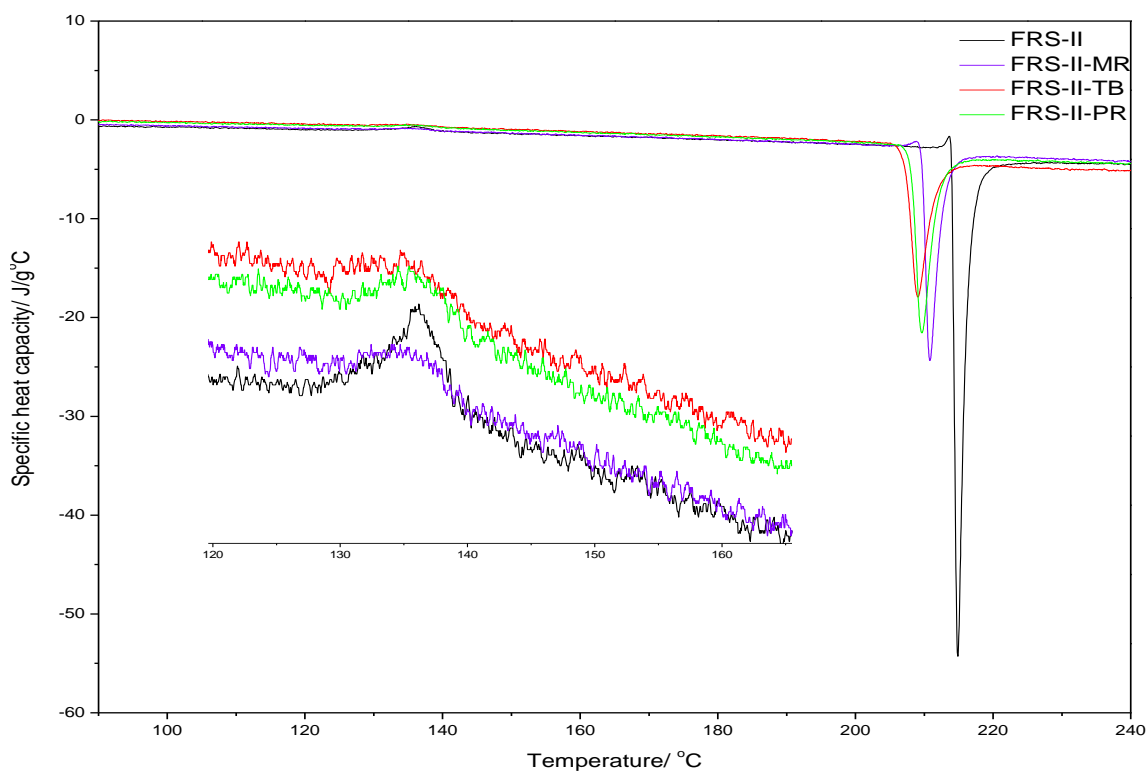
Figure 5.18 DSC thermograms of FRS-II samples; untreated and dye-treated polymorphs

PXRD patterns for SFN-β chromogenically treated with PR, TB and MR have been compared to the untreated polymorph (Fig 5.19). Peaks at °2θ values of 10.55, 14.43, 20.57, 21.24 and 22.72 agreed within ± 0.20° of untreated data. Peak intensities varied more significantly due to preferred orientation of samples.
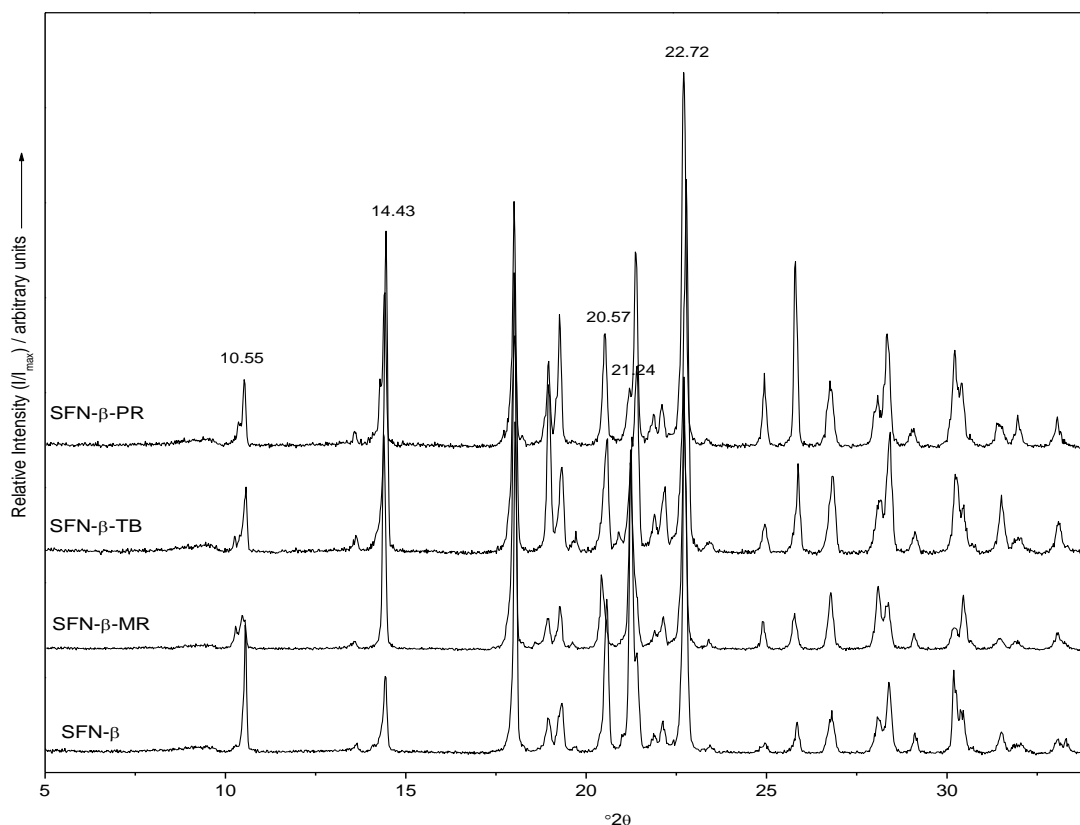
Figure 5. 19 PXRD patterns of SFN-β samples; untreated and dye-treated polymorphs.

DSC thermograms of SFN-β samples are shown in Fig 5.20.

Three endothermic transitions $T_f = 128.3 \pm 1.3\,^{\circ}\text{C}$; $\Delta H_f = 6.9 \pm 3.0$ Jg^{-1}, $T_f = 156.0 \pm 1.3\,^{\circ}\text{C}$; $\Delta H_f = 1.33 \pm 0.5$ Jg^{-1} and $T_f = 162.3 \pm 0.3\,^{\circ}\text{C}$; $\Delta H_f = 121.0 \pm 3.5$ Jg^{-1} were observed for SFN-β attributable to incomplete β →γ transformation, melting of residual SFN-β and melting of SFN-γ, respectively.

Chromogenically treated samples show only two events i.e. the β → γ and the melting of SFN-γ.

| Sample	β → γ	melting of SFN-γ.
SFN-β-MR	$T_f = 112.7 \pm 0.5\,^{\circ}\text{C}$ $\Delta H_f = 10.7 \pm 0.2$ Jg^{-1}	$T_f = 163.4 \pm 0.2\,^{\circ}\text{C}$ $\Delta H_f = 140 \pm 1.0$ Jg^{-1}
SFN-β-TB	$T_f = 129.0 \pm 0.5\,^{\circ}\text{C}$ $\Delta H_f = 9.6 \pm 1.0$ Jg^{-1}	$T_f = 162.4 \pm 0.5\,^{\circ}\text{C}$ $\Delta H_f = 143 \pm 1.0$ Jg^{-1}
SFN-β-PR	$T_f = 112.5 \pm 0.5\,^{\circ}\text{C}$ $\Delta H_f = 8.0 \pm 1.0$ Jg^{-1}	$T_f = 163.3 \pm 0.3\,^{\circ}\text{C}$ $\Delta H_f = 131.0 \pm 1.0$ Jg^{-1}
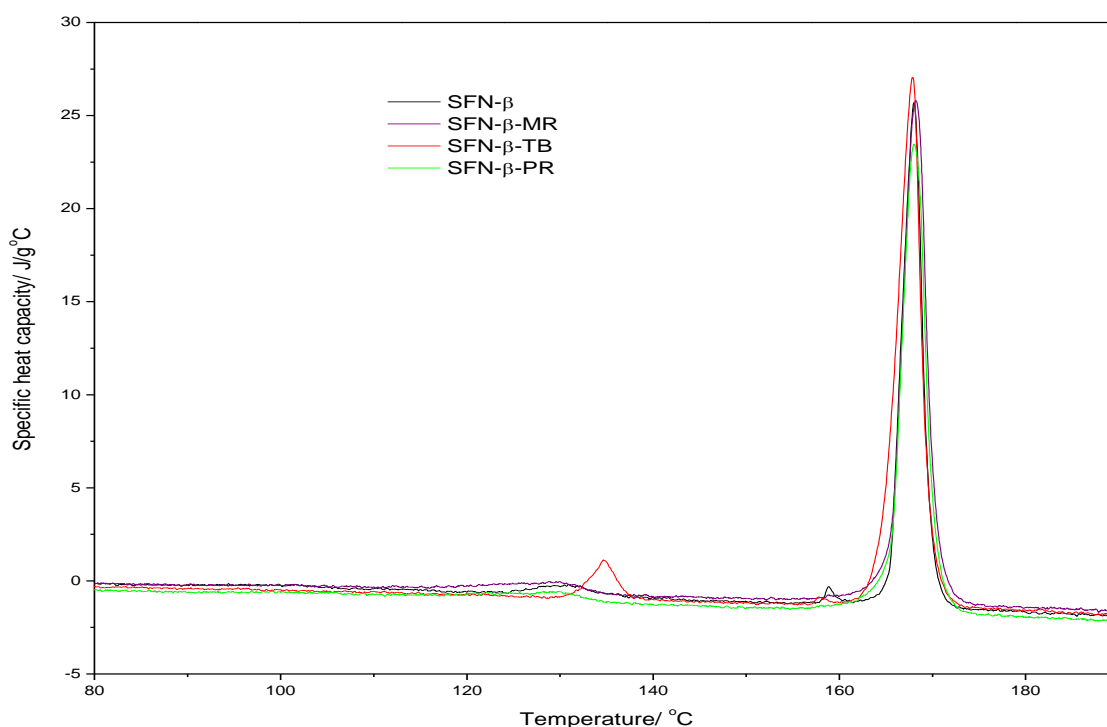
Figure 5.20 DSC thermograms of SFN-β samples; untreated and dye-treated polymorphs.

PXRD patterns for SFN-γ chromogenically treated with PR, TB and MR have been compared to the untreated polymorph (Fig 5.21). Peaks at °2θ values of 11.55, 13.43, 19.69, 24.25 and 29.36 agreed within ± 0.20° of untreated data. Peak intensities varied more significantly due to preferred orientation of samples.

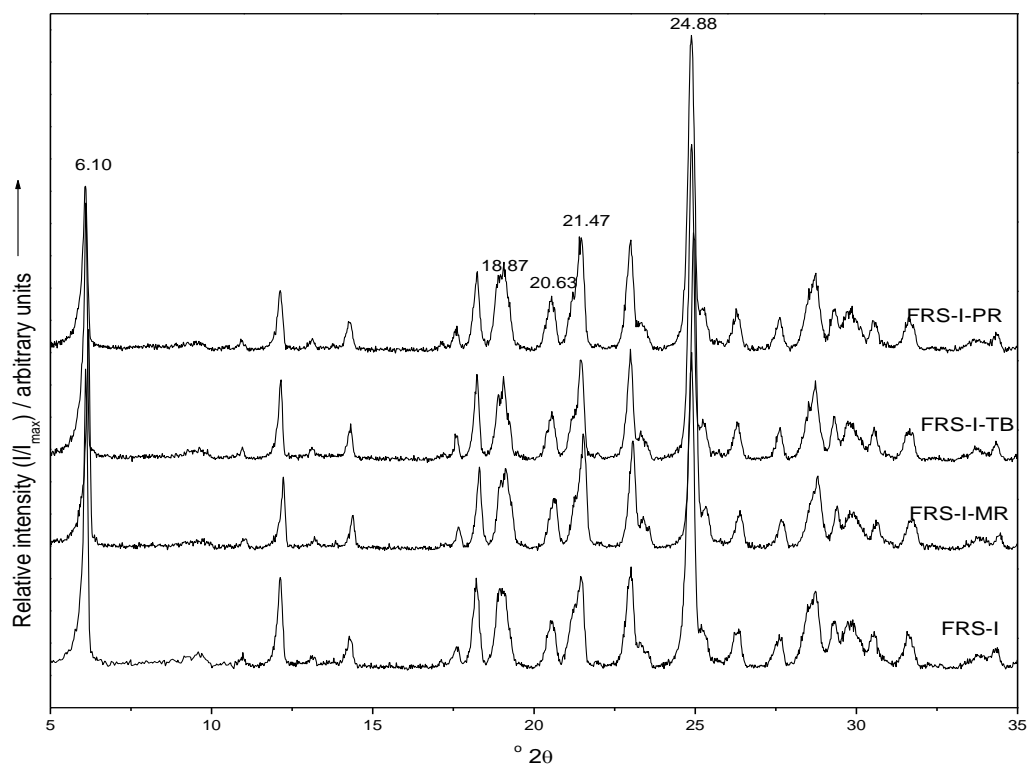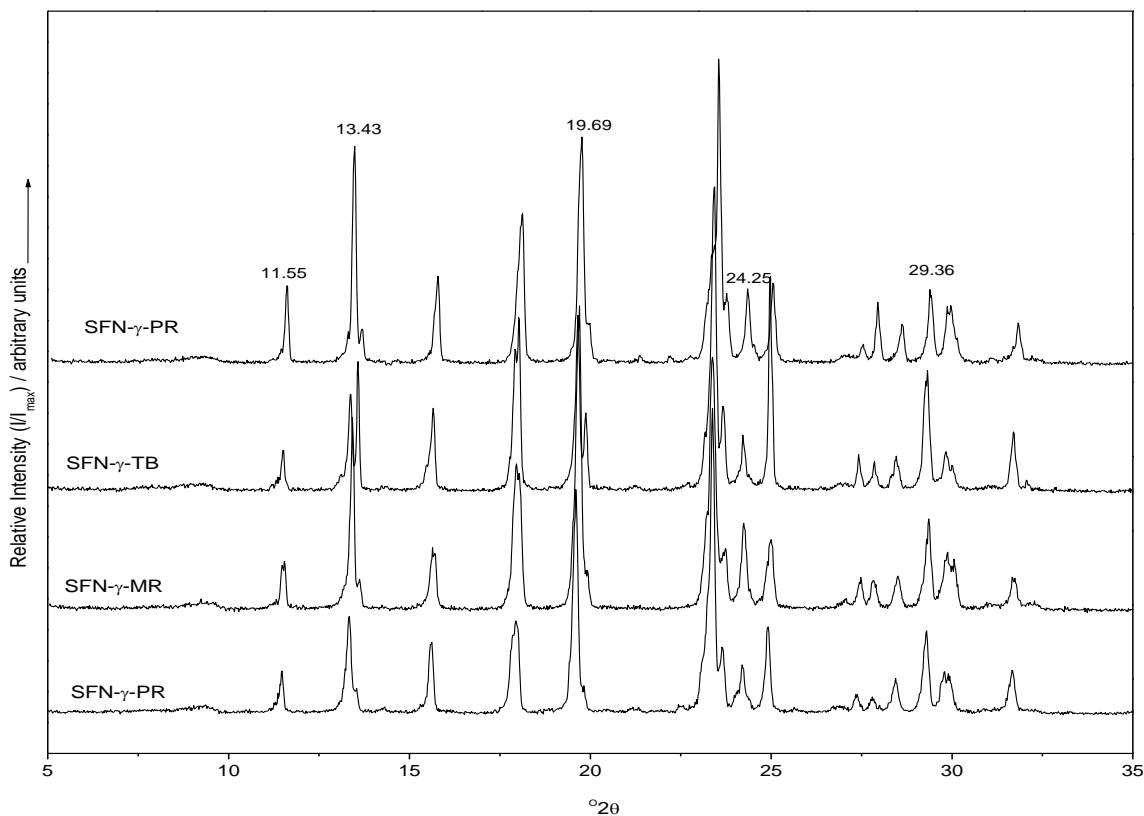**Figure 5. 21** PXRD patterns of SFN-γ samples; untreated and dye-treated polymorphs.

DSC thermograms of SFN-γ chromogenically treated with PR, TB and MR have been compared to the untreated polymorph (Fig 5.22). A single endothermic peak is observed for all samples, this endotherm is attributed to melting (fusion). The onset temperature (T_f) and enthalpy of fusion ΔH_f values are:

$T_f =162.3\pm0.3$ºC and $\Delta H_f =146.0\pm1.0$ Jg^{-1};

$T_f =163.7\pm0.5$ºC and $\Delta H_f =147.0\pm1.0$ Jg^{-1};

$T_f =162.6\pm0.5$ºC and $\Delta H_f =144.0\pm1.0$ Jg^{-1},

$T_f =163.7\pm0.5$ºC and $\Delta H_f =147.0\pm1.0$ Jg^{-1}

for SFN-γ, SFN-γ -MR, SFN-γ-TB and SFN-γ –PR, respectively.
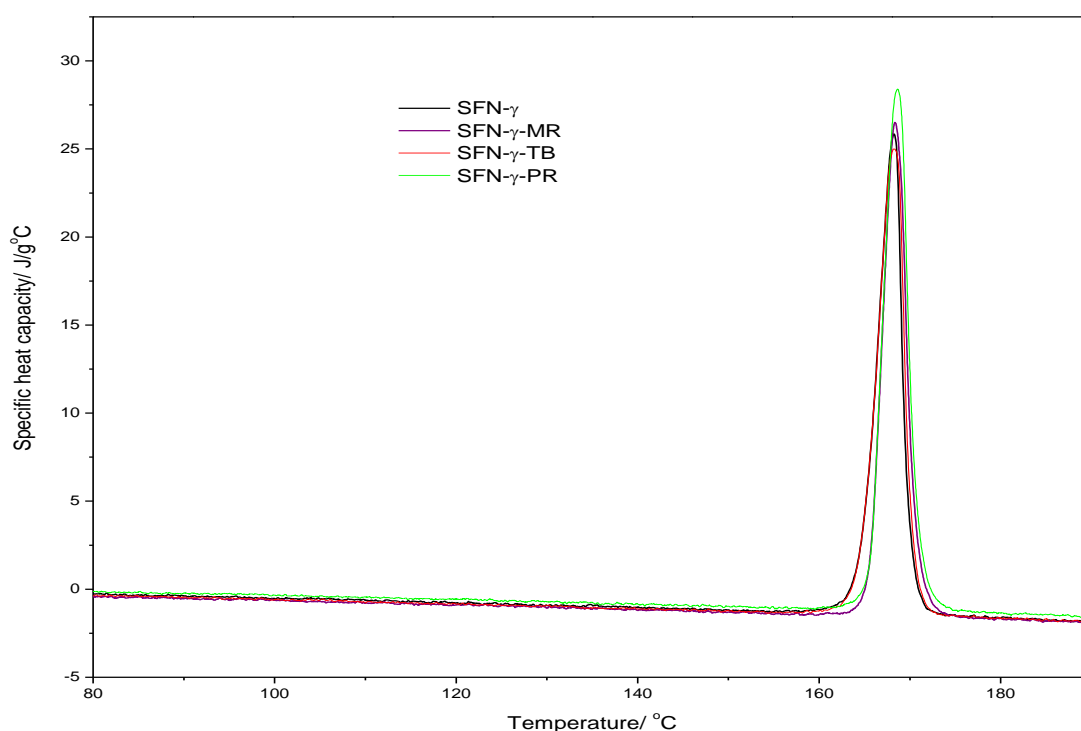
Figure 5.22 DSC thermograms of SFN-γ samples; untreated and dye-treated polymorphs.

Diffractograms, spectra and thermograms of the drug polymorphs examined before and after treatment with dye were not significantly different. The results for the analysis of chromogenically treated polymorphs using PXRD and DSC give indications that within the detection limits of the instrument, chromogenic treatment does not alter the crystal lattice structure of the polymorphs.

5.3.2 Surface area measurements

The specific surface area (SSA) by BET measurements reveal the non-porous nature of the polymorphs compared to inorganic solids such as silica. All the polymorphs have low SSA (Table 5.1), FRS-I showed the highest area of $1.70 m^2 g^{-1}$ and FRS-II and CFN-I show lower areas of $0.13\ m^2 g^{-1}$ and $0.08 m^2 g^{-1}$ for respectively. It was not possible to determine the SSA for the remaining polymorphs because the proportion of nitrogen adsorbed was so low that the high vapour pressure of the nitrogen gas introduces error in the SSA calculation.

Table 5. 3 Specific surface area (SSA) of model polymorphic samples.

	IMC-α	IMC-γ	CBZ-I	CBZ-III	CFN-I	CFN-II	FRS-I	FRS-II	SFN-β	SFN-γ
SSA / $m^2 g^{-1}$	-	-	-	-	0.08	-	1.70	0.13	-	-

SSA values for several polymorphs were not determined because of the calculation error introduced by extremely low proportion of nitrogen adsorbed.

5.3.3 DRVS analysis of indomethacin polymorphs - Crystal structure and surface characterisation

Normalised DRVS spectra of the IMC polymorphs treated with PR, TB and MR are shown in Figs. 5.23, 5.24 and 5.25, respectively. Alongside each are photographs of the polymorph with adsorbed dye showing the colours which gave rise to the DRVS spectra.

For PR adsorption, a single band at λ=460 nm is shown for IMC-α-PR, whereas fused bands at λ=460 and 525 nm are observed for IMC-γ-PR. The spectrum of IMC-α-PR is of the dye adsorbed in the yellow mono-deprotonated form (PRH⁻). For IMC-γ-PR, the dye adsorbed as both the red unionised (PRH$_2$) form and the yellow PRH⁻ form. The intensity of the band assignable to PRH⁻ indicates a slightly higher proportion of adsorbed PRH⁻ to PRH$_2$. The perceived sample colours are yellow and orange for IMC-α-PR and IMC-γ-PR respectively. Absorption bands for PR-treated IMC are red shifted when compared to solution values of 433 nm (PRH⁻) and 506 nm (PRH$_2$).
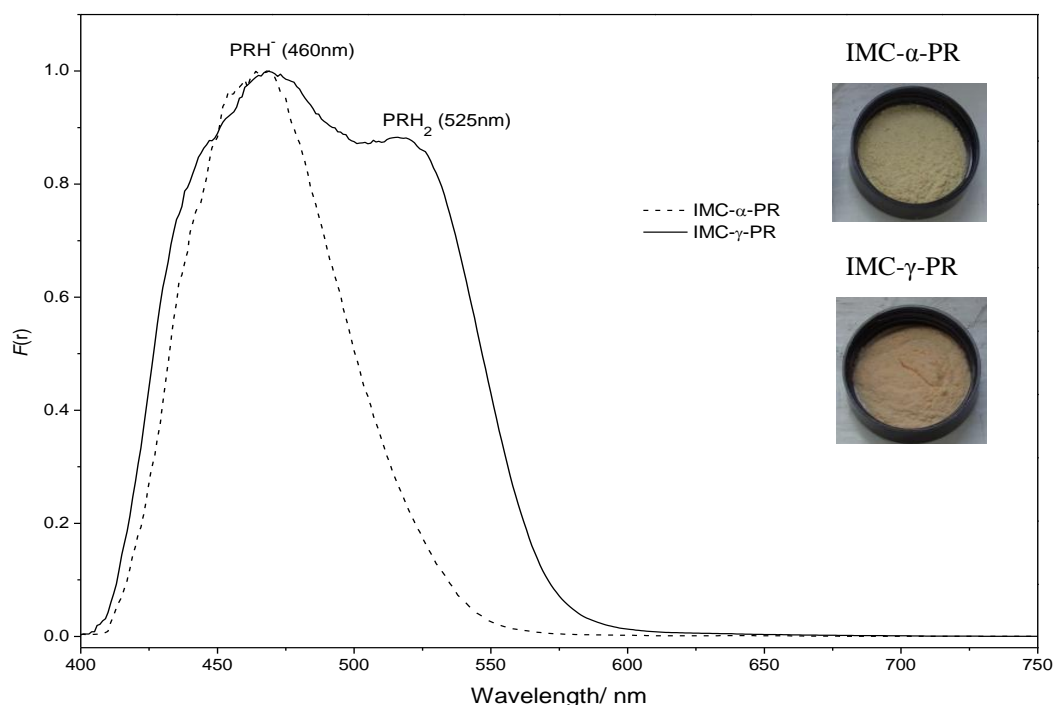
Figure 5. 23 Normalised DRVS spectra of treated IMC polymorphs; IMC-α-PR (solid line) and IMC- γ-PR (dashed line).

For TB adsorption, a single band at λ=465 nm is shown for IMC-γ and IMC-α, and therefore spectra for both polymorphs are of dye adsorbed in the yellow TBH⁻ form. This value is red-shifted when compared to the solution *value (λ= 434 nm).*

Figure 5. 24 Normalised DRVS spectra of dye treated IMC samples; IMC-α-TB (solid line) and IMC-γ-TB (dashed line).

Spectra for both IMC-α-MR and IMC-γ-MR show a broad band at λ=512 nm. This band could well correspond to the red neutral MRH species (solution λ_max of 490nm). A λ=572nm shoulder band corresponding to the zwitterionic form (solution value of 560 nm) is just discernable for IMC-α-MR. The perceived colour for both samples are red, IMC-γ-MR being the more intensely coloured.
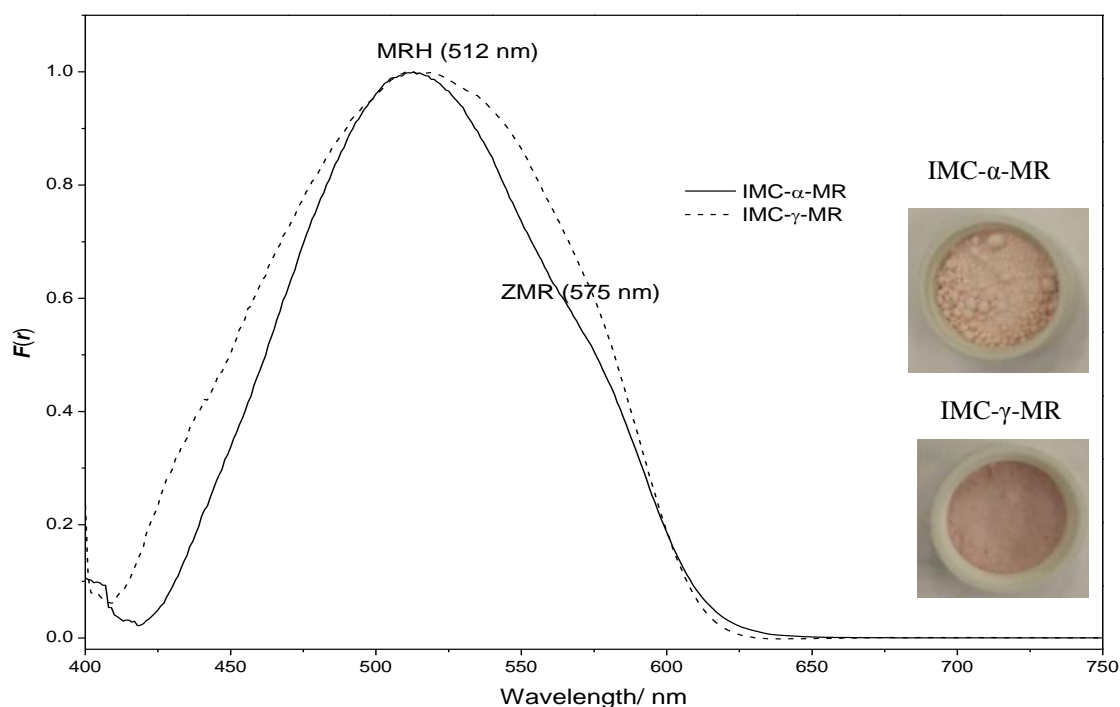
Figure 5. 25 Normalised DRV spectra of dye treated IMC samples; IMC-α-MR (solid line) and IMC-γ-MR (dashed line).

Discussion

The surface of IMC polymorphs coated with PR and TB appears yellow and their DRVS spectra contain the absorption band associated with the mono-deprotonated form of these sulfonphthalein dyes. This suggests the presence of Brønsted or Lewis base sites on the surface. These sites are more prevalent on the IMC-α surface, because the IMC-γ DRVS spectrum shows a second adsorption band corresponding to the red unionised PRH_2, indicating that the surface of IMC-γ has less of the basic functionality, leaving some of the dye unionised.

The pKa of the sulphonic acid group in PR is -0.90±0.30, so the presence of both absorption bands in roughly equal proportions suggests a surface acidity close to the pKa of the dye. However the most acidic functional group in the IMC molecule is a carboxylic acid (pKa of 3.96±0.30) and so this seems unlikely. The presence of this form of the dye is therefore more likely to derive from dye-dye association.

For TB adsorption, both polymorphs show similar behaviour. This is surprising, because the results with PR indicate a difference in surface basicity, and TB is a very similar chemical structure, differing only in the presence of a methyl and isopropyl group. However, since the dyes were applied at a constant concentration (0.1 mg/g) and not a constant molarity (TB = 0.20 µmol/g, PR = 0.28 µmol/g), there were less TB molecules on the surface of the polymorphs. If the difference in basicity was relatively small and the number of basic groups on the surface was sufficient to react with all the TB molecules, even with the less basic IMC-γ, there would be no free TB molecules to dimerise or associate.

In order to ascertain if the difference in the results with PR and TB could be associated with the difference in molar concentration on the surface, the IMC polymorphs were coated with a higher concentration of 0.2 mg/g of TB. Figure 5.26 shows the resulting DRVS spectra and for comparison these have been overlaid with the spectra obtained for the lower concentration of TB.

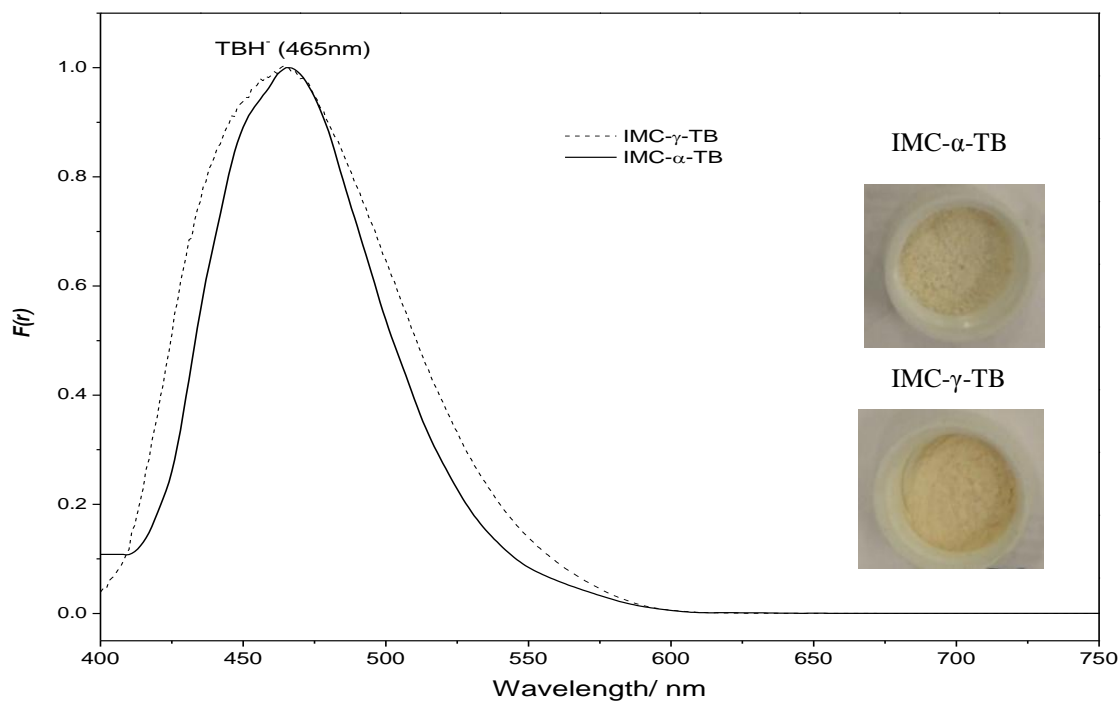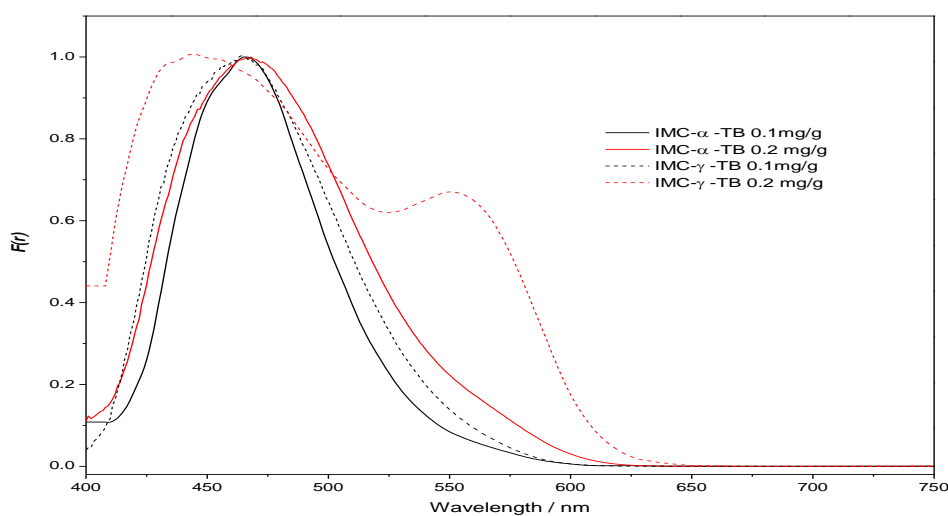**Figure 5. 26** Normalised DRV spectra of dye treated IMC samples; IMC-α-TB (solid line) and IMC-γ-TB (dashed line) showing 0.1 mg/g and 0.2 mg/g dye loading.

From the spectra in Fig 5.26 it is clear that increasing the TB concentration has made no significant difference to the results for IMC-α, but the absorption band for the unionised dye is now seen for IMC-γ at the higher dye loading. This would seem to confirm the earlier suggestion that the TBH_2 band results from association of excess TB molecules. However the lack of this band for IMC-α even at the higher concentration would suggest that the difference in basicity is greater than was originally thought.

In a study of drug-excipient interactions, IMC was coated with TB and the surface pH studied[1]. The authors did not specify which polymorphic form was used although this was likely to be IMC-γ since this is the commercially available form. They applied TB at a concentration of 0.22 mg/g and observed both absorbance bands with DRVS. They measured the pH using the slurry pH method and recorded a value of 4.4. However they also compared the UV-Vis spectra of solutions of TB and found that the observed DRVS spectrum of the IMC surface gave the best correlation to a solution at pH 1.7. For other drugs studied, the slurry pH method offered good correlation with the DRVS spectra of drug coated with indicator dye, so this result presented an anomaly. They attributed this difference to a change in the pKa of the dye in the adsorbed state. However in the light of the current work, it would seem more likely that the presence of the TBH_2 absorbance band was due to dye-dye association because of the concentration of dye used. As discussed earlier it is extremely unlikely that a surface populated with carboxylic acid groups should have an acidity equivalent to pH 1.7.

If the surface basicity of the polymorphs derived from the presence of a strong base, some presence of absorption bands for the PR^{2-} and TB^{2-} species might have been detected. These bands absorb in solution at 558 nm and 598 nm and would be expected to be red shifted on the surface. No bands in this region were observed, suggesting that the surface basicity derives from a weak base.

For MR adsorption, the red MRH is the prevalent species for both polymorphs. The DRVS spectra of IMC-α sample does not contain the deprotonated form of MR. The absence of the deprotonated species could imply that the MR carboxylic acid group, with pKa = 3.66±0.36 is not strong enough to protonate the Lewis base site on IMC polymorph surface. The presence of adsorbed zwitterionic MR suggests supramolecular dye/ surface interactions that may involve hydrogen bonding[16].

The molecule of IMC contain C=O groups (from the secondary amide and carboxylic acid), which could act as Lewis base sites. The two lone pair of electrons on oxygen can interact with hydrogen ion from the dye molecules. The surface acidity or basicity differences between IMC-α and IMC-γ could result from the accessibility of the C=O group on the surface.

A closer look at the crystal structure of the polymorphs of IMC suggest a higher surface carboxylic acid C=O content for IMC-α relative to IMC-γ. The crystal structure of IMC-γ consists of mutually hydrogen bonded dimers (Fig 5.27) that are described as centrosymmetric (or having a centre of symmetry or inversion point).
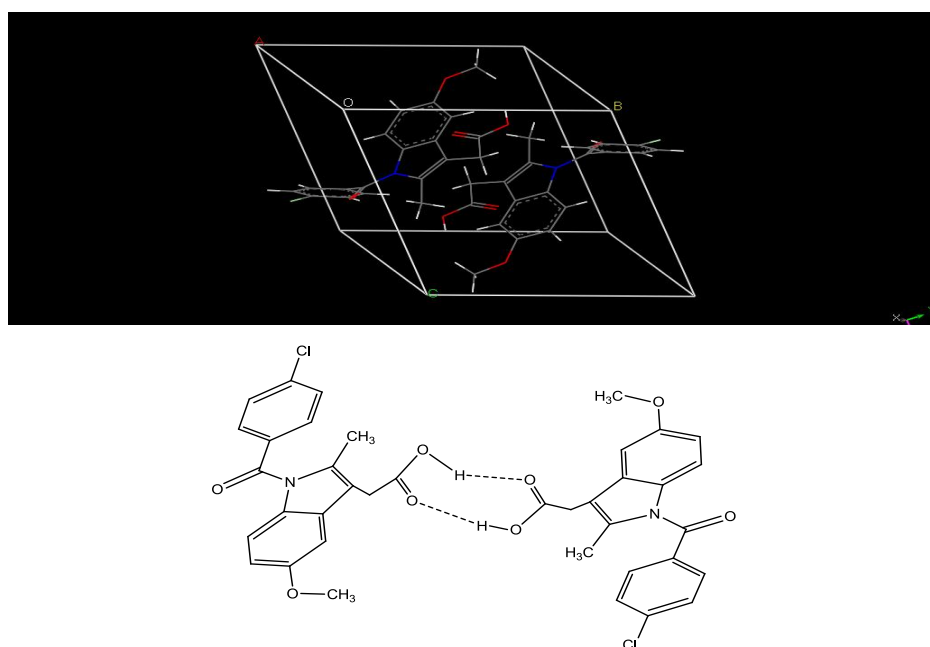
Figure 5. 27 The unit cell of IMC-γ showing crystallographic axes (above) and the centrosymmetric dimers (below) present in the crystal structure of IMC-γ showing hydrogen bonding (dashed line) between carboxylic acid groups. *Colour code: grey-carbon, white-hydrogen, blue-nitrogen, red-oxygen and green-chlorine.*

The dimers are formed by the carboxylic acid moiety and the accessibility of these groups is hindered by the indole and phenyl moieties of each molecule. The crystal structure is also supported by edge-to-face C-H....π and π-π interactions (Fig 5.28)[17].
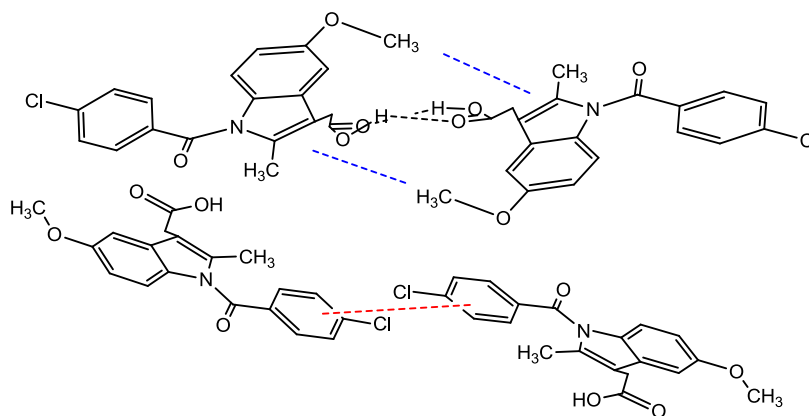
Figure 5. 28 Weak edge to face C-H⋯π interactions (blue dashed line) involving methoxy H and indole ring π system between molecules related by a centre of symmetry in the crystal structure of IMC-γ. The π-π interaction (red dashed line) between centrosymmetric chlorophenyl rings in IMC-γ crystal packing across the centrosymmetric carboxylic acid dimer.

In the crystal structure of IMC-α, molecules exist as trimers in which two of the molecules form a hydrogen bonded carboxylic acid dimer, and the third molecule forms a hydrogen bond between the carboxylic acid and the amide carbonyl in the dimer (Fig 5.29).

The difference in the chemical reactivity of IMC-α and IMC-γ towards ammonia gas was determined by Chen *et al*[18]. Their work revealed that IMC-α reacted with ammonia gas via the carboxylic acid group to give an ammonium salt. However, the γ form showed little reactivity. The reactivity of α (in powdered and single crystal samples) towards ammonia gas, was proposed to be as a result of the surface accessibility of the carboxylic acid hydrogen bonded to the secondary amide carbonyl. The surface accessibility of the C=O groups for IMC-α could be responsible for the greater extent of deprotonation of dye molecules compared to IMC-γ.
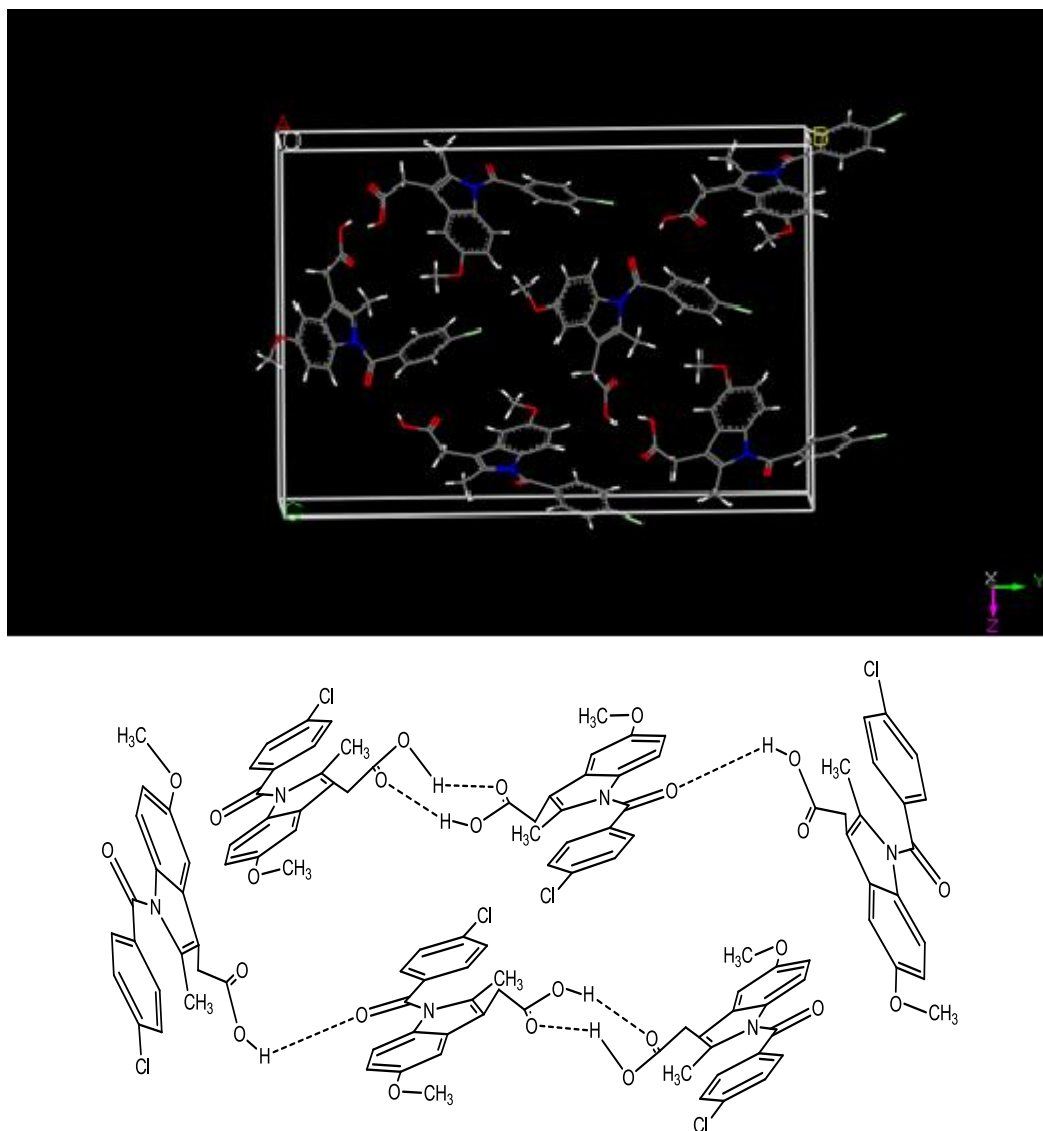
Figure 5. 29 The unit cell of IMC-α showing crystallographic axes (above) and the trimer structure in the crystal structure of IMC-α, showing two molecules forming a mutually bonded dimer and the third molecule forming a single hydrogen bond between its carboxylic acid group and the amide carbonyl. *Colour code: grey-carbon, white-hydrogen, blue-nitrogen and red-oxygen.*

The differentiation of IMC polymorphs by adsorption of TB or PR molecules is proposed to be because of two main interactions: protonation of the IMC C=O group and the physical adsorption of unionised molecules (Scheme 1.1). The deprotonation of dye molecules by IMC-γ is less extensive than IMC-α, hence the physical adsorption of unionised species.

For MR adsorption, both polymorphs show the dominant dye-surface interaction of physical adsorption of unionised species. However, the observed differential coloration may be attributable to the higher proportion of interaction of the zwitterionic species with C=O, possibly by hydrogen bonding (see scheme 1.2 below).

$$C=OH_2^{+\ -}InH$$

$$InH_2$$

///////////   /////////// In = TB or PR   **SCHEME 1. 1**

protonation   physical
adsorption

$$C=O--ZMR$$

$$MRH$$

///////////   ///////////   **SCHEME 1. 2**

hydrogen bonding   physical
adsorption
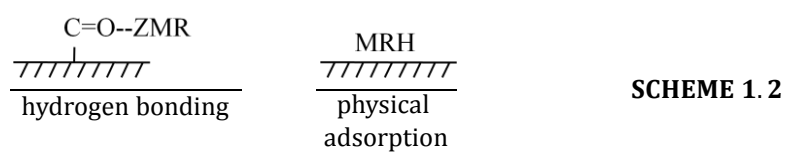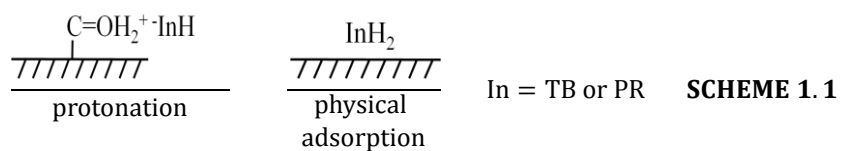
5.3.4 DRVS analysis of carbamazepine polymorphs- crystal structure and surface characterisation

Normalised DRVS spectra and pictures of the polymorphs of CBZ treated with PR, TB and MR are shown in Figs 5.30, 5.31 and 5.32 respectively. The observed colour for samples with adsorbed PR is very light orange. Their DRVS spectra show that CBZ-III absorbs at 450nm, showing a very broad band, and CBZ-I absorbs at 446 and 580 nm. In both cases, bands are red shifted when compared to solution values of 433 nm (PRH^-) and 557 nm (PRH_2).

The spectrum of CBZ-III showed mainly the yellow PRH^- species. However since the sample was light orange, it seemed likely that its broad 450 nm peak corresponded to the absorbance of the yellow PRH^- and red PRH_2 species.
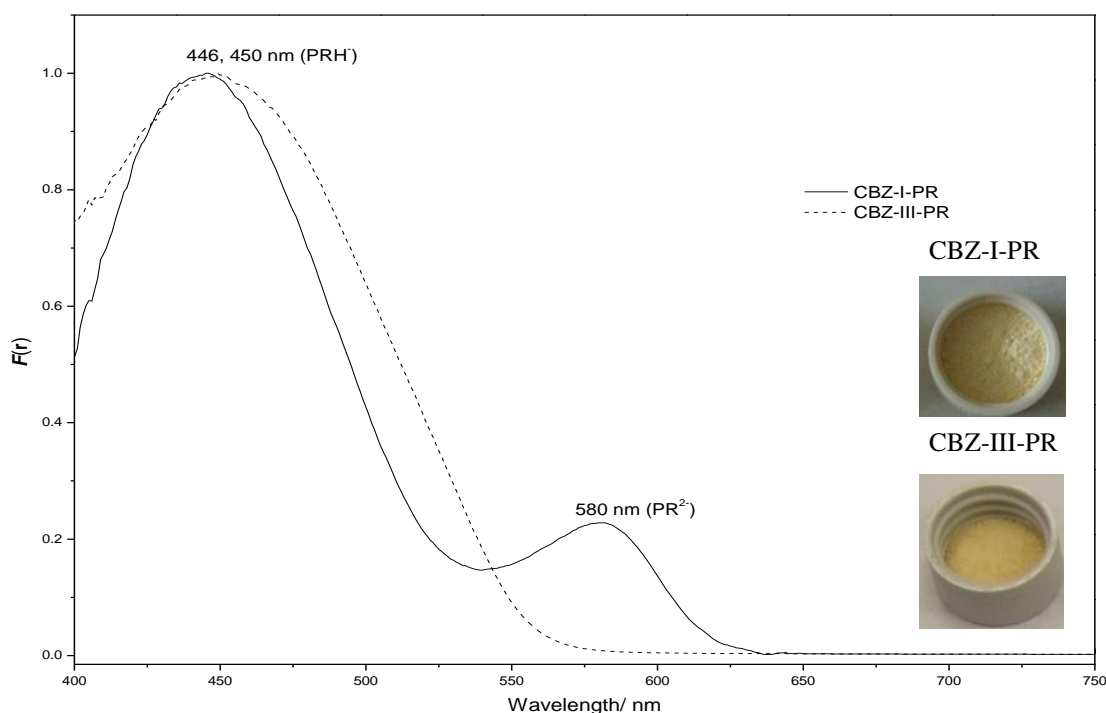
Figure 5. 30 Normalised DRVS spectra of dye treated CBZ samples; CBZ-I-PR (solid line) and CBZ-III-PR (dashed line).

The sample pictures and DRVS spectra of the polymorphs of CBZ treated with thymol blue indicator are shown in Fig. 5.31. The observed colour for CBZ-I-TB is yellow and CBZ-III-TB is orange. There are two TB species in the CBZ-III sample; the red unionised form (λ= 551nm) and yellow monodeprotonated form (λ=467 nm). CBZ-I has only the TBH$^-$ species, as indicated by the single band at 467 nm. Values are red shifted compared to solution values.
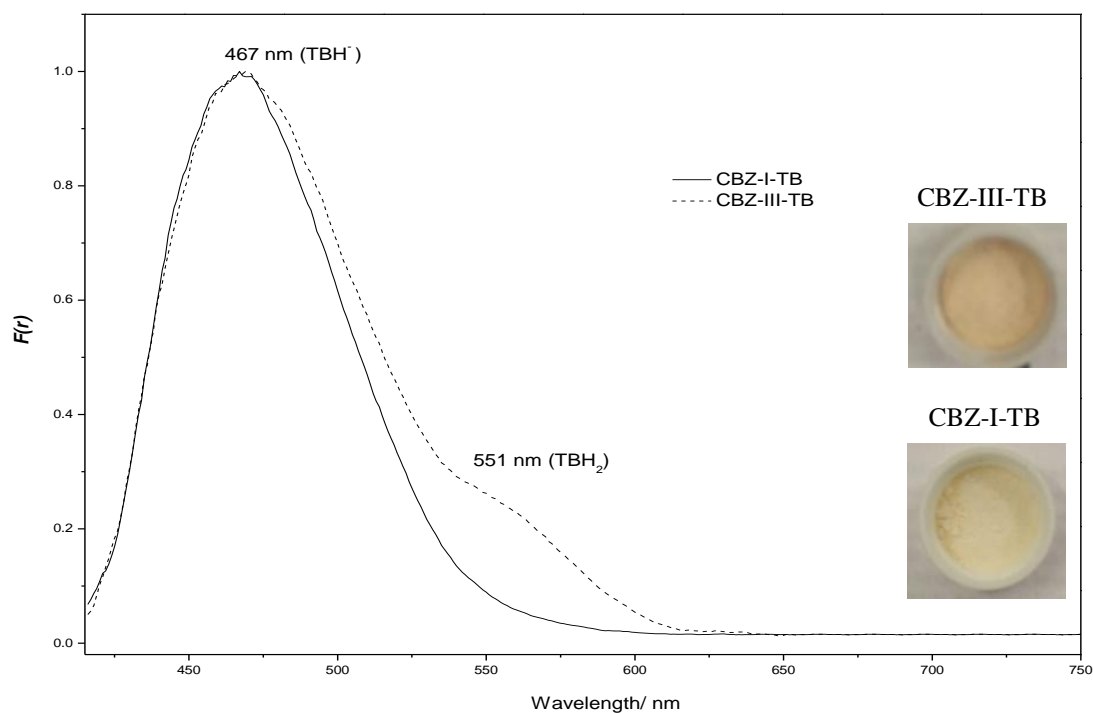
Figure 5. 31 Normalised DRVS spectra of 0.1mg/g dye treated CBZ samples; CBZ-I-TB (solid line) and CBZ-III-TB (dashed line).

The DRVS spectra of the polymorphs of CBZ treated with MR indicator are shown in Fig. 5.32 Both samples were orange, with CBZ-I being the darker of the two. λ_{max} for CBZ-I and CBZ-III are at 495 nm and 440 nm respectively. CBZ-I also shows a shoulder at 435 nm and in CBZ-III the shoulder occurs at 525 nm. The 435nm band in both spectra is attributable to MR$^-$ (solution λ_{max} value of 423 nm). The 495 nm band could be the neutral form; it occurs very close to solution value of 490 nm.
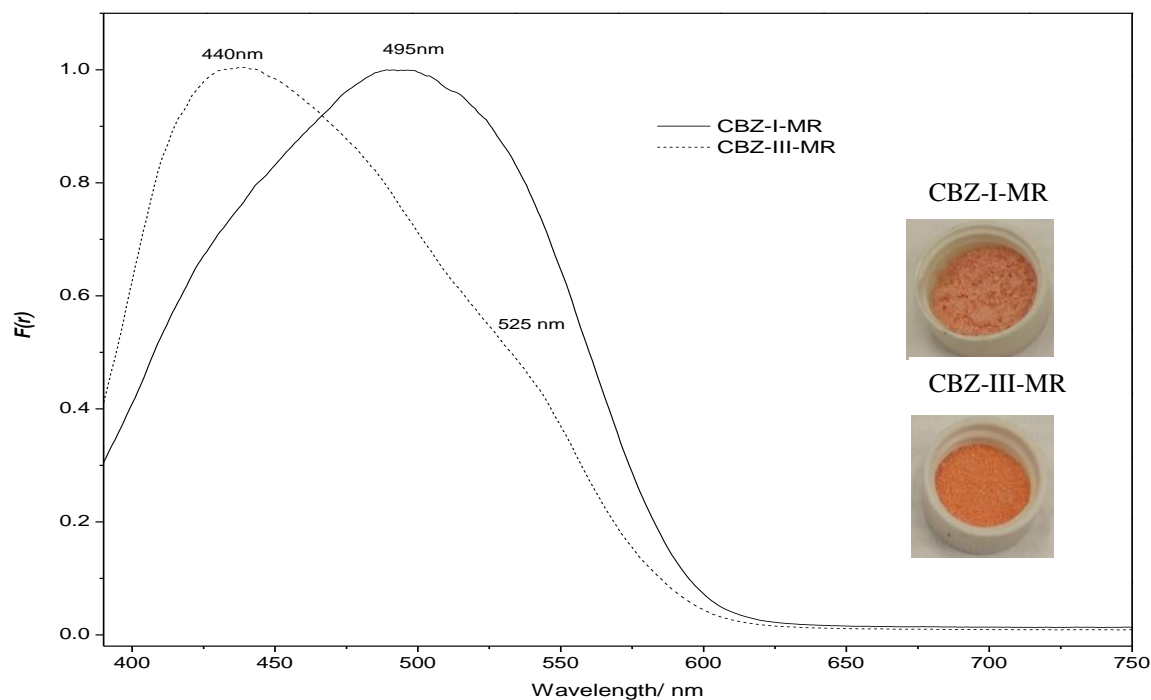
Figure 5. 32 Normalised DRVS spectra of dye treated CBZ samples; CBZ-I-MR (solid line) and CBZ-III-MR (dashed line).

Discussion

The CBZ-I surface deprotonated the adsorbed TB and PR to a greater than CBZ-III. The DRVS spectrum of CBZ-I showed a mixture of the PRH$^-$ and PR^{2-} , while the spectrum for CBZ-III showed only PRH$^-$. These suggests presence of surface base sites

For TB adsorption, CBZ-I ionised the adsorbed molecules to the TBH$^-$ form only. CBZ-III did not completely deprotonate the adsorbed dye and hence a mixture of TBH$^-$ and TBH$_2$ was observed, albeit with a higher proportion of the TBH$^-$ form.

Despite the higher molar concentration of adsorbed PR compared to TB, the deprotonation of adsorbed TB on CBZ-III is incomplete. Steric hindrance could be a contributing factor. The TB molecule contains isopropyl ring substituents which could affect accessibility to ionisable surface functional groups. The TB^{2-} form is absent for both polymorphs, and this suggests that the TBH^- species is not strong enough to protonate the base functionalities exposed on the surface.

In MR adsorption, deprotonation of dye molecules is greater in CBZ-III than CBZ-I, in disparity with PR and TB adsorption. This disparity suggests that MR may, in addition to acid/base character, be responding to other surface/dye interactions. MR visible solution spectra have been shown to be affected not only by proton transfer equilibria (ie pH) but by the polarity of their solution environment[9].

The acid/base nature of the amide ($-CONH_2$) functional group and its surface accessibility would be expected to have a major influence on the ionisation of the adsorbed dye molecules. The acid/base behaviour of amides is complex. The amide group has been shown to exist as in aqueous media as an equilibrium mixture of the protonated, neutral and/ or deprotonated forms over a wide pH range[19]. Using the classification described in chapter 2 Table 2.5, CBZ can act as a very weak acid (pKa 13.94±0.20) and an extremely weak base (pKa -0.49±0.20). The effect of molecular packing on the surface exposure of the amide functionality should therefore be examined for both polymorphs. The crystal structure of the polymorphic forms of CBZ show more similar features than any of the five model polymorphic systems used in this *work*. Molecular packing in CBZ polymorphs are very similar as they both form dimers via hydrogen bonding between the amide groups (Fig 5.33).
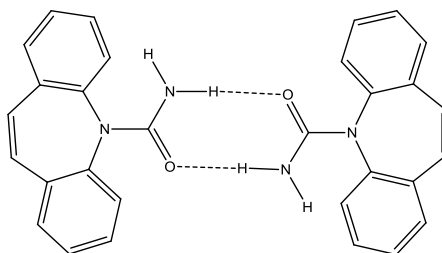
Figure 5. 33 The carboxamide dimer present in the crystal structure of CBZ polymorphs. The dimer hydrogen bonds are represented by black dotted lines.

The pattern of weak C-H....O interactions that connect dimer units differs between the polymorphs[20]. In CBZ-III amido oxygen acts as a donor to one hydrogen atom, (Fig 5.34), while in CBZ-I, it acts as a donor to two hydrogens (Fig 5.35). The packing of molecules in CBZ-III is more compact. In CBZ-I the pattern of weak CH....O hydrogen bonds allow voids to be formed that can increase the accessibility of the NH group for hydrogen bonding. This void has been suggested as a reason for the lower yield stress of CBZ-I compared to CBZ-III[21]. The accessibility of the $CONH_2$ group on the surface of CBZ-I is responsible for faster kinetics of formation of the hydrated form[22] because of hydrogen bonding between the amide group and water.
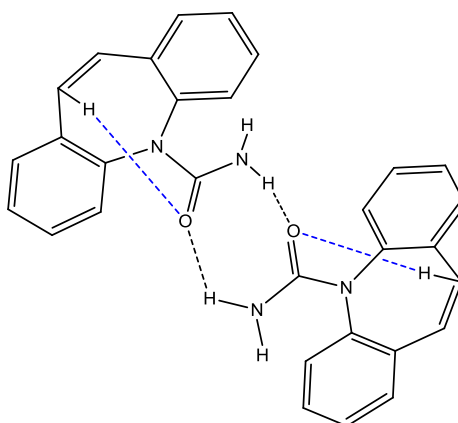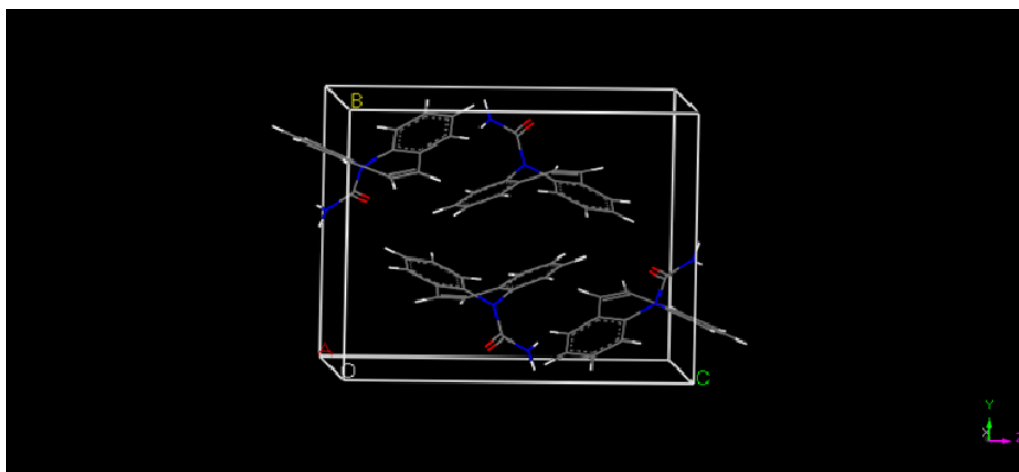
Figure 5.34 The unit cell structure of CBZ-III showing crystallographic axes (above) and the pattern of weak C-H....O hydrogen bonds (blue dotted lines) that gives CBZ-III its more compact crystal structure, thus decreasing the accessibility of the carboxamide group. *Colour code: grey-carbon, white-hydrogen, blue-nitrogen and red-oxygen.*
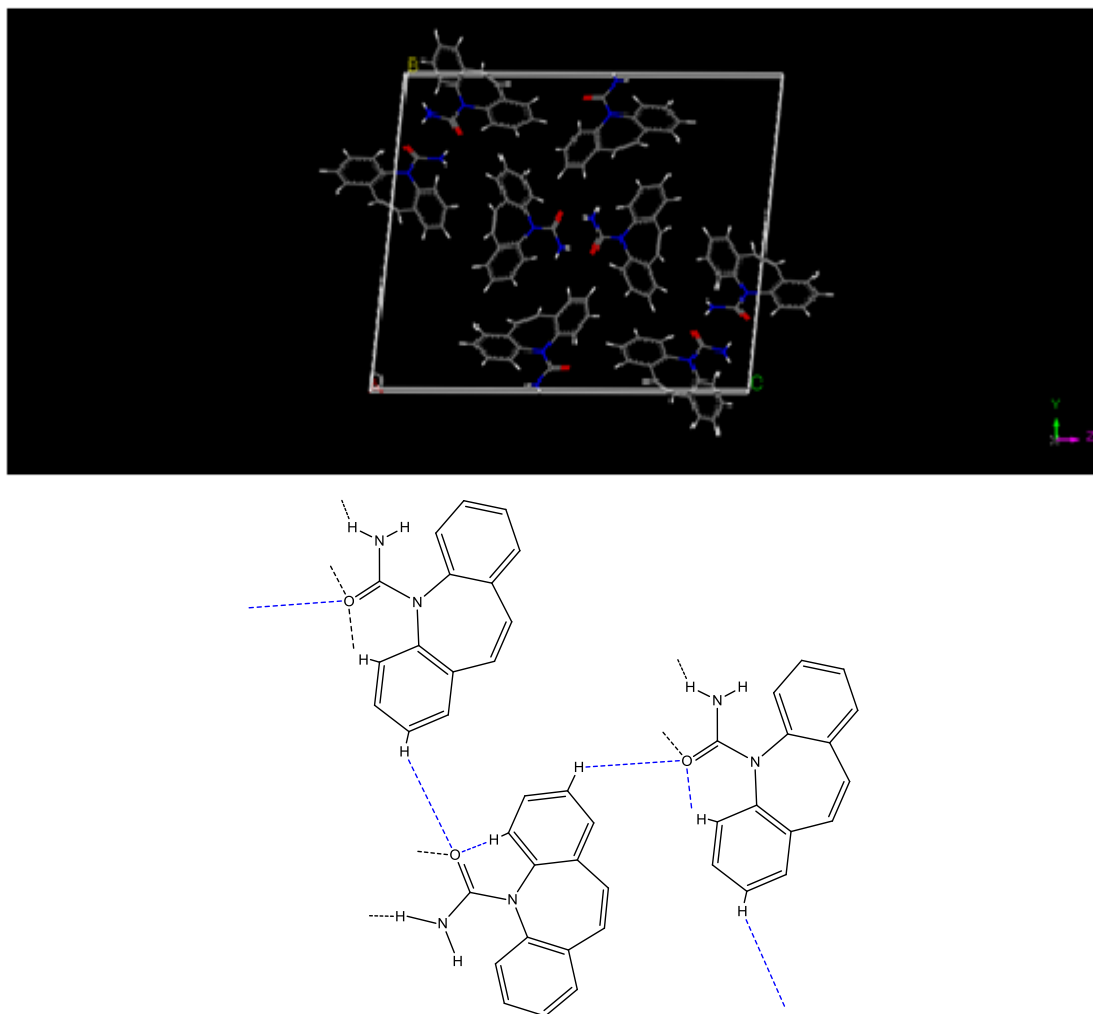
Figure 5. 35 The unit cell structure of CBZ-I showing crystallographic axes (above) and the pattern of weak C-H....O hydrogen bonds (blue dotted lines) that give CBZ-I a less compact crystal structure (below), thus increasing the accessibility of the carboxamide H. For simplicity, only one component of the dimer unit is shown. *Colour code: grey-carbon, white-hydrogen, blue-nitrogen and red-oxygen.*

A schematic representation of plausible interactions between dye molecules and the surfaces of the polymorphs is shown as Schemes 1.3 and 1.4. DRVS spectral differentiation of CBZ polymorphs by PR and TB adsorption could be because of the protonation of surface amide functionalities and the physical adsorption of dye molecules, probably by van der Waals interaction (Scheme 1.3). For PR adsorption, the dominant dye-surface interaction for both CBZ-I and CBZ-III is that of protonation of the amide group by PRH_2, but spectral differentiation is afforded by the protonation of amide group by PRH^-.

Differential colouration by TB adsorption is because of the physical adsorption of the TBH_2 possibly by van der Waals interactions. Polymorphic differentiation by MR is because of protonation of the amide group, and the adsorption of MRH (Scheme 1.4). CBZ polymorphs ionise a proportion of adsorbed MR molecules to MR^-. The remaining molecules of MR could adsorb via hydrogen bonding or van der Waals interactions.

SCHEME 1.3

SCHEME 1.4
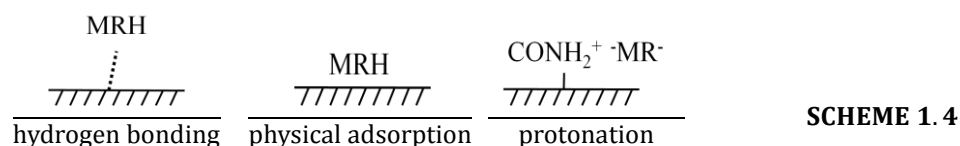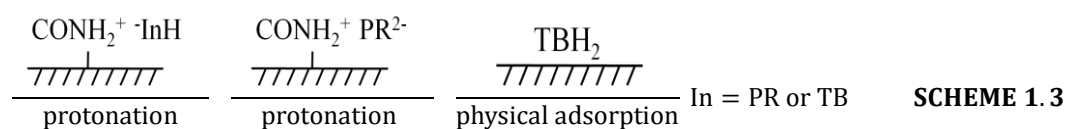
5.3.5 DRVS analysis of caffeine polymorphs- crystal structure and surface characterisation

Sample pictures and normalised DRVS spectra of PR, TB and MR-treated CFN polymorphs are displayed in Figs 5.36, 5.37 and 5.38, respectively.

CFN-II-PR has an orange hue while CFN-I is pink. Two bands are observed for CFN-II, yellow PRH^- (430 nm) and red PRH_2 (514 nm). CFN-I shows one band at 520 nm for red PRH_2. Solution values for these bands are 433nm and 503nm respectively.
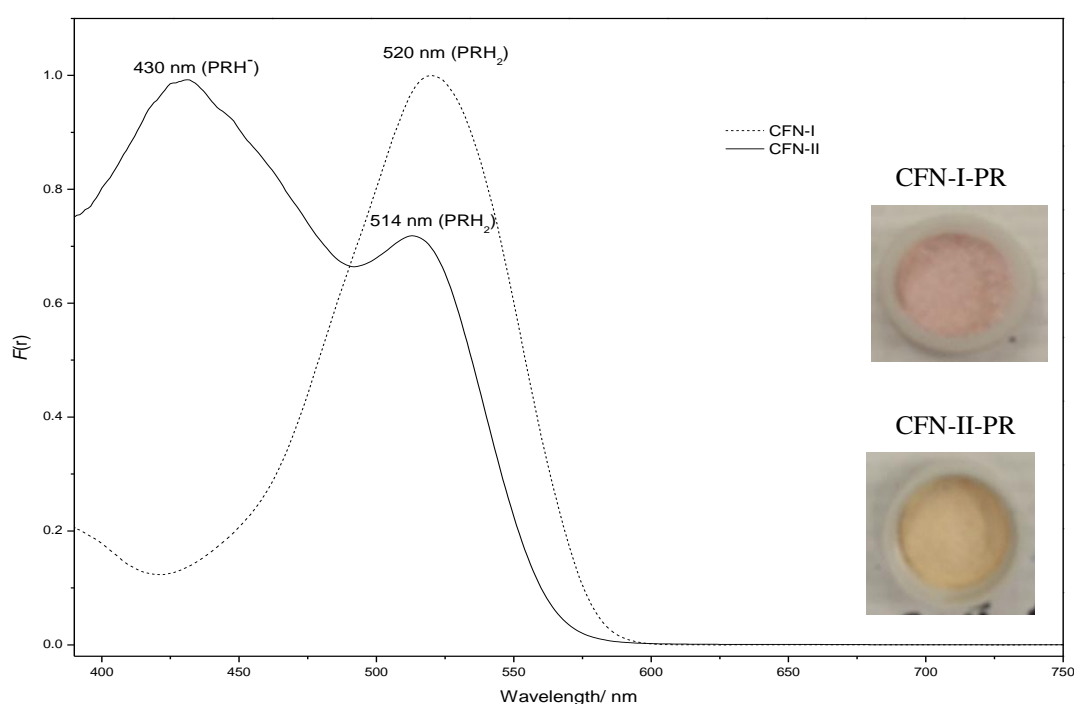
Figure 5.36 Normalised DRV spectra of dye treated CFN samples; CFN-I-PR (solid line) and CFN-II-PR (dashed line).

Yellow CFN-I-TB shows a single band at λ=440 nm and orange CFN-II-TB shows two bands at 440 nm and 550 nm. The bands at 440 nm and 550 nm correspond to TBH⁻ and TBH₂ respectively. These bands are very close to solution value of 434 nm and 547 nm.
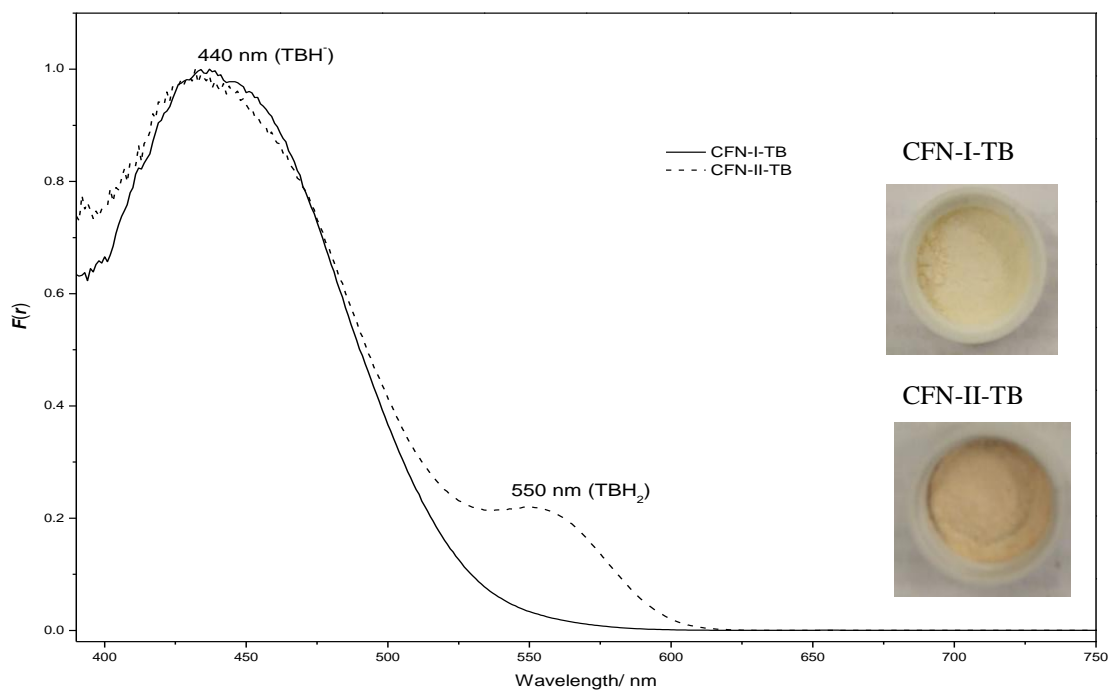
Figure 5.37 Normalised DRVS spectra of dye treated CFN samples; CFN-I-TB (solid line) and CFN-II-TB (dashed line).

DRVS spectra for both MR treated samples show a λ_{max} at 500 nm with a discernable shoulder at 435 nm. For orange CFN-II-MR the 435 nm shoulder band is more discernable. CFN-I-MR had a red hue and its shoulder band is less pronounced. The shoulder band is attributable to yellow MR^- (solution value of 429 nm). The band at 500 nm is assignable to red MRH, and this value is red-shifted compared to solution value of 490 nm.

Figure 5. 38 Normalised DRVS spectra of dye treated CFN samples; CFN-I-MR (solid line) and CFN-II-MR (dashed line).

Discussion

DRVS bands for dye ionisation on solid samples are close to those obtained from solution studies, unlike those obtained for other drug polymorphs like IMC and CBZ. For instance the yellow TBH^- species showed a 6nm red shift for CFN polymorphs compared to a 31 nm shift for IMC polymorphs. The reason for this is discussed later.

The DRVS results suggest that the deprotonation of dye molecules by CFN polymorphs is complex. The extent of deprotonation of PR and MR is more extensive for CFN-II compared to CFN-I, but with TB the reverse is true. It is counterintuitive that although PR and TB have similar chemistries, the deprotonation effects are reversed. The basic character of caffeine is ascribed to the imine group (pKa = 0.52±0.70) and the tertiary amine group (pKa =-3.83±0.20) as shown in Table 5.1. The accessibility of these groups on the surface would greatly influence dye deprotonation.

The single crystal structure of CFN polymorphs is complicated by the positional disorder of the caffeine molecules (Fig 5.39 and 5.40). These polymorphs are referred to as "rotator phase" crystals, i.e. the molecules retain translational order but exhibit dynamic orientational disorder and exhibit sufficient characteristics to be called crystalline compounds[23, 24]. The dynamic orientational disorder is very extensive in CFN-I and all molecules show whole molecule disorder.
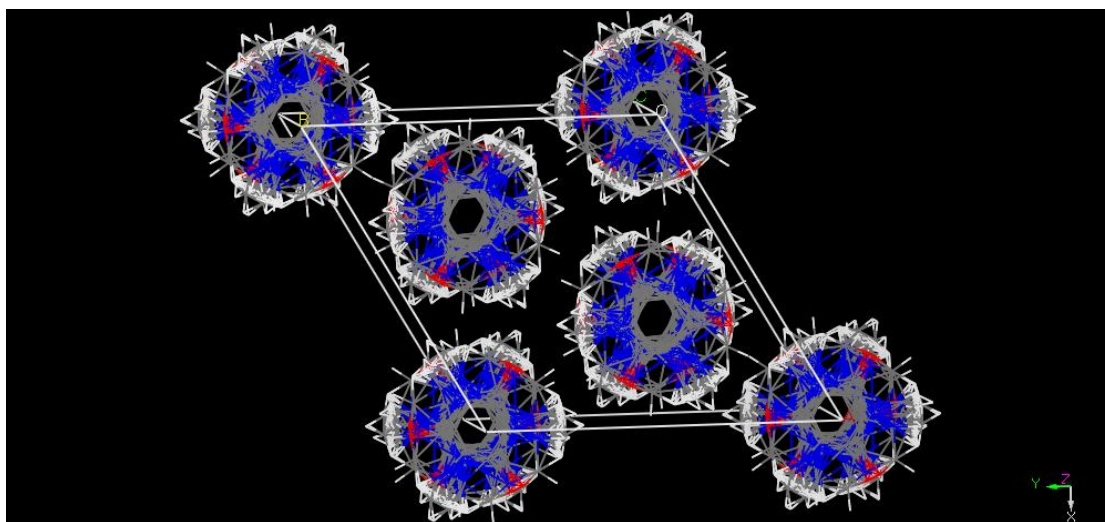
Figure 5. 39 The unit cell structure of CFN-I showing fully disordered molecules *Colour code: grey-carbon, white-hydrogen, blue-nitrogen and red-oxygen.*

CFN-II has three types of molecules, a fully ordered molecule and two other molecules partially disordered to different degrees.
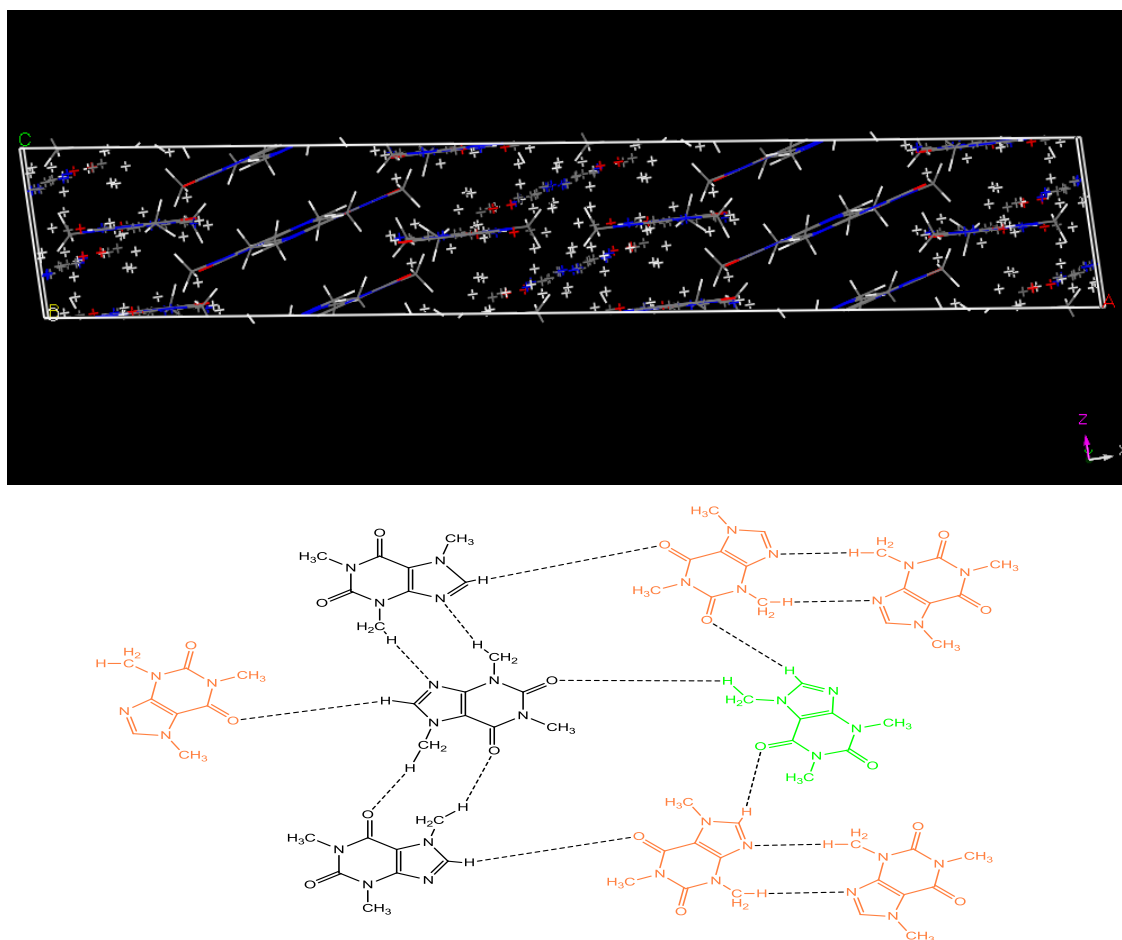
Figure 5. 40 The unit cell of CFN-II showing π- stacking of molecules (above) and a pattern of weak hydrogen bonds between molecules in CFN-II (below). Black, orange and green represent the fully ordered, 50:50 and 65:35 disordered molecules, respectively.

The packing motif in CFN-I is more symmetrical, containing a hexagonal packing and π-stacked columns of caffeine molecules. A complete analysis of the more symmetrical packing motif of CFN-I by single crystal studies is hampered by the highly disordered molecules. The unit cell of CFN-II shows π-stacks of caffeine molecules and the plane containing the primary lateral interactions between molecules in CFN-II is shown in Fig 5.39. These lateral interactions are hydrogen bonds of the form C-H.....X, where X is oxygen or nitrogen, also the caffeine molecules are π stacked in columns. This propensity of caffeine molecules for extensive but weak hydrogen bonding, could mean that adsorbed dye molecules could be responding to hydrogen bonding potential rather than acidity.

As reported by Kahr et al[8] visible spectra of MR is sensitive to hydrogen bonding. In their work the differential coloration of MR in dye-inclusion crystals of 2,5 dihydrobenzoic acid has been reported to be as a result of an increase in intermolecular hydrogen bonding character. As noted earlier, DRVS bands for dye ionisation with CFN polymorphs are close to the solution values. This proximity could be indicative of the dynamic positional disorder present in their crystal structures. Other polymorphic systems used in this study do not exhibit dynamic molecular disorder.

5.3.6 DRVS analysis of sulfanilamide polymorphs- crystal structure and surface characterisation

The DRVS spectra of PR-treated SFN polymorphs are displayed in Fig 5.41. Light orange SFN-β and dark orange SFN-γ both show two bands at 450 nm and 574 nm which correspond to yellow PRH⁻ (433 nm in solution) and red PR²⁻ (557 nm in solution).
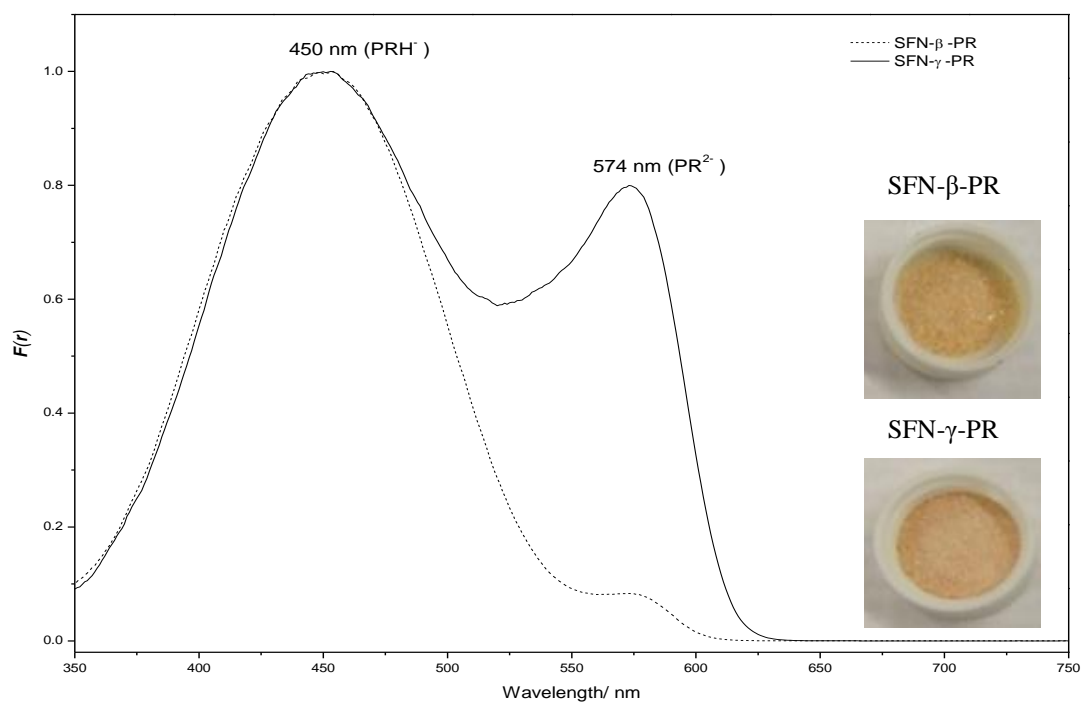
Figure 5. 41 Normalised DRVS spectra of dye treated SFN samples; SFN-γ-PR (solid line) and SFN-β-PR (dashed line).

The sample pictures and DRVS spectra of the polymorphs of SFN treated with TB indicator are shown in Fig. 5.42. Green SFN-γ absorbs at 454 nm and 604 nm which is indicative of the yellow mono-deprotonated and blue di-deprotonated species respectively. Yellow SFN-β absorbs at 454 nm, and therefore contains only the adsorbed TBH⁻. Values recorded are red shifted compared to solution values.
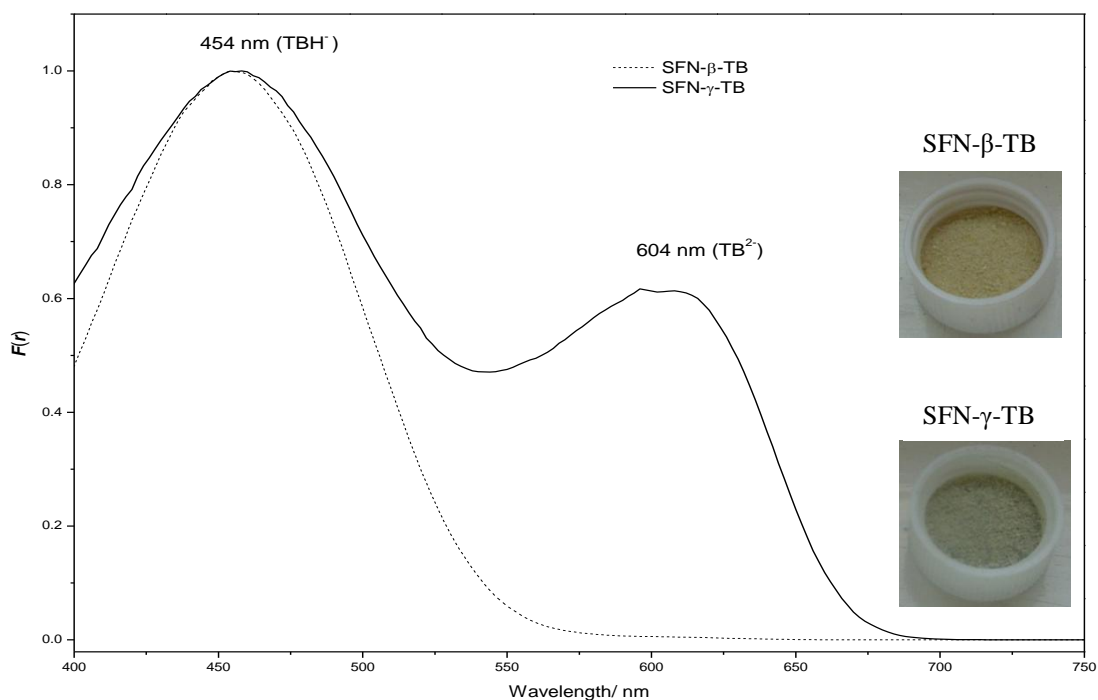
Figure 5.42 Normalised DRVS spectra of dye treated SFN samples; SFN-γ-TB (solid line) and SFN-β-TB (dashed line).

The observed colour of polymorphs of SFN treated with MR indicator is orange with SFN-γ-MR being the lighter of the two. DRVS spectra are shown in Fig. 5.43. The λ_{max} of the light orange SFN-γ-MR was 450 nm, while the dark orange SFN-β-MR absorbed at 440 nm and 572 nm. The higher energy band in both samples corresponds to the yellow MR^- species (λ_{max} of 429 nm in solution). SFN-β-MR also contains the zwitterionic MR species, because of its lower energy band at 572 nm.

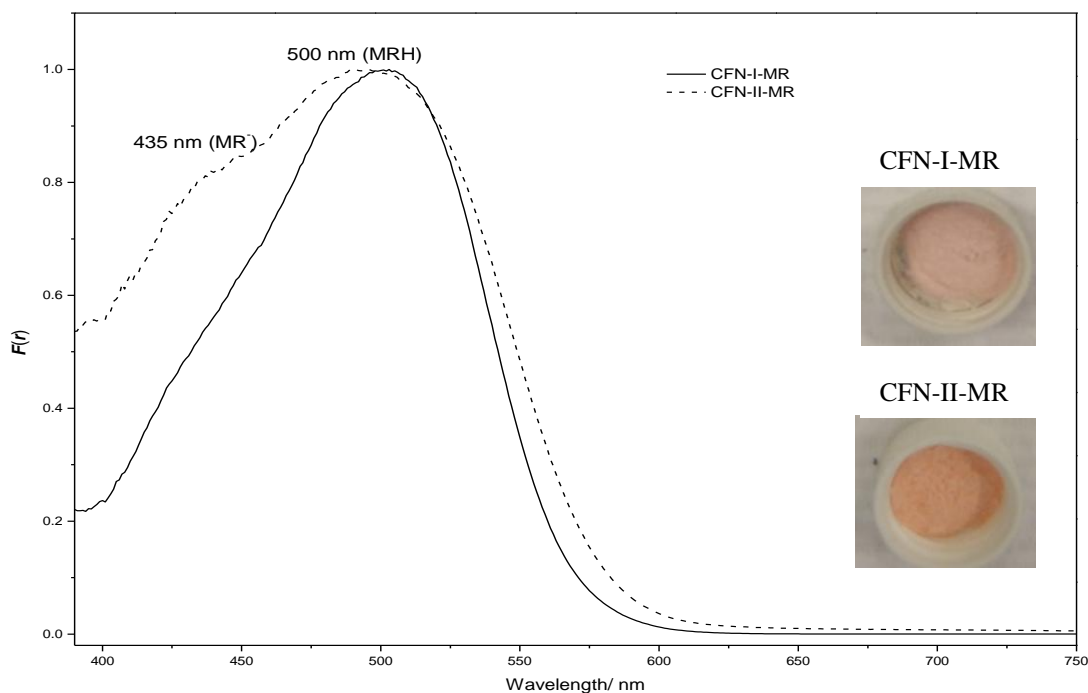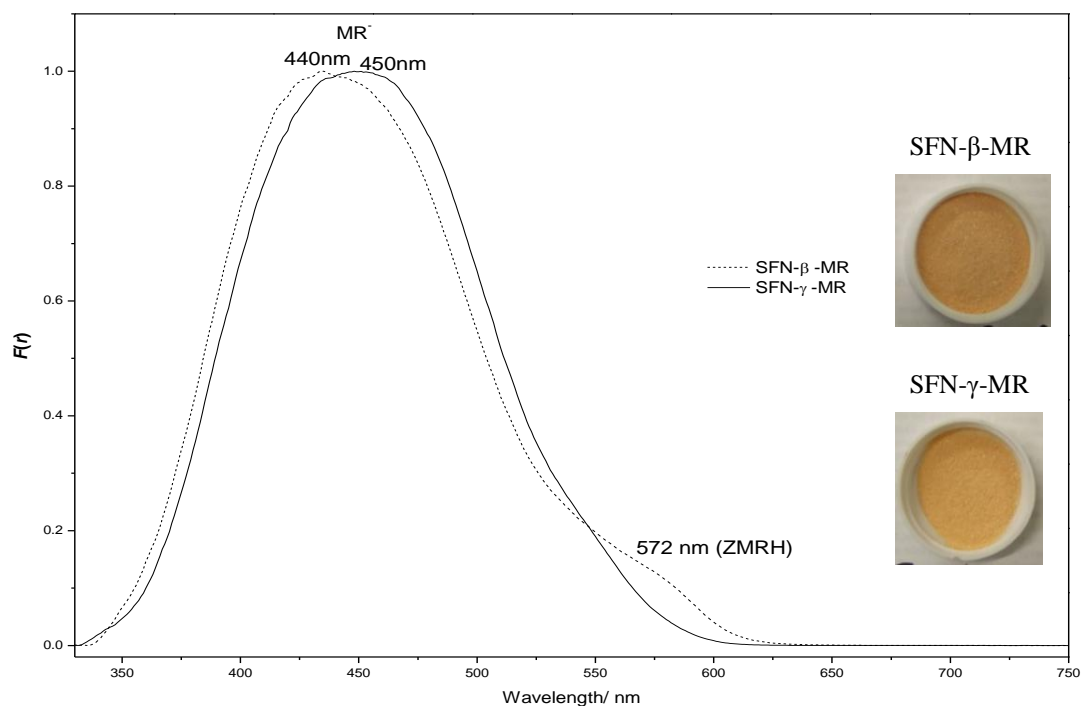**Figure 5.43** Normalised DRV spectra of dye treated SFN samples; SFN-γ-MR (solid line) and SFN-β-MR (dashed line).

Discussion

In all cases, the deprotonation of adsorbed dye molecules is more extensive for SFN-γ compared to SFN-β (i.e. the proportion of adsorbed PRH^-, TB^{2-} and MR^- is greater for SFN-γ). This suggests that SFN-γ has a higher content of basic sites on the surface.

Two ionisable functional groups would play a dominant role in dye deprotonation. These two groups are the basic amine group $-NH_2$ (pKa 1.85±0.10) and the sulfonamide $-SONH_2$ group, which acts as a weak acid (pKa 10.10±0.10) and an extremely weak base (pKa -7.73±0.70).

The amine group is a stronger base than the sulfonamide group, so the deprotonation of dye molecules is greatly influenced by the surface accessibility of $-NH_2$. The packing motif for both polymorphs could provide insight into the higher basicity of SFN-γ.

The unit cell structure and the packing motif of SFN-γ is shown in Fig 5.44. In the crystal packing of SFN-γ, sulfonamide groups form a dimer where each of the O atoms is engaged in one NH…O bond. Four dimeric units are linked via the other sulfonamide oxygen to form a larger ring structure (Fig 5.44). The packing motif of four dimeric units corresponds to two unit cells.
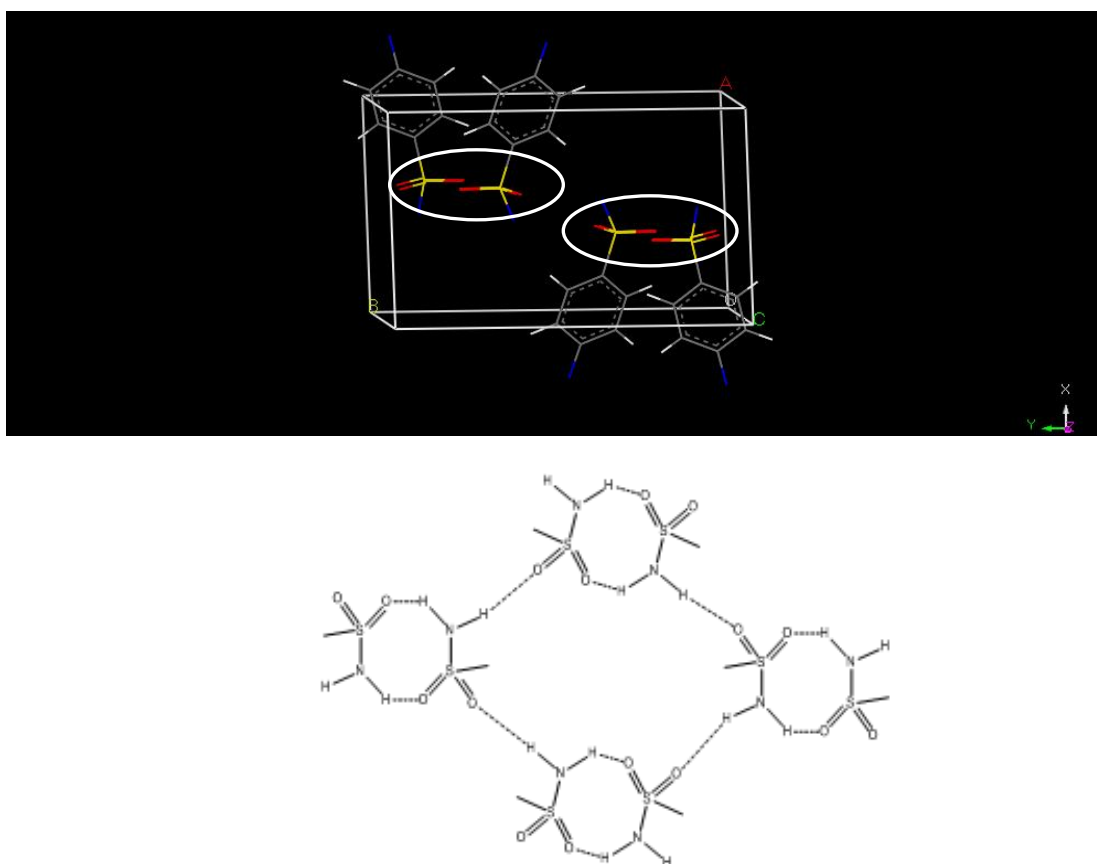
Figure 5. 44 The unit cell structure of SFN-γ (above), with dimers formed between sulfonamide groups. The packing motif of SFN-γ (below), based on N-H···O interactions, shows four dimers and a ring structure linking the dimers. For clarity, molecules are represented by the sulfonamide groups. *Colour code: grey-carbon, white-hydrogen, blue-nitrogen, red-oxygen and yellow-sulphur.*

The unit cell structure and the packing motif of SFN-β is shown in Fig 5.45. The crystal packing of SFN-β is not composed of dimers but two ring structures based on the NH…O bond. Similar to SFN-γ , the packing motif of two ring structures has been constructed based on two unit cells.
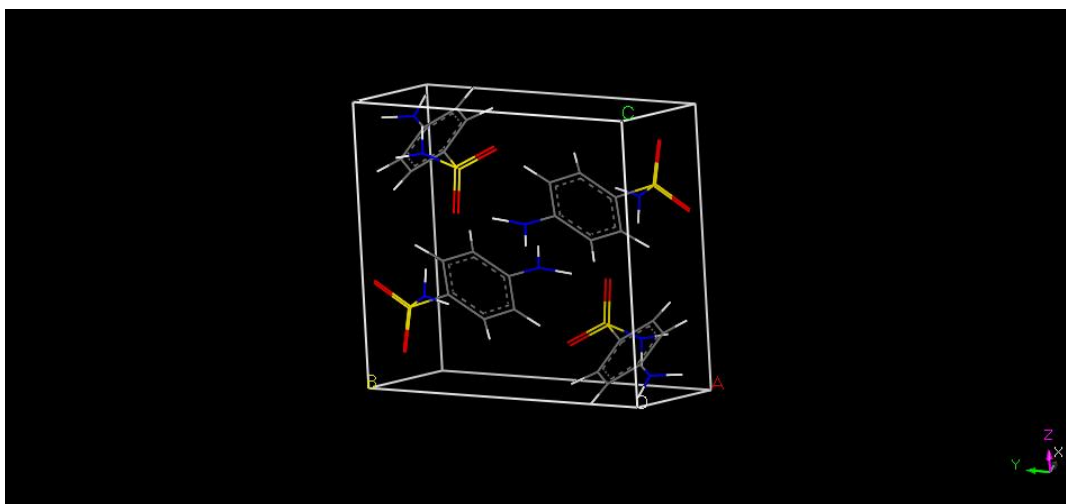
Figure 5.45 The unit cell structure of SFN-β (above), with dimers formed between sulfonamide groups. The packing motif of SFN-β based on N-H⋯O interactions, showing the two types of ring structures. For clarity, molecules are represented by the sulfonamide groups. *Colour code: grey-carbon, white-hydrogen, blue-nitrogen, red-oxygen and yellow-sulphur.*

In both polymorphs the packing motif arising from the NH...O interaction between sulfonamide groups is linked to the same motif via hydrogen bonding between aniline and sulfonamide groups. Fig 5.46 shows the hydrogen bonds of the form NH···N and NH···O that link the sulfonamide ring structure. Therefore, a recurring feature of the packing in both forms of SFN is the presence of NH...O hydrogen bonded chains of adjacent sulfonamide groups, and aniline-sulfonamide group hydrogen bond interactions[25]. However, for SFN-γ, the sulfonamide NH...O bond is shorter (and therefore stronger) than both aniline hydrogen bonds. The opposite is true for SFN-β[25].

Furthermore, by NMR studies the chemical environment experienced by the aniline nitrogen is very similar in the solid and solution states, and SFN-γ shows greater mobility of the phenyl ring [26]. The higher mobility of the phenyl ring, and the weaker aniline hydrogen bonds in SFN-γ, can increase the surface accessibility of the NH_2 group. This could therefore explain the more basic surface of SFN-γ compared to SFN-β.
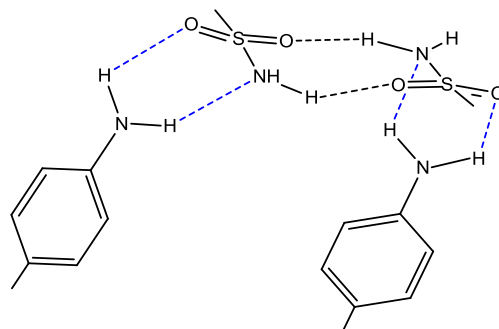
Figure 5.46 Hydrogen bonding of the form NH···N and NH···O that links the sulfonamide ring structure. Aniline hydrogen bonds are represented by blue dashed lines and sulfonamide hydrogen bonds are represented by black dashed lines. Molecules are represented by sulfonamide groups and aniline groups for clarity.

The dye-surface interactions that allow for differentiation of SFN polymorphs are shown in Scheme 1.5, 1.6 and 1.7.

$NH_3^+ PR^{2-}$ $SONH_3^+ PRH^-$ $SONH_3^+ PR^{2-}$ $NH_3^+ \cdot PRH$ **SCHEME 1.5**

$SONH_3^+ TBH^-$ $NH_3^+ TB^{2-}$ $NH_3^+ \cdot TBH$ **SCHEME 1.6**

MRH $NH_3^+ MR^-$ $SONH_3^+ MR^-$ **SCHEME 1.7**
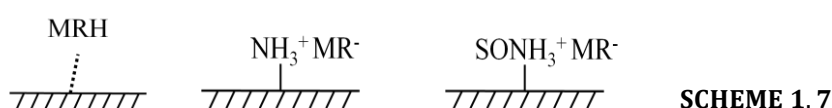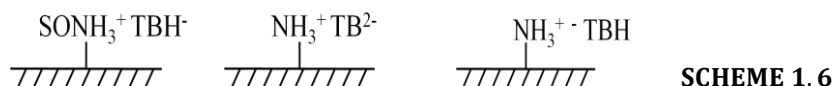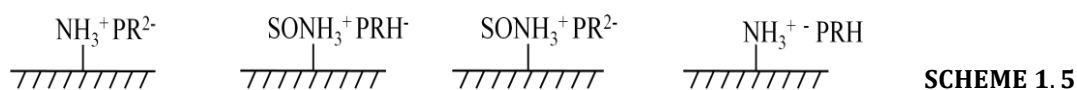
For PR adsorption, SFN-γ shows a higher extent of deprotonation, which is suggestive of a higher concentration of surface base sites, and in particular the $-NH_2$ site. For TB adsorption, both forms show protonation of sulfonamide and amine groups as the dominant dye-surface interactions. However, differential colouration is attributable to the further deprotonation by $-NH_2$.

For MR adsorption, both forms show protonation of sulfonamide and amine groups as the dominant dye-surface interaction. Nevertheless, interaction of the surface of SFN-β with zwitterionic MR, possibly by hydrogen bonding, causes differential colouration.

5.3.7 DRVS of furosemide polymorphs- crystal structure and surface characterisation

The DRVS spectra of PR-treated FRS polymorphs are displayed in Fig 5.47. The yellow coloured samples both show similar spectra. A single band at 450 nm corresponding to monovalent PRH^- is evident, but is red-shifted when compared to the solution value of 433 nm. The surface acidity of both forms are very similar by PR, and the absence of the divalent species could be a natural consequence of its acidity ($pK_a = 3.04 \pm 0.36$).
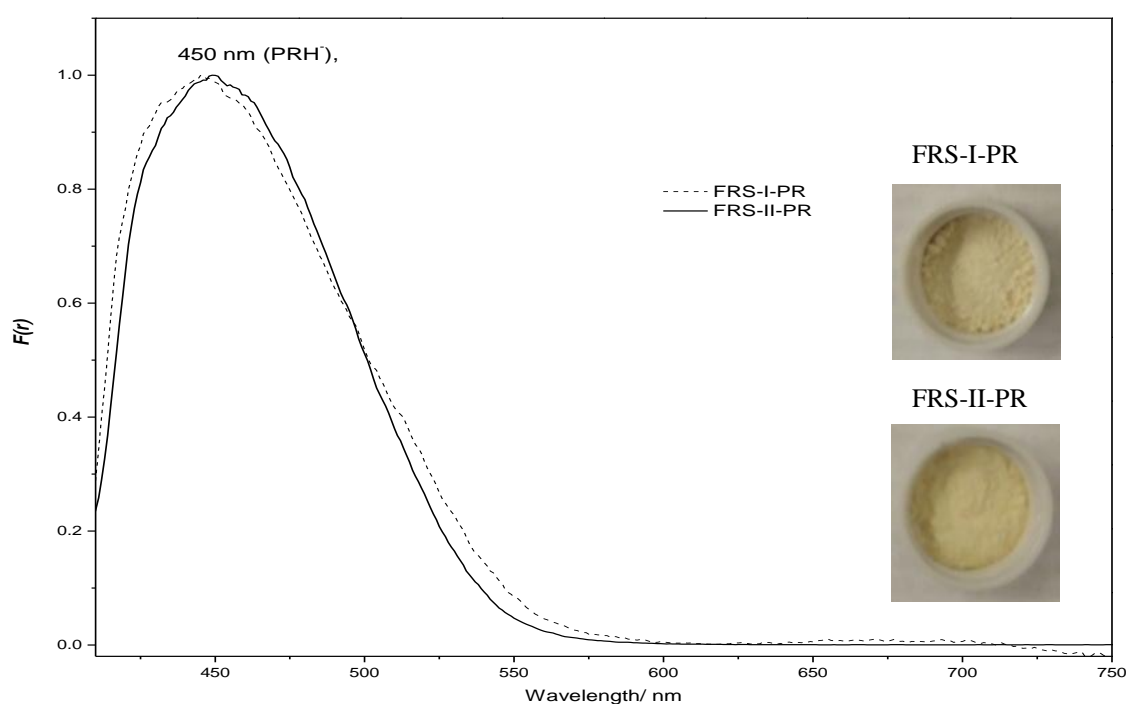
Figure 5. 47 Normalised DRVS spectra of dye treated FRS samples; FRS-II-PR (solid line) and FRS-I-PR (dashed line).

The DRVS spectra of TB-treated FRS polymorphs are displayed in Fig 5.48. Orange coloured FRS-I-TB absorbs at 444 nm and 545 nm which correspond to TBH$^-$ (434 nm in solution) and TBH$_2$ (557 nm in solution) respectively. Orange FRS-II-TB also shows two bands at 451 nm and 556 nm which are also attributed to TBH$^-$ and TBH$_2$. The unionised species is more prevalent in the FRS-I sample compared to FRS-II
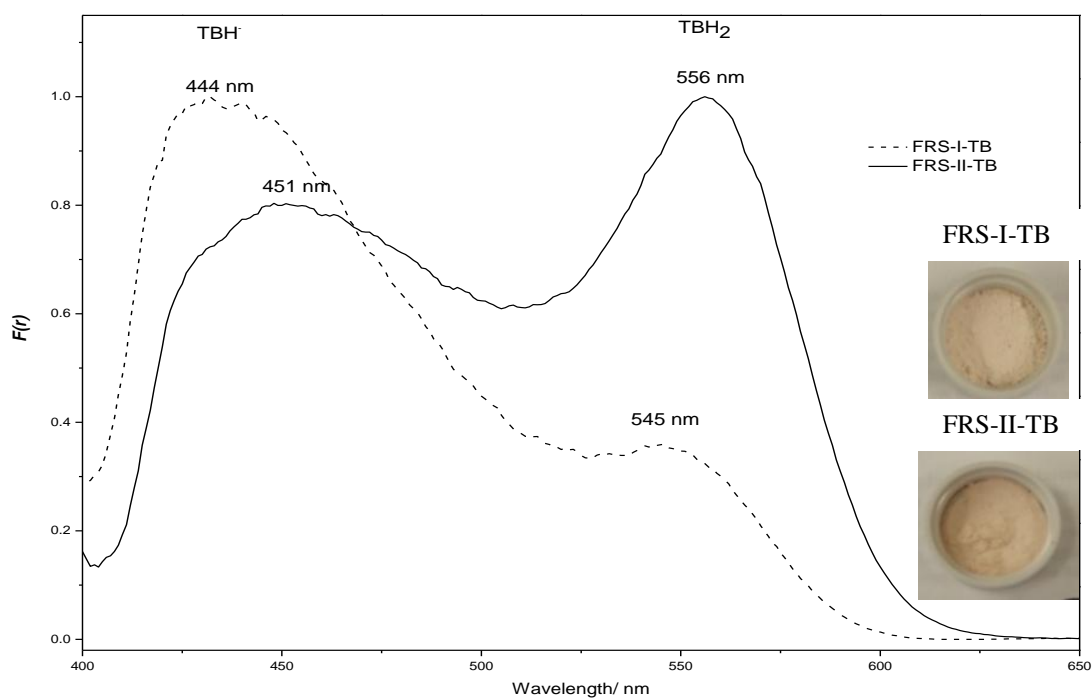
Figure 5. 48 Normalised DRVS spectra of dye treated FRS samples; FRS-II-TB (solid line) and FRS-I-TB (dashed line).

The observed colour polymorphs of FRS treated with MR indicator is pink. DRVS spectra are shown in Fig. 5.49. The λ_{max} values of 521 nm and 531 nm are observed for FRS-I-MR and FRS-II-MR respectively. The band in both samples could well be the neutral and/or protonated MR species (solution λ_{max} of 490 nm and 525 nm respectively). A shoulder band at 561 nm is seen for FRS-I-MR and FRS-II-MR, indicative of the zwitterionic form (solution value of 550 nm).
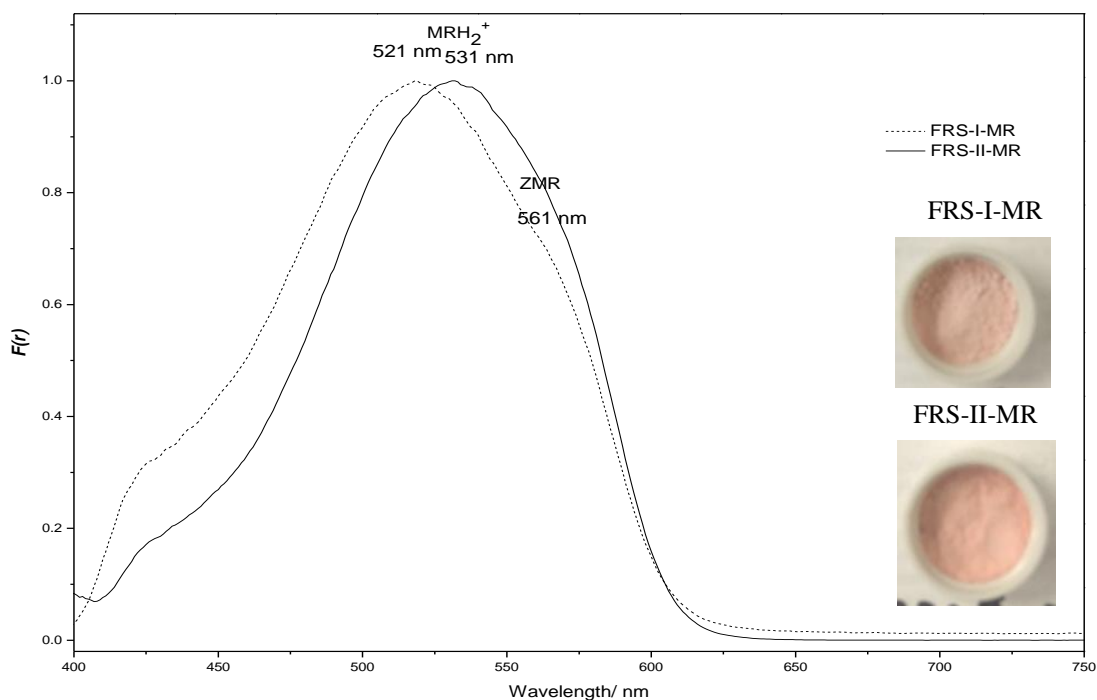
Figure 5. 49 Normalised DRVS spectra of dye-treated FRS samples; FRS-I-MR (solid line) and FRS-II-MR (dashed line).

<u>Discussion</u>

The polymorphs of FRS showed the strongest acidic character compared to the other polymorphic systems studied herein. In the spectra for PR, both polymorphs show only the PRH- species, and this indicates that FRS surfaces do not contain acidic sites greater in strength than the sulphonic acid group (pK_a -0.90±0.30).

For TB adsorption, there is a high proportion of TBH_2 present, even though the molar dye loading is lower. This suggests the presence of strong acid sites, rather than the physical adsorption of dye molecules due to lack of available acid sites. The acidic sites on FRS therefore have a comparable strength to the TB sulphonic acid group.

For MR the protonated and zwitterionic species dominate.

FRS has three main acid/base functional groups, namely carboxylic acid (pKa 3.04±0.36), sulfonamide (pKa 9.79±0.60 - weak acid; pKa -7.72±0.70- extremely weak base) and secondary amino group (pKa -2.49±0.36- extremely weak base). The dominance of the carboxylic acid groups relative to the other two acid/base groups could therefore be responsible for the surface acidic character of FRS samples.

As the crystal structure of FRS-II is unavailable, it is not possible to examine the fundamental differences or similarities in crystal structure for both FRS polymorphs. However, dye adsorption, especially of TB, reveals that FRS-II has a higher surface acid content. The unit cell structure for FRS-I is shown Fig 5.50. Four molecules and their intermolecular interactions represented by centrosymmetric sulfonamide N-H⋯O dimers associated by hydrogen bonds involving a single sulfonamide O atom are illustrated[27].
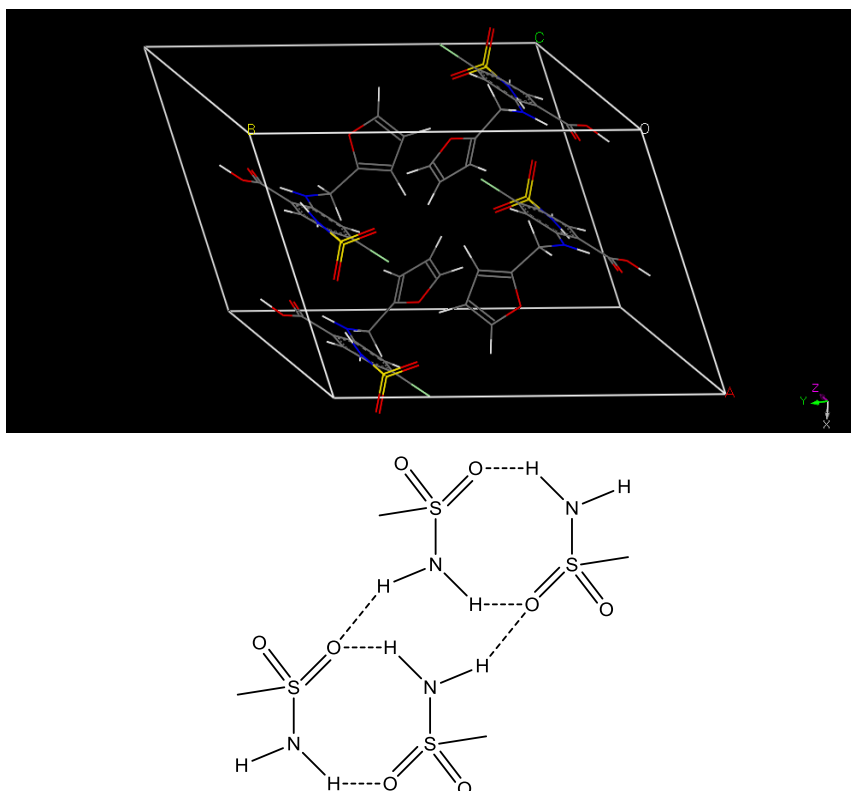
Figure 5. 50 The unit cell structure of FRS-I (above) showing four molecules and their intermolecular interactions represented by centrosymmetric sulfonamide N-H⋯O dimers associated by hydrogen bond involving a single sulfonamide O atom.

As the acidic character of the surfaces of FRS samples could be attributable to carboxylic acid groups, its packing motif should be considered. The carboxylic acid group forms mutual hydrogen bonded dimers (Fig 5.51) as well as intramolecular hydrogen bonds with adjacent amino hydrogen atoms, forming a rigid anthranilic acid moiety[27]. These dimer units extend via weak C-H…O interactions between furfuryl oxygen and aryl hydrogen to form a corrugated sheet structure (Fig 5.52). This corrugated structure involving carboxylic acid could explain the lower content of this group on the surface compared to FRS-II.
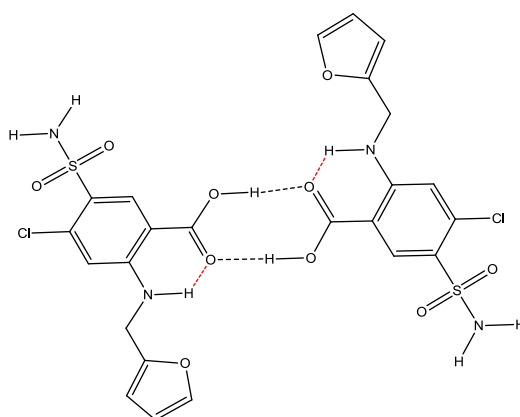
Figure 5.51 Hydrogen bonded dimer between carboxylic acid groups in FRS-I. Carboxylic acid hydrogen bond is represented by black dashed line and the intramolecular hydrogen bond between C=O and secondary amine H is represented as red dashed line.
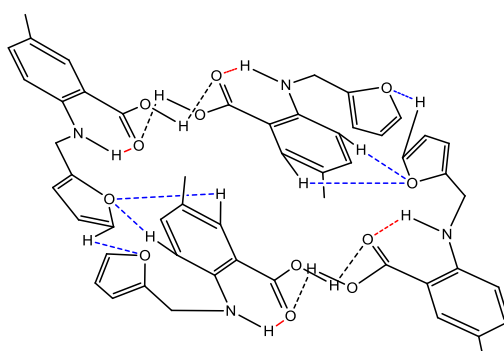
Figure 5. 52 Corrugated sheet structure formed by carboxylic acid groups in FRS-I Carboxylic acid hydrogen bonds are represented by a black dashed line, the intramolecular hydrogen bond between C=O and a secondary amine H is represented as red dashed line and the weak C-H…O interactions between furfuryl O and aryl H are represented by a dashed blue line.

5.4 Concluding remarks

The differentiation of two polymorphs each of IMC, CBZ, CFN, FRS and SFN by the DRVS analysis of adsorbed PR, TB and MR dyes have been shown. High purity solids (>99%) were used so as to eliminate or minimise the effect of surface impurities on dye-surface interactions. The effect of adsorbed water on surface-dye interactions was not comprehensively studied, but all polymorphic systems are non-hygroscopic. They adsorb less that 0.2% water even at 77% RH. DRVS measurements were obtained for samples that had been stored at 0% RH.

Visual differentiation by colouration of the polymorphs by at least two of the probe pH indicator dyes was achieved. This is strongly indicative of the variation in acid/base surface chemistry among the polymorphs. Whilst pKa values are not strictly appropriate for adsorption on solid surfaces, strength of the acid or base groups of the drug molecules have been used to explain the behaviour of the adsorbed dyes.

The surface (based on the crystal structure and molecular packing) can influence the accessibility of acid/base molecular functionalities. Differential coloration of the dye adsorbed by the metastable polymorph showed a greater extent of dye deprotonation when compared to the stable polymorph. Good correlation in terms of relative extent of deprotonation of sulfonphthalein dyes by polymorphic pairs was observed, except for CFN polymorphs.

The dynamic orientational disorder displayed by caffeine molecules in both polymorphic forms could be the reason for some of the observed anomalies. The relative extent of deprotonation of sulfonphthalein dyes by the polymorphic pairs for drug substances with very weak acidic/basic character (such as CFN and CBZ), did not agree with that for the azo dye, methyl red. This difference indicates that MR could be responding to hydrogen bonding potential instead of surface acidity.

CFN polymorphs gave DRVS absorption bands for yellow PR and TB close to solution values (within ±3nm) while other polymorphic system's DRVS absorption bands are red-shifted by ≥10 nm with respect to solution values. This could reflect the positional disorder present in the caffeine molecule.

High purity (>99%) drug substances were used in this study and the DRVS results presented herein are for polymorphs that have been prepared according to crystallisation conditions discussed in Chapter 4. The effect of changes in surface area, crystal defects, particle size/morphology and preparing polymorphs using other crystallisation techniques (such as supercritical fluid technology) on the DRVS spectra have not been determined. However for polymorphs prepared using the methods given in chapter 4, good reproducibility was observed.

5.5 References

1. M. Puppedi, E. Zannou, M. Vasanthavada, A. Dontabhaktuni, A. Royce, Y. Joshi and A. Serajuddin, *Journal of Pharmaceutical Sciences*, 2008, **97**, 1831-1842.

2. B. W. Glombitza, D. Oelkrug and P. C. Schmidt, *European Journal of Pharmaceutics and Biopharmaceutics*, 1994, **40**, 289-293.

3. B. W. Glombitza and P. C. Schmidt, *European Journal of Pharmaceutics and Biopharmaceutics*, 1995, **41**, 114-119.

4. C.-A. Scheef, D. Oelkrug and P. C. Schmidt, *European Journal of Pharmaceutics and Biopharmaceutics*, 1998, **46**, 209-213.

5. R. Govindarajan, A. Zinchuk, B. Hancock, E. Shalaev and R. Suryanarayanan, *Pharmaceutical Research*, 2006, **23**, 2454-2468.

6. P. Major, *PhD Thesis* University of Greenwich, Kent, 2010.

7. C. Drummond, F. Grieser and T. Healy, *Journal of the Chemical Society, Faraday Transactions 1*, 1989, **85**, 561-578.

8. D. E. Cohen, J. B. Benedict, B. Morlan, D. T. Chiu and B. Kahr, *Crystal Growth & Design*, 2007, **7**, 492-495.

9. G. Seu, *Dyes and Pigments*, 1995, **29**, 227-240.

10. C. Reichardt, *Chemical Reviews*, 1994, **94**, 2319-2358.

11. C. Reichardt, *Pure and Applied Chemistry*, 2004, **76**, 1903-1919.

12. C. Reichardt, *Pure and Applied Chemistry*, 2008, **80**, 1415-1432.

13. Z. Wu, H. Joo, I.-S. Ahn, S. Haam, J.-H. Kim and K. Lee, *Chemical Engineering Journal*, 2004, **102**, 277-282.

14. S. Brunauer, P. H. Emmett and E. Teller, *Journal of the American Chemical Society*, 1938, **60**, 309-319.

15. Anonymous, Solubility Information for Products, http://www.sigmaaldrich.com/united-kingdom/technical-services/uk-technical-services1.html, Accessed 25th July, 2010.

16. R. Giustetto and O. Wahyudi, *Microporous and Mesoporous Materials*, 2011, **142**, 221-235.

17. P. J. Cox and P. L. Manson, *Acta Crystallographica Section E-Structure Reports Online*, 2003, **59**, O986-O988.

18.   X. Chen, K. R. Morris, U. J. Griesser, S. R. Byrn and J. G. Stowell, *Journal of the American Chemical Society*, 2002, **124**, 15012-15019.

19.   F. C. K. Chiu and C. M. Y. Lo, *Journal of the American Society for Mass Spectrometry*, 2000, **11**, 1061-1064.

20.   A. L. Grzesiak, M. D. Lang, K. Kim and A. J. Matzger, *Journal of Pharmaceutical Sciences*, 2003, **92**, 2260-2271.

21.   R. J. Roberts and R. C. Rowe, *International Journal of Pharmaceutics*, 1996, **129**, 79-94.

22.   F. Tian, T. Rades and N. Sandler, *AAPS PharmSciTech*, 2008, **9**, 390-394-394.

23.   G. D. Enright, V. V. Terskikh, D. H. Brouwer and J. A. Ripmeester, *Crystal Growth & Design*, 2007, **7**, 1406-1410.

24.   M. Descamps, N. l. T. Correia, P. Derollez, F. Danede and F. d. r. Capet, *The Journal of Physical Chemistry B*, 2005, **109**, 16092-16098.

25.   T. Gelbrich, A. L. Bingham, T. L. Threlfall and M. B. Hursthouse, *Acta Crystallographica Section C*, 2008, **64**, o205-o207.

26.   A. Porteri, R. Harris, R. Fletton, R. Lancaster and T. Threlfall, *Magnetic Resonance in Chemistry*, 2004, **42**, 313-320.

27.   N. J. Babu, S. Cherukuvada, R. Thakuria and A. Nangia, *Crystal Growth & Design*, 2010, **10**, 1979-1989.

Chapter 6: Investigation of the surface chemistry of indomethacin polymorphism by morphology simulation

6.1 Introduction

The differentiation of drug polymorphs by dye adsorption and diffuse reflectance visible spectroscopy (DRVS) has been demonstrated in Chapter 5. The nature of the interaction of dye with the surface of the polymorphs, and hence the resulting colour, is governed by the surface chemistry. Knowledge of the surface structure at a molecular level is therefore vital in understanding the mechanism for the differential colouration of polymorphs by adsorbed dye molecules.

Given the crystal structure (obtained by single crystal or powder X-ray diffraction methods) and the Miller index, the surface structure of any exposed crystal face can be determined. For large crystals (~1 cm) the Miller index of individual faces can be obtained directly by single crystal X-ray crystallography or reflecting goniometry[1]. For micro-crystallites, their small size precludes indexing of the exposed faces by single crystal X-ray crystallography or reflecting goniometry. However *in silico* calculation of crystal morphology can be used[1, 2].

The simulation of crystal morphology is based on single crystal data and crystal growth algorithms. The validity of the results generated by computer modelling can be examined experimentally. The calculated morphology can be examined by microscopy (SEM/ optical), the Miller indices of the dominant faces can be examined by powder X-ray diffraction[2, 3], and the surface functional groups (especially of the dominant faces) can be examined by contact angle measurements or hygroscopicity studies. Contact angle is a quantitative means of assessing the wettability of a surface by a probe liquid. The lower the angle of contact the probe liquid makes with the solid surface the better the wetting, and for higher contact angles the poorer the wetting.

In this chapter the surface structure of powdered samples of indomethacin (IMC) polymorphs have been investigated.

The crystal morphologies and surface structures for both forms IMC-α and IMC-γ were modelled using the commercially available morphology simulation program, Materials Studio version 5.1 (Accelrys Inc., San Diego, CA, USA).

The results of computer modelling were examined by SEM, X-ray diffraction and contact angle measurements to validate morphology, Miller indices and surface chemistry, respectively. The water uptake by the polymorphs was also examined to supplement contact angle studies.

6.2 Experimental procedures

6.2.1 Materials

Indomethacin polymorphs, IMC-α and IMC-γ were prepared as detailed in section 4.2.2.1 (Chapter 4).

6.2.2 Computer modelling of crystal morphology and crystal surface by the growth morphology model

Commercially available morphology modelling software such as Materials Studio 5.1 has been developed to predict the external morphology of a crystalline material from its internal crystal structure. Crystals form by growth and attachment of molecular layers (growth slices) to a growing crystal surface. The growth morphology model has been successfully applied to predicting crystal morphology of organic crystals. It combines energetics and intermolecular bonding patterns to predict the shape of crystals and the structure of exposed surfaces from single crystal [4].

The growth morphology model assumes that the growth rate of the crystal face (or slice) is proportional to its attachment energy. Therefore, faces with the lowest attachment energies are the slowest growing and, therefore, have the most morphological importance[5]. The attachment energy E_{att}, which is the energy per molecule released when a new slice of depth d_{hkl} is attached to a growing crystal surface is expressed in Equation 6.1[6].

$$E_{att} = E_{latt} + E_{slice}$$ Equation 6.1

where E_{latt} = Lattice energy of the crystal E_{slice} = Energy of a growth slice of thickness d_{hkl}. E_{slice} is the sum of energy of all bonds per mole within the slice.

The energies of bonds that interconnect the individual slices make up E_{att}. In molecular crystals, the sum of the bond energies over all bonds in a crystal adds up to the lattice energy E_{latt}. E_{att} is calculated for a series of stable (suitable) slices which can be chosen by the construction of a crystal graph.

The crystal graph is a network of strong attractive bonds in the crystal, from which growth slices or planes are built. The crystal graph functionality can be used to create interactions between molecular fragments in a crystal. Once the crystal graph is defined, it is in principle possible to generate all two-dimensional connected nets of strong crystal bonds. The attachment energy is calculated for all connected nets. From the attachment energy calculation, and hence the growth rate, a centre-to-face distance is assigned to each face. This information is used to deduce the morphology using a Wulff plot[7]. If more than one connected net exists for given Miller indices {*hkl*}, the most stable (the lowest absolute value of the attachment energy) is defined as the growth plane.

Force field type and parameters must be selected in order to allow for the morphology calculation. A force field is a mathematical expression that describes the potential energy of a system using energy terms for covalent and non-covalent intermolecular forces (e.g. van der Waals, hydrogen bonding and electrostatic or coulombic interactions) and parameters sets such as atomic mass, van der Waals radius and bond lengths and angles. This model is based on the assumption that no surface relaxation takes place. This has been shown to be significant in the case of inorganic systems such as the oxides of iron and aluminium, but works well in the case of many organic molecular systems where surface relaxation is not significant.

The morphology simulation and analysis were performed using the Morphology module, integrated into the Materials Studio version 5.1 (Accelrys Inc., San Diego, CA, USA). The computational procedures are as follows:

- Geometric optimisation of crystal structure: polymorph structures in crystal structure file formats were loaded from the CCSD and geometrically optimised. Geometry optimisation ensured that the bond types in the molecules were chemically correct.

- The Dreiding force field was selected. It contains a term that describes hydrogen bond interactions explicitly.

- The atom-based summation method was selected for van der Waals, electrostatic and hydrogen bond interactions, with a real space cut-off distance set at 20Å.

6.2.3 Powder X-ray diffraction (PXRD)

Powder x-ray diffraction data were obtained at room temperature on a Bruker D8 advanced X-ray diffractometer (Figure 6.1) fitted with a goniometer with a θ-θ geometry and exit slits. The copper Kα radiation (λ=1.54056Å) used was generated at a power of 40 kW and 40 mA. The data was collected over an angular range of 5° to 35° 2θ and a scan rate of 0.05° per second. Approximately 0.1mg of sample was sprinkled on a zero background obliquely cut silicon crystal (Figure 6.1) using a spatula. The silicon crystals have been cut such that they do not diffract X-rays. Measurements were performed in triplicate.

Figure 6. 1 Bruker D8 advanced X-ray diffractometer fitted with a goniometer with a θ-θ geometry (*left*). Zero background obliquely cut silicon crystal (*right*).

6.2.4 Scanning electron microscopy (SEM)

SEM micrographs of all samples were obtained using a Cambridge Instruments Stereoscan 360 at an accelerating voltage of 20 kV. Secondary electron images were collected from samples sputter coated in gold (2 minutes at 1kV, 30mA, Edwards S150B).

6.2.5 Contact angle measurement by capillary rise method

The contact angle made by a probe liquid with a surface reflects the physical and chemical composition of the surface. The contact angle is measured directly by goniometry as the angle between three phases i.e. liquid-surface-air.

A high contact angle means poor wetting and vice versa. The indirect dynamic method for measuring contact angle (or advancing contact angle) frequently applied to powder-form solids is the capillary rise method. In the capillary rise experiment, a glass tube with a filter base is filled with the powder to be measured, and this is suspended from a balance as it is lowered into a vessel containing the liquid (see Fig 6.2). After the glass tube has contacted the liquid, the speed at which the liquid rises though the bulk powder is measured by recording the increase in mass as a function of time. The experimental set-up for the capillary-rise method is shown in Fig 6.2.
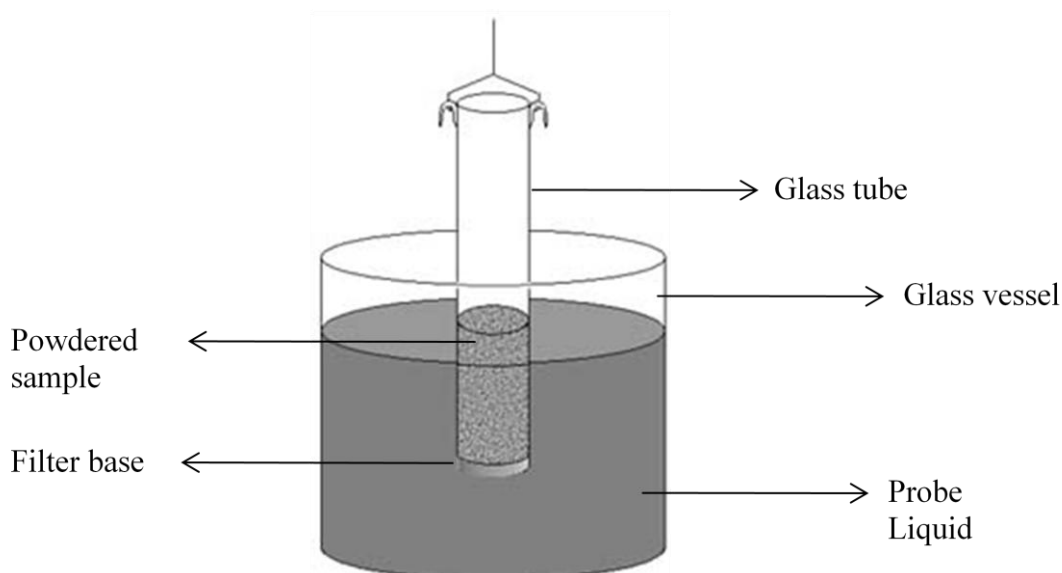
Figure 6.2 The experimental set-up capillary-rise method to calculate the contact angle of powdered samples**.**

When liquid rises through a bulk powder, the powder could be regarded as a bundle of capillaries. This means that for the calculation of the advancing angle, the Washburn equation which applies to capillaries can be used:

$$h^2 = \frac{(k.\bar{r})\,\cos\theta\gamma_{liq}}{2\eta}\,t \qquad\qquad \text{Equation 6.2}$$

Where h is the height of the powder in the tube wetted by the liquid; the constant k describes the orientation of the capillaries; $\bar{r}$ is the mean capillary radius; η is the viscosity of the liquid; γ_{liq} is the surface tension of the liquid; θ is the advancing contact angle and t is the flow time. $(k.\bar{r})$ is a constant that depends on the packing density of the powdered sample.

The wetted length term is related to the mass of penetrating liquid, m_{liq} as expressed in equation 6.3.

$$h = \frac{m_{liq}}{A.\rho_{liq}} \qquad \text{Equation 6.3}$$

where A is the area through which the liquid flows, ρ_{liq} the density of the liquid and m_{liq} the mass of the penetrating liquid.

By substituting h into Equation 6.2, one obtains an expression shown in equation 6.4. This can be used to analyse results obtained by capillary rise experiments that measures increase in mass as a function of time.

$$m_{liq}^2 = \frac{(A.k.\bar{r})\ \rho_{liq}^2 \cos\theta\, \gamma_{liq}}{2\eta} t \qquad \text{Equation 6.4}$$

The new product term $(A.k.\bar{r})$ is known as the capillary constant C for a given powder packing. C is a measure of the geometry of the spaces or pores between particles in the sample.

A typical mass^2 versus time plot for capillary rise experiment is shown in Fig 6.3. The slope of the linear region (stage 2) is used for the determination of contact angle and capillary constant. Four main stages are identified. Stage 1 is the initial stage where the weight gain is influenced by the mesh materials used to hold the powdered sample in the tube. In stage 2 the weight gain is influenced by the wetting of the particle surfaces. The slope of stage 2 is the important parameter used to calculate capillary constant and contact angles. In Stage 3 intra and inter particle spaces are filled and in stage 4 all the spaces have been filled and weight gain is fairly constant. It is not unusual for stage 2 and stage 3 to be indistinguishable in a capillary rise experiment because of the nature of the probe liquid and sample interactions.
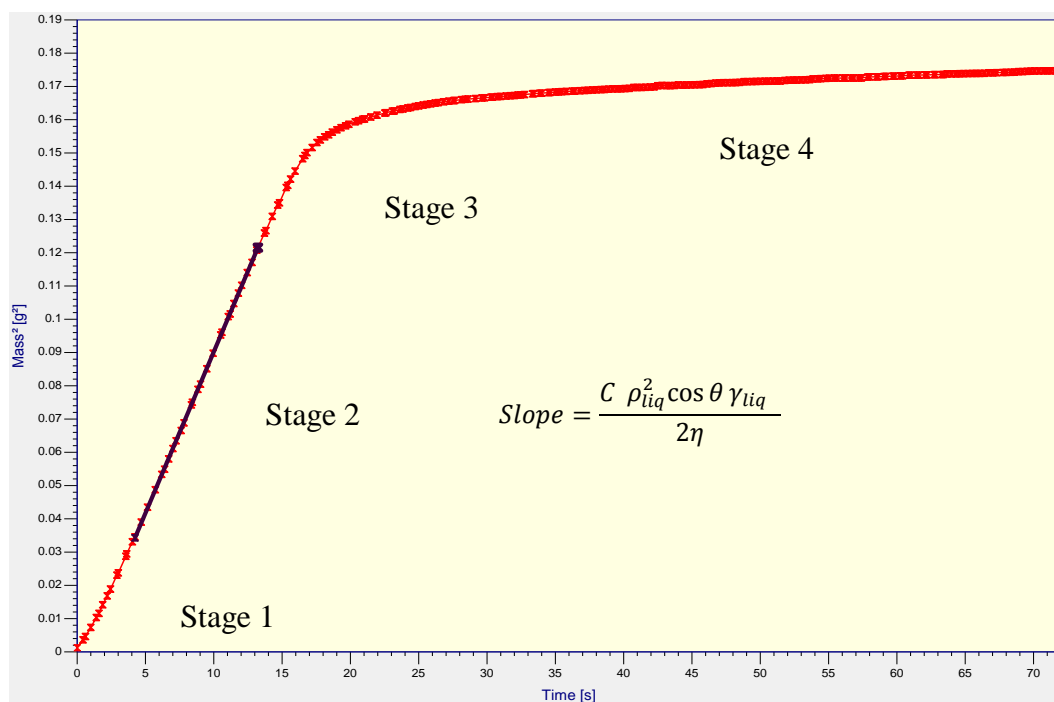
Figure 6. 3 A typical mass^2 versus time plot from a capillary rise experiment. Stages 1-4 are explained in the text.

The capillary constant can be determined for any sample under perfect wetting conditions i.e. advancing angle $\theta = 0°$, using an optimally wetting liquid e.g. hexane. The determination of the capillary constant using the optimal wetting liquid is performed first. Then the advancing contact angles for other liquids can be determined using the capillary constant. The validity of the capillary rise method is subject to certain conditions:

- laminar flow exists in the bulk material,
- density of the powder is uniform,
- the capillary constant and structure of the bulk material remains constant during the measurement.

Capillary rise measurements were performed using a KRUSS K100 tensiometer equipped with an electronic balance with a sensitivity of 0.005 g. A glass tube of 0.8 cm diameter and 6 cm length was filled with sample, 1 g in the case of IMC-γ and 0.6g for IMC-α. The glass tube was closed at the bottom by a filter paper fixed by a stainless steel ring. The powder bed was settled by tapping the tube gently on a bench.

Probe liquid (80 ml) was placed in the glass vessel of volume 121.5 ml. The glass tube containing the sample was mounted on the electronic balance, and was then immersed into the probe liquid at a depth of 2.0 mm. The weight gain was recorded, taking 3 measurements per second for 300 seconds.

The rate of penetration of probe liquid up the powdered sample bed was recorded as a plot of mass^2 versus time. The capillary constant using hexane was determined as an average of three consecutive measurements on a sample. Contact angle measurements of IMC-α and IMC-γ using ethylene glycol, water and formamide were made in duplicate.

6.2.6 Hygroscopicity studies of indomethacin polymorphs

Hygroscopicity studies involve investigation of the rate and extent of water uptake at certain relative humidity (RH) values and temperatures. The extent of the interaction between water molecules and a surface depends on how hydrophilic the surface is. Hygroscopicity studies can therefore provide insight into the polarity of a surface. The water uptake by the polymorphs was achieved by traditional water vapour sorption analysis. The sample of interest is placed in a dessicator over a saturated salt solution of the desired RH and the increase in sample weight is monitored over a given time. Indomethacin polymorphs which had been stored at 0% RH over calcium chloride were accurately weighed to approximately 0.5 g and placed in a dessicator equilibrated at 23.5ºC and 77% RH. The RH condition in the dessicator was achieved using a saturated solution of ammonium phosphate. Weight changes were monitored at intervals over 12 days. The polymorphic purity of the samples was established using PXRD, DSC and Raman.

6.3 Results and Discussion

6.3.1 Computer simulated morphology

The simulated morphologies for IMC-α and IMC-γ were a needle and a plate, shown in Fig 6.4(a) and Fig 6.5(a) respectively. The observed morphologies of IMC-α and IMC-γ from SEM are also shown in Fig 6.4(b) and Fig 6.5(b) respectively. The observed and simulated morphology for both polymorphs show good agreement. These results show the validity of the computer simulation for the determination of crystal morphology.

(a)
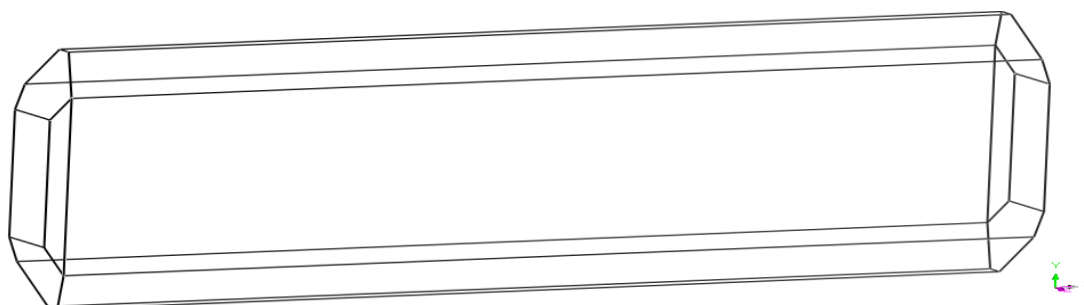
(b)
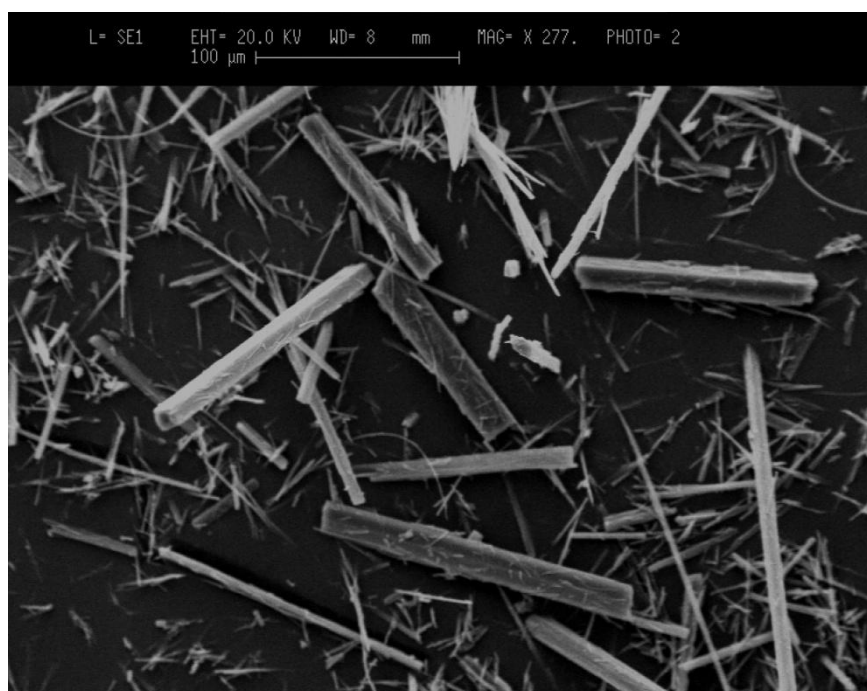
Figure 6.4 The (a) simulated and (b) observed needle morphology of IMC-α.

(a)
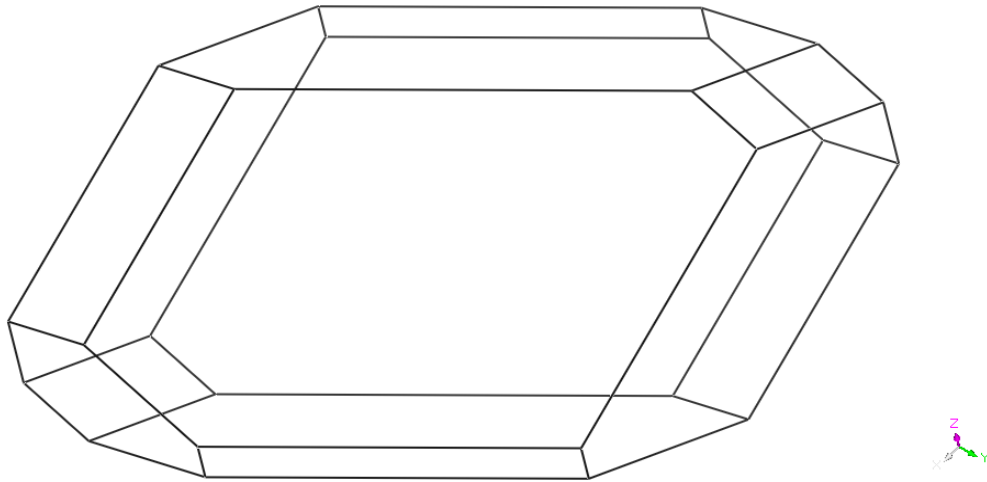
(b)
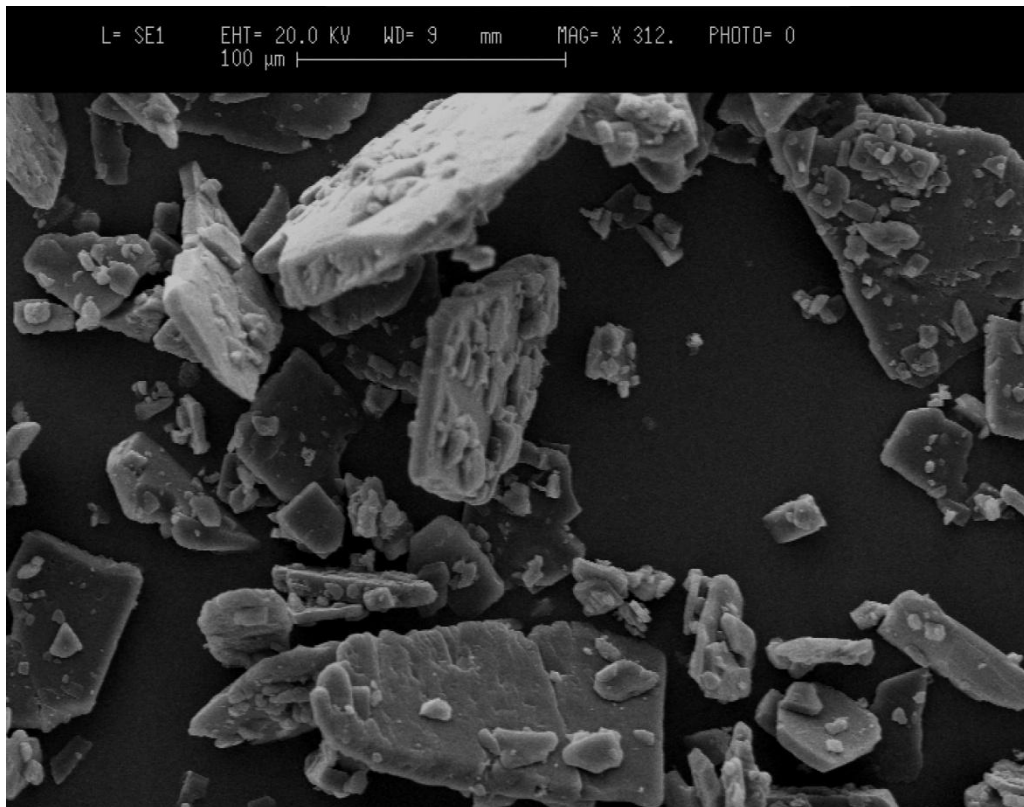
Figure 6.5 The (a) simulated and (b) observed plate morphology of IMC-γ

6.3.2 Powder X-ray diffraction study of morphologically dominant crystal faces

The morphology of the crystals of IMC-α (needle) and IMC-γ (plate) are inherently predisposed to preferred orientation. This means that crystallites will lie exposing their most dominant face, thereby causing the PXRD intensities corresponding to these dominant faces (and their family of planes) to be overstated. PXRD studies on a few crystals which have been carefully aligned to promote the preferred orientation enables the dominant faces in the simulated morphologies of both polymorphs to be further examined.

Figure 6.6 shows the PXRD pattern for IMC-α. The most intense bands have been indexed using simulated PXRD data.

Figure 6. 6 The PXRD pattern for particles of IMC-α sprinkled on a zero background sample holder. Most intense bands have been index using simulated PXRD data.

Table 6.1 shows results of growth morphology modelling containing Miller indices of unique facets of the crystal, slice depth d_{hkl}, total attachment energy and attachment energy contributions from van der Waals (vdW), electrostatic (Electro) and hydrogen bond (H-bond) interactions and percentage total facet area. Nine unique facets namely (001), (011), (0-11), (020), (0-20), (100), (10-1), (110) and (1-10) have been calculated. It is worth noting that although 16 faces are simulated for IMC-α (Fig 6.5a) some faces belong to the same family. For example the 001 are 00-1 belong to the same family, and so have the same chemistry.

Table 6. 1 Data generated from growth morphology simulation for IMC-α

hkl	Slice depth d_{hkl} / Å	E_{att} (Total) /Kcalmol^{-1}	E_{att}(vdW) /Kcalmol^{-1}	E_{att}(Electro) /Kcalmol^{-1}	E_{att} (H-ond) /Kcalmol^{-1}	% Total facet area
0 0 1	18.099	-23.3695	-31.3469	7.838816	0.138627	56.4
0 1 1	14.722	-52.8483	-32.6817	-17.3901	-2.77659	15.3
0 -1 1	14.722	-52.8483	-32.6817	-17.3901	-2.77659	15.3
0 2 0	12.655	-84.4016	-48.6298	-35.8381	0.066395	2.2
0 -2 0	12.655	-84.4016	-48.6298	-35.8381	0.066395	2.2
0 2 1	10.3712	-97.292	-55.573	-38.937	-2.78177	-[*]
1 0 0	5.44565	-197.53	-141.588	-56.0075	0.065653	3.6
1 0 -1	5.32820	-196.693	-138.399	-58.3596	0.06554	1.5
1 1 0	5.32382	-201.906	-143.026	-58.9734	0.093303	1.8
1 -1 0	5.32382	-201.906	-143.026	-58.9734	0.093303	1.8

[*]*(0 2 1) is not one of unique facet calculated by the growth morphology model by is but is the most intense peak in the PXRD.*

The most intense peaks in the PXRD pattern correspond to 021, 020, 040 and 022 crystal planes, with intensity decreasing in that order. In terms of crystal morphology the (020) and (040) are coincidental and they are parallel to each other; their PXRD peaks have the same intensity. In the same vein, (022) and (011) are coincidental and are parallel to each other. From the simulated morphology, the three most dominant faces are (001), (011) and (0-11), with total facet areas of 56.4%, 15.3% and 15.3% respectively. In contrast, the most dominant facet according to PXRD is the (021) surface. However the (020) and (011) surfaces from PXRD match the calculated predictions.

The simulation data does not take into account the growth conditions. The crystals where grown by rapid crystallisation from a saturated ethanolic solution by the addition of cold water. This could kinetically hinder the growth of for example the 001 face which is the most dominant surface (56.4% of total surface area) in the simulated morphology. The attachment energies for the (021), (020) and (011) surfaces (-97.292, -84.402 and -52.848 Kcalmol^{-1} respectively) have higher absolute energies than (001) surface, so will grow faster.

Fig 6.7 shows the PXRD pattern for IMC-γ. The most intense bands have been indexed using simulated PXRD data. The three most intense diffraction peaks reflections correspond to (10-1), (020) and (022). The (020) and (022) planes are coincidental with the (010) and (011) respectively. The faces in from the simulated morphology calculation.
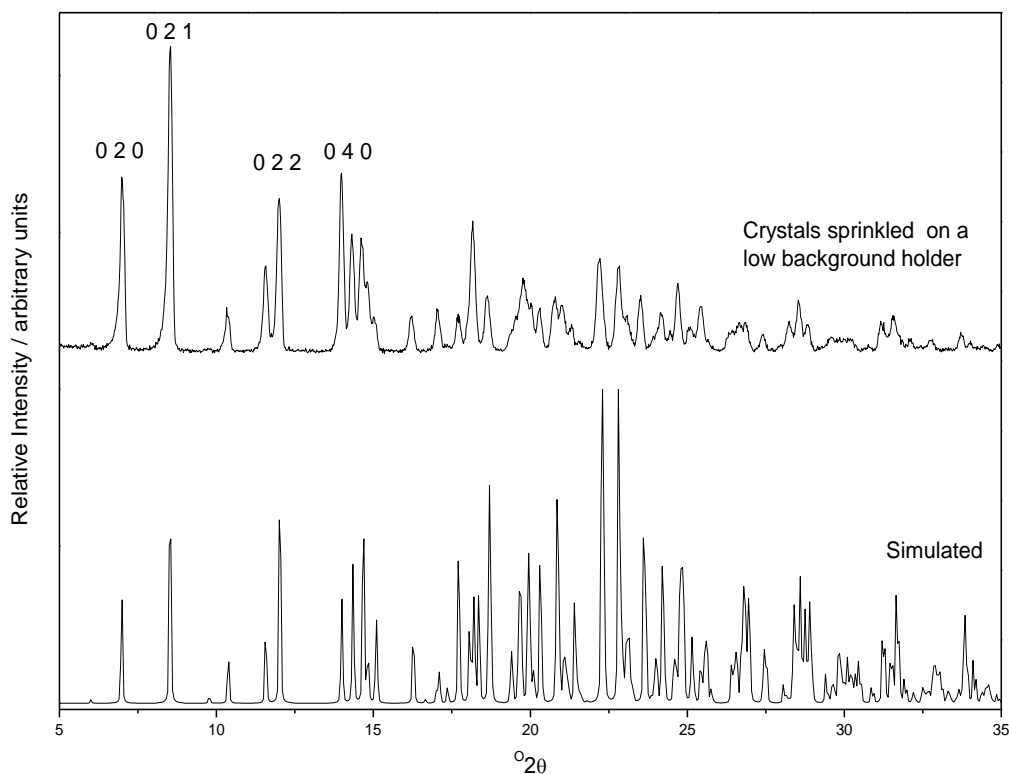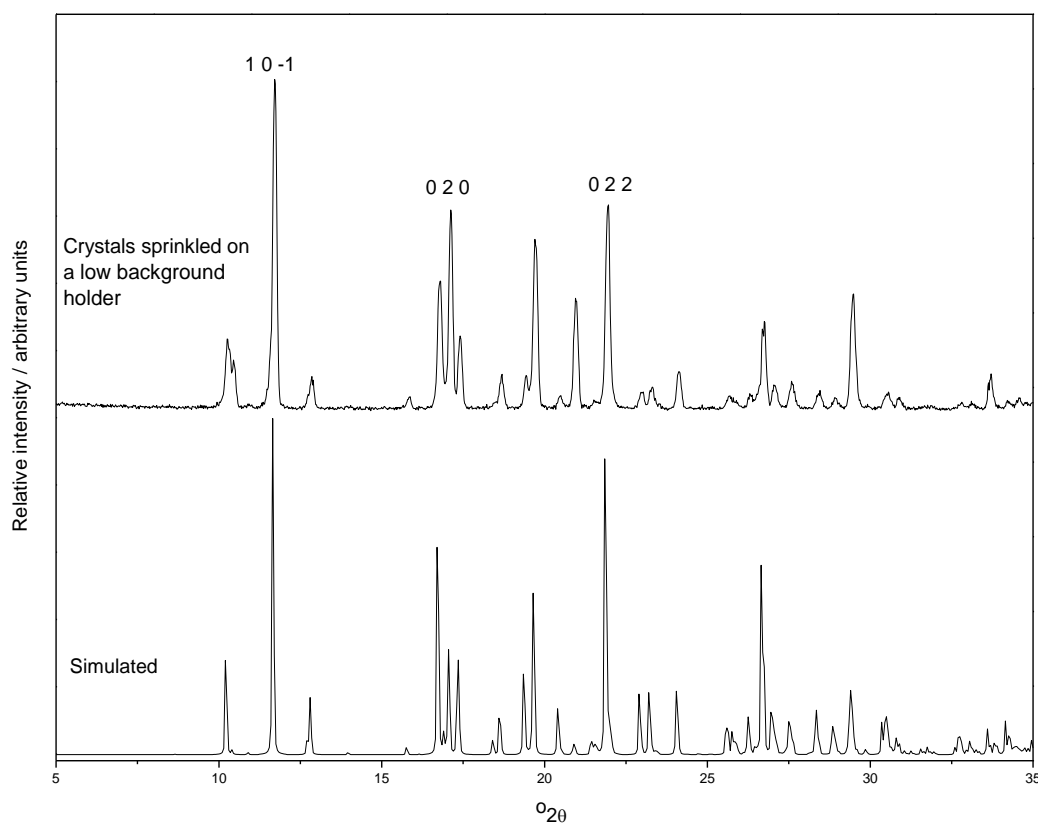

Figure 6. 7 The PXRD pattern for particles of IMC-γ sprinkled on a zero background sample holder. Most intense bands have been index using simulated PXRD data.

Table 6.2 shows results of growth morphology modelling. Seven unique facets namely (010), (100), (001), (011), (10-1), (1-1-1) and (110) have been calculated. The surfaces corresponding to the intense PXRD peaks are crystal faces in the simulated morphology. In fact they correspond to the three dominant faces 011, 10-1 and 010, with percentage surface area of 33.2%, 29.0% and 19.5% respectively. In contrast to IMC-α, crystallisation of IMC-γ is thermodynamic. The IMC-γ crystals grow slower allowing morphological dominance of the most stable surfaces i.e. surfaces with the lowest absolute attachment energy. The dominant faces by PXRD (10-1), (011) and (010) have the lowest absolute attachment energies of 35.281, 31.226 and 48.188 Kcalmol^{-1} respectively.

Table 6. 2 Data generated from growth morphology simulation for IMC-γ.

hkl	Slice depth d_{hkl} / Å	E_{att} (Total) /Kcalmol^{-1}	E_{att}(vdW) /Kcalmol^{-1}	E_{att}(Electro) /Kcalmol^{-1}	E_{att} (H-bond) /Kcalmol^{-1}	% Total facet area
0 1 0	10.227	-48.1879	-28.0779	-20.1168	0.006805	19.5
1 0 0	8.657	-69.1971	-23.9936	-38.3252	-6.87831	5.5
0 0 1	8.502	-56.8736	-19.6207	-30.3745	-6.8784	6.0
0 1 1	8.126	-31.2259	-25.4784	-5.75633	0.008852	33.2
1 0 -1	7.590	-35.2805	-25.7051	-9.58478	0.009314	29.0
1 -1 -1	6.960	-55.759	-25.1305	-23.7507	-6.87784	3.4
1 1 0	6.912	-51.836	-20.7489	-24.2109	-6.87621	3.4

6.3.3 Surface chemistry, contact angle measurements and hygroscopicity

The surface structures of the dominant faces were determined by PXRD analysis.

For IMC-α the faces are (021), (020) and (011) as shown in Figure 6.8 overleaf. In the surface structure of (020) and (011) faces, the chlorophenyl groups are predominantly exposed on the surface. The (021) surface contains predominantly chlorophenyl functionality but the carboxylic acid hydrogen and the carbonyl oxygen of the amide group can be seen near the surface. It is therefore expected that the surface of IMC-α will be largely hydrophobic because of the chlorophenyl functionalities but also capable of hydrogen bonding via the carboxylic hydrogen and carbonyl oxygen, respectively.

For IMC-γ the faces are (011), (10-1) and (010) as shown in Figure 6.9. In the surface structure of (011), phenyl hydrogen atoms are exposed on the surface. In the (10-1) surface, the methyl ether functionality is exposed. The carbonyl oxygen and chlorophenyl functionalities are exposed in the same ratio in the (010) surface. As with IMC-α, it is expected that the surface of IMC-γ is hydrophobic and capable of dipole-dipole interactions because of carbonyl oxygen.

Both polymorphs present surfaces that are largely hydrophobic but IMC-α has a more hydrophilic or acidic surface because of the presence of the carboxylic acid groups seen near the surface of the dominant (021) surface.

(a)

(b)

(c)
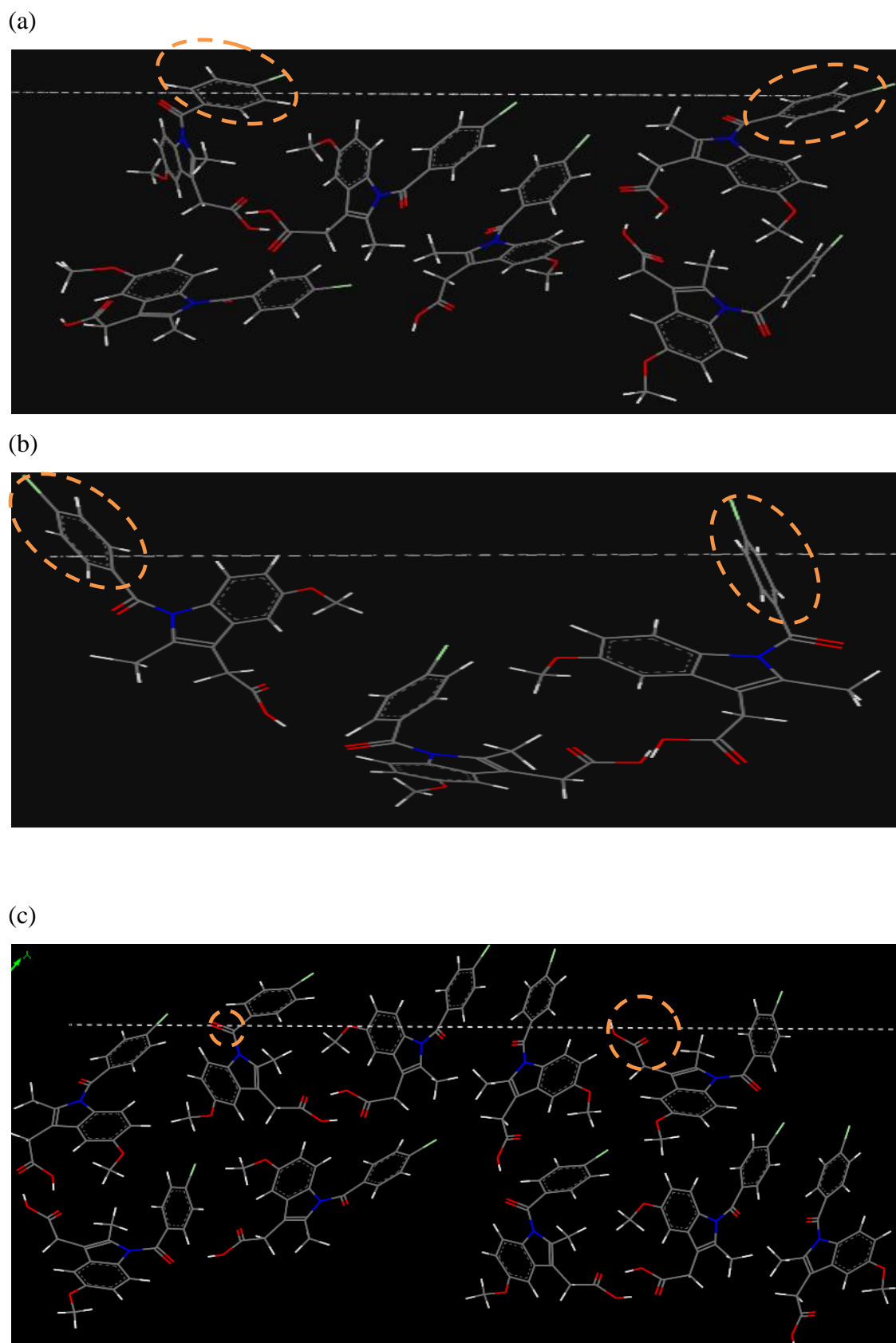
Figure 6. 8 Surface structure of faces (a) 011, (b) 020 and (c) 021 of IMC-α.

Colour code : grey-carbon, white-hydrogen, blue-nitrogen and red-oxygen.

(a)

(b)

(c)
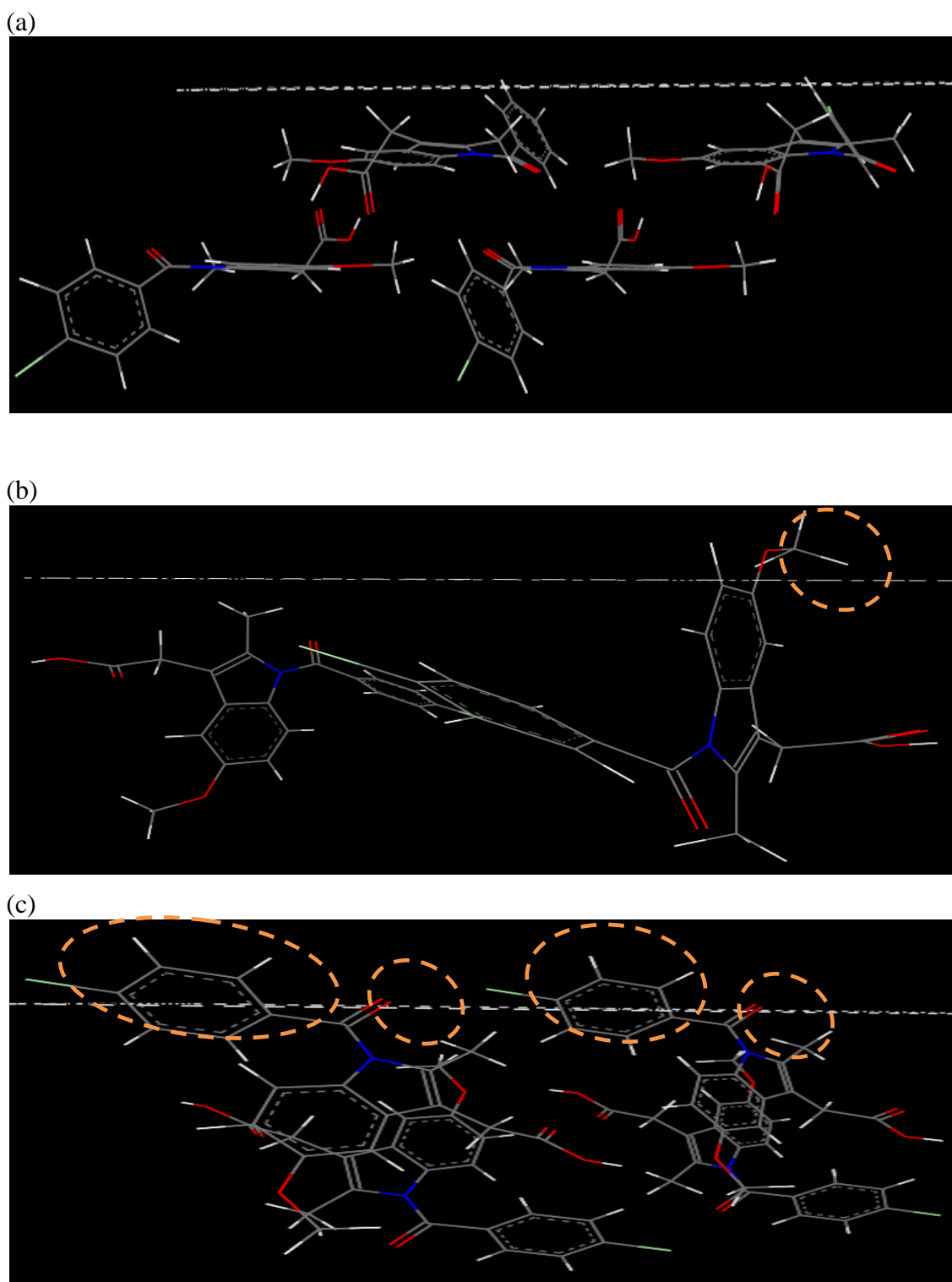
Figure 6. 9 Surface structure of faces (a) 011, (b) 10-1 and (c) 010 of IMC-γ.

Colour code : grey-carbon, white-hydrogen, blue-nitrogen and red-oxygen.

Capillary constants were reproducible, and an example is shown in Figure 6.10 for IMC-γ.
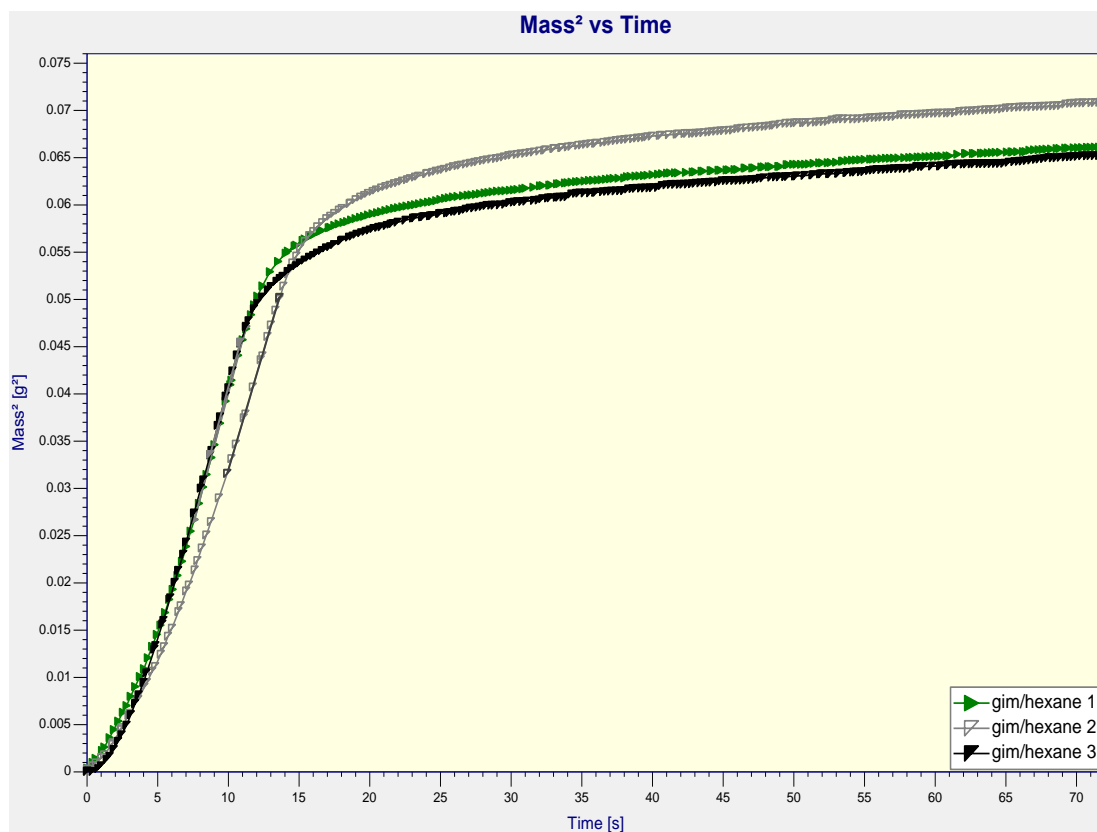
Figure 6.10 Mass^2 versus time plot for the capillary rise of n-hexane through IMC-γ powder bed for the determination capillary constant.

The typical penetration for water, ethylene glycol and formamide as they diffuse against gravity (under capillary action) in the powder beds of IMC-γ and IMC-α are shown in Fig 6.11, Fig 6.12 and Fig 6.13 respectively. The linear range corresponding to stage 2 of the capillary rise experiment is not discernable for water and ethylene glycol; hence contact angles were not calculated. It was observed for both polymorphs that water penetrated a height corresponding to less than 20 % of the powder bed, while ethylene glycol penetrated above 20% height during the course of the experiment in spite of the huge difference in viscosity.

The penetration will depend on the capillary constant C, viscosity of the liquid, and the ability of the liquid to wet the powder. A more viscous liquid is expected to penetrate more slowly, especially if the less viscous liquid is a poor wetting liquid.

The viscosities of water and ethylene glycol are 1.002 mPa.s and 21.810 mPa.s respectively.
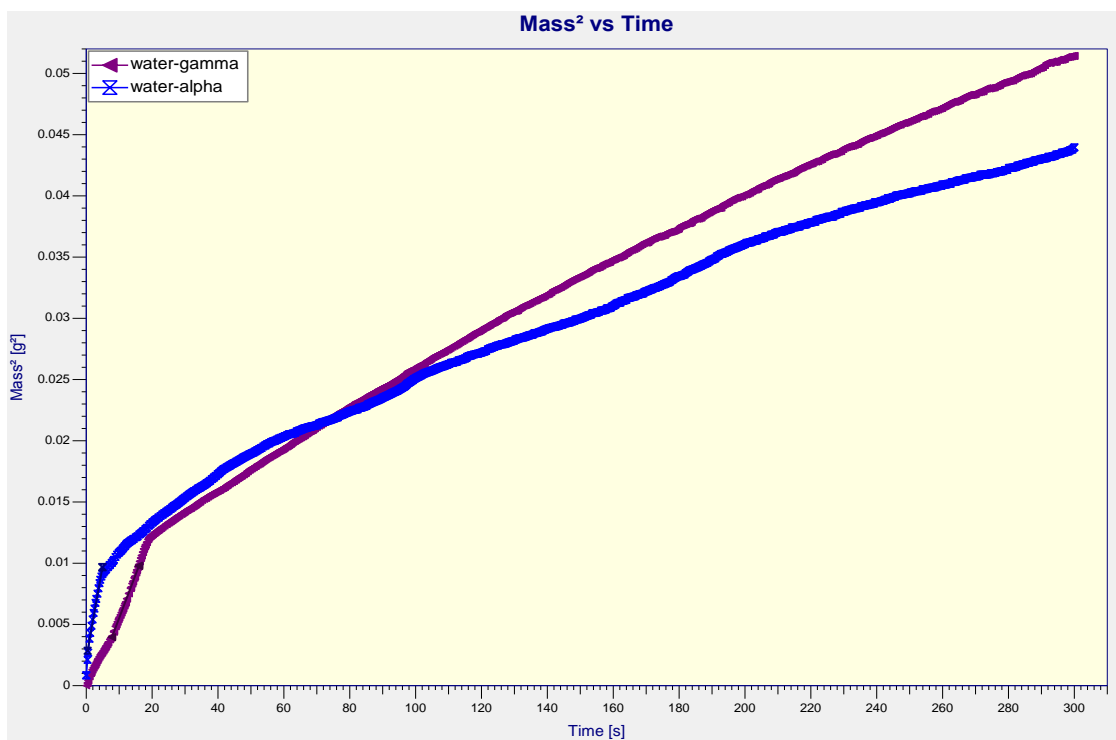
Figure 6.11 Typical penetration profiles of water through the powder bed of IMC polymorphs.
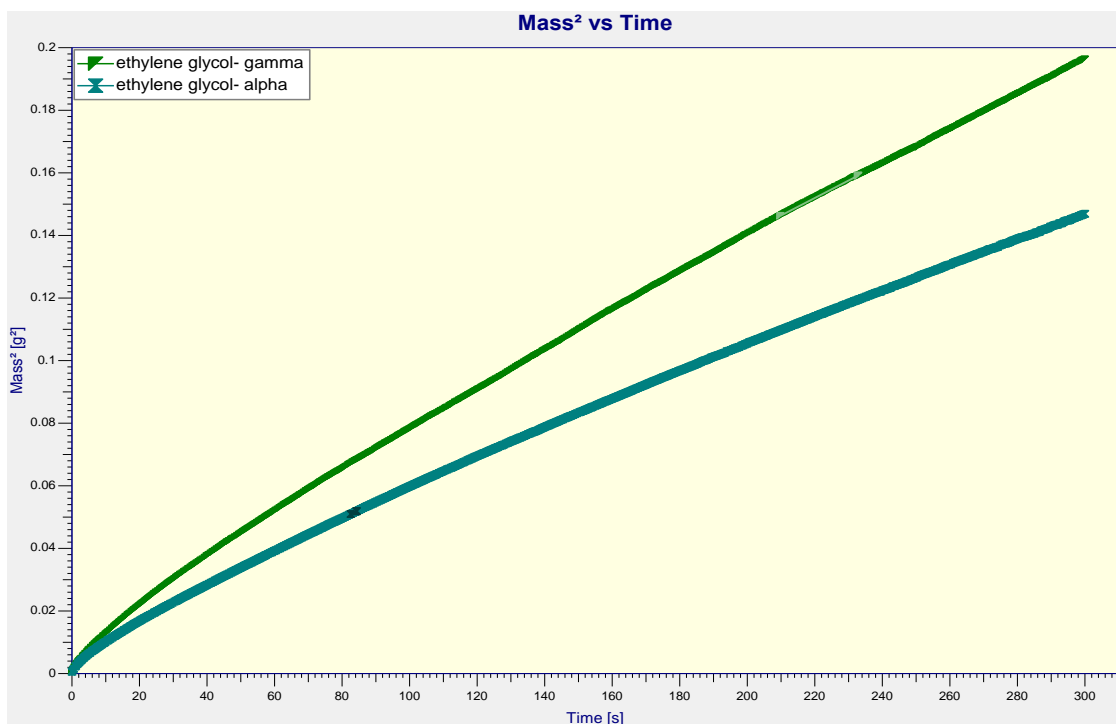
Figure 6. 12 Typical penetration profiles of ethylene glycol through the powder bed of IMC polymorphs.
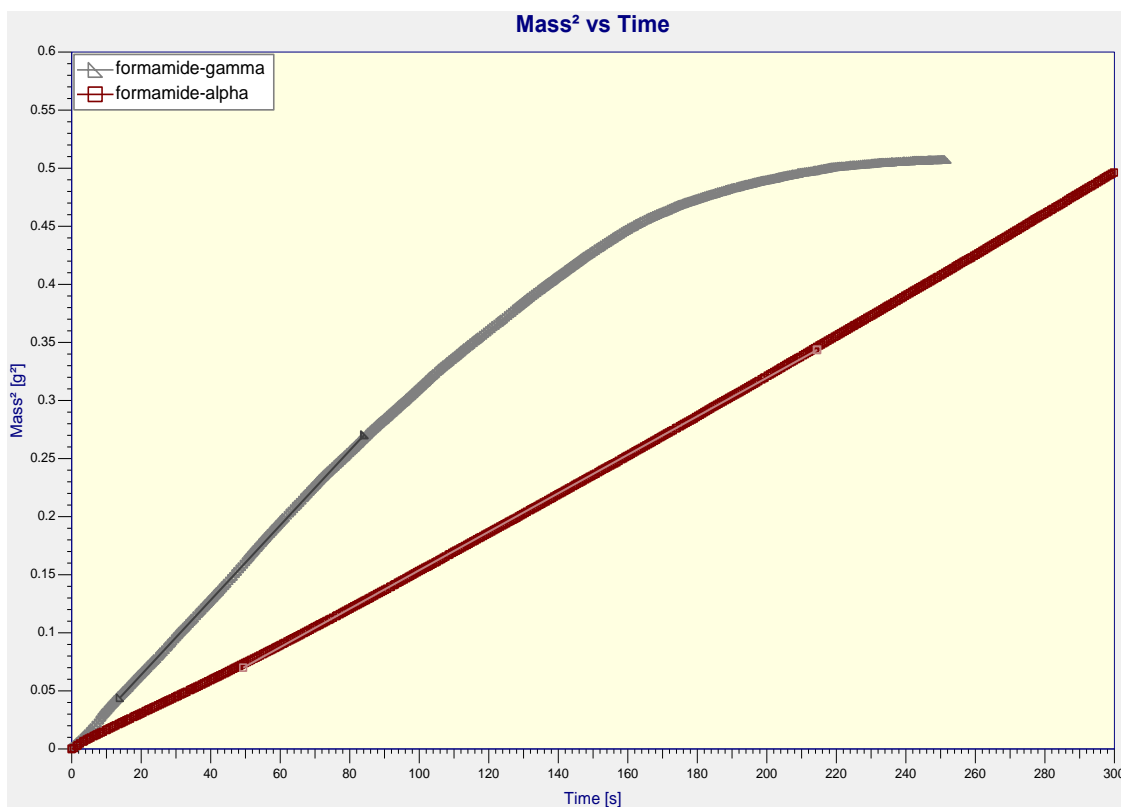
Figure 6. 13 Typical penetration profiles of formamide through the powder bed of IMC polymorphs.

In both polymorphs the penetration of water, although less viscous than ethylene glycol, is very slow, probably hindered by the hydrophobic nature of their surfaces. These observations are reflective of the chemistry of the dominant crystal faces as examined earlier, where their surfaces contain hydrophobic chlorophenyl and ether groups.

The penetration profiles for water in IMC-α and ethylene glycol in IMC-α and IMC-γ can be described as gently sloping curves, which is characteristic of systems where the powder bed swells, thereby changing the geometry of the spaces between particles, C. This means that C does not remain constant during an experiment, so the Washburn equation is not adequate for the determination of advancing contact angle in these cases.

The penetration profile of formamide for IMC-γ shows the typical stages for capillary rise experiments and the advancing contact angle was calculated using the linear fitting range.

For IMC- α, this is discernable but the curve did not plateau during the course of the experiment. The advancing contact angle (47.19±4.66^{o}) was only therefore calculated for IMC-γ.

Results for the contact angle, the physicochemical properties of the probe liquids and C for IMC-γ and IMC-α are shown in Table 6.3.

Table 6. 3 Summary of parameters from solvent penetration experiments.

	Surface tension mN/m	Density/ gcm^{-3}	Viscosity/ mPa.s	IMC-α CA/C	IMC-γ CA/C
Hexane	18.40	0.661	0.326	3.7278x10^{-6} cm^{-5}	2.1741x10^{-6} cm^{-5}
Ethylene glycol	48.00	1.110	21.810	-	-
Formamide	58.00	1.133	3.607	-	47.19^{o}±4.66^{o}
Water	72.80	0.998	1.002	-	-

n=3

Contact angle determination by liquid penetration did not successfully characterise the differences in surface chemistry between IMC polymorphs because of several problems such as swelling of the powder bed in the case of ethylene glycol, and slow penetration of water.

From the adsorption of water on the surface, hydrogen bond interactions could be inferred. The water uptake profiles for IMC polymorphs are shown in Fig 6.14.
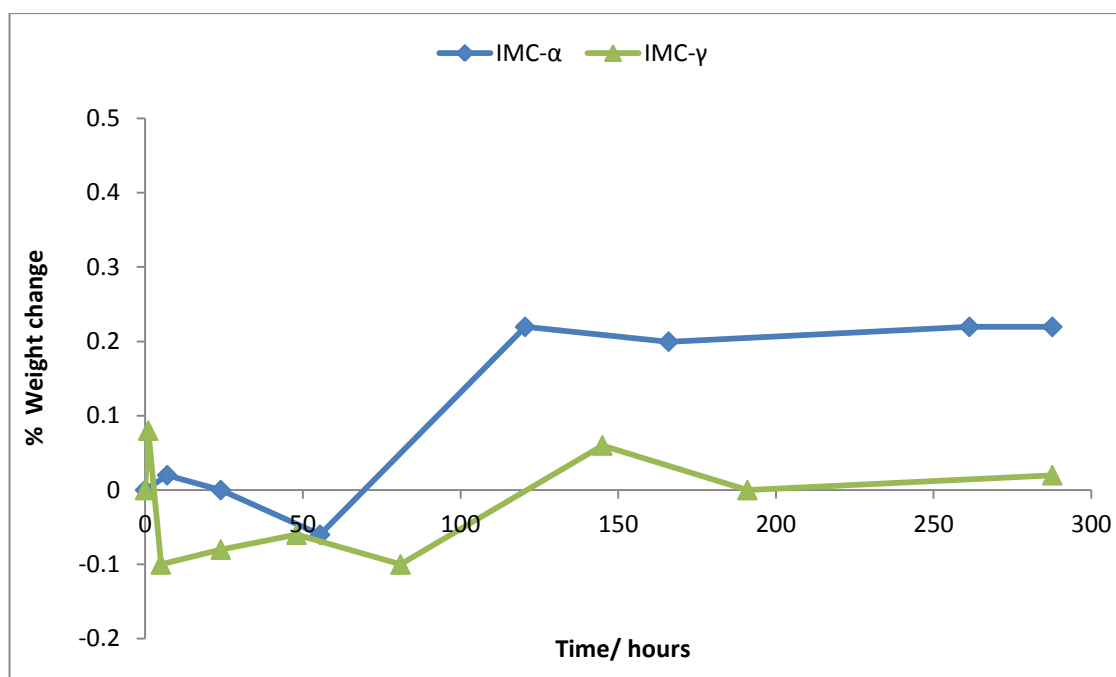
Figure 6. 14 Moisture uptake profile of IMC polymorphs at 77% RH for 12 days.

The polymorphs of IMC are non-hygroscopic; moisture uptake at 77% RH for 12 days did not exceed 0.5%. However the moisture uptake for IMC-α at 0.2% is tenfold greater than IMC-γ uptake of 0.02%. Their surfaces are largely hydrophobic because the overall water uptake was low, but IMC-α had a higher water uptake. These results are similar to those reported by other workers using the automated dynamic vapour sorption method[8]. This higher water uptake by IMC-α could be reflective of hydrogen bonding between water molecules and C=O groups (from the carboxylic acid and secondary amide) exposed on the 021 surface.

The exposure of the carboxylic acid and secondary amide group on the 021 surface of IMC-α could be responsible for the higher degree of ionisation of dye molecules recorded in Chapter 5. These results do not preclude the exposure of ionisable carboxylic acid groups on the surface of IMC-γ, but suggest that they are not present in its dominant surfaces.

6.4 Conclusions

Insights into the surface structure of the polymorphs of IMC at a molecular level have been provided by computer modelling of crystal morphology and experimental means. The surface chemistry of the polymorphs of IMC-α and γ have been examined by the in-silico growth morphology method and experimental PXRD, SEM, contact angle and hygroscopicity measurements. The morphologies of the polymorphs simulated by the growth morphology model showed good agreement with morphologies observed using SEM. The dominant crystal faces of IMC-γ by PXRD analysis showed good agreement with simulated results, while IMC-α showed only fair agreement. This fair agreement is attributable to the rapid crystallisation method used to obtain IMC-α crystals, which kinetically hinders the growth of the more stable crystal faces.

Contact angle measurements show a relatively slow penetration rate of water through the powder beds of the polymorphs of IMC. This is indicative of the largely hydrophobic nature of their surfaces. Only the contact angle of formamide with IMC-γ was obtained, because the gently sloping penetration profiles for water and ethylene glycol invalidate the use of the Washburn equation. The hydrophobic nature of their dominant surfaces was also confirmed by PXRD analysis and growth morphology calculations. Although the surfaces of both polymorphs are largely hydrophobic in nature, hygroscopicity studies and surface structure analysis suggest that IMC-α (with a tenfold higher water uptake than IMC-γ at 77%RH) contains more surface carboxylic acid groups, responsible for the greater extent of ionisation of adsorbed dye molecules as recorded in chapter 5.

6.5 References

1.   Y. H. Kiang, H. G. Shi, D. J. Mathre, W. Xu, D. Zhang and S. Panmai, *International Journal of Pharmaceutics*, 2004, **280**, 17-26.

2.   Y. H. Kiang, C. Y. Yang, R. J. Staples and J. Jona, *International Journal of Pharmaceutics*, 2009, **368**, 76-82.

3.   K. R. Morris, R. F. Schlam, W. Cao and M. S. Short, *Journal of Pharmaceutical Sciences*, 2000, **89**, 1432-1442.

4.   D. S. Coombes, C. Richard, A. Catlow, J. Gale, A. Hardy and M. Saunders, *Journal of Pharmaceutical Sciences*, 2002, **91**, 1652-1658.

5.   J. Prywer, *Journal of Crystal Growth*, 2004, **270**, 699-710.

6.   R. Docherty, G. Clydesdale, K. J. Roberts and P. Bennema, *Journal of Physics D: Applied Physics*, 1991, **24**, 89.

7.   G. A. Wolff and J. G. Gualtieri, *The American Mineralogist*, 1962, **47**, 562-584.

8.   C. Dabing, University of Minnesota, Minnesota, 2009, p. 293.

Chapter 7: Monitoring polymorphic transformation by diffuse reflectance visible spectroscopy (DRVS)

7.1 Introduction

Polymorphic transformations can have a significant influence on the processing and storage of crystalline powders. Change in crystalline structure of an API affects the therapeutic effectiveness and the stability of the drug product. Therefore the ability to monitor the effect of processing and detect polymorphic transformations is an important aspect of drug manufacture[1]. The transformation from one polymorphic form to another can be thermally, mechanically or moisture-induced. For instance, the traditional wet granulation method for the preparation of tablets involves several stages such as high speed mixing, wetting, drying at elevated temperatures and compression. These stages could potentially change the crystalline structure of an API.

Solid state phase (polymorphic) transformations are generally based on overlapping mechanisms of nucleation, growth and impingement[2, 3]. Nucleation represents the beginnings of the interface between the old solid phase and the new solid phase. It is the generation of a nucleation site (nucleus) of the new phase from the old phase. The nucleus, which consists of several molecules or atoms, is the critical size at which energy is released if the nucleus grows. The growth mechanism examines the expansion of nuclei, which could be volume controlled (long-range growth) or interface-controlled (short-range growth within the immediate vicinity of the interface). Impingement examines the various constraints on nucleation and growth of nuclei. For example whether two nuclei coalesce or one ingests the other, and also if the growth of nuclei is isotropic or anisotropic.

Monitoring polymorphic transformation involves solid-state kinetic evaluation, so as to determine transformation rate and thereby to determine transformation mechanism.

Solid-state kinetic evaluation typically involves modelling the fraction transformed as a function of time by linear regression analysis. Equation 7.1 represents a generic integral rate equation for solid state kinetics

$$g\ (\alpha)\ =\ kt \qquad \text{Equation 7.1}$$

where g is a function of the extent of reaction, α is the fraction of phase transformed or extent of growth of new phase, k is the rate constant, and t is time. $g\ (\alpha)$ can be determined by modelling α as a function of time to produce a linear relationship. The slope of the line will give will give the rate constant.

The kinetics of the phase transformation is heterogeneous in nature, which means that several factors affect the kinetics of transformation. These factors include activation energy of nucleation and growth, difference in the crystal imperfections, sublimation, particle size and morphology, and variation in growth rate along crystallographic axes. These factors contribute to the development of different models used in the characterisation of the kinetics of solid state phase transformation. Table 7.1 shows a list of kinetic models for solid-state reactions and Fig 7.1 shows the accelaratory, deceleratory, linear or sigmoidal shape of their respective isothermal α vs time curves.

Table 7.1 Common kinetic models for solid-state reactions[3, 4].

Model	Differential Form^a $f(\alpha)=\frac{1}{k}\frac{d\alpha}{dt}$	Integral Form^a $g(\alpha)=kt$
Power law (P2)	$2\,\alpha^{(1/2)}$	$\alpha^{(1/2)}$
Power law (P3)	$3\,\alpha^{(2/3)}$	$\alpha^{(1/3)}$
Power law (P4)	$4\,\alpha^{(3/4)}$	$\alpha^{(1/4)}$
Avarami-Erofe'ev (A2)	$2(1-\alpha)[-\ln(1-\alpha)]^{1/2}$	$[-\ln(1-\alpha)]^{1/2}$
Avarami-Erofe'ev (A3)	$3(1-\alpha)[-\ln(1-\alpha)]^{2/3}$	$[-\ln(1-\alpha)]^{1/3}$
Avarami-Erofe'ev (A4)	$4(1-\alpha)[-\ln(1-\alpha)]^{3/4}$	$[-\ln(1-\alpha)]^{1/4}$
Contracting area (R2)	$2(1-\alpha)^{1/2}$	$[1-(1-\alpha)^{1/2}]$
Contracting volume (R3)	$3(1-\alpha)^{2/3}$	$[1-(1-\alpha)^{1/3}]$
1-D diffusion (D1)	$1/2\alpha$	α^2
2-D diffusion (D2)	$[-\ln(1-\alpha)]^{-1}$	$[(1-\alpha)\ln(1-\alpha)]+\alpha$
3-D diffusion-Jander eqn.(D3)	$3(1-\alpha)^{2/3}/2(1-(1-\alpha)^{1/3})$	$[1-(1-\alpha)^{1/3}]^2$
Ginstling–Brounshtein (D4)	$(3/2((1-\alpha)^{-1/3}-1)$	$1-(2\alpha/3)-(1-\alpha)^{2/3}$
Zero-order (F0/R1)	1	α
First-order (F1)	$(1-\alpha)$	$-\ln(1-\alpha)$
Second-order (F2)	$(1-\alpha)^2$	$(1-\alpha)^{-1}-1$
Third-order (F3)	$(1-\alpha)^3$	$0.5\,((1-\alpha)^{-2}-1)$

^{a}In some references f(α) and g(α) have opposite designations.
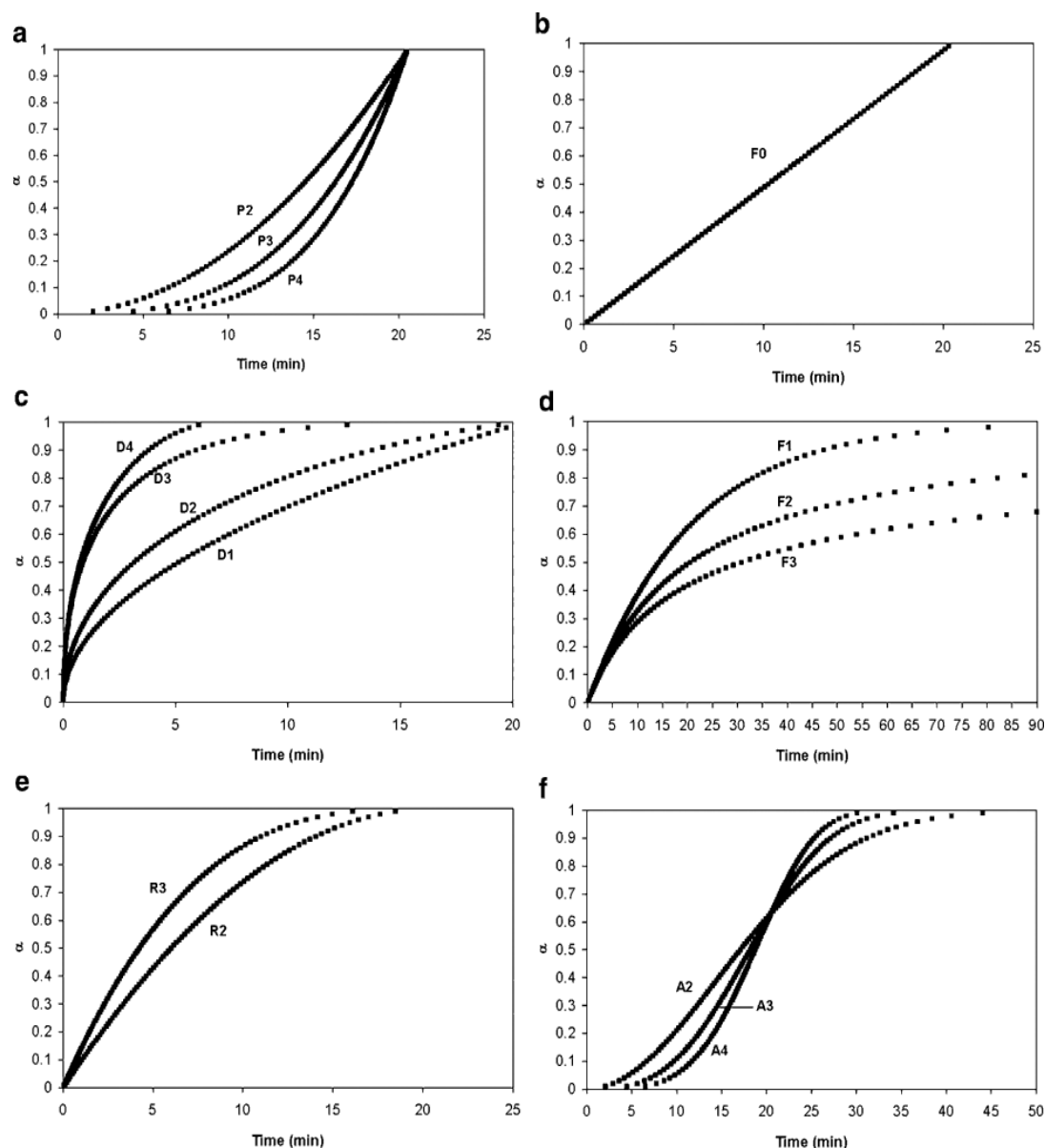
Figure 7.1 Shapes of the isothermal α vs time plots for solid-state reaction models (Table 7.1); data simulated for $k = 8.17$ x 10^{-4} s^{-1}: **a**, acceleratory; **b–d**, deceleratory; **e**, linear; **f**, sigmoidal.[3, 4]

A variety of analytical techniques have been employed to characterise the kinetics of polymorphic transformation *in situ*. Examples include NIR[5, 6], vibrational spectroscopy[7, 8], variable environment powder X-ray diffraction[9] and temperature-controlled simultaneous small/wide angle X-ray scattering[10]. Including also a study of the kinetics of the conversion of sulfanilamide (SFN) polymorphs by energy dispersive XRD[11]. Monitoring processes, especially by *in situ* methods, offers better understanding of the intrinsic properties of systems, thus improving process control.

This study reports on a novel method for monitoring thermally induced conversion of polymorphs using DRVS and kinetic evaluation of the generated data. The polymorphs of sulfanilamide (SFN) were examined. Two polymorphs SFN-β and SFN-γ are enantiotropically related and the conversion order SFN-β → SFN-γ can be induced at elevated temperatures. The DRVS technique used in this study has not been developed for *in situ* data acquisition but with promising results and the advantage of rapid data acquisition, it could drive the development of DRVS as a PAT tool for online monitoring of polymorphic transformation. Currently, fibre-optic DRVS probes suitable for *in situ* characterisations of solids and suspensions have been developed and are in use[12-15].

7.2 Experimental

7.2.1. Calibration of DRVS response using reference samples

To establish a relationship between DRVS response and amount of polymorph transformed, calibration samples were prepared. Six SFN-TB calibration reference samples were prepared with the polymorphs in the ratio 0.0:1.0, 0.2:0.8, 0.4:0.6, 0.6:0.4, 0.8:0.2 and 1.0:0.0 of SFN-γ-TB to SFN-β-TB.

The SFN-β and SFN-γ samples were screened using sieves to determine the particles size; the majority had a particle size greater than 450μm. SFN-β-TB and SFN-γ-TB were then prepared as detailed in sections 5.2.4. The samples were characterized by PXRD and DSC to confirm polymorphic form, and also to ensure that crystalline integrity is maintained after chromogenic treatment.

DRVS data was collected for the calibration standards (the instrumental conditions are detailed in section 5.2.4.) Raw DRVS data was treated by the AA smoothing algorithm described in chapter 3 and then normalised as recorded in section 3.6.3. Spectral data was recorded in the region from 400nm-750nm, and the data collection time was 5secs per spectrum. Untreated SFN-β was used as a reference blank for DRVS measurements.

7.2.2 *Kinetic studies by isothermal monitoring of SFN-β transformation by DRVS*

Eight thin-walled glass vials were each loaded with 400mg of SFN-β-TB. The vials were individually introduced into an oil bath equilibrated at 128°C for different durations. Figure 7.1 shows the apparatus used for isothermal heating of the sample.

At time points of t= 7.5, 10, 30, 60, 90, 180, 240 and 360 seconds the samples were removed and analysed immediately (without quenching) by DRVS.
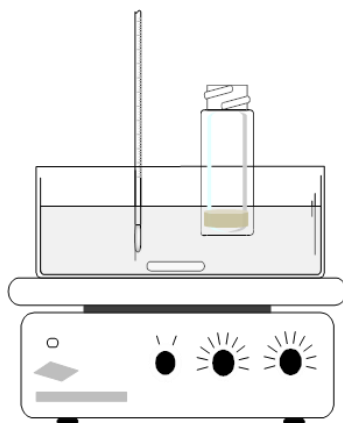
Figure 7.2 Experimental apparatus for the polymorphic conversion of SFN-β → SFN-γ under isothermal conditions at 128°C.

At the reaction extremity of t=360s, the remaining sample was analysed using DSC to ensure complete transformation. The instrumental conditions for DSC analysis are detailed in section 4.3.2. DSC data for the sample at t=360s was compared with that of the 1.0:0.0 (SFN-γ-TB: SFN-β-TB) calibration reference sample.

7.3 Results and discussion

7.3.1 Calibration of DRVS response

The DRVS spectra for the calibration reference samples of are overlaid in Figure 7.3. Two overlapping bands occur at 454 nm and 604 nm, with increasing amounts SFN-γ-TB the height of the 604 nm band increases.
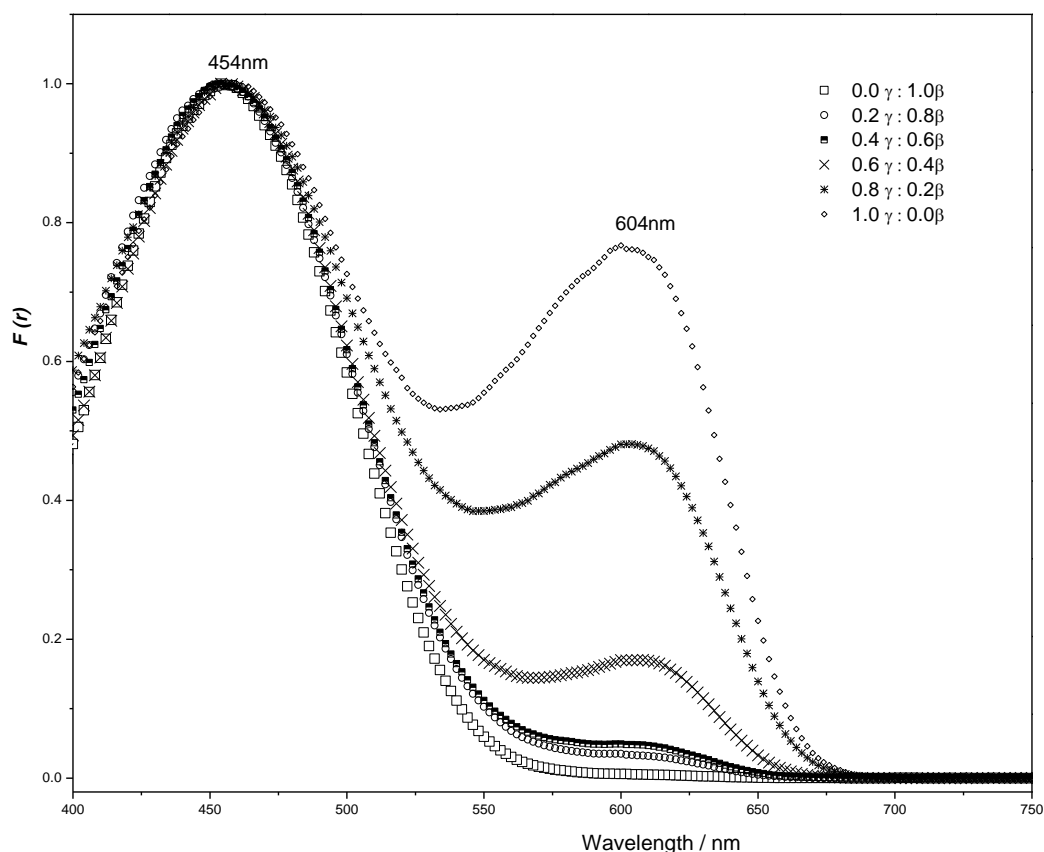
Figure 7. 3 DRV spectra (normalised) for the calibration samples containing fractional amounts of dye treated SFN polymorphs.

The calibration is based on the ratio of peak heights i.e $F(r)_{604nm/454nm}$. Absolute peak heights were not used because of potential variations in sample irradiation and specular reflectance (usually caused by non-focal positioning of sample). As the peaks were not baseline resolved, the bands were deconvoluted using the Gaussian curve fitting algorithm before a ratio of peak heights was determined. UV-Vis bands have been shown to follow the Gaussian model, i.e. spectral bands are symmetrical with respect to wavelength [16].

An example of the deconvolution of overlapping DRVS peaks by the Gaussian curve fitting algorithm is shown in Fig 7.4. High correlation values ($R^2 \geq 0.998$) for the Gaussian curve fitting indicate the excellent fit (See Table 7.2).
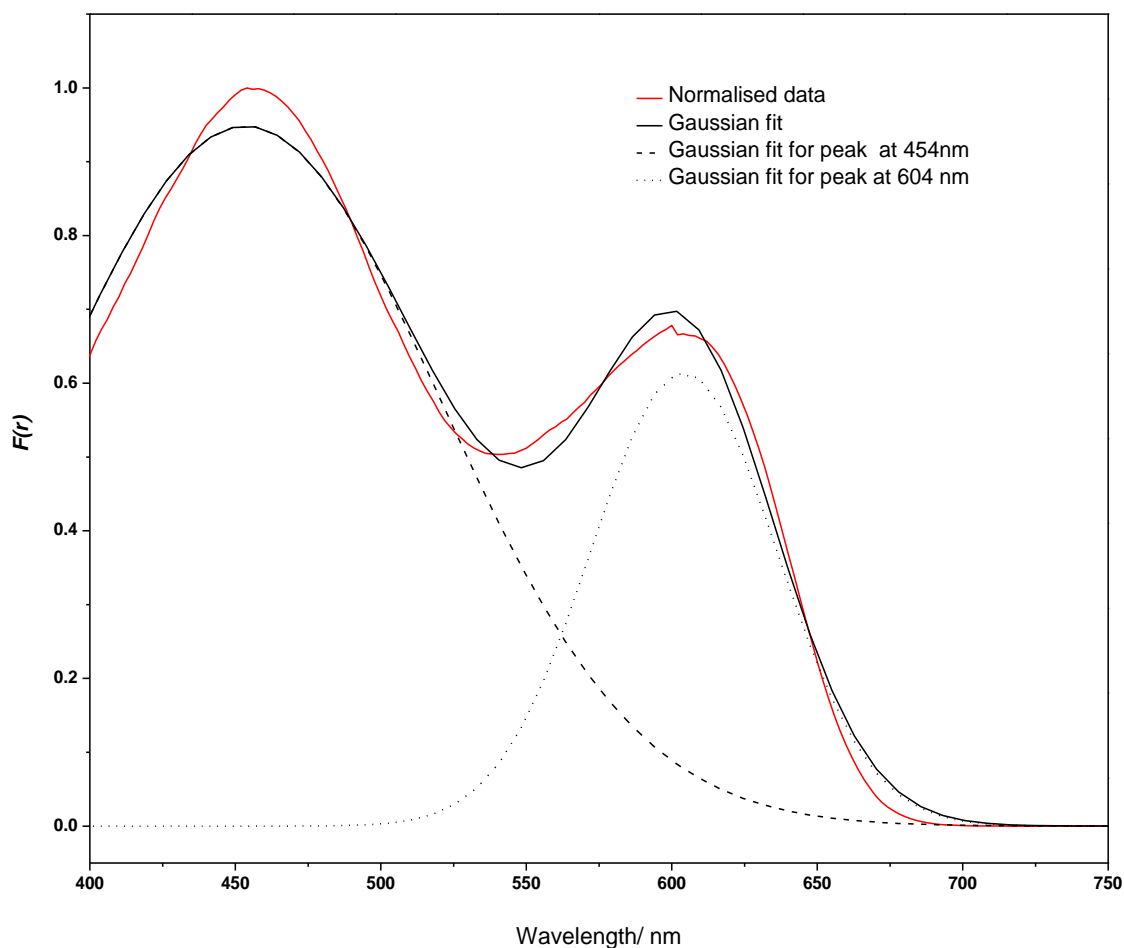
Figure 7.4 An example of the deconvolution of overlapping DRVS peaks by Gaussian curve fitting algorithm.

Table 7. 2 Correlation (R^2) values of Gaussian curve fitting for the calibration reference samples.

Calibration reference sample SFN-γ-TB:SFN-β-TB	Fractional amounts SFN-γ-TB (α)	R^2 (Gaussian)
0.2:0.8	0.2	0.999
0.4:0.6	0.4	0.999
0.6:0.4	0.6	0.999
0.8:0.2	0.8	0.998
1.0:0.0	1.0	0.998

Fig 7.5 shows the calibration plot of $F(r)_{604nm/454nm}$ versus fractional amounts SFN-γ-TB. The plot shows the relationship between the peak height ratio and fractional amounts. This is analogous to the calibration plot of ratio of peak heights versus pH for TB in solution.
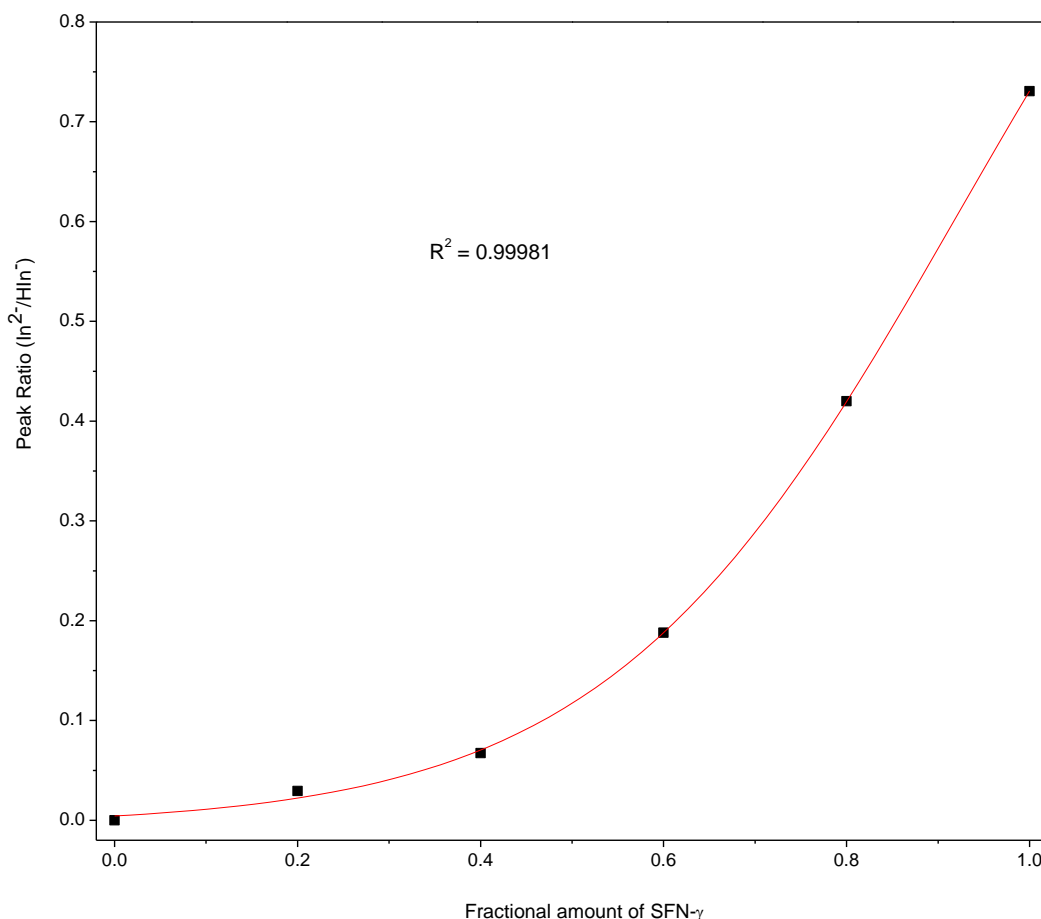
Figure 7.5 Calibration plot of $F(r)_{604nm/454nm}$ versus fractional amounts SFN-γ-TB.

7.3.2 Kinetic evaluation of the SFN-β→ γ transformation by DRVS

The normalised DRVS spectra (showing two main bands at 454 nm and 604 nm) collected as the transformation proceeded at 128±0.5ºC are shown in Fig 7.6. It clearly shows that the β→γ transformation can readily be followed by the emergence and subsequent increase in the reflectance of the band of λ=604nm. The transformation seems to be complete at t=180 as the increase in the height of 604nm band after this time point is not significant. The spectra were deconvoluted using the Gaussian curve fitting algorithm and the peak ratios ($F(r)_{604nm/454nm}$) were correlated to the fractional amount of SFN- γ for each time point using the calibration plot constructed earlier.
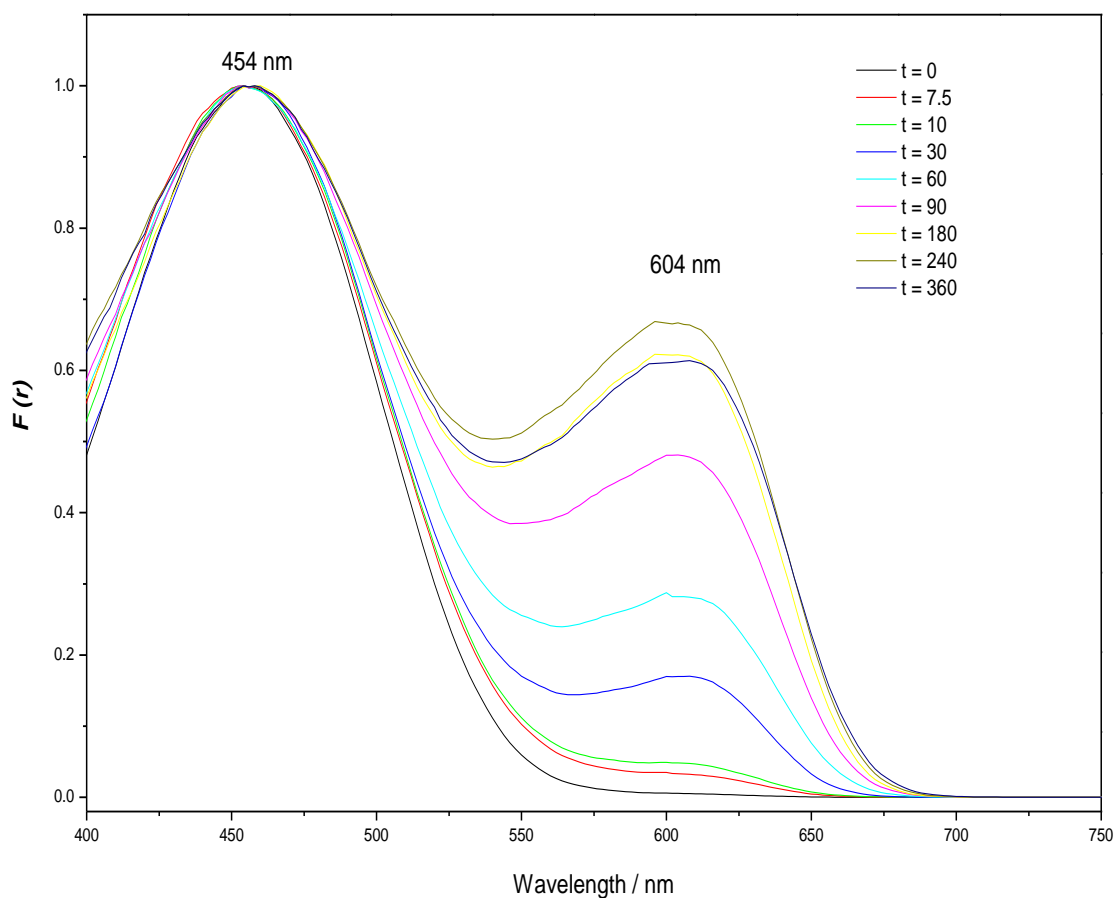
Figure 7.6 DRVS data for the β→γ transformation in sulfanilamide at 128°C.

Table 7.3 shows Gaussian R^2 for the time points and α values derived using the calibration plot.

Table 7.3 Gaussian R^2 for the time points and α values derived using the calibration plot.

Time point/s	Fractional amount of SFN-β transformed(α)	R^2 (Gaussian)
7.5	0.24	0.989
10	0.31	0.992
30	0.58	0.993
60	0.69	0.991
90	0.84	0.990
180	0.94	0.992
240	**0.95**	0.991
360	0.93	0.992

Using the calibration plot constructed the transformation did not seem to go to completion as the highest fractional amount α_{max} was 0.95. DSC thermograms at the reaction extremity of t=360s and calibration reference sample 1.0:0.0 of are shown in Fig 7.7.
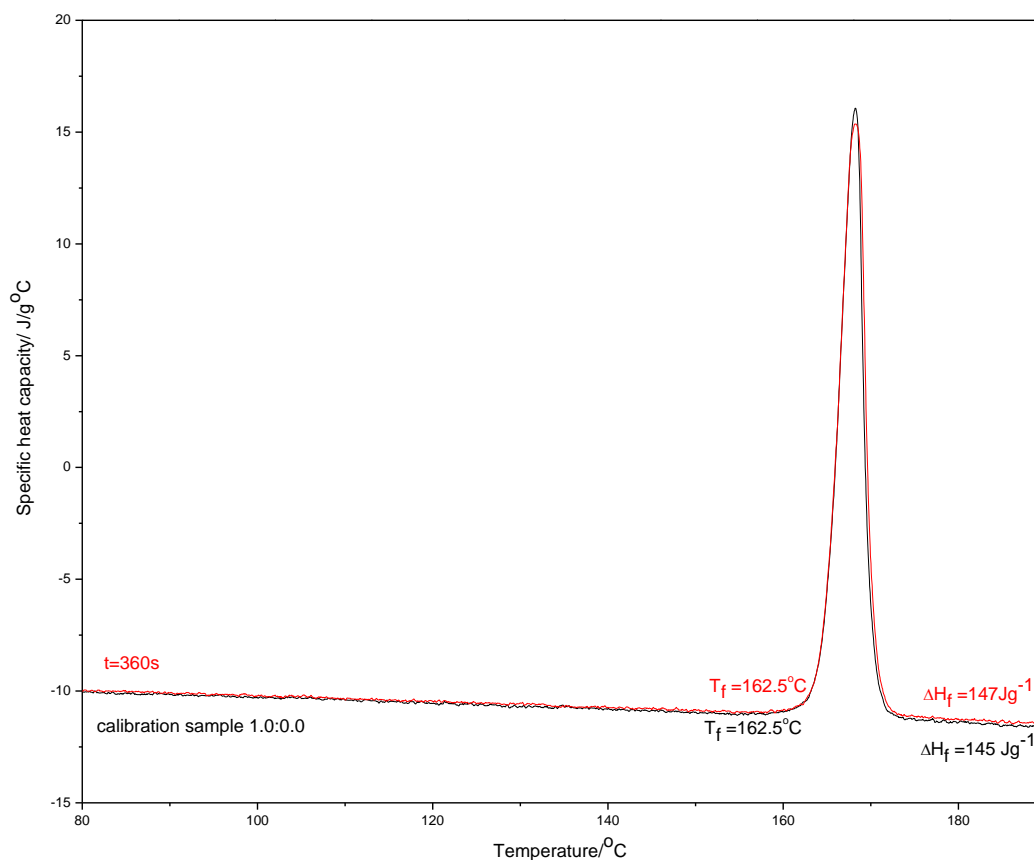
Figure 7.7 DSC thermograms the t=360s sample (red) and calibration reference sample 1.0:0.0 (black).

The melting behaviour observed for the t=360 sample agrees with thermal data for the 1.0:0.0 calibration reference sample. One endotherm is observed for both samples with onset of melting at 162.5ºC and enthalpy of fusion of 145Jg^{-1} and 147 Jg^{-1} for the 1.0:0.0 and t=360 samples respectively shows good correlation. Because the samples show identical thermal behaviour, the fractional amounts obtained using the calibration plot were rescaled by normalising the data with respect to α_{max}. The reasons for the disparity in α results could be differences in the homogeneity of the samples. Spinning the sample during data acquisition may help even out inhomogeneities.

The rescaled data plotted as fraction of SFN-β transformed (α/α_{max}) versus time as shown in Fig 7.8. It shows a deceleratory transformation curve that starts to plateau at t=180 s.
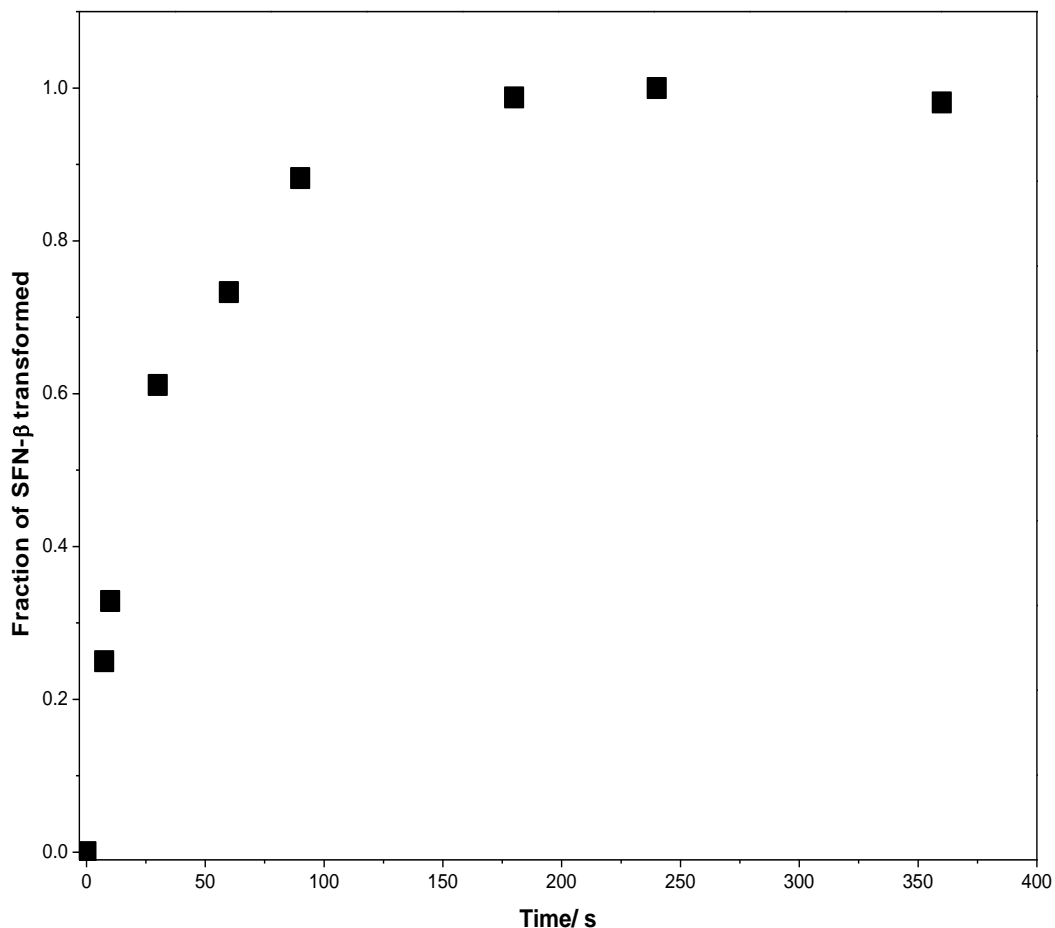
Figure 7.8 The rescaled α versus time plot for the β to γ polymorphic transformation of SFN at 128 °C.

The rescaled experimental kinetic data within the range of $\alpha_{t=7.5}$ and $\alpha_{t=180}$ was fitted to sixteen solid-state kinetics models by linear regression analysis. Results are shown in Table 7.4. It is possible to eliminate a model if it shows poor intercepts, slopes, or R^2 values. Good fit for the models are based on near to zero intercept, high R^2 values and non-negative slopes. Results for the models that gave reasonable values, (namely the First order, D4, D3, D2, R3 and A2) are graphically represented in Fig 7.9.

Table 7.4 Models used for the kinetic evaluation of β→γ transformation of sulfanilamide.

Model	Equation	Slope (x 10^{-2}s^{-1})	Intercept	R^2
First Order (F1)	$-\ln(1-\alpha) = kt$	2.43	0.078	0.992
Ginstling-Brounshtein (D4)	$1-(2\alpha/3) -(1-\alpha)^{2/3}$	0.17	0.003	0.988
3-D Diffusion (D3)	$[1-(1-\alpha)^{1/3}]^2$	0.35	-0.037	0.986
2-D Diffusion (D2)	$[(1-\alpha)\ln(1-\alpha)] + \alpha$	0.53	0.048	0.965
Contracting Volume (R3)	$(1-\alpha)^{1/3} = kt$	0.39	0.109	0.975
Contracting Area (R2)	$(1-\alpha)^{1/2} = kt$	0.43	0.183	0.940
Avarami-Erofe'ev (A2)	$[-\ln(1-\alpha)]^{1/2} = kt$	0.89	0.585	0.978
Avarami-Erofe'ev (A3)	$[-\ln(1-\alpha)]^{1/3} = kt$	0.55	0.723	0.955
Avarami-Erofe'ev (A4)	$[-\ln(1-\alpha)]^{1/3} = kt$	0.40	0.790	0.940
1-D Diffusion (D1)	α^2	0.53	0.140	0.893
Power Law (P4)	$\alpha^{1/4}$	0.15	0.779	0.701
Power Law (P3)	$\alpha^{1/3}$	0.19	0.718	0.712
Power Law (P2)	$\alpha^{1/2}$	0.40	0.357	0.587
Zero Order (F0/R1)	α	0.40	0.378	0.794
Second-Order (F2)	$(1-\alpha)^{-1} - 1$	0.52	-14.9	0.823
Third Order (F3)	$0.5((1-\alpha)^{-2} - 1)$	2471.9	-795.4	0.774

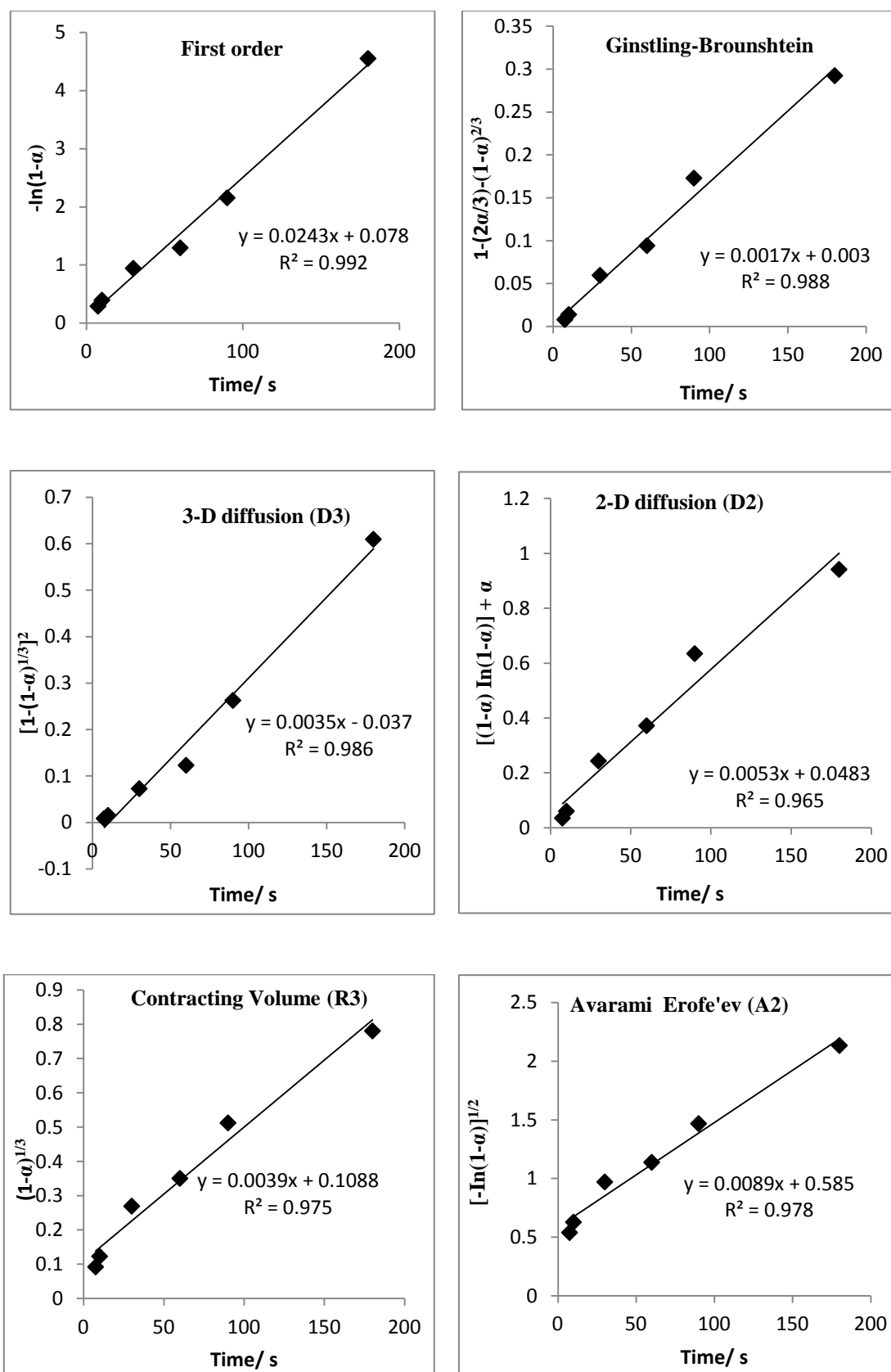**Figure 7.9** Linear regression analysis of the β to γ polymorphic transformation of SFN at 128°C using named solid state kinetic models.

The ability to describe the kinetics of a polymorphic transformation by more than one kinetic model is common, but in this case the first order kinetic model described the transformation with the best R^2 value. First order transformation means that the kinetics is entirely nucleation-controlled and each SFN-β crystallite within the sample forms only a single SFN-γ nucleus that grows at a constant rate to transform the entire crystal and hence the entire sample. This finding is confirmed by the reported hot-stage microscopic observation of $\beta \rightarrow \gamma$ polymorphic transformation in a single crystal of SFN at 129 ºC[11]. The observation showed the SFN-γ initiating at a single nucleation site and then growing as a single crystal within the SFN-β crystal.

The study of transformation of SFN-β to SFN-γ *in situ* using energy dispersive XRD by Sheridan *et al* [11] suggested that kinetics is <u>dominated</u> by nucleation but not entirely nucleation controlled. Particle size distribution, reaction temperature and the non in-situ method employed herein could explain the differences in the transformation mechanism reported herein compared to that reported by Sheridan[11]. Sheridan *et al* used a particle size of $\leq 50\mu m$, and here a $\geq 450\mu m$ particle size is used. They also studied polymorphic transformation at several temperatures, the highest of which was 122.8ºC, compared to 128ºC used in this work. In general, in solid-state kinetics, parameters such as particle size and size distribution affect solid state transformations, but the importance of these parameters decreases with increasing temperature[3, 4].

7.4 Conclusions

The kinetics of the polymorphic transformation of sulfanilamide polymorphs have been monitored using chromogenic treatment with TB dye and DRVS. The thermally-induced transformation fitted the first order solid state kinetic model ($R^2 = 0.992$) giving a rate constant of 2.43 x 10^{-2} s^{-1}. With suitable adaptation, perhaps with a fibre optic probe and reducing the scan time to <5 secs / spectrum, the results suggest that this technique could be used for *in situ* measurement to allow monitoring and control of drug polymorphic form. In particular it would be ideal for the study of rapid phase transformation, since the transformation was complete in about 180 seconds.

7.5 References

1. G. G. Z. Zhang, D. Law, E. A. Schmitt and Y. Qiu, *Advanced Drug Delivery Reviews*, 2004, **56**, 371-390.

2. F. Liu, F. Sommer, C. Bos and E. Mittemeijer, *International Materials Reviews*, 2007, **54**, 193-212.

3. A. Khawam, in *Pharmacy*, University Of Iowa, Iowa, 2007, p. 350.

4. A. Khawam and D. R. Flanagan, *ChemInform*, 2006, **37**, no-no.

5. T. Norris, P. K. Aldridge and S. Sonja Sekulic, *Analyst*, 1997, **122**, 549-552.

6. S. E. Barnes, T. Thurston, J. A. Coleman, A. Diederich, D. Ertl, J. Rydzak, P. Ng, K. Bakeev and D. Bhanushali, *Analytical Methods*, 2010, **2**, 1890-1899.

7. M. Szelagiewicz, C. Marcolli, S. Cianferani, A. Hard, A. Vit, A. Burkhard, M. von Raumer, U. Hofmeier, A. Zilian, E. Francotte and R. Schenker, *Journal of Thermal Analysis and Calorimetry*, 1999, **57**, 23-43-43.

8. L. E. O'Brien, P. Timmins, A. C. Williams and P. York, *Journal of Pharmaceutical and Biomedical Analysis*, 2004, **36**, 335-340.

9. J. Han and R. Suryanarayanan, *International Journal of Pharmaceutics*, 1997, **157**, 209-218.

10. A. D. Edwards, B. Y. Shekunov, R. T. Forbes, J. G. Grossmann and P. York, *Journal of Pharmaceutical Sciences*, 2001, **90**, 1106-1114.

11. A. K. Sheridan and J. Anwar, *Chemistry of Materials*, 1996, **8**, 1042-1051.

12. S. M. Bennici, B. M. Vogelaar, T. A. Nijhuis and B. M. Weckhuysen, *Angewandte Chemie International Edition*, 2007, **46**, 5412-5416.

13. C. P. Stemmet, J. C. Schouten and T. A. Nijhuis, *Chemical Engineering Science*, 2010, **65**, 267-272.

14. in *Drug Discovery & Development Magazine*, New Jersey, USA, April 2010, p. Issue 4 page 8.

15. Diffuse reflectance immersion probe, http://www.solvias.ch/english/services-products/process-analytical-technology/fiberoptic-probes/diffuse-reflectance-immersion-probes/index.html, 2010.

16. L. Antonov and S. Stoyanov, *Applied Spectroscopy*, 1993, **47**, 1030-1035.

Chapter 8: Summary and Future work

8.1 Summary

This thesis has investigated the development of a novel approach to the analysis and surface characterisation of drug polymorphism, with the aim of extending to *in situ* measurement. This study has shown for the first time the characterisation of two polymorphs each of indomethacin (IMC), carbamazepine (CBZ), caffeine (CFN), furosemide (FRS) and sulfanilamide (SFN), by the adsorption of phenol red (PR), thymol blue (TB) and methyl red (MR), and diffuse reflectance visible spectroscopy (DRVS).

Visual discrimination by differential coloration of the polymorphs by at least two of the probe pH indicator dyes was attained. This is strongly indicative of the variation in acid/base surface chemistry between the polymorphs. The mechanism for differential coloration has been explored based on the crystal structure, and how molecular packing can influence the accessibility of acid/base molecular functionalities. The agreement among the three dyes in terms of relative surface acidity between the polymorphic pairs was good except for TB-treated CFN polymorphs, and MR-treated CBZ polymorphs. The dynamic orientational disorder displayed by caffeine molecules in both polymorphic forms could be the reason for that disparity, while in the case of CBZ polymorphs, MR could be responding to hydrogen bonding potential.

DRVS absorption bands for most polymorphic systems are red-shifted by ≥ 10 nm of solution values, while CFN polymorphs gave DRVS absorption bands for yellow PR and TB close to solution values (within ± 3nm). This could be reflective of the positional disorder present in the caffeine molecule. The crystal structures of the polymorphs are examined in order to explore the relationship between crystal packing and the nature of the interactions between the dye and the polymorph surface. These influence the degree of ionisation of dye molecules seen in DRVS spectra, giving colour differences that reveal underlying variations between the surfaces of polymorphs on a molecular scale.

Insights into the surface structure of the polymorphs of IMC at a molecular level have been provided by computer modelling of crystal morphology and experimental means. The surface chemistry of IMC-α and γ have been examined by the *in silico* growth morphology method, and by experimental PXRD, SEM, contact angle and hygroscopicity measurements. The morphologies of the polymorphs simulated by the growth morphology model showed good agreement with morphologies observed using SEM. The dominant crystal faces of IMC-γ by PXRD analysis showed good agreement with simulated results, although IMC-α showed only fair agreement. This fair agreement is attributable to the rapid crystallisation method used to obtain IMC-α crystals, which kinetically hinder the growth of the more stable crystal faces, and the fact that the most dominant face predicted by morphology simulation (001) is not a PXRD diffracting plane.

Contact angle measurements show a relatively slow penetration rate of water through the powder beds of the polymorphs of IMC. This is indicative of the largely hydrophobic nature of their surfaces. Only the contact angle of formamide with IMC-γ was obtained because the gently sloping penetration profiles for water and ethylene glycol invalidate the use of the Washburn equation. The hydrophobic nature of their dominant surfaces was also confirmed by PXRD analysis and growth morphology calculations. Although the surfaces of both polymorphs are largely hydrophobic in nature, hygroscopicity studies and surface structure analysis suggest that IMC-α (with a ten fold higher water uptake than IMC-γ at 77%RH) contains more surface carboxylic acid groups responsible for the greater extent of deprotonation of adsorbed dye molecules.

The kinetics of the polymorphic transformation of sulfanilamide polymorphs have been monitored using chromogenic treatment with TB dye and DRVS. The emergence and increase of the band at λ=604nm as the solid state transformation occurred allowed the transformation to be readily followed. A steady change in colour from yellow to green during thermal treatment was visually evident. The transformation fitted the first order solid state kinetic model, giving a rate constant of $2.43 \times 10^{-2}\ s^{-1}$.

With suitable adaptation, the results suggest that visible spectroscopy could be used for in situ measurement to allow monitoring and control of drug polymorphic form. It would also be well suited for the study of rapid phase transformations.

8.2 Future Work

The key to full understanding of the mechanism of differential coloration of adsorbed dye molecules by polymorphs is the comprehensive characterisation of surface structure. It would be of interest to further investigate the surface chemistry of polymorphs by a multidisciplinary approach using complimentary experimental techniques. These techniques could include secondary ion mass spectrometry (SIMS), surface energy measurements using liquid contact angles and ampoule-breaking calorimetry.

Secondary Ion mass spectrometry (SIMS) is a surface analytical technique used to analyze the composition of solid surfaces by sputtering the surface of the specimen with a focused primary ion beam and collecting and analysing ejected secondary ions[1]. The sampling depth for SIMS is about 1-2nm, and characterisation of polymorphic systems by SIMS has not been demonstrated, so one would have to perform a lot of careful control experiments. With a reasonably large dataset, multivariate analysis may be able to distinguish the two polymorphs, and from the fragment ions, it may be possible to conclude that one had higher surface acid/base content than the other.

A critical evaluation of the acid base components of the surface energy of polymorphs using liquid contact angles could be carried out. A good approach for this study would be to look at liquid contact angles with macroscopic crystals using the van Oss-Good-Chaudhury method[2] to determine acid and base components for surface energy. However, one would still have to be very careful that the surfaces were not contaminated and X-ray photoelectron spectroscopy (XPS) and SIMS would be useful in this regard
.

Ampoule-breaking calorimetry can also be carried out to investigate the surface energertics of polymorphs. Ampoule-breaking calorimetry refers to the determination of the heat of dissolution when a solid is dissolved in a liquid.

Results from solution calorimetry give quantitative analytical measurements of polymorphic forms and can be correlated to other surface analytical techniques to provide insight into the nature of surface functional groups.

It was not possible to determine the surface area for all polymorphic systems because the proportion of nitrogen adsorbed was very low. It would be worth determining surface area using krypton gas, which has a lower vapour pressure. The surface area if determined can allow one to express acidity/basicity of the surface per unit area. Computational methods were employed in chapter six to determine the surface structure of IMC polymorphs. Simulating the interaction of a dye with different crystal faces by docking would help the fundamental understanding of dye –surface interactions.

The investigation into the thermally-induced polymorphic transformations of SFN polymorphs by DRVS could be further extended in order to build kinetic models of the transformation for better control of such process. This could involve studying transformation isothermally at other temperatures in order to determine the activation energy from a plot of ln k versus 1/T (giving a slope of –E/R and intercept of ln A) according to the Arrhenius equation:

$$k = Ae^{-E/RT}$$

Overall, the work reported in this thesis shows for the first time the surface characterisation of drug polymorphs based on the diffuse reflectance visible spectroscopic analysis of adsorbed pH indicator dyes. Differential coloration of adsorbed dyes reveals differences in surface chemistry at a molecular level. The intrinsic differences in the surface chemistry of crystalline drug polymorphs may be observed macroscopically as variations in properties such as chemical reactivity, stability and processing behaviour (e.g. compressibility, ease of wetting and powder flow)[3, 4]. Therefore, the DRVS analysis presented in this thesis may be a viable analytical method that pharmaceutical manufacturers can use to characterise the surface chemistry of polymorphs. Furthermore, thermally-induced polymorphic transformation has been successfully studied using this novel approach. Polymorphic transformations may occur during any stage of pharmaceutical processing and upon

storage of a drug substance. Characterisation of these transformations is important since the polymorphic form can significantly influence its processing behaviour and pharmacological activity. Results from polymorphic transformation studies could drive the development of DRVS as a process analytical tool (PAT) for *in situ* monitoring of polymorphic transformation during drug manufacture.

8.3 References

1.   C. Dass, *Modern mass spectrometry - Instrumentation and Applications in Diverse fields*, John Wiley & Sons, New Jersey, 2007.

2.   C. J. Van Oss, R. J. Good and M. K. Chaudhury, *Langmuir*, 1988, **4**, 884-891.

3.   X. Chen, K. R. Morris, U. J. Griesser, S. R. Byrn and J. G. Stowell, *Journal of the American Chemical Society*, 2002, **124**, 15012-15019.

4.   A. Heinz, C. J. Strachan, K. C. Gordon and T. Rades, *Journal of Pharmacy and Pharmacology*, 2009, **61**, 971-988.